

$C\beta$ C-Beta CBETA Conceptual Design Report

Cornell-Brookhaven ERL Test Accelerator

Editors: G. Hoffstaetter and D. Trbojevic

Contributors: J. Barley, I. Bazarov, A. Bartnik, I. Ben-Zvi, S. Berg, S. Brooks, D. Douglas, J. Dobbins, B. Dunham, R. Eichhorn, R. Gallagher, C. Gulliford, G. Hoffstaetter, Y. Li, M. Liepe, W. Lou, G. Mahler, f. Meot, M. Minty, R. Patterson, S. Peggs, V. Ptitsin, T. Roser, D. Sabol, E. Smith, J. Tuozzolo, D. Trbojevic, N. Tsoupas, H. Witte

May 5, 2016

Contents

1	Introduction [Georg]- 2nd draft 05/04	9
1.1	Executive Summary	9
1.2	Primary motivations	9
1.3	The L0E experimental hall at Cornell	10
1.4	NS-FFAG optics in an ERL	11
1.5	Phased Schedule	12
1.6	Optics and beam dynamics	14
1.7	Beam breakup	16
1.8	Injector	17
1.9	SRF cryomodule	18
1.10	RF power	19
1.11	Beam instrumentation and bunch patterns	19
1.12	Control system	20
1.13	Conclusion	21
2	Accelerator Physics	23
2.1	Accelerator Layout [Chris] - 1st draft due 04/28	23
2.2	Optics overview [Dejan] - 1st draft due 04/25	23
	References	26
2.3	Injector (IN) [Colwyn] - 1st draft due 04/28	26
2.3.1	Modeling the Injector Using General Particle Tracer	26
2.3.2	Low Emittance Measurements	27
2.3.3	High Current Measurements	27
2.3.4	Matching the Injector and Linac to the FFAG with Space Charge	27
2.4	Linac (LA) [Chris] - 1st draft due 04/28	28
2.5	Splitters (S1-4, T1-4) [Chris] - 1st draft due 04/28	28
2.6	FFAG arcs (FA, FB, ZA, ZB) [Scott] - 1st draft due 04/28	28
2.6.1	Hard Edge Design	29
2.6.2	Field Maps	30
2.7	Beam Stop (BS) [Chris] - 1st draft due 04/28	35
2.8	High-Energy Loop for Users [Dejan] - 1st draft due 04/25	38
2.9	Bunch patterns [Stephen] - 1st draft due 04/28	38
2.10	CSR [Chris] - will there be results?	40
2.11	Space Charge [Colwyn] - 1st draft due 04/28	40
2.12	Wakefields [Billing] - 1st darft due 05/04	41
2.13	Touschek scattering [Chris] - will there be results?	41
2.14	Beam Loss due to Gas Scattering [Gang Wang] - 2nd draft due 04/28	41
2.15	Orbit & Optics correction [Chris] - 1st draft due 04/28	42

2.16	Tolerances [Dave] - 1st draft due 04/22	42
2.17	Start-to-End Simulation [Chris] - 1st draft due 05/04	42
2.18	Beam instabilities: BBU	42
2.18.1	Introduction	42
2.18.2	Bmad Simulaion Overview	42
2.18.3	Bmad Simulation Result	42
2.19	Halo [William] - will there be results?	44
2.20	Collimation [Chris] - 1st draft due 05/04	44
	References	44
3	FFAG Magnets [Dejan]	45
3.1	Iron-based Permanent Magnet Design [Holger] - 1st draft due 04/28	45
3.1.1	General Concept	45
3.1.2	Finite Element Simulations	46
3.1.3	Requirements and Basic Magnet Design	46
3.1.4	Temperature Compensation	47
3.1.5	Quadrupole Corrector	47
3.1.6	Engineering	47
3.1.7	Magnet Designs for Different Energies	49
3.1.8	Corrector Magnets [Nick] - 1st draft due 04/28	49
3.2	Backup magnets: Halbach-type Design [Stephen] - 1st draft due 04/28	49
3.2.1	Comparison of Features vs. Iron Poled Magnets	49
3.2.2	Halbach Magnet Design	51
3.2.3	Tracking and Compatibility with FFAG Lattice	54
3.2.4	Window-Frame Correctors [Nick]	57
3.2.5	Halbach Magnet R&D and Shimming Results	64
3.2.6	Plan for BNL Cbeta Halbach Prototypes	71
3.2.7	Manufacturing Pipeline and Vendors	72
3.2.8	Early Cost Estimates for Wedge Blocks	73
3.3	Magnet Stands [Georg] - 1st draft due 04/28	74
3.4	Power supplies [John Barley]	74
3.4.1	Dipole and Quad Power Supplies for the Spreaders	74
3.4.2	Corrector Magnet Power Supplies	74
4	Injector [Bruce]- 2nd draft 05/04	81
4.1	Introduction	81
4.2	The DC Photoemission Gun	81
4.3	Photocathodes	88
4.4	The Laser System	89
4.5	Buncher System	92
4.6	Injector Linac	93
4.6.1	Introduction	93
4.6.2	Injector cavities	94
4.6.3	Injector input coupler	95
4.6.4	Wakefield and HOM calculations	98

4.6.5	Injector HOM dampers	100
4.6.6	Injector RF stability requirements and LLRF	101
4.6.7	RF Power System for the Injector Linac	103
4.6.8	Injector cryomodule	106
	References	111
5	Linac and RF systems[Matthias]- 1st draft due 04/28	113
5.1	Introduction	113
5.2	Module Layout	113
5.3	Cryomodule layout, design choices and components	113
5.4	Cryogenic Cooling Scheme	114
5.5	Piping Manifold	115
5.6	Mechanical Design	115
5.7	The Thermal Shield	116
5.8	SRF Cavities	117
5.9	HOM absorbers	119
5.10	Vacuum Vessel	120
5.11	Alignment	120
5.12	Fundamental Power Couplers	121
5.13	Magnetic Shielding	122
5.14	Parallel Flows	122
5.15	Assembly Process	122
5.16	Preparation for Testing	123
5.17	First Cool-down	123
5.18	Cool-down Cycles	124
5.19	RF Test Results	124
5.20	Tuning and Microphonics	124
5.21	Principles Governing the Baseline Design	125
5.22	Cavity	127
5.22.1	Cavity operating parameters: Q_0 , E_{acc} , and Q_{ext}	128
5.22.2	The baseline ERL cavity	128
5.22.3	RF design	128
5.22.4	Mechanical design	134
5.22.5	Cavity fabrication	136
5.22.6	Cavity treatment	138
5.23	Tuner	138
5.23.1	Design of the main Linac cavity tuner	139
5.24	HOM load	140
5.24.1	ERL main linac HOM load	142
5.25	Input coupler	143
5.25.1	ERL main Linac coupler design	143
5.26	Superconducting quadrupole and dipoles	145
5.26.1	Quadrupole design	145
5.26.2	Dipole design	146
5.26.3	Installation in the cryomodule	147

5.27	Cryomodule beam position monitor	147
5.28	Cryomodule	147
5.28.1	ERL Linac modifications to TTF-III technology	149
5.28.2	Cryomodule beamline components and lengths	150
5.28.3	Cryomodule components and assembly	150
5.28.4	Beamline string assembly	150
5.28.5	Cold mass assembly fixture and HGRP attachment	151
5.28.6	Beamline string attachment to HGRP	152
5.28.7	Cavity magnetic shielding and tuner	152
5.28.8	Liquid He, 5 K gas manifolds and thermal intercepts	153
5.28.9	100 K manifolds and thermal shield	153
5.28.10	Vacuum vessel and magnetic shield	155
5.28.11	Cryomodule and cavity alignment	156
5.28.12	Linac cryomodule heat loads	156
5.28.13	Cryomodule vacuum system	157
5.28.14	Cryomodule instrumentation	158
5.29	Manufacturing plan	159
5.29.1	Main Linac prototype cryomodule	159
5.29.2	Main Linac 64-module production	159
5.30	Tunnel Filling	160
5.30.1	General Considerations	160
5.30.2	Utility considerations	161
5.30.3	Safety considerations	161
	References	161
6	Cryogenics[Eric Smith]- 2nd draft 05/04	167
6.1	Overview	167
6.1.1	Thermal loads expected	167
6.1.2	Use of existing Wilson Lab cryoplant	167
6.1.3	Subsystem Components	167
6.2	Heat Exchanger Cans	167
6.2.1	Construction and Interfacing	167
6.2.2	Prior performance	167
6.3	Cryogenics for the Injector Cryomodule	167
6.3.1	Construction and Interfacing	167
6.3.2	Prior performance	168
6.4	Cryogenics for the Main Linac Cryomodule	168
6.4.1	Construction and Interfacing	168
6.4.2	Prior performance	168
6.5	Sensors and Controls for the cryogenics system	168
6.6	Safety Issues (that have already been considered for our prior test operations) .	168
6.7	Aspects still under development	168
	References	168

7	Vacuum System [Yulin]- 1st draft due 04/28	169
7.1	Layout	169
7.2	Requirements and Design	169
7.3	Construction, Installation and Operation	170
7.3.1	FFAG Arcs and Straight Sections	170
7.3.2	Spreaders and Recombiners	171
7.3.3	Ion Clearing	171
7.3.4	Construction and Installation	171
7.3.5	Pumping	172
7.3.6	Instrumentation	172
7.4	Vacuum Pumping Simulations	173
	References	173
8	Diagnostics and Control[Dobbins]- 1st draft due 04/15	177
8.1	Introduction	177
8.1.1	Beam position measurement system	177
8.1.2	Bunch Arrival Monitors	179
8.1.3	Beam Size	179
8.1.4	Beam Loss Monitors	180
	References	180
9	Personnel Safety[Heltsley]- 1st draft due 04/28	181
9.1	General considerations	181
9.2	More on Radiation Safety	183
9.3	Accident Rate and Training Compliance	183
9.4	Cbeta-specific safety challenges	184
9.4.1	New collaborators	184
9.4.2	Radiation safety	184
9.4.3	Cryogenic safety	185
9.4.4	Electrical safety	185
	References	185
10	Commissioning	187
10.1	Overview	187
10.2	Injector and Merger	187
10.2.1	Injector through Merger	187
10.2.2	Injector though Linac	187
10.3	FFAG First Pass	187
10.3.1	First Splitter	187
10.3.2	FFAG	188
10.3.3	Second Splitter	188
10.3.4	First Pass Energy Recovery	188
10.4	First Pass High Current	188
10.5	Multiple Passes	188
10.6	Summary	188

References	188
11 Cost Estimate[Bruce]- 1st draft 05/04	189
References	189

1 Introduction [Georg]- 2nd draft 05/04

[TODO: fix all references]

1.1 Executive Summary

The Cornell-BNL FFAG-ERL Test Accelerator ($C\beta$) will be a unique resource to carry out accelerator science and enable exciting research in nuclear physics, materials science and industrial applications.

$C\beta$ will comprise the first ever Energy Recovery Linac (ERL) based on a Fixed Field Alternating Gradient (FFAG) lattice. In particular, we plan to use a Non Scaling FFAG (NS-FFAG) lattice that is very compact and thus space- and cost- effective, enabling multiple passes of the electron beam in a single recirculation beam line, using the superconducting RF (SRF) linac multiple times. The FFAG-ERL moves the cost optimized linac and recirculation lattice to a dramatically better optimum.

The prime accelerator science motivation for $C\beta$ is proving that the FFAG-ERL concept works. This is an important milestone for the BNL plans to build a major Nuclear Physics facility, eRHIC, based on producing 21 GeV electron beams to collide with the RHIC ion beams [1]. A consequence of the $C\beta$ work would be the availability of significantly better, cost-effective, compact CW high-brightness electron beams for a plethora of scientific investigations and applications, such as X-ray sources, dark-matter and dark-energy searches, industrial high-power Free-Electron Laser (FEL) applications, and much more.

$C\beta$ brings together the resources and expertise of a large DOE National Laboratory, BNL, and a leading research university, Cornell. $C\beta$ will be built in an existing building at Cornell, for the most part using components that have been developed under previous R&D programs, including a fully commissioned world-leading photoemission electron injector, a large SRF accelerator module, and a high-power beam stop. The only elements that require design and construction from scratch is the FFAG magnet transport lattice.

This white paper describes a project that promises to propel high-power, high-brightness electron beam science and applications to an exciting new level. The collaborative effort between Brookhaven and Cornell will be a model for future projects between universities and national lab, taking advantage of the expertise and resources of both to investigate new topics in a timely and cost-effective manner.

1.2 Primary motivations

BNL is planning to transform RHIC to eRHIC by installing a new electron accelerator in the existing tunnel, providing polarized electrons with ^3He ions, or with ions from deuterons to Uranium. Significant simplification and cost reduction is possible by configuring eRHIC

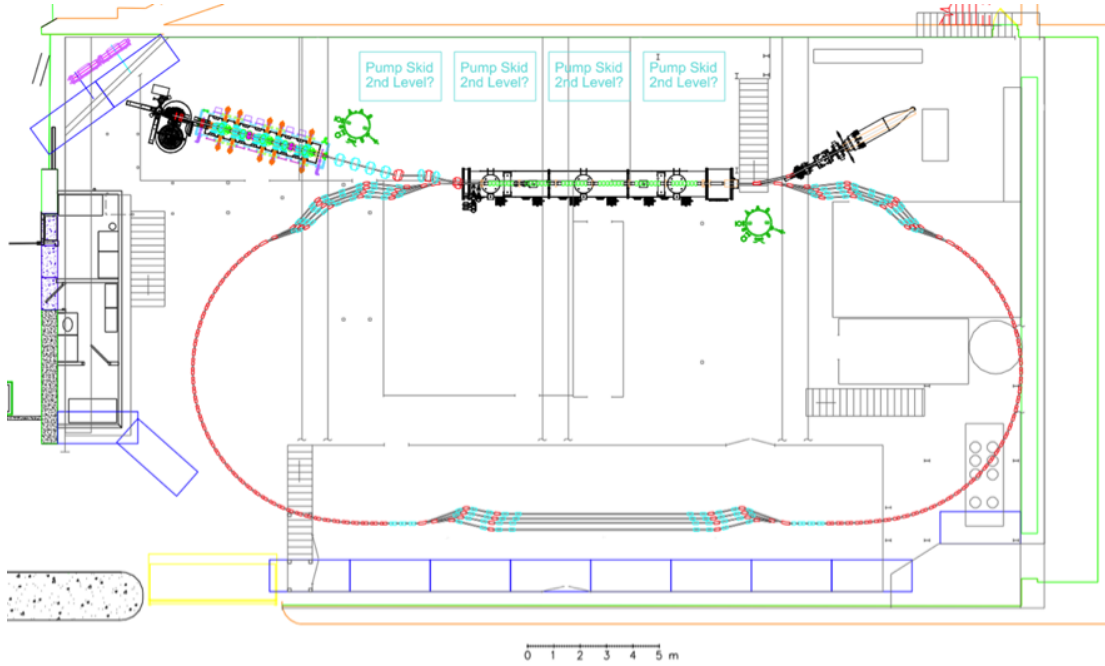


Figure 1.3.1: Possible floor plan of the Cornell-BNL FFAG-ERL Test Accelerator in the L0E experimental hall in Wilson laboratory.

with non-scaling, Fixed-Field Alternating Gradient (NS-FFAG) optics in combination with an ERL. Two NS-FFAG beamline arcs placed on top of each other allow multiple passes through a single superconducting linac. Such magnets and optical techniques will be prototyped in the Cornell-BNL FFAG-ERL Test Accelerator ($C\beta$), along with other innovative accelerator technologies, commissioning eRHIC instrumentation and confirming the theories for multi-pass recirculative beam breakup.

The high beam power and high brightness provided by $C\beta$ will also enable exciting and important physics experiments including dark matter and dark energy searches [2], Q-weak tests at lower energies [3], proton charge radius measurements, and an array of polarized-electron enabled nuclear physics experiments. High brightness, narrow line width gamma rays can be generated by Compton scattering [4] using the ERL beam, and can be used for nuclear resonance fluorescence, the detection of special nuclear materials, and an array of astrophysical measurements. The energy and current range of $C\beta$ will also be ideal for studying high power FEL physics for materials research and for industrial uses.

1.3 The L0E experimental hall at Cornell

Figure 1.3.1 shows the $C\beta$ lattice in the L0E experimental hall in Wilson laboratory at Cornell, while Tab. 1.3.1 lists the primary accelerator parameters. Figure 1.3.1 illustrates that there is sufficient space for all of the required hardware. At the bottom and at the right of the accelerator are external walls. The upper wall separates the area from the Cornell Electron Storage Ring (CESR), while on the left side are X-ray stations of the Cornell High Energy

Table 1.3.1: Primary parameters of the Cornell-BNL FFAG-ERL Test Accelerator.

Parameter	Value	Unit
Linac energy gain	61	MeV
Injection energy	6	MeV
Injector current (max)	100	mA
Linac passes	8 total: 4 accelerating + 4 decelerating	
7 energy sequence	67, 128, 189, 250, 189, 128, 67	MeV
RF frequency	1300	MHz
Bunch (laser) repetition rate	325	MHz
Circumference harmonic	333	
Accelerator circumference	64.34	m
Revolution period	0.2146	μ s
Normalised RMS emittance	2	μ m
Bunch Length	2 to 3	ps
Typical arc beta functions	0.5 (ranges from 0.05 to 2.5)	m
Typical RMS beam size	50 (ranges from 20 to 80)	μ m
Bunch charge: commissioning	1 to 125	pC
physics operation (CW)	1 to 500	pC

Synchrotron Source (CHESS).

The most expensive $C\beta$ components — the injector and the linac cryomodule — are already built and are available for use at Cornell. The L0E location is already served by significant accelerator infrastructure and other resources, including a liquid helium plant. $C\beta$ is an important part of future plans at Cornell for accelerator research, nuclear physics research, materials studies, and ERL studies.

1.4 NS-FFAG optics in an ERL

A first NS-FFAG proof-of-principle Electron Model for Multiple Applications (EMMA) was built and operated at Daresbury Laboratory in The broader concept of an FFAG was revived recently, but is not new, originally developed by three independent groups in the 1950's [6,7,8]. However, FFAG optics have not yet been used in combination with an ERL, a combination that is at the heart of the eRHIC design, and which is a core motivation for $C\beta$ accelerator physics prototyping. In eRHIC the advantages of NS-FFAG optics are evident: many passes with a shorter superconducting linac and only two electron beamlines in each RHIC arc sector. The $C\beta$ implementation will enable these prototype magnet and optical technologies to be studied. Advanced understanding of NS-FFAG beam dynamics will also spin-off into related applications, such as hadron therapy, gantry optics, multi-pass neutron generators, and Accelerator Driven Subcritical Reactor (ADSR) systems.

The NS-FFAG concept was originally developed as a solution for fast acceleration of short lifetime muons. Small dispersion functions lead to magnet apertures that are much smaller than with scaling FFAG optics [9]. General advantages include:

1. Energy range factors of 4 or 5 with constant, possibly permanent magnets.
2. Small physical aperture, small magnet size, and small orbit offsets.
3. Linear magnetic fields often enable the use of displaced quadrupoles.
4. Large dynamic apertures, with no non-linear magnets or fields.
5. Extreme focusing — very small Twiss and dispersion functions.

General disadvantages of NS-FFAG optics are:

1. Tune and chromaticity variation with energy.
2. Time-of-flight depends parabolically on beam energy deviation from the central reference energy.

1.5 Phased Schedule

Installation, commissioning and exploitation of C β will be performed in phases over several years. Installation and commissioning of the first ERL-FFAG (a single-turn machine) will be possible within two years, with multi-turn experiments using both 1.3GHz and 433MHz hardware occurring in the following years as the hardware becomes available. Note that as $433\text{MHz}=1.3\text{GHz}/3$, a 180 degree phase shift line can be designed for both, producing 1.5 RF periods at 1.3GHz and 0.5 periods at 433MHz. The major schedule phases, broken into stages and goals are:

A. Linac cryomodule only (year 1) *IN PROGRESS*

Clean out test area, move injector and linac module. Test injector for high current and cryomodule with RF and low current beam.

1. Clear out the experimental hall (3 months) *DONE*
2. Install the injector and linac cryomodule (3 months) *IN PROGRESS*
3. Install cryogenics and RF power (2 months)
4. Commission the injector and cryomodule (3–6 months)

B. Single-turn ERL-FFAG (26–86MeV, year 2)

Install FFAG loop with magnets for the lower energy range (up to 86MeV) and run the Cornell linac module in single-turn ERL mode with energy gain tunable between 20 and 80MeV. An electromagnetic optics matching line will be installed at both ends of the linac to match to the FFAG, adjustable for any linac energy in the range.

1. Install FFAG magnets and rest of return loop for low energy operation, including matching lines for a single energy (4 months)
2. Commission single-turn ERL-FFAG (3 months)
3. FFAG energy scan optics and correction studies (5 months)

World-first capabilities demonstrated:

- ERL using FFAG recirculating arc;
- NS-FFAG line with momentum acceptance factor of 4;
- Permanent magnets used as primary steering magnets for either FFAG or ERL return arcs (as in eRHIC);
- Adiabatic transitions from curved to straight FFAG lattices.

C. 4-turn ERL-FFAG with BNL 433MHz module (86MeV, year 3)

Install the BNL 433MHz cavity instead of the 1.3GHz Cornell one, in order to test current thresholds at the higher levels appropriate for eRHIC. The BNL cavity will operate with ~ 20 MeV energy gain per turn but with four ERL passes, so the other three optics matching splitter arms will be installed at both ends of the linac module. This can be operated as a 1, 2, 3 or 4-turn ERL with top energy of 26, 46, 66 or 86MeV. This step has some flexibility as in theory the extra splitter arms could initially be commissioned without the 433MHz module, or vice versa.

1. Install additional splitter lines for 4-turn operation (4 months)
2. Move 1.3GHz module to the side, install BNL 433MHz cavity (2 months, in parallel)
3. Commission BNL cavity running to dump (1 month)
4. Commission splitter lines settings and FFAG return loop with up to 4 turns (3 months)
5. Perform high-current experiments: BBU threshold etc. (4 months)

World-first capabilities demonstrated:

- Multi-pass superconducting ERL;
- Simultaneous transmission of factor 4 energy range through a NS-FFAG (and adiabatic transitions);
- Highest-ever energy NS-FFAG (beating EMMA at 20MeV).

D. Full-energy 4-turn with Cornell 1.3GHz module (286–326MeV, year 4 onwards)

The Cornell module can accelerate by up to 70–80MeV per pass, so by reinstalling it and upgrading the strength of the FFAG magnets by adding more PM material, it can be operated as a 4-turn ERL with a top energy of 286–326MeV for both FFAG and physics experiments.

1. Upgrade FFAG magnets in arcs for high energy operation (4 months)
2. Re-commission FFAG return loops at high energy and 1.3GHz module in multi-turn ERL mode (4 months)
3. FFAG experiments driven by BNL (open ended)
4. Physics experiments using high-energy beam driven by Cornell (open ended)

World-first capabilities demonstrated:

- Highest-ever energy NS-FFAG (again!)

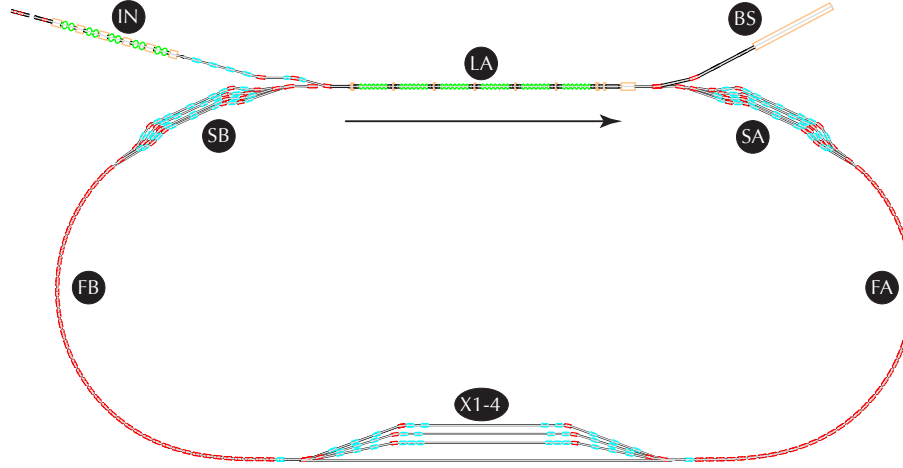


Figure 1.6.1: Major optical components. IN - Injector. LA - linac. SA, SB - splitter-combiner sections. FA, FB - FFAG arcs. X1-4 - experimental and diagnostic beamline sections. BS - beam stop.

The injector has already been tested, but needs to be relocated to a new area, re-commissioned, and The main linac cryomodule will not have undergone any testing before its installation. The first commissioning step is to cool down the entire system to 2 K, taking from one week to one month. Once cold, each cavity will be tested individually using a 5 kW solid state amplifier. Multi-cavity tests will be performed when more amplifiers are available. Cavity Q's will be measured, and the operation of the tuners, couplers and HOM's will be checked. Testing will take 3 to 6 months.

1.6 Optics and beam dynamics

Figure 1.6.1 shows the major optical components. Starting from the injector (IN), the beam is merged into the linac (LA) at 6 MeV, and accelerated in the first pass by 70 MeV. This lowest energy beam is separated from beams at other energies when entering the first splitter-combiner section (SA). It merges back with the other beams to travel on the 76 MeV stable orbit in the FFAG arc (FA), before being separated again in the experimental/diagnostic beamline section (X1-4), merging into FFAG arc (FB), followed by a second splitter-combiner section (SB) for matching into another accelerating pass in the linac. The process continues with 4 arc energies of 146 MeV, 216 MeV and 286 MeV, for a total of four accelerating passes. The path length on the fourth pass is chosen so that re-entry into the linac is on the decelerating phase, and so that energy is recovered in the remaining four passes through the linac. Finally the spent 6 MeV beam is directed to the beam stop (BS), which also includes 6D beam diagnostics.

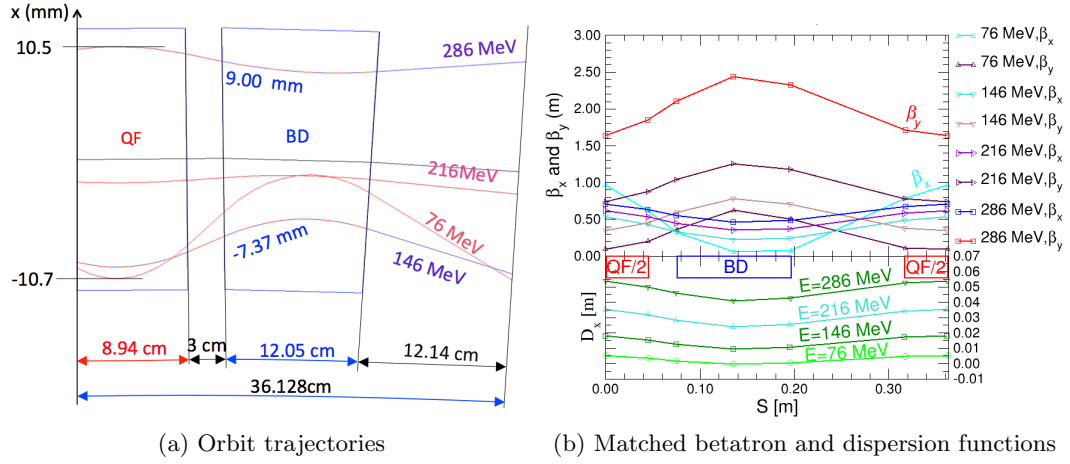


Figure 1.6.2: Radial offsets of the design orbits at the 4 arc energies, and matched betatron and dispersion values through the arc cell.

Table 1.6.1: NS-FFAG arc cell behavior. The path length through two FFAG arcs depends parabolically on the deviation of the arc energy from a reference value, because design orbits are radially offset by differing amounts from the arc magnet centers.

Arc energy MeV	H tune	V Tune	Path length difference mm
76	0.406	0.282	11.6
146	0.180	0.112	-81.3
216	0.126	0.059	-71.1
286	0.100	0.033	0

The somewhat complicated splitter-combiner sections are necessary for orbit correction and to match the relatively large transverse beams in the They also tune the net path lengths and momentum compaction factors to ensure efficient energy recovery. The experimental area offers space for further optics tuning and diagnostics. The arcs of the racetrack are made of doublet NS-FFAG cells, with a focusing quadrupole QF that is radially displaced by 5.4 mm, and a defocusing magnet BD that could be a displaced quadrupole, or a combined function magnet with only mid-plane symmetry.

Figure 1.6.2 shows the radial orbit offsets for the 4 arc energies, and the small values of the matched cell betatron and dispersion functions resulting from the very strong focusing, while Fig. 1.6.3 shows cross sections of the BD and QF magnets. Table 1.6.1 lists the tune-per-cell values and the path length differences for the 4 arc energies, while Tab. 1.6.2 shows the parameters of the arc unit cell.

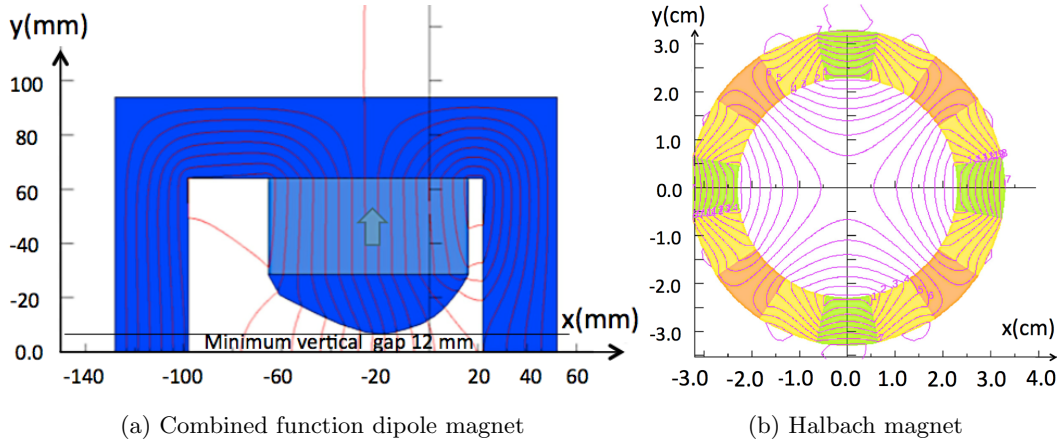


Figure 1.6.3: The BD defocusing iron-dominated combined function H-type magnet, with iron in dark blue and permanent magnet material in light blue. The QF focusing Halbach permanent magnet quadrupole, with an overall diameter of about 70 mm. There is ample room for vacuum pipe placement, despite orbit offsets in the range from -6 mm to +16 mm. All systematic multipole errors below 12-pole are zero, thanks to the 4-fold symmetry.

1.7 Beam breakup

The beam current in a conventional linear accelerator is typically limited by the electrical power available for acceleration. This limit is lifted in ERLs because the beam energy is fed back into the accelerating fields, but a new limit to the current is created by the beam-breakup instability (BBU). Higher Order Modes (HOMs) excited by the beam passing — more than once — through the SRF cavities give rise to the recirculative beam-breakup instability, when the current is too large, and/or when there are too many passes. This leads to large beam-trajectory oscillations and beam loss. A bunch traversing a cavity with a small dipole-HOM field receives a transverse kick. When this bunch returns to the same cavity it will therefore excite dipole-HOMs, thanks to the transverse offset caused by the initial transverse kick. If

Table 1.6.2: Lengths and angles of elements in the arc cell, defining a reference curve made of circular arcs and straight lines.

Element	Length mm	Bend angle mrad	Dipole field T	Gradient T/m
QF	89.4	24.219	0.21	-39.1
Drift 1	30.0			
BD	120.5	87.051	-0.56	25.42
Drift 2	121.4			
Total	361.3	$-2\pi/100$		

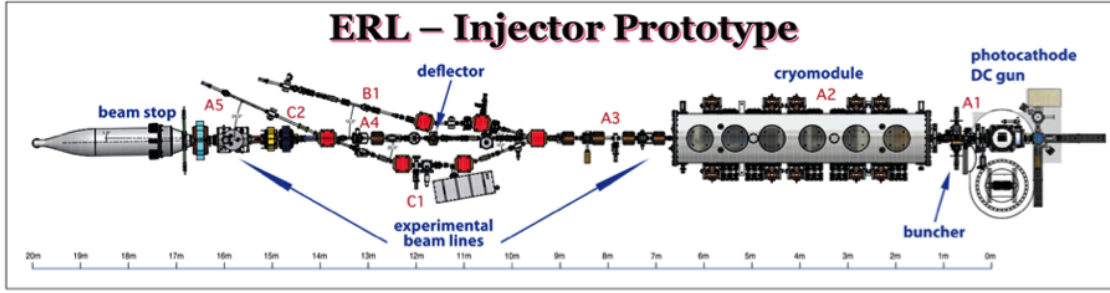


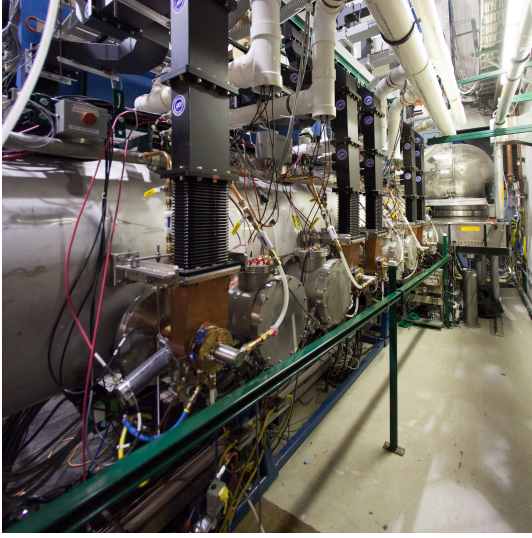
Figure 1.8.1: The photoemission injector currently operating at Cornell accelerates the beam to 6 MeV.

it excites the dipole-HOM in phase with the prior HOM field, then the transverse kick will increase and can eventually cause the beam to be lost.

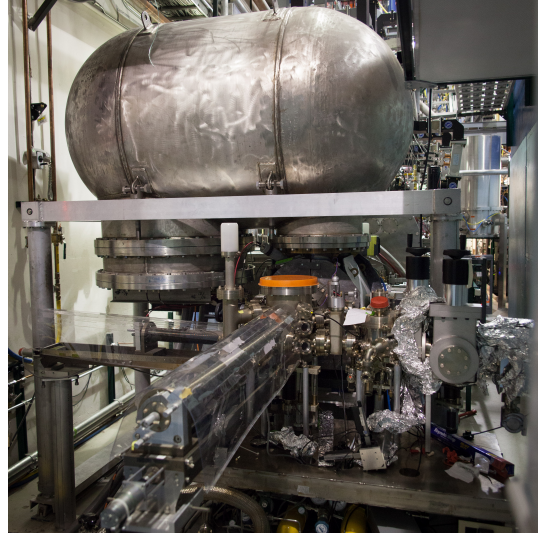
A rigorous theory shows that BBU can become very restrictive in multi-turn ERLs, with a threshold current that decreases with increasing N as $1/[N(2N - 1)]$, where N is the total number of accelerating passes [10]. Note that N can be large — it is 16 in a recent eRHIC design. Comparisons to theory were excellent in the experimental investigations of BBU at the JLAB FEL-ERL — including horizontal-vertical coupling, but only with one pass [11]. Multi-turn BBU has been studied at CEBAF, although not in an ERL [12]. The Cb accelerator will be the first to experimentally investigate multi-turn BBU in an ERL, a vital activity for eRHIC. Detailed simulations, using the codes developed at Cornell University for the HOM parameters of the designed ERL linac cryomodule [13] show that the BBU threshold for the proposed ERL test is between 40 and 350 mA depending on the betatron phase advance of the recirculating arcs. Thus, the simulated threshold is sufficiently high for the proposed ERL test loop with $N = 4$.

1.8 Injector

The photoemission electron injector shown in Fig. 1.8.1 and Fig. 1.8.2 is fully operational, and requires no further development. It has achieved the world-record current of 75 mA [14,15,16], and record low beam emittances for any CW photoinjector [17], with an equivalent brightness that outperforms the best existing storage rings by a substantial factor, if the injected beam were accelerated to a similar energy. Cornell has established a world-leading effort in photoinjector source development, in the underlying beam theory and simulations, with expertise in guns, photocathodes, and lasers. The strength of the injector group is in combining various cathode advances and innovations with the world's brightest photoinjector. This ability to both formulate the frontier questions for high brightness source development, and also to implement the solutions, makes breakthroughs in accelerator science possible.



(a) Injector cryomodule



(b) DC gun

Figure 1.8.2: The photographs show (from right to left) the high voltage DC gun, an emittance compensation section, the RF buncher, and the cryomodule. Accelerated beam is then directed into a beamline or into the beam stop.

1.9 SRF cryomodule

Figure 1.9.1 shows the full-scale prototype cryomodule that was developed and constructed as part of the It consists of six 7-cell 1300 MHz SRF cavities, including HOM absorbers and RF power couplers. The cavity geometry is carefully designed to maintain high Q while maximizing the beam breakup threshold current [18]. Cryomodule construction is complete, and the device is available for use in this project. The cryogenics necessary to cool the linac and injector cryomodules are available from the Wilson Lab cryoplant. Additional hardware will be required to transfer the cryogens from the cryoplant to the cryomodules, including heat exchanger cans, valve boxes and 2 K pump skids.

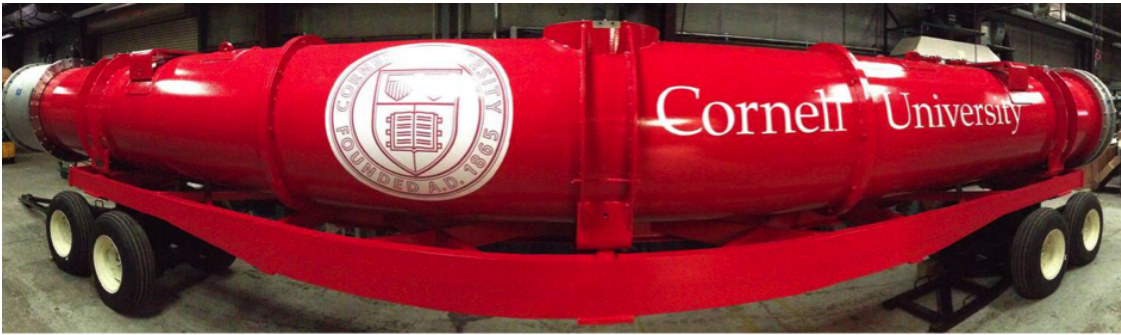


Figure 1.9.1: The full-scale prototype 1300 MHz cryomodule that is available for $C\beta$ use.

1.10 RF power

The injector delivers up to 500 kW of RF power to the beam at 1300 MHz. The buncher cavity uses a 16 kW IOT tube, which has adequate overhead for all modes of operation. The injector cryomodule is powered through ten 50 kW input couplers, using five 130 kW CW klystrons. The power from each klystron is split to feed two input couplers attached to one individual 2-cell SRF cavity. An additional klystron is available as a backup, or to power a deflection cavity for bunch length measurements. The main linac cryomodule will be powered by 6 individual solid-state RF amplifiers with 5 kW average power per amplifier. Each cavity has one input coupler. One amplifier is currently available for testing purposes, so an additional 5 amplifiers are needed for this project.

1.11 Beam instrumentation and bunch patterns

Beam instrumentation will support three operational modes:

1. Initial commissioning: one bunch with about 0.1 nC/bunch..
2. Physics operation: CW-like beams, for example with one accelerating (and one decelerating) low charge bunch in every RF period.
3. Dedicated experiment: eRHIC-like trains, typically with bunches spaced by more than 2 ns (3 RF buckets), and no more than 5 nC per bunch.

Figure 1.11.1 illustrates bunch pattern behavior in Physics operation mode, observing bunches as they pass a reference point at the end of the linac. Since each bunch is accelerated four times and decelerated four times, the maximum injection rate (that avoids overlapping bunches) is one quarter of the RF frequency. Overlap avoidance also requires the revolution harmonic, 279, to be an odd number. The maximum energy turn is shorter (or longer) than the other turns by half a wavelength, returning each bunch with the correct phase for deceleration.

The instrumentation design and commissioning strategy for CW, single-pass ERL operation is documented in [19]. With multi-pass ERL operation, a time-isolated ‘diagnostic’ bunch needs to be monitored. Bunch properties — including beam intensity and loss, position, energy, phase, transverse and longitudinal beam sizes — will be measured at different energies in the splitter-combiners, experimental straights, and in the beam stop. Optical function measurements enable beam emittance determinations. The broad range of beam parameters in the different operating modes requires careful study to determine if different hardware and/or signal processing electronics will be required.

Instrumentation prototyping goals motivated by eRHIC include developing and demonstrating:

1. A high time resolution BPM design. (BNL R&D is ongoing in FY15/16.)
2. Ion-clearing mechanisms to eliminate conventional ion trapping and fast ion instabilities.
3. High-bandwidth diagnostics for resolving beam sizes in the FFAG cells.

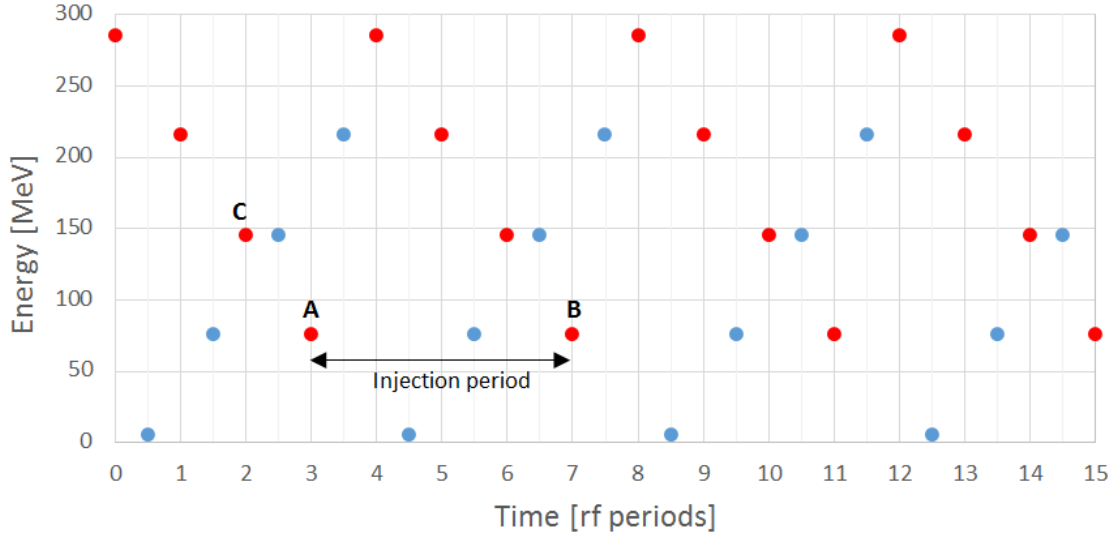


Figure 1.11.1: Bunches passing a reference point at the end of the linac, in **physics operation** mode with one accelerating bunch (and one decelerating bunch) in every RF period. Red and blue dots represent accelerating and decelerating bunches, respectively. Bunch B, injected 4 periods after bunch A, also has an energy of 76 MeV. Bunch C was injected 280 periods before bunch A, and so has an energy of 146 MeV because it has passed through the linac twice.

1.12 Control system

The accelerator will use EPICS [20] in order to minimize development time, ensure scalability, and avoid performance limitations. This choice enables the use of hardware and software already developed at Cornell and at BNL. It also provides access to well-defined interfaces at both the server and client levels that are used at many accelerator facilities, since EPICS has a large user base in the accelerator community. EPICS also has well defined developer interfaces and infrastructure allowing rapid development for new systems.

The control system enables supervisory control, automation, and operational analysis, with a scope that extends from the equipment interface to accelerator operators, and to experimenters and technical staff. It includes global systems such as timing, deterministic data communication, network communication, control room operations, automation and optimization, in addition to the computers and software required to implement and integrate all subsystems. The topmost layer of the client-server architecture provides access for non-real time activities, for example high level physics modeling using live or stored data. Accelerator operation and monitoring take place in a middle layer. A dedicated equipment layer, lower down, interfaces to specific equipment through point-to-point protocols. Other low level layers synchronize sub-systems (such as vacuum controls and personnel protection systems) with the accelerator at lower rates.

1.13 Conclusion

We have described a proposed collaborative effort between Brookhaven National Laboratory and Cornell University to design, build, and test a new type of energy recovery linac.

The FFAG-ERL has the potential to deliver excellent beam quality at a cost that is reasonable, compared to the current state-of-the-art, for a wide range of physics and applied physics applications.

This collaborative effort would be a model for future joint national laboratory/university projects, taking advantage of the expertise and skills that both offer, to develop exciting new technologies in a timely and cost-efficient manner.

This FFAG-ERL prototypes important features of the BNL eRHIC project.

All major technical components except for the FFAG arcs already exist at Cornell University, and have mostly been commissioned. Suitable space exists at Cornell, and planning for its refurbishment has already started.

2 Accelerator Physics

2.1 Accelerator Layout [Chris]- 1st draft due 04/28

2.2 Optics overview [Dejan]- 1st draft due 04/25

The revival of scaling Fixed Field Alternating Gradient (S-FFAG) accelerators in the recent two decades is very evident. They were previously developed in the 1950s, independently by Keith R. Symon [2] , Tihiro Okhawa [?] , and Andrei Kolomenski [?]. The S-FFAG have a very large momentum acceptance with beams accelerated within a constant magnetic field that varies across the aperture according to the scaling law $B \sim B_o(r/r_o)^k$, where k should be as large as possible ($k \sim 150$). The S-FFAGs revived concept mostly happened in Japan: initially the proof of principle (POP) proton accelerator at KEK was followed by the 150 MeV proton accelerator (presently at the Kyushu University), the 150 MeV accelerator at Osaka University, and many smaller size electron S-FFAGs built for different applications such as food processing. Although S-FFAGs have the advantages of fixed magnetic fields, zero chromaticity with fixed tunes, synchrotrons are still the dominant accelerators in spite of their requirement of pulsed magnets. This is mostly due to significantly smaller aperture requirements: a few cm in synchrotrons compared to 1 m for S-FFAGs, where large aperture magnets have to accommodate the orbit offsets. The international muon collider collaboration [4] proposed acceleration with a fixed magnetic field accelerators as the muon lifetime is very short and very difficult to switch fast enough the magnetic field using the synchrotron. The Electron Recovery Linacs cannot use synchrotrons as well it is not possible to change the magnetic field as fast as the electron acceleration occurs. So far, only the multiple beam lines were the solution have been used. The single FFAG can solve this problem.

To reduce the large required aperture Δx of S-FFAG author (D. Trbojevic [?]) came independently to the concept of Non-Scaling FFAG's (NS-FFAG) using the relationship between orbit offset Δx and momentum offset δp defined as $\Delta x = D_x * \delta p/p$. There was a publication by C. Johnstone [6] a few months earlier about a FODO cell NS-FFAG. Reduction of the aperture corresponds to a reduction of the dispersion function. If the dispersion is of the order of a few centimeters (3-4 cm) the orbit offsets will be 15-20 mm for $\delta p/p = 50\%$ or a total energy range of 3 times for relativistic particles. An additional important novelty in the NS-FFAG is that the magnetic field is a linear function across the aperture: $B_y = B_0 + G(s)x$ and $B_x = G(s)y$ in contrast to the non-linear radial field variation required in S-FFAGs. All magnets are linear combined function magnets. Abandoning the scaling law makes the tunes vary with energy, as well as the chromaticity. The time of flight is a parabolic-shaped function of energy. The minimum emittance for the synchrotron light source lattices also require minimum of the average value of the dispersion action function $\langle H \rangle$ defined as: $H(D, D') = (D/\sqrt{\beta})^2 + (D'\sqrt{\beta} + \alpha D/\sqrt{\beta})^2$ where D is the dispersion function, D' is the slope of the dispersion function, β and α are the betatron functions ([7],

[8]). The normalized dispersion coordinates are: $\xi = D/\sqrt{\beta}$ and $\chi = D'\sqrt{\beta} + \alpha D/\sqrt{\beta}$ or $H(D, D') = \xi^2 + \chi^2$. Consider a particle of momentum p and a reference particle with momentum p_0 and charge q ; the momentum offset is $\delta = (p - p_0)/p_0$. The reference particle is on a reference orbit (assumed planar) with local radius of curvature $\rho_0(s)$ and vertical field $B_0(s)$; the magnetic rigidity of the reference particle is $B_0\rho_0 = p_0/q$. The average value of the dispersion action $\langle H \rangle = (1/L) \int_0^L H(s) ds$, and the minimum is obtained by: $\partial(\langle H \rangle)/\partial D_0 = 0$, and $\partial\langle H \rangle/\partial(\beta_0) = 0$. The results obtained from two derivatives are the initial values of the horizontal betatron function β_o and of the dispersion function D_o at the beginning of the central defocusing bending magnet. The minimum orbit offsets are obtained if these two conditions are satisfied as previously shown [7]. An example of NS-FFAG minimum emittance lattice is shown in Fig. 2.2.1) The normalized dispersion function in the basic cell is shown in Fig. 2.2.2)

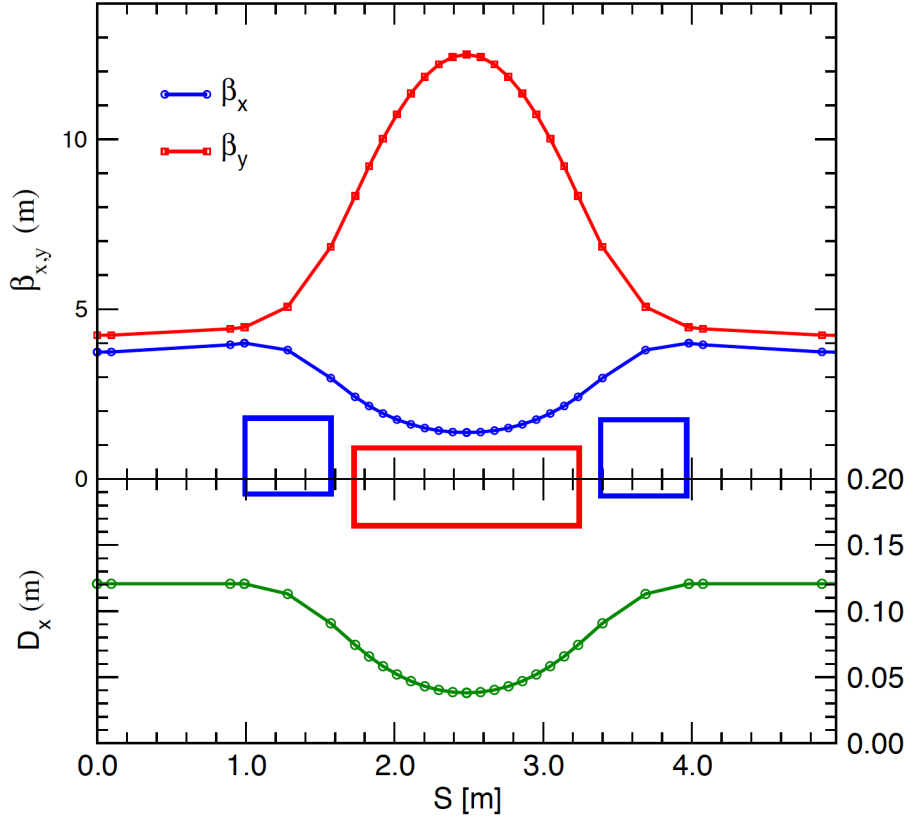


Figure 2.2.1: Betatron functions and dispersion in the basic cell with a central combined function dipole at the central energy

for three different cell designs: triplet cell shown in Fig. 2.2.1), and the FODO and doublet cells designed with the same magnets. The measure of the normalized dispersion function H is shown as the vector \sqrt{H} . It is evident that the triplet configuration is advantageous with

respect to the two other cases as the maximum orbit offsets, difference in the path length are the smaller [?].

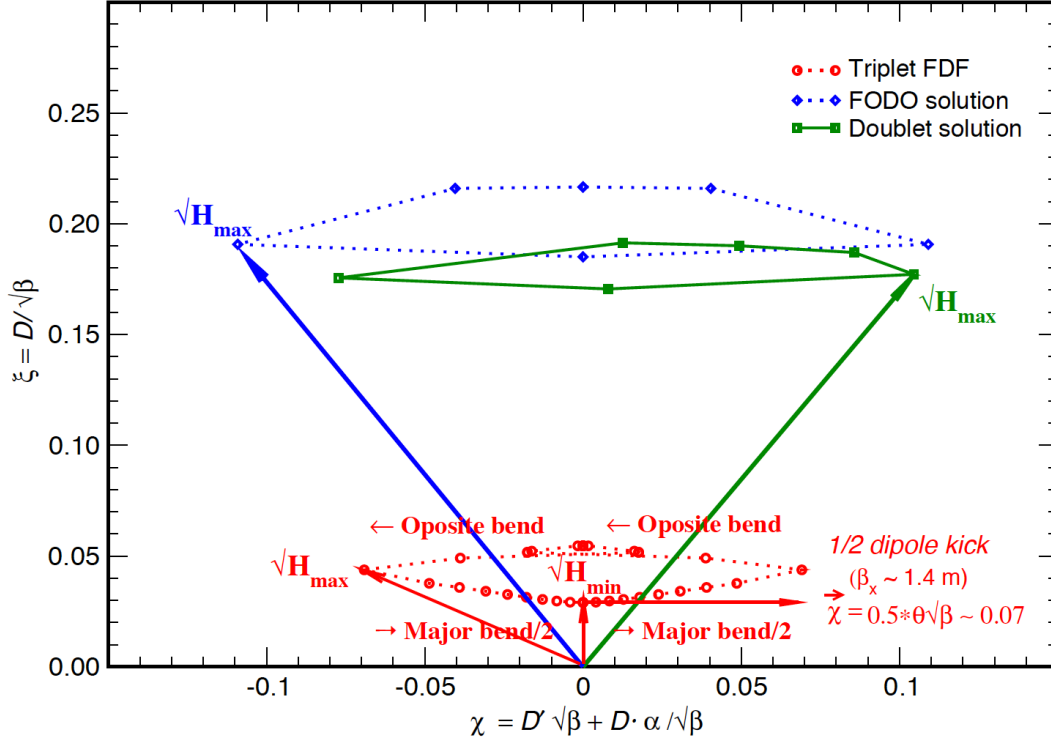


Figure 2.2.2: Normalized dispersion function in the basic cell for three designs: FODO cells, Doublets, and our TRIPLETS using the same magnets.

Applying the triplet configuration in the NS-FFAG becomes very difficult in the case of limited available space, as it was the case in the first NS-FFAG accelerator the proof of principle Electron Model for Many Application-EMMA [9] . The Cornell NS-FFAG arcs have limited available space and the triplet configuration might be too difficult to apply as two small drifts between the two focusing magnet, and the defocusing combined function magnet are only possible to use with Halbach magnet type as the interaction between neighboring magnets is very small. The iron dominated permanent magnets have significantly stronger cross-talk and required larger distance between the magnets. In the optimum triplet configuration the drift length might be a problem. The size of the magnets depends directly on the maximum orbit offsets within the magnets as the smaller the orbit offsets the smaller the magnet pole tips are. The optimum solution for the NS-FFAG cell are two kinds of combined function magnets: one with larger gradient focusing type with a small value of dipole field and the other with a smaller gradient of defocusing type, providing most of the bending dipole field. A compromise can be

achieved by using the displaced quadrupoles obtaining the combined function effect. This is on the expense on the magnet size and larger distance between the magnets to reduce the cross talk between the iron dominated magnets. The smallest values of the gradients was obtained by displacing focusing and defocusing quadrupoles in opposite directions. This condition makes the good field region to be at the two maximum orbit offset - one of the focusing quadrupole radially outward of the circular arc, and the other one of the defocusing magnet on the inward radial side of the magnet.

References

- [1] T. Ohkawa, University of Tokyo, Tokyo, Japan, FFAG structure suggested earlier at a Symposium on Nuclear Physics of the Physical Society of Japan in 1953 (private communication).
- [2] K. R. Symon, Phys. Rev. 100, 1247 (1955).
- [3] A. Kolomensky et al., Zh. Eksp. Teor. Fiz. 33, 298 (1957).
- [4] C. Ankenbrandt et al., "Status of muon collider research and development and future plans," Phys. Rev. ST Accel. Beams 2 (1999) 081001.
- [5] D. Trbojevic, E. D. Courant, and A. Garren, Sep 1999. Prepared for Workshop on Studies on Colliders and Collider Physics at the Highest Energies: Muon Colliders at 10-TeV to 100-TeV (HEMC 99), Montauk, New York, 27 Sep - 1 Oct 1999. Published in AIP Conf.Proc.530:333-338,2000. Also in *Montauk 1999, Colliders and collider physics at the highest energies* 333-338.
- [6] C. Johnstone, et al., Fixed Field Circular Accelerator Designs, PAC99, New York.
- [7] D. Trbojevic, E. D. Courant, and M. Blaskiewicz, Phys. Rev. ST AB 8, 050101 (2005).
- [8] Shinji Machida, "Fixed field alternating gradient" ASTeC, STFC Rutherford Appleton Laboratory, Didcot, United Kingdom, arXiv preprint, <https://arxiv.org/ftp/arxiv/papers/1302/1302.2026.pdf>
- [9] "Acceleration in the linear non-scaling fixed-field alternating-gradient accelerator EMMA", Machida, S. et al. Nature Phys. 8 (2012) 243-247 FERMILAB-PUB-12-308-AD.

2.3 Injector (IN) [Colwyn]- 1st draft due 04/28

2.3.1 Modeling the Injector Using General Particle Tracer

The injector dynamics are strongly space charge dominated. Consequently, the 3D space charge simulation code General Particle Tracer is used as the base model of the injector dynamics.

Description of Field Maps, Etc

1. DC Gun
2. Solenoid
3. Buncher Cavity
4. 3D Cavity Fields - made for zero current measurements, may need new fields for high current simulations

Modeling the Initial Electron Distribution

Can create arbitrary shaped distributions using subrandom sequences. Useful for simulating injector dynamics with measured laser data.

2.3.2 Low Emittance Measurements

In order to determine the injector settings that produce optimal emittances and peak currents, we ran Multi-Objective Genetic Algorithm (MOGA) optimizations using the 3D space charge code General Particle Tracer (GPT).

Measurements in the Merger Section

90% normalized transverse emittances for 19 (77) pC/bunch were 0.23 ± 0.02 ($0.510.04$) μm in the horizontal plane, and $0.140.01$ ($0.290.02$)m in the vertical plane, were measured respectively. These emittances were measured with a corresponding bunch length of $2.10.1$ (3.0 ± 0.2) ps, respectively. In each case the rms momentum spread was determined to be on the order of 10^{-3} . The beam energy was between 7.5-8 MeV.

Measurements in the Straight Section

2.3.3 High Current Measurements

65 mA World Record

2.3.4 Matching the Injector and Linac to the FFAG with Space Charge

MOGA optimizations for 100 pC/bunch, 6 MeV injector energy, and linac energy gain of 48.5 MeV have been performed in order to investigate the trade-off between the transverse normalized emittances and how well the Twiss parameters after the linac can be matched. 1 plot here showing optimal front. There is some trade-off at 100 pC. Further studies are underway to see if adding additional quads can reduce the trade-off.

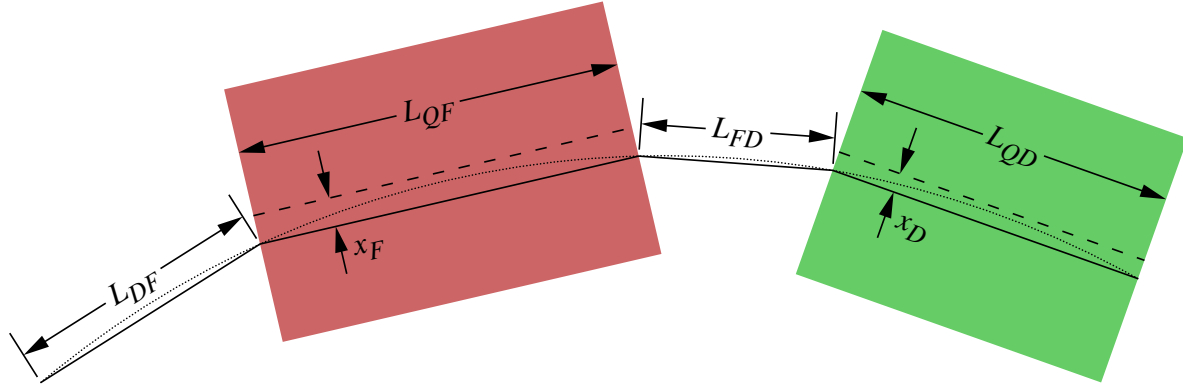


Figure 2.6.1: Arc cell geometry. The dotted line is an arc of a circle. The dashed lines are the centers of the quadrupoles.

2.4 Linac (LA) [Chris]- 1st draft due 04/28

2.5 Splitters (S1-4, T1-4) [Chris]- 1st draft due 04/28

2.6 FFAG arcs (FA, FB, ZA, ZB) [Scott]- 1st draft due 04/28

Each arc cell contains a focusing (F) and defocusing (D) quadrupole in a doublet configuration. The magnets have fields formed by iron poles, and are driven by permanent magnets.

The quadrupole axes are not centered on a reference orbit, but are offset from one another. The geometry we define for the arc cell is shown in Fig. 2.6.1. The magnets are laid out along a circle with a fixed radius. Each magnet or drift length is the length of a chord of that circle. The axis of each magnet is displaced from its chord by a given amount.

Engineering constraints create the basic constraints for the design:

- The long drift will be at least 11 cm of usable space to accommodate a variety of devices.
- The short drift will be at least 5 cm long to accommodate a BPM.
- The actual drifts will be slightly longer to allow for overhang of corrector coils and other magnet hardware.
- There will be at least 12 mm clearance from the closed orbits to the inside of the beam pipe, and the beam pipe could be up to 3 mm thick.
- The beam pipe will have an annular cross-section in the midplane.
- The size of the room dictates a maximum arc radius of around 5 m.

Because the orbits in the defocusing quadrupole are concentrated on the inside portion of the magnet, whereas in the F quadrupole they are distributed over a wider horizontal range and more toward the outside of the magnet, the requirement for the annular beam pipe cross-section brings the beam pipe very close to, if not under, the inside pole of the D quadrupole.

The beam pipe constraints therefore effectively require the D quadrupole to have a minimum size. As a result, there is no real gain in having the D quadrupole have a good field region below 34 mm.

The design proceeds in two stages. In the first stage, we create a hard-edge design that we will target. In the second stage, we lay out magnets according to the geometry of the hard edge design, and field maps will be created. These field maps are then adjusted to create lattice behavior very close to the hard-edge design.

2.6.1 Hard Edge Design

For a quadrupole with iron poles, driven by permanent magnets, the outer transverse size of the magnets is approximately proportional to $B_1 r_p^2$ where B_1 is the gradient and r_p is the pole radius. In practice our quadrupoles have large transverse sizes, so we will try to minimize that transverse size in our lattice design. This will mean in practice making the magnet sizes equal. This could be accomplished with the D and F magnets having different gradients and pole radii, but doing so only appears to result in a gain of 10% or so. Thus we choose the magnets to have identical gradients and beam excursions. Shorter drifts are also more favorable for magnet size, so we keep the drifts as short as tolerable from engineering constraints, namely 12 cm and 7 cm. Our studies showed that the magnets were smaller if excursions were smaller and the magnet aperture could reduce with that excursion. We thus constrain the beam excursions to the minimum good field region of 34 mm defined by the beam pipe constraints discussed above.

Given the size constraint of the hall and keeping specifications for the magnets reasonable, our studies indicated that a maximum energy of 200 MeV and a 5 degree bend angle per arc cell were a good choice.

Large horizontal tunes and low vertical tunes also reduce requirements on the magnets. However, the horizontal tune per cell will be constrained to be below 0.5 at low energy. Furthermore, we want to have some headroom at both the low and high energy end. Thus we constraint the horizontal half-integer tune to be at 49 MeV and the high energy vertical tune to be 0.036.

The design thus has 5 constraints (two tunes, orbit excursions in the two magnets, and centering the beam on the reference circle), and we have 5 adjustable parameters (a common gradient, two horizontal magnet displacements, and two magnet lengths). After optimization, the designs were adjusted slightly to make the magnet lengths an integer number of mm, relaxing the constraints on the high energy tune and the magnitude of the orbit excursion (allowing the vertical tune and the orbit radius to get slightly higher). The resulting design is given in Table 2.6.1.

Note that the gradients in the hard edge design are different despite what we said above. This is because the D quadrupole is shorter than the F quadrupole, and when the magnets are realized, the D quadrupole would have a lower gradient than the F quadrupole if it had the same transverse size as the F quadrupole. Thus the hard-edge design has the D gradient set to 93.5% of the F gradient to compensate for this. The 93.5% came from the iterative design process with field maps described below.

Table 2.6.1: Hard edge design parameters.

Injection Total Energy (MeV)	6	
Maximum Total Energy (MeV)	200	
Linac Passes	4	
Reference Radius (m)	5.156737	
L_{DF} (mm)	120	
L_{FD} (mm)	70	
α	F	D
$L_{Q\alpha}$ (mm)	135	125
x_α (mm)	-7.509	+20.783
Gradient (T/m)	+13.431	-12.558

2.6.2 Field Maps

The geometric layout from Table 2.6.1 and Fig. 2.6.1 was used to lay out the magnets. The physical length of the quadrupole iron matches the hard-edge quadrupole length. Three field maps are then constructed, each of which contains the iron for the all of the magnets in the cell. The field maps differ in whether the permanent magnets are installed in the individual magnets or whether there is just air in their place. The field maps thus have F, D, or both F and D powered.

Individual scaling factors are applied to the F and D field maps, and the field maps are translated thereby adjusting x_F and x_D . These four parameters are varied to and closed orbits are found for the field maps so as to meet four constraints: the low energy horizontal and high energy vertical tunes are set to their design values; the beam is centered on the reference circle; and the maximum orbit excursions in the magnets are identical. In practice the high energy vertical tune target is raised to 0.039 to keep the tunes for all energies below the maximum above 0.036, since the tune reaches its minimum somewhat below the maximum energy with the field maps (whereas its minimum is at the highest energy for the hard edge model).

To estimate corrections for the differences, due to nonlinear behavior in the iron, between the sum of the F and D field maps and the combined field map, we adjust these same parameters to match the tunes, center radius, and excursion difference with the field maps summed to those same quantities with the combined field map.

A new set of field maps is then created with different amounts of permanent magnet material and different values for x_F and x_D based on the corrections estimated from this calculation. The process is repeated until the the combined field map matches the behavior of the design lattice.

We carried out this process on earlier iterations of the lattice, and gained a good idea of what the corrections would be. We applied these corrections to the hard edge design from Table 2.6.1, using the factors given in Table 2.6.2. The gradients for the resulting field map are shown in Fig. 2.6.2. Further iterations could be performed, but we were ultimately satisfied with the performance of this first pass. The magnetization given in that table is an

Table 2.6.2: Additions to the hard edge displacements for the real magnets, and the magnetization of the permanent magnets in the magnets, determined using field maps.

x_F (mm)	+3.364
x_D (mm)	-2.626
Magnetization (T)	1.0954

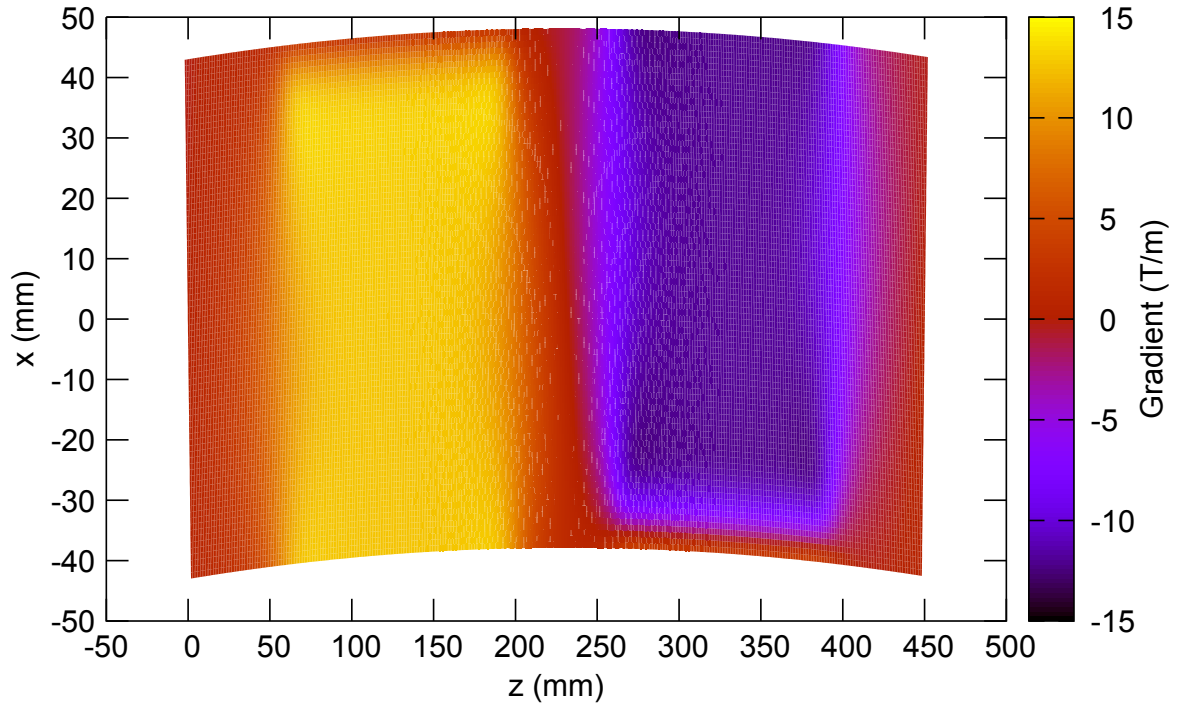


Figure 2.6.2: Gradients in the radial direction for the field map we used.

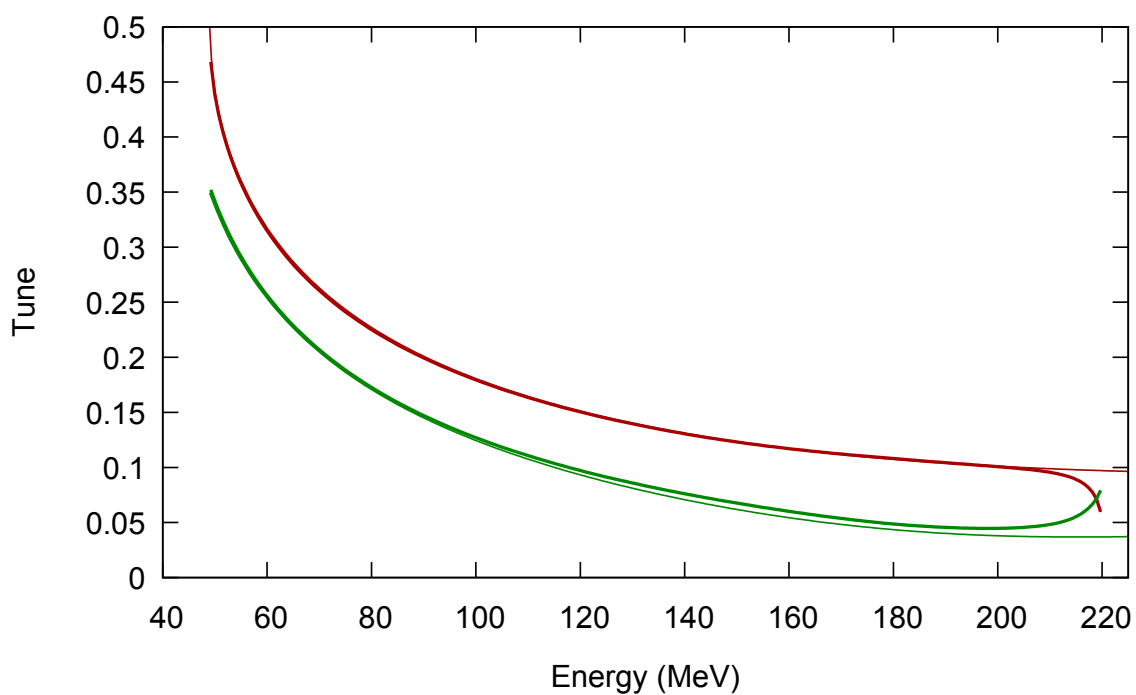


Figure 2.6.3: Horizontal (higher) and vertical (lower) tunes as a function of energy. Thick lines are for the field map, thin lines are the hard edge design.

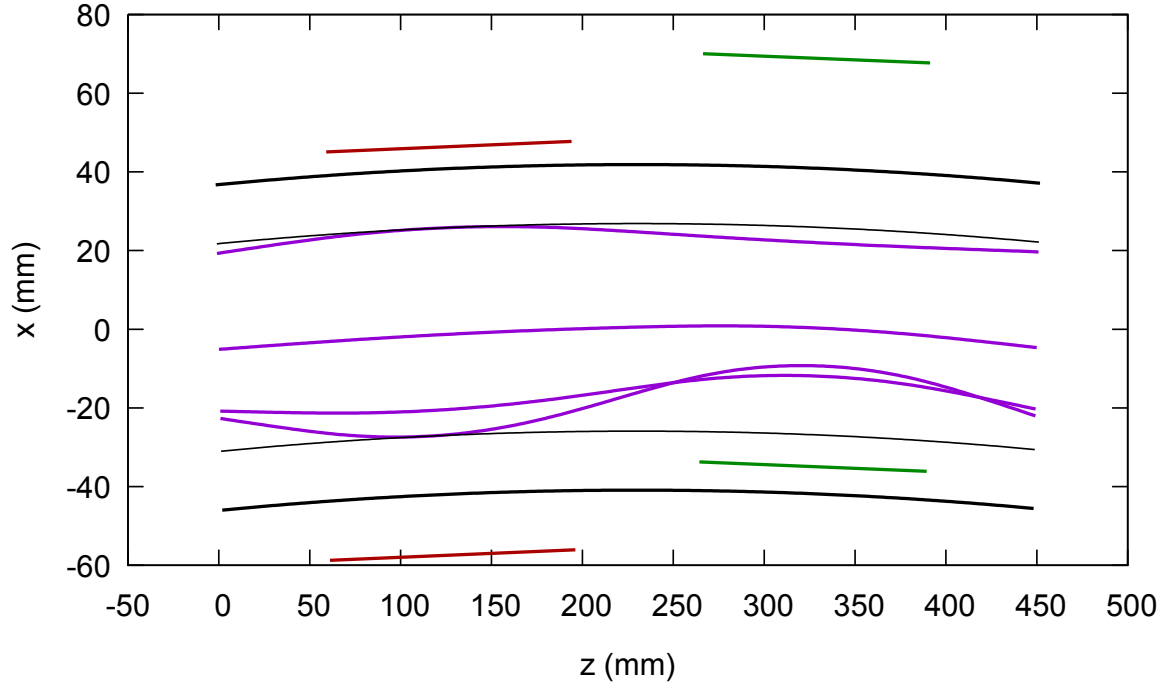


Figure 2.6.4: Closed orbits, stay-clear regions for a pipe, and magnet pole positions. Violet lines are closed orbits at the design energies. Thick lines are arcs which have a minimum horizontal distance of 15 mm from the beam; they outline the minimum enclosed region for a 3 mm thick beam pipe in the midplane. Thin lines are arcs at the extremes of the horizontal beam excursion. They bound a region where the inside height of the pipe must be at least 12 mm. Short straight lines are the position where the magnet pole is at its minimum height.

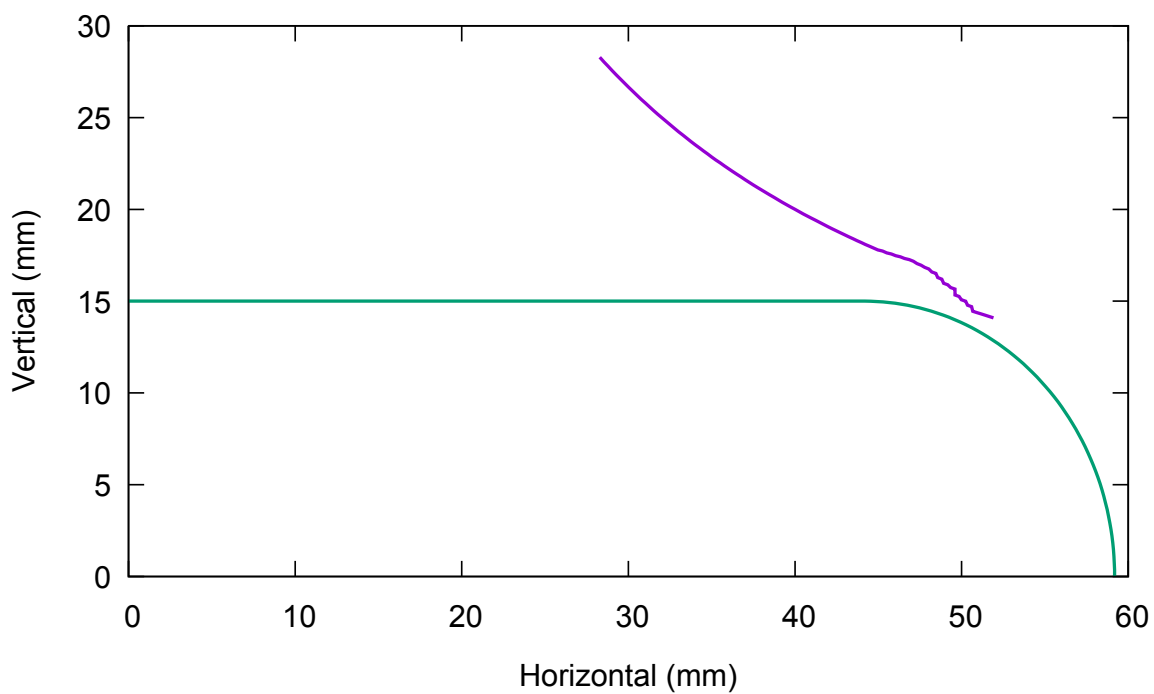


Figure 2.6.5: Inner edge of the pole face (voilet) and the minimum approach of a region required for an annular region that stays 15 mm away from the beam everywhere (also see Fig. 2.6.4). This point of closed approach is at a corner of the D magnet.

effective magnetization that includes temperature compensation material and space required for assembly. Figure 2.6.3 shows the tunes we obtained, and Fig. 2.6.4 shows the closed orbits.

Figure 2.6.4 in combination with Fig. 2.6.5 show that the magnet poles can clear a beam pipe that meets the requirements. There is over 2 mm or horizontal distance between the pole and the stay-clear region for the pipe. That space should be maintained in the beam pipe design, and a mechanism to shift the magnets horizontally should be in place in case a systematic deviation in the production magnets from the design field maps occurs.

2.7 Beam Stop (BS) [Chris]- 1st draft due 04/28

The primary beam dump must intercept the full beam current at the end of the energy recovery process, and safely dissipate the beam power as waste heat. The dump was originally designed to handle 600 kW of average power at a maximum energy of 15 MeV. For this project, the maximum current is 40 mA with an recovered energy of 6 MeV, so the existing hardware will be more than adequate.

The range of 15 MeV electrons is less than 8 g/cm² in practical beam dump materials, and thus the beam power is deposited over a very small depth. The natural beam spot size is quite small, even after energy recovery. The effective area of the beam then needs to be expanded to more than 1 m² where it intercepts the surface of the dump, to reduce the power density in the dump material to a level that can be safely handled. This expansion can be accomplished by several techniques, such as strongly defocusing the beam, rastering the beam over a larger area, or intercepting the dump surface at a shallow angle. All of these methods will be employed for the primary dump. Clearly the dump material must have a reasonably high-thermal conductivity, to limit the maximum temperature at the uncooled entrance face of the dump. As there is no significant shower multiplication from 15 MeV electrons, the surface of the dump, which is furthest from the cooling water, will have the highest temperature.

The only practical choice for the primary dump material is aluminum. Aluminum offers the very significant advantages of a high-photoneutron threshold (13.3 MeV) and relatively low-residual radioactivity comprised primarily of short-lived isotopes. The relatively low-residual radioactivity of aluminum is a significant consideration for the ultimate disposal of a decommissioned beam dump. The aluminum used will be an alloy, and the various alloying elements have lower photo-neutron thresholds. These elements will be responsible for a fraction of the residual radioactivity of a 15 MeV aluminum dump. Copper has a significantly lower photoneutron threshold, and much higher residual radioactivity of longer-lived isotopes. Beryllium would be exceptionally expensive, and has a very low photoneutron threshold. Carbon, as pyrolytic graphite, is mechanically difficult, and has an extremely anisotropic thermal conductivity.

The dump must remain fully functional during several decades of operation at very high average power. With an aluminum dump, it is especially critical to control the water chemistry to avoid corrosion. Therefore, heat will be removed from the primary beam dump with a closed circuit de-ionized (DI) water circulation system, which will be continuously powered. The only acceptable metals in this system are aluminum and stainless steel. The water chemistry will be carefully monitored at all times to assure proper pH, resistivity, and the absence of harmful ions.

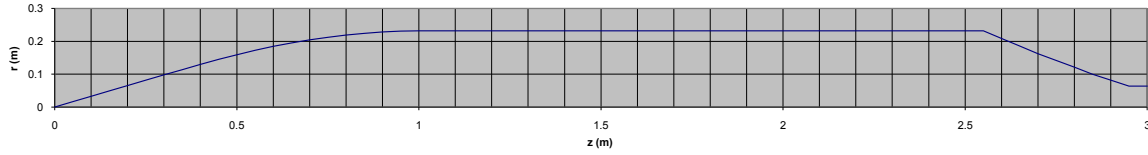


Figure 2.7.1: The inner surface profile of the beam dump

It is very desirable to minimize the deposition of beam power directly in the cooling water, to minimize hydrogen production through radiolysis [1]. At the same time, it is desirable to locate the cooling water as close as practical to the interior surface of the dump to minimize thermal effects. These realities led directly to the use of a dump shaped like an ogive (pointed arch) of revolution, similar to a high-power klystron collector. Even with an optimum thickness dump wall, there will be enough radiolysis in the cooling water to require monitoring the hydrogen level in the closed cooling circuit. It is anticipated that the modest quantities of hydrogen generated can be vented to the atmosphere, with no need for hydrogen recombination systems. Were hydrogen recombination to prove necessary, reliable hydrogen recombination systems were developed for the high-power beam dumps at SLAC, and were duplicated, with improved instrumentation, for the high-power dumps at Jefferson Lab [1, 2]. The 15 MeV beam energy is far too low to produce either tritium or ^7Be through spallation of oxygen, so there will be no direct long-lived radioactivity in the DI water circuit. Heat will be removed from the closed DI water circuit with a water-to-water heat exchanger. The pumps, deionization and filtration equipment, surge tank, hydrogen-venting scheme, and water-to-water heat exchanger will be located remote from the dump itself, to allow servicing and to eliminate any potential for radiation damage. All plumbing and piping in the closed-circuit system will be of either aluminum or stainless steel.

The primary dump will be a powerful source of prompt, low-energy gamma radiation as well as a modest flux of low-energy neutrons. The primary radiation shielding for the dump will consist of steel and concrete blocks that completely surround it. Detailed calculations of the total radiation from the dump have been made with the code MCNPX.

If the dump were to be operated in normal air, significant quantities of nitric acid could be produced by radiolysis of nitrogen, leading to the production of nitric oxide, which oxidizes to form nitrogen dioxide, which, with water, forms nitric acid. As a consequence, dump area may need to be purge with an inert gas to eliminate the possibility of nitric acid formation. This solution has proven very effective with the two high-average power (1 MW) beam dumps routinely operated at Jefferson Laboratory.

Although it is very desirable to isolate the dump from the accelerator vacuum system, this is simply not possible. For example, even in a beryllium window, the power deposition from the dE/dx losses of a 100 mA average current beam is 30 kW per mm of window thickness (the window thickness is irrelevant for cooling considerations). It is certainly not practical, and likely not possible, to remove such a large amount of heat from a thin window in vacuum. Thus, the beam dump will of necessity be within the accelerator vacuum system. A differential vacuum pumping system will be used to isolate the high-gas load from the dump when operating at high average beam power from the much lower pressure in the beam line from



Figure 2.7.2: The completed beam dump before installation of the shielding blocks.

the accelerator. Finally, a reasonably fast-acting, RF shielded gate valve will be located well upstream of the beam dump, to provide protection to the accelerator in the event of a dump failure. This is very important as the superconducting Linac is relatively close to the primary beam dump.

The profile of the inner surface is shown in Fig. 2.7.1. The 3-meter-long dump was assembled from three shorter segments by electron beam welding. A photograph of the completed dump is shown in Fig. 2.7.2. Water cooling channels are machined in the outer surface of the dump body, which is mounted inside an aluminum jacket. To reduce thermal stresses, the dump body is free to move longitudinally within the jacket. GEANT was used to calculate the power deposition in the dump body, and ANSYS calculations then determined the temperatures throughout the dump, the thermal stresses, etc. The results of some of these calculations are given in Fig. 2.7.3. Beam on-off cycles are sudden, and result in rapid temperature changes, which in turn may lead to eventual fatigue failure. The water flow was chosen to limit the maximum temperature differentials in the dump, leading to a very large number of temperature cycles before the onset of fatigue failure. For the design of a 60 gpm water flow, the flow velocity is only 1.71 m/sec. Erosion of water channels will therefore not be a problem.

Two active devices are used to enlarge the beam area at the dump surface – a quadrupole that strongly over-focus the beam, and a sextupole with the coils powered such that one can make an arbitrary ellipse shape. The final result of the quadrupole field and sextupole kick is a raster pattern that move the beam spot in a circular path at 60 Hz. If either of these devices failed, the dump would rapidly overheat, quite possibly to the point of damaging, or even melting the dump surface, particularly if there were a transition from nucleate to film boiling at the water-metal interface. Redundant hardwired interlocks will assure that each of the beam focusing and rasterring magnets is properly powered. On any interlock failure, the beam will be aborted. Similar interlocks will be provided on the cooling water flow, pressure differential, and temperature. Field strengths, cooling requirements, and sweep amplitudes of the said system for this design are based on previous operational experience.

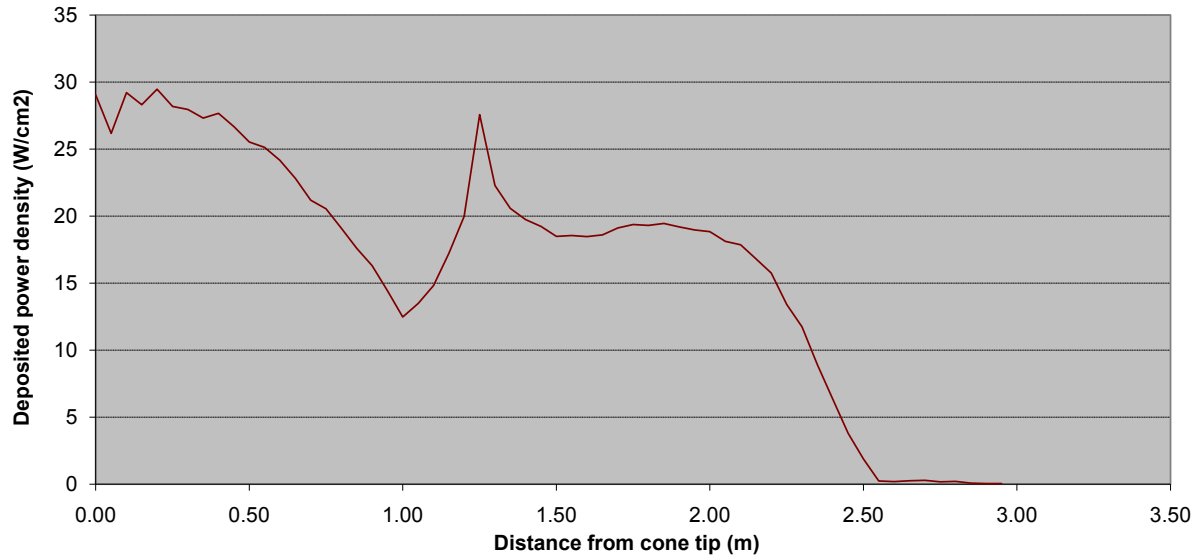


Figure 2.7.3: Energy deposition for 600 kW beam power at optimized condition

It is important that the beam is not only properly enlarged, but that it is also correctly positioned in the dump. A quadrant detector at the entrance to the dump will assure the correct beam size and position at the dump entrance, while upstream BPMs will assure the correct entrance angle. Each element of the quadrant detector will cover close to 90 degrees of azimuthal angle, and will intercept a very small fraction of the beam. The elements must be water-cooled, protected from RF heating, and the ceramics providing electrical isolation shielded from the possibility of charging from stray scattered electrons. Basically, each element is a low-efficiency Faraday cup, and thus must be thick enough to assure beam electrons are dumped. Interlocks on the amplitude of the DC and 60 Hz left-right and up-down difference signals assure that the quadrupole over-focusing and raster amplitude are correctly set, and that the beam centroid is properly centered on the dump.

The existing beam dump has been tested up to power levels of 350 kW, so no problems are expected with the maximum beam parameters of 6 MeV and 40 mA for the Cbeta project.

2.8 High-Energy Loop for Users [\[Dejan\]](#)- 1st draft due 04/25

2.9 Bunch patterns[\[Stephen\]](#)- 1st draft due 04/28

C β will support multiple operating modes, single pass and multi-pass/multi-energy, pulsed and CW, with and without energy recovery. Many of these modes are only intended for commissioning and machine studies. High current running of C β is only possible with energy recovery. How the beam position monitor(BPM) system operates will be a function of the operating mode.

The RF cavities in the C β linac operate at 1300 MHz. The injector must supply bunches at a sub-harmonic of this frequency. The multiple passes of these bunches through C β produce

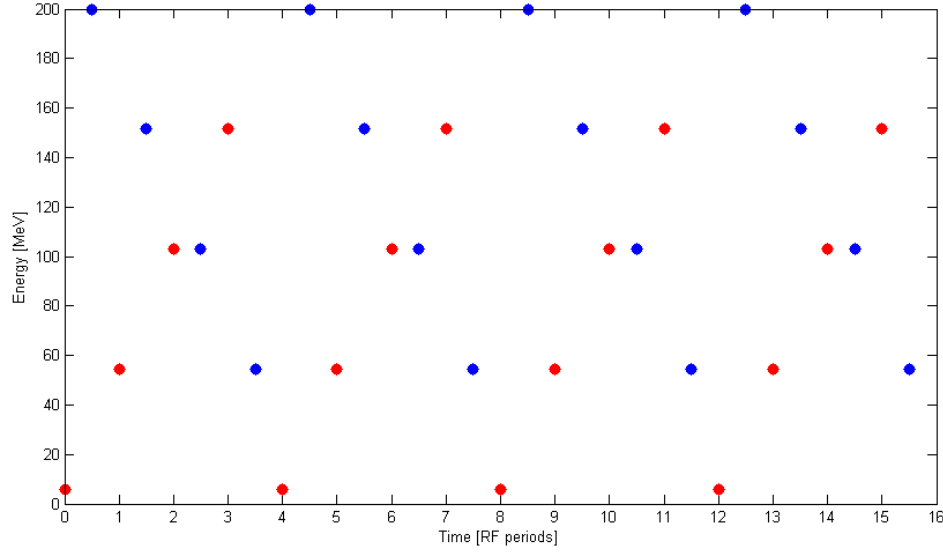


Figure 2.9.1: Bunches passing a reference point at the start of the linac, with one accelerating bunch and one decelerating bunch in every RF period. Red and blue dots represent accelerating and decelerating bunches, respectively.

inter-bunch timing patterns which depend on the injection frequency and the revolution period. Additionally the decelerating bunches much have a timing which is an integer + one-half RF cycles offset from the accelerating bunches.

Figure 2.9.1 illustrates the bunch timing pattern at the start of the the linac for bunches injected at 325 MHz (1300/4 MHz).

For the case of injection at 325 MHz the BPMs would see a different energy bunch with a different orbit every half RF cycle (385 ps). To resolve the orbit of each species the BPMs would need to be able to resolve signals from bunches separated by this amount. Moreover the FFAG optics correction requires being able to make orbit measurements at many locations, perhaps up to every other arc magnet cell. This would require a large number of high bandwidth electronics channels which would be prohibitively expensive. Additionally, the aggressive schedule for $C\beta$ precludes the development of new electronics solutions. A survey of existing BPM electronics indicates the ability to resolve bunches separated by several ns.

Injection at lower frequencies produces more widely spaced bunches, however the time spacing of the bunches is generally irregular with some inter-bunch gaps being large and some small. The revolution period of $C\beta$ is 333 RF cycles. For this revolution period a unique case exists for injection at 1300/63 MHz (20.635 MHz). This case results in regularly spaced bunches separated by nine RF buckets modified by the fact that accelerating bunches are offset by 1/2 RF cycle relative to decelerating bunches. The result is that the BPM will see signals from different energy beams separated by 8 1/2 or 9 RF cycles, i.e between 6 and 7 ns, within the time resolution capability of existing BPM system implementations. In this case a time-domain BPM system would acquire position information on each bunch which would then be averaged by species over multiple turns.

This mode of operation would provide orbit information for each species at each BPM which will be essential for machine commissioning. During commissioning injection can be further modulated (limited to trains of bunches at 1300/63 Mhz) to allow operation at very low currents but with bunch charge representative of high current operation. Injection at 1300/63 MHz will allow for for a per energy beam current of 2 mA at 100 pC bunch charge and therefore enables achievement of all the Key Performance Parameters.

Note the following provisos to this solution:

- This solution is tied to a specific revolution period, 333 RF cycles. If the revolution period is changed this solution can be broken.
- In full energy recovery operation, i.e. 4 accelerating and 4 decelerating passes in the linac, the bunch injected into the linac and the bunch being decelerated for delivery to the dump are only 1/2 RF cycle apart. There are no BPMs in the linac so this is not an issue in the linac. however there are two sections of beam-line, the first between the ring injection point and the linac and the second between the linac and the exit to the dump, where resolving these two bunches will not be possible.
- Shaping of the BPM pick-up signal to a relatively flat top pulse without a long tail is required. This was accomplished in EMMA using a strip-line coupler and a mixer. [?]
...

To operate at higher currents the injection scheme must change. One possible scheme is injection at 325 MHz (1300/4 MHz) with periodic gaps in the bunch stream containing a single pilot bunch. This is illustrated in Figure 2.

For the BPMs to see the pilot bunch separated from other bunches of different energy beams it is additionally necessary for the gap containing the pilot bunch to be preceded and followed by additional gaps separated from the pilot bunch gap by a revolution period. Figure 3 shows the gap containing pilot bunch plus additional preceding and following gaps.

The same time domain BPM electronics that is used in the low frequency injection scheme serves here also. Each BPM measures the pilot bunch as it passes with successively increasing then decreasing energy.

2.10 CSR[Chris]- will there be results?

2.11 Space Charge[Colwyn]- 1st draft due 04/28

In addition to being simulated through the injector and linac,space charge effects through the first pass (55 MeV) of the CBETA lattice have been simulated using a high energy Gaussian beam space charge model found in BMAD (ref). This model has been benchmarked for the simple case of a long drift against the 3D space charge code General Particle Tracer (GPT). These results demonstrate that space charge is negligible for the lowest energy passes in CBETA, and thus only require simulation through the injector through the first linac pass, and subsequently from the last linac pass to the dump.

Plots: (1) BMAD space charge benchmark against GPT in drift.

(2) BMAD comparison 1st CBETA pass space charge on/off.

2.12 Wakefields[Billing]- 1st darft due 05/04

2.13 Touschek scattering[Chris]- will there be results?

2.14 Beam Loss due to Gas Scattering[Gang Wang]- 2nd draft due 04/28

Electrons in the beam can interact with residue gas molecules left in the vacuum chamber, leading to beam losses and formation of the beam halo. In addition, the lost high energy electrons may further induce desorption of the vacuum chamber and quenches the superconducting components.

Beam losses due to two types of beam-gas scattering have been analytically estimated for c-ring: elastic scattering and Bremsstrahlung. The elastic scattering of the electrons in the beam off the residue gas molecules can change the trajectory of the electrons and excite betatron oscillation. If the scattering angle is larger than the deflection angle aperture set by the collimator, the electrons will get lost at the location of the collimator [1, 2]. In the process of Bremsstrahlung, an electron in the beam scatters off the gas nucleus and emit a photon, which results in an abrupt energy change of the electron. If the energy change is beyond the energy deviation aperture, the electron will also be lost [1]. Using the parameters listed in table 1, the beam losses due to gas scattering in the c- ring are analytically estimated and shown in fig. 1. Due to their low charge state, beam losses due to H2+ and CO2+ are found at least one order of magnitude less than that induced by N7+. To estimate beam losses in the worst case scenario, we assume that the collimator (or limiting aperture of the ring) locates at the final pass of the linac, our estimates show that the total beam losses ranges from 100 pA to 400 pA as transverse aperture (I.R.) varying from 2 cm to 1 cm.

More accurate estimates can be achieved through element-by-element simulation with the detailed lattice design and environment parameters.

Table 2.14.1: Parameters used in the estimates of beam losses due to beam-gas scattering.

	Arcs	Linac
Electron bunch charge	0.256 nC	
Repetition frequency	162 MHz	
Ion species	H2+, N7+, CO2+	
Avg. beta function	0.5 m	50 m
Temperature	300 K	2 K
Gas Pressure	1 nTorr	10-3 nTorr

2.15 Orbit & Optics correction[Chris]- 1st draft due 04/28

2.16 Tolerances[Dave]- 1st draft due 04/22

2.17 Start-to-End Simulation[Chris]- 1st draft due 05/04

2.18 Beam instabilities: BBU

2.18.1 Introduction

Beam breakup instability (BBU) occurs in recirculating accelerators when a recirculated beam interacts with higher-order-modes (HOM) of the accelerating cavities. The most dominant HOM is the dipole HOM which gives transverse kick to the beam bunches. The off-orbit bunches return to the same cavity and excite more dipole HOMs which, if in phase with the first dipole HOM, can kick the bunches more in the same direction. The effect can build up and eventually result in beam loss. With more recirculation passes, BBU can significantly limit the beam current[?]. The maximum achievable current is called the threshold current (I_{th}). The design goal for the current of C-beta 1-pass machine is 100mA, and simulation is required to check whether I_{th} is above this limit.

2.18.2 Bmad Simulaion Overview

Cornell University has developed a simulation software called Bmad to model relativistic beam dynamics in customized accelerator lattices. Subroutines have been written to simulate BBU effect and find I_{th} for a specific design. The complete lattice provided to the program must include at least one multi-pass cavity with HOM(s) assigned to it. It is possible to assign HOMs of different orders to a single cavity, and also a different set of HOMs to other cavities. Parameters such as bunch frequency and numerical tolerances can be specified to the program.

For each simulation, the program starts with a test current and records the voltage of all assigned HOMs over time. As the beam pass by the cavities, the momentum exchange between the bunches and wake fields are calculated, as well as the new HOM voltages. If all HOM voltages are stable over time, the test current is considered stable, and a new greater current will be tested. In contrast, if any HOM voltage is unstable, a smaller current will be tested. Usually I_{th} can be pinned down within the numerical tolerance under 50 trial currents. A single simulation on a C-beta 1-pass hybridized lattice, with 10 dipole HOMs assigned to each of the 6 cavities, takes up to 20 minutes. Hybridization is a process of merging certain lattice components into an equivalent Taylor map (up to linear order) to save simulation time. In BBU simulation, only cavities with HOM(s) assigned are essential, so other lattice structures can be hybridized. A BBU simulation on a complete C-beta 1-pass lattice can take hours, making hybridization necessary to efficiently find I_{th} for various HOM assignments.

2.18.3 Bmad Simulation Result

Dipole HOMs of a single C-beta SRF cavity have been simulated by Nick Valles [1]. Random errors were introduced to each ellipse parameter of the cavity shape, resulting in a spectrum of dipole HOMs, and their characteristics (R/Q, Q, and f) were measured. Each random

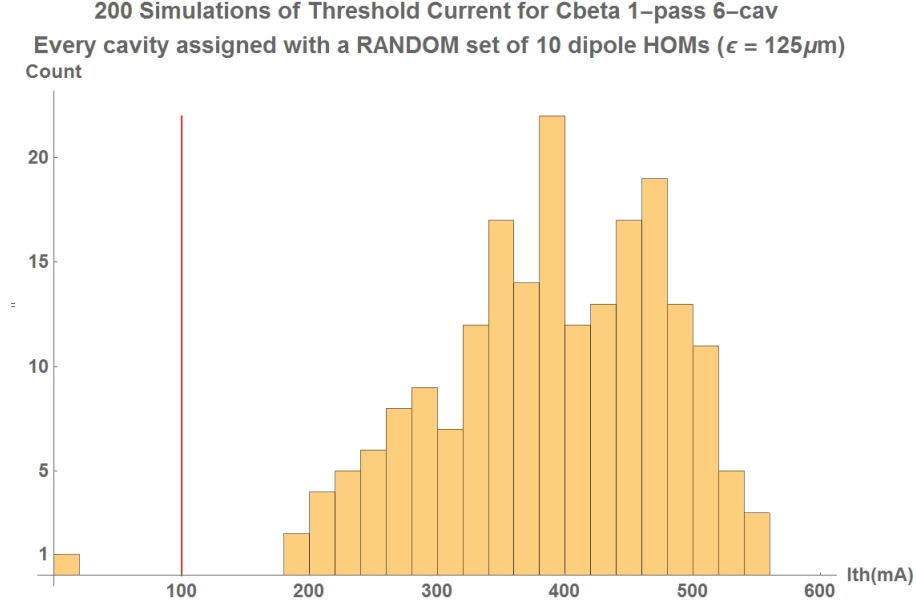


Figure 2.18.1: BBU simulation results for random HOM assignments ($\epsilon = 125\mu m$)

error came from a uniform distribution, with 4 different error cases: ± 125 , 250 , 500 , and $1000 \mu m$. For simplicity, we use ϵ to distinguish between the error cases: " $\epsilon = 125\mu m$ " means the errors introduced come from a $\pm 125 \mu m$ uniform distribution. For each error case, 400 unique cavities were created, and the top 10 worst dipole HOMs (ones with greater HOM figure of merit) were recorded for each unique cavity.

Since C-beta has 6 cavities, there are two sensible ways to assign the HOMs:

- 1) Assign all 6 cavities with the same unique cavity (same ϵ)
- 2) Assign each cavity with a randomly picked unique cavity (same ϵ)

The second way better represents the reality since the 6 cavities are not truly identical. However, the first way could provide us insight on the lowest possible I_{th} , since all cavities have identical HOMs. With four different ϵ , there are 8 possible assignment schemes in total. All schemes have been applied to run multiple BBU simulations on the C-beta 1-pass hybridized lattice. Three schemes are presented, with results shown in histograms:

- 1) Random HOM assignment with $\epsilon = 125\mu m$
- 2) Same HOM assignment with $\epsilon = 125\mu m$
- 3) Random HOM assignment with $\epsilon = 250\mu m$

Random HOM assignment with $\epsilon = 125\mu m$

Out of 200 simulations, 197 of them have I_{th} above 200mA, exceeding the 100mA goal. However, one simulation fails to compute I_{th} , and the result is regarded as 0mA. This could imply that the particular combination of dipole HOMs strongly limits the current, or the program experienced error. The average I_{th} is 389 mA.

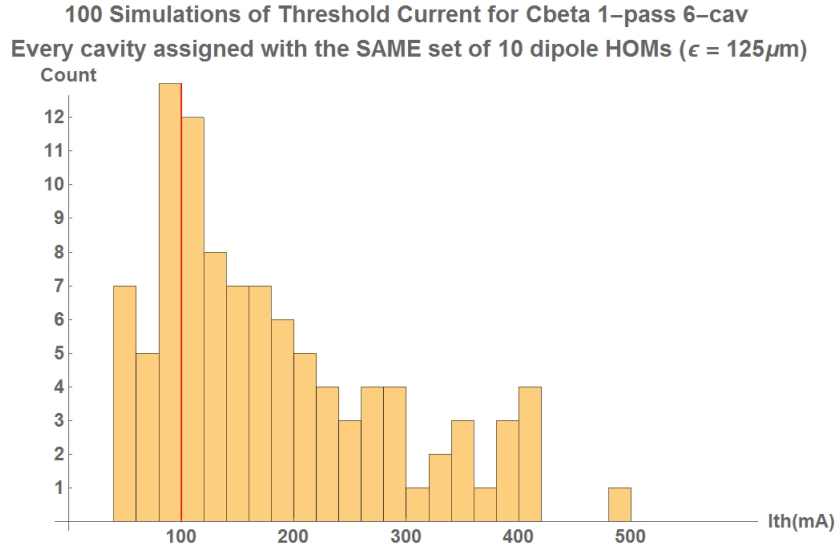


Figure 2.18.2: BBU simulation results for same HOM assignments ($\epsilon = 125\mu m$)

Same HOM assignment with $\epsilon = 125\mu m$

Compared with random assignment of HOMs, when the cavities are assigned with the same HOMs, I_{th} tends to be lower. This is expected since identical HOMs effect can build up more easily. 25 out of the 100 simulations have I_{th} below the 100mA target, and the average I_{th} is 182 mA. Note that in general, realistic cavities do not have identical HOMs.

Random HOM assignment with $\epsilon = 250\mu m$

2.19 Halo[William]- will there be results?

2.20 Collimation[Chris]- 1st draft due 05/04

References

- [1] Walz, D. R., *et al.* *Beam Dumps, Energy Slits and Collimators at SLAC—Their Final Versions and First Performance Data.* IEEE Transactions on Nuclear Science, **14** (3), pages 923–927 (1967).
- [2] Wiseman, M., *et al.* *High power electron beam dumps at CEBAF.* In *Proceedings of the 1997 Particle Accelerator Conference 3*, pages 3761–3763. Vancouver, B.C., Canada (1997).

3 FFAG Magnets [Dejan]

3.1 Iron-based Permanent Magnet Design [Holger]- 1st draft due 04/28

3.1.1 General Concept

Iron-dominated magnets for c were developed as a low-risk option. The magnets rely on established accelerator magnet design and manufacturing techniques as far as possible. The design idea of the quadrupoles is a copy of the permanent magnet quadrupoles used for the Fermilab Recycler, which have been in use for a number of years¹. Relying on the experience of the Fermilab personnel in deciding for this approach was also an important factor. The light source in Brazil follows a very similar approach, which could also be a valuable resource for information².

Figures 1 and 2 illustrate the concept. In general the magnet is a standard quadrupole, but the necessary flux is generated by several permanent magnets which are placed around the pole. The advantage of this design is that this is largely a conventional approach, that means the field quality in principle will only be determined by the pole shape (for which ample experience exists). As the permanent magnets are only providing magnetic flux, the mechanical and magnetic tolerances of the permanent magnets are easy to handle. This is important as the permanent magnets will be the component in the design with the largest tolerances (magnetically and mechanically).

The permanent magnets themselves have a very simple shape (block shape), which multiple suppliers can provide. Industry is well accustomed to this shape of permanent magnet, which means short lead-times and reduced cost. A further advantage of this design is that the quadrupole strength can be adjusted easily with a pole winding, this will be discussed later on in this report. A further significant advantage is the fact that these magnets can be temperature compensated. NdFeB possesses a negative temperature coefficient, which otherwise would lead to a change in gradient of 0.1%/K. Temperature compensation will be discussed in a separate section of this report.

Magnet to magnet reproducibility can be expected to be high due to the use of laminations (shuffling), the matching of a large number of small permanent magnets to provide the same amount of flux and the aforementioned temperature compensation. These concepts will be addressed in more detail in the following sections.

This design approach also has a number of disadvantages. The first is that due to the lattice the magnets need to be placed closely together. This leads to unwanted flux leakage and crosstalk, as the distance between magnets becomes comparable to the distance between the poles. Due to a horizontal offset of the magnets with respect to each other each side of one quadrupole sees a different cross-section of the neighbouring quadrupole, which means for each half of the quadrupole this effect is slightly different. This leads to an imbalanced quadrupole,

where one side is stronger than the other side. In recent lattices this effect has been small (\sim percent level) and quite possibly does not cause a problem. In addition, this effect can be compensated for as will be shown later. As mentioned earlier, unwanted temperature effects of NdFeB can be compensated for, but the downside of this is that the performance of the quadrupole will be lower by 20% in comparison to an uncompensated magnet. Correction coils are difficult to accommodate due to space restraints, even though in most recent designs this has been less of a problem. The magnets tend to be large to obtain an optimum working point for the permanent magnets.

3.1.2 Finite Element Simulations

The magnets described in this report have been simulated with the commercial finite element software package COMSOL Multiphysics, which is a combined 2D and 3D code. For the mesh a second order (quadratic) element is used for accuracy reasons. 3D models usually employ a Tetrahedral mesh; regions of specific interest (for field maps) use an extruded quadrilateral mesh (Hexahedron). Periodic boundary conditions are used at the end of the coil to mimic an infinitely long series of magnets. For permanent magnets we assume NdFeB grade N49M with a Br of $1.37 - 1.42$ T. For iron we use a non-linear BH-curve which is equivalent to ultra low-carbon steel (better than AISI 1006). The BH data has been measured from material recently purchased for a different project. For 3D problems an iterative solver is used (Conjugate Gradients, Multigrid). 2D problems are solved with a direct solver (MUMPS).

3.1.3 Requirements and Basic Magnet Design

One of the promising candidates for a possible c lattice is shown in Figure 3. The lattice was specifically optimized to be compatible with iron dominated magnets. The lattice requires relatively low gradient quadrupole magnets (16.7 T/m). A special feature of this lattice is that the focusing and defocusing magnets differ only in length; required gradient and beam excursion are identical.

Figure 4 shows a possible magnet design for this lattice. Shown in blue is the iron part of the magnet; the permanent magnets are located above and next to the pole in grey. It is assumed that 80% of the available volume will be filled with permanent magnetic material. The remaining 20% are required for temperature compensation.

Figure 5 shows the region around the pole of the magnet. Shown in gray is the stay-clear area around the beam, which is sufficient to accommodate a suitable beam pipe. The maximum possible clearance for this design is 16.5 mm from each point of the beam aperture.

Figure 6 shows the simulated gradient on the centre plane of the magnet. As shown, the magnet delivers a gradient of 27.5 T/m with a gradient quality of 0.6%. A gradient quality of 1% was requested and should be tolerable; the primary effects of a departure from linearity of the field profile are a change in the tune range and orbit excursion. Nonlinear effects from this nonlinearity are significantly smaller than those that arise from the magnet ends. An updated pole achieved a gradient quality of 0.23% with a similar gradient strength.

In a 3D simulation (see Figure 7) the design exceeded the required performance for the integrated gradient (123%-127%) as well as the peak gradient (101%-106%) in the centre of the magnet.

3.1.4 Temperature Compensation

NdFeB permanent magnets are envisaged to be used for this project. One disadvantage of NdFeB is the temperature coefficient, which means B_r changes with small changes in temperature. The temperature coefficient, defined as $(B/B)/T$, is about $-1.1 \times 10^{-3}/K$. The temperature dependence of this magnet can be compensated for by a method pioneered by Fermilab1 (CERN tested this for a very similar design). The principle idea is that strips of NiFe are placed next to the permanent magnets, parallel to the magnetization direction of the NdFeB as shown in Figures 8 and 9. 30-32% Ni-Fe possesses a relatively low Curie temperature around $60^\circ C$. The NiFe strips act as temperature dependent magnetic shunts, shunting away a certain amount of magnetic flux. If the temperature increases the permanent magnets will be less powerful, but at the same time the NiFe shunts will be less effective. If the volume ratios are correct (about 20% NiFe) temperature effects over a range of 10-20K can be excluded. The interleaving of permanent magnets with NiFe strips does not influence the gradient quality.

This can be seen in Figure 10 for a different lattice, which shows an almost perfect compensation between $20^\circ C$ and $30^\circ C$.

3.1.5 Quadrupole Corrector

The quadrupole component of each magnet can be changed with a simple pole winding. It is anticipated that this will be implemented for every magnet. An example of this is shown in Figure 16. Figure 17 shows the calculated power dissipation per m length of the magnet. A current density of $2A/mm^2$ is sufficient to change the quadrupole level by more than 5%. A second design with a slightly larger yoke achieved a 10% variation with a coil thickness of 5mm and a power dissipation of 70W. A change in gradient quality was not observed.

3.1.6 Engineering

The yoke of the quadrupole magnets for c will be made from laminations, each up to 2mm thick. Stamping will ensure good mechanical tolerances for the pole; at the same time this process is very cost efficient. Quotes obtained for the test magnet indicate a cost of 0.70 per lamination. *The total cost for one of the test magnets would be between 120 and 161. This does not include the cost for the punch tool, which is estimated at 25k.* The presently considered lattice requires a magnet with a larger yoke, for which quotes have not been obtained. One of the requirements for the c magnets is small magnet to magnet variability. Laminations are ideally suited for this, as the individual laminations can be shuffled. This process is well established and has been used for example for the Fermilab Main Injector magnets1 and the ALBA light source2. By shuffling the geometric and magnetic property variations are averaged over different magnets. The force on the individual laminations for the test magnet have been evaluated using the Maxwell stress tensor. The results are shown in Figure 26.

Permanent Magnet Tolerances

Permanent magnets are subject to mechanical as well as magnetic tolerances. Typically, the total magnetization varies by up to 3%. The standard variation of the magnetization angle

according to manufacturers is 3° (guaranteed 5°). Tighter tolerances of the angle are possible (1°), but drive the cost1.

For the iron dominated quadrupoles most of the variations of the magnetic properties are not crucial. It is essential that each pole receives the same amount of magnetic flux from its permanent magnets. This can be ensured in two different ways: either by matching permanent magnets or by using shunts.

Using a simple algorithm it can be shown that out of a pool of 125 permanent magnets it is possible to select four sets of 25 permanent magnets (which is what is approximately required for each pole) so that the total magnetization of each set varies very little (less than 0.01%). This study was carried out assuming permanent magnets with a total variation of the magnetization of 5%. A smaller magnet variation will lead to a smaller overall variation for each of the sets. Required for this is only the knowledge of the magnetic moment of each permanent magnet in the main direction, which can be measured in-house. Some manufacturers of permanent magnets offer this as a service.

It is also possible to compensate different strengths of the individual poles of the quadrupole by using shunts, similar to the concept for compensating crosstalk and temperature variation. Geometric variations of the permanent magnets are likewise less crucial. Thickness variations (which are not likely) can be compensated for with shims of soft iron. Length and height variations do not play a role.

Assembly

For assembly of the quadrupoles a grid concept was developed, which is shown in Figures 27 and 28. An aluminium frame is placed onto the pole and the individual permanent magnets are placed onto the grid. The holding force of the permanent magnets (about 20 kg) in combination with the support from the grid is strong enough to keep the permanent magnets in place despite the repulsive force between the individual permanent magnets. This was verified in a test, as shown in Figure 30.

The space in between the permanent magnets can be used for magnetic shunts for temperature and crosstalk compensation as shown in Figure 29. The back-yoke can be lowered onto the pole without moving the permanent magnets, which was also verified in a trial.

Once a quarter of each quadrupole has been assembled, all four quarters can be combined to a full quadrupole as shown in Figure 31.

Status of Prototype

The yoke parts have been manufactured and are expected at BNL end of February 2016. Permanent magnets have been ordered from two different manufacturers. The first manufacturer is a company very well acquainted with the requirements of particle accelerators and light sources. The delivered permanent magnets will be measured by the company using a Helmholtz coil setup.

The second manufacturer is a Chinese based company, which is substantially cheaper. These permanent magnets will not be measured by the manufacturer. It is planned to measure the magnetization of the permanent magnets using the Helmholtz coil setup at NSLSII; a special holder for their setup has already been manufactured. The permanent magnets of the Chinese

producer are expected to arrive before March 1st. The other permanent magnets are not expected before end of March 2016.

To complete the trial cell assembly funds of \$150k are requested by the Magnet Division of BNL. The funds are for the engineering and manufacturing of an assembly jig and the assembly of the quadrupoles.

3.1.7 Magnet Designs for Different Energies

If the energy for c is restricted to 200 MeV, the size of the magnets can be significantly reduced. Figures 36 and 37 show a cross-section of the geometry and the complete cell. The magnet size is reduced by 25% and the permanent magnet material required will be smaller by about 60%. The beam excursion is approximately the same, so the same pole as for the 250 MeV lattice can be employed. The geometry is optimized to generate 80% of the gradient in comparison to the 250 MeV magnet design.

An attractive option could be to boost the performance of a magnet suitable for 200 MeV operation for a 250 MeV lattice. Figures 38 and 39 show the geometry of the pole winding and the gradient as a function of current density. The figure shows that with a current density of 5 A/mm² a gradient can be achieved which should be suitable for 250 MeV operation. It should be noted that the pole winding has a thickness of 10 mm, so will penetrate further into the drift sections. At these current densities cooling will be required, which has not been investigated.

3.1.8 Corrector Magnets [Nick]- 1st draft due 04/28

3.2 Backup magnets: Halbach-type Design[Stephen]- 1st draft due 04/28

An iron-free Halbach permanent magnet design was investigated for Cbeta, which attains higher field strengths (allowing 250MeV top energy), less cross-talk and smaller magnets. It is described in the subsections below.

3.2.1 Comparison of Features vs. Iron Poled Magnets

A summary is provided in table 3.2.1 to illustrate the technology differences between choosing a Halbach magnet design and an iron-dominated permanent magnet design in an accelerator. Permanent magnet materials all have a temperature dependence and this can be compensated in the magnet in various ways. The iron quadrupole uses a technique from the Fermilab recycler where the permanent magnet blocks sandwiched in the iron yoke are mixed with NiFe alloy whose magnetisation contribution varies in the opposite way as magnetisation of the blocks, to provide a temperature range of 20°C or more with virtually no field strength variation. In the Halbach magnets, the field and magnetisation directions are not parallel, so this method does not work because the NiFe alloy would not provide compensating magnetisation in the correct direction. Instead, the dipole and quadrupole correctors, which would be present in the design anyway, are used to compensate the field variation, which manifests as an overall

reduction factor in field strength and is therefore linear as a function of position like the magnets themselves.

Table 3.2.1: Comparison of iron and Halbach-type magnets.

	Iron Poles	Halbach
Field quality + tuning	Determined by iron pole shape. Adjustment would be via conventional pole shimming.	Determined by block magnetisation vectors. Adjustment via floating shims/iron wires just inside aperture.
Field strength + tuning	Iron shunts to partially short-circuit flux applied to outside. Also block pre-measurement and sorting. EM quad corrector coils around poles.	Determined by block magnetisation vectors. Tune with EM normal quad and dipole online correctors (see correctors' below).
Temperature sensitivity + compensation	0.1%/K for NdFeB but can (at $\sim 20\%$ strength penalty) incorporate NiFe material to passively compensate.	0.1%/K for NdFeB, cancelled by using EM normal quad and dipole online correctors.
Cross-talk in doublet + compensation	Few percent cross-talk, can be corrected with shunts.	Negligible cross talk, $\mu \sim 1$ linear field superposition.
Correctors (online/EM)	Normal quadrupole can be coils would around each pole. Others require special coils put within the bore.	Window-frame outside Halbach magnet using field superposition, because Halbach is magnetically transparent.

To compensate temperature changes, the correctors could be set either using data from the orbit position feedback, or a local field monitor. If the corrector coils themselves are water-cooled (as they are in the most recent design), it is possible to circulate a layer of water just outside the Halbach magnet blocks first, to stabilise their temperature to the extent that temperature compensation of any sort is no longer needed.

3.2.2 Halbach Magnet Design

The optimised FFAG cell required the QF magnet to be very close to a symmetrical quadrupole, i.e. with zero field at the centre. To simplify matters, the bore location was adjusted slightly so that QF really was exactly symmetrical, so that its design is that of a conventional Halbach quadrupole. Cross-sections of the two magnets are shown in figure 3.2.1 below.

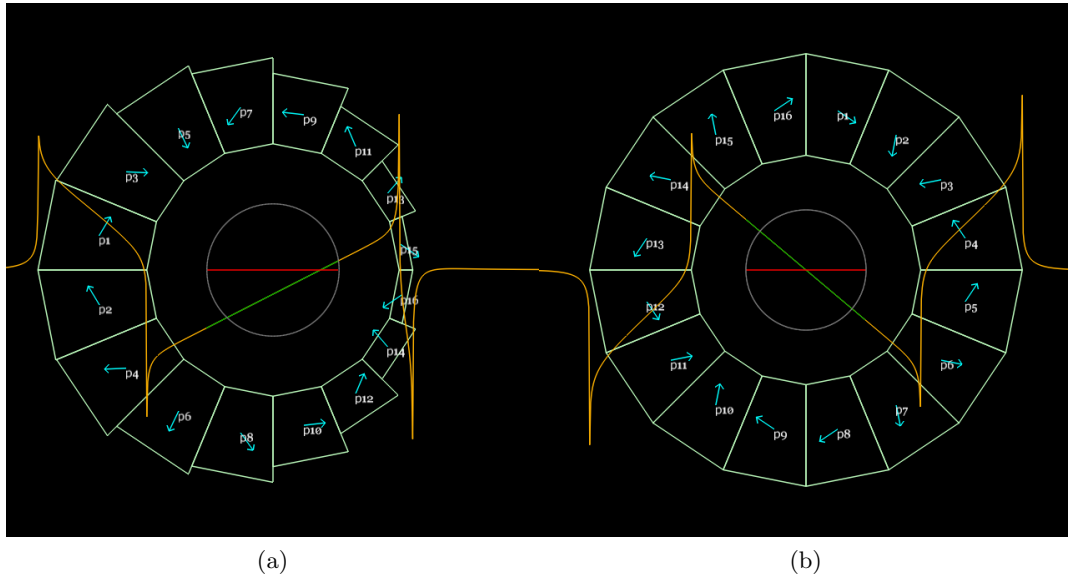


Figure 3.2.1: (Left) BD magnet. (Right) QF magnet. Orange graph is vertical field component B_y on the $y=0$ axis, with varying x position. The green segment is the field within the region required by the beams, which is supposed to be linear. Magnetisation axis is shown by blue arrows in each block.

The BD magnet on the other hand contains a significant dipole component: in fact, all the beams go through the negative B_y field region, which bends electrons clockwise in the L0E hall. The design of the BD magnet is also not a conventional Halbach arrangement: it requires a combination of dipole and quad, whereas conventional annular arrangements can only do one pure multipole at a time. It was considered to nest conventional dipole and quadrupole Halbach magnets but the outer magnet has to be quite large in that case. It was noticed that on one side of the nested magnet, the magnetisations were mostly cancelling anyway, so optimisation was run on a design with only a single layer of permanent magnet wedges, but with variable thickness and different magnetisation directions. This achieved a very accurate ($< 10^{-5}$ in the linear model) combined function integrated field as required, a result that was replicated to high accuracy ($\sim 10^{-4}$) by OPERA-3D simulations. It also uses much less material than a nested design.

Magnet Simulation and Codes

Two codes were used in the design and simulation of these Halbach magnets, which have shown good agreement as shown in this section. The simpler of the two is PM2D written by Stephen Brooks, which is a current sheet approximation of the fields from permanent magnet polygons in 2D. This provides an accurate model of the “average” field (integrated field divided by permanent magnet piece length) through the magnet, provided two conditions hold:

- The materials stay in the linear part of their B-H curve. In fact, if this is violated, the magnets will experience permanent demagnetisation, so any valid design ought to satisfy this condition. PM2D can also evaluate the demagnetising flux from the other blocks at any point to ensure it does not go beyond the coercive force (H_{cj}) of the material.
- $\mu_r = 1$ for all materials. This is almost true of NdFeB, which has a μ_r of about 1.025.

PM2D was used for the initial optimisation of the wedge sizes in the BD magnet, which tried to reduce the error multipoles to zero by changing their thickness and magnetisation direction independently keeping the required symmetry in the $y=0$ midplane. This requires many iterations of the design to be simulated, so a faster code is preferred during this design stage, before coordinates of the wedge corners are generated as input for the 3D magnet simulation.

The second code used, by Nick Tsoupas for 3D simulations, is OPERA-3D, which is industry standard. Very good agreement was attained between the two codes (on integrated field multipoles) when the materials were not in the demagnetising regime. Once the design was set, OPERA-3D was always used to do the final simulation and 3D field map generation.

Running in OPERA-3D required that a specific material grade and B-H curve was chosen for the permanent magnet blocks. These grades and curves vary by manufacturer, so a grade from AllStar Magnetics was selected, which is the manufacturer for blocks for the Cbeta prototype magnets currently under order and shipping at the end of March 2016. The grade N35SH was selected, which combines a medium strength of 35 MGauss.Oe (the maximum available being ~ 52 MGauss.Oe) with a good resistance to external demagnetising fields. This is what the “SH” suffix means: a strong resistance to heat, which stems from its high H_{cj} demagnetising field value (2.24 T) at room temperature. The strength translates into a residual field B_r of 1.207 T.

After OPERA-3D models were run, a best fit with the magnetisation “ B_r ” value used in PM2D, which assumes $\mu_r = 1$, was found (1.1939 T), which represents the average magnetisation from the material including the small reduction from regions of reverse flux with μ_r being slightly larger than 1. This lies between B_r and H_{cb} of the material as expected. With this value, the PM2D designs could be loaded directly into OPERA-3D (with the N35SH material) and the strength would be correct, with no further design modifications required.

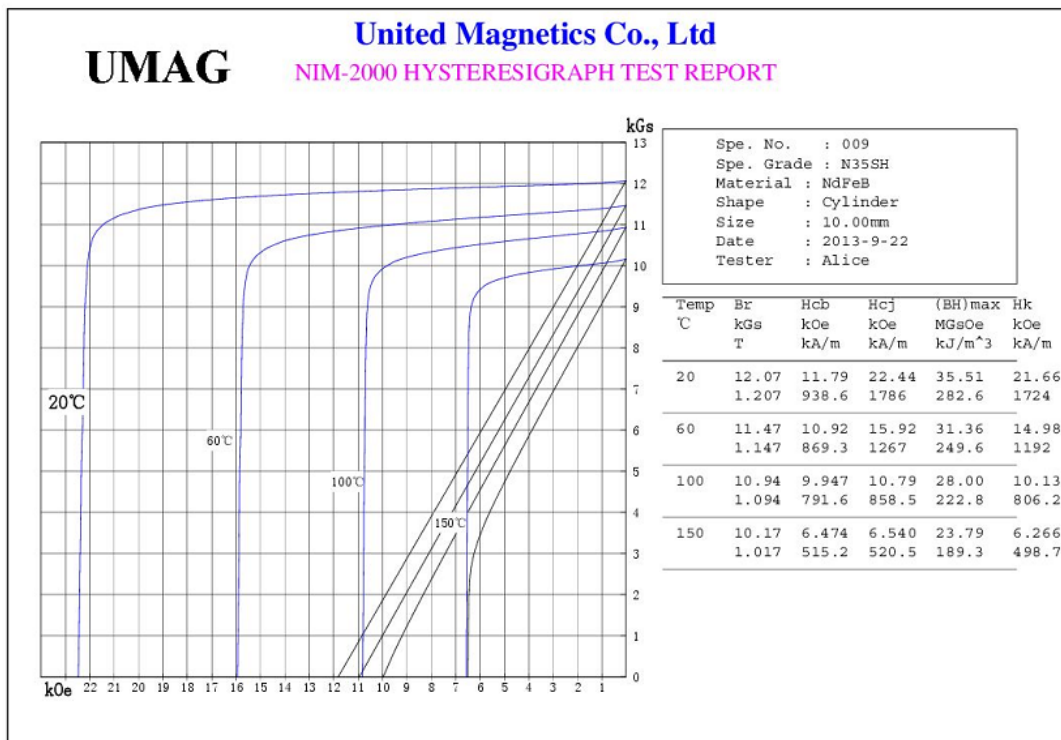


Figure 3.2.2: B-H curve of the AllStar Magnetics N35SH NdFeB permanent material, at various temperatures.

3.2.3 Tracking and Compatibility with FFAG Lattice

Once OPERA-3D field maps have been generated, they can be loaded back in to the Muon1 tracking code, which is the same code used for the original lattice optimisation done with field models rather than field maps.

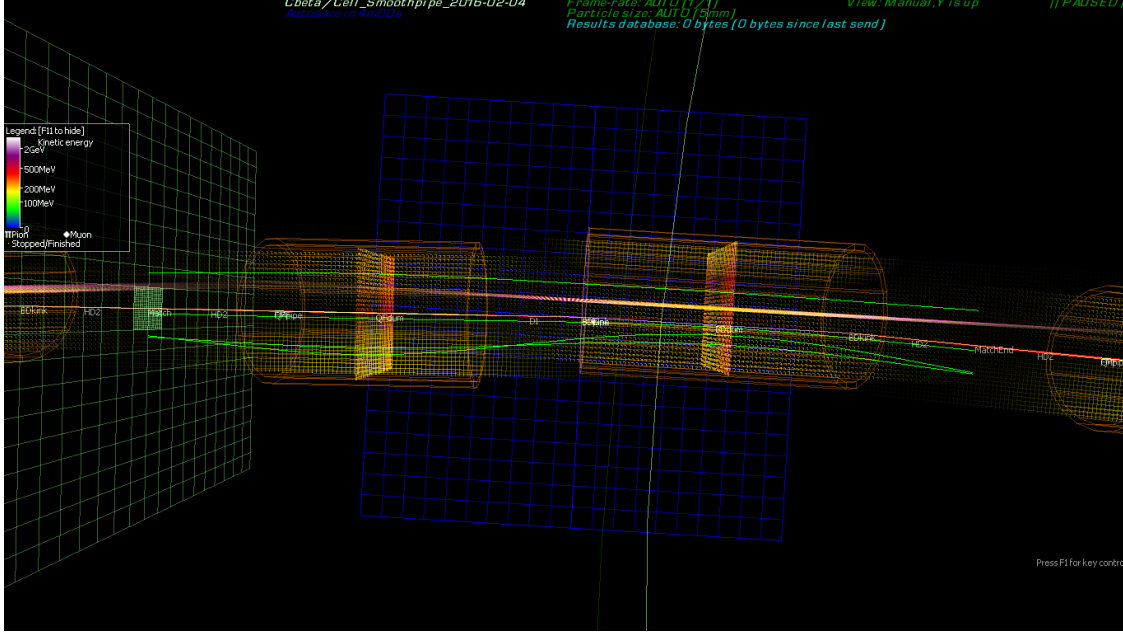


Figure 3.2.3: Matched orbits (green) for the four Cbeta energies through an FFAG arc cell made with OPERA-3D field maps generated from Halbach magnets. The orange cylinders represent the approximate apertures of the vacuum pipe and the grids are 1cm per square.

Figure 3.2.3 above shows such a simulation, where Muon1 has found “closed orbits” for each energy, which exit the cell at the same position and angle that they enter. The closed orbits found through field maps will be slightly different than those found for the original field model in the lattice-design optimisation, but as shown in the figure 3.2.4 and table 3.2.2 below, the discrepancy is not very large ($<1\text{mm}$).

Table 3.2.2: Transverse position (X , in metres) of the four closed orbits, calculated with Muon1 soft-edged field models or OPERA-3D field maps, at the midpoint of the long drift in the Cbeta FFAG arc cell.

Energy (MeV)	x (m) (model)	x (m) (fieldmaps)
250	0.016825	0.01668
189	-0.00201	-0.00237
128	-0.01296	-0.01349
67	-0.01246	-0.01292

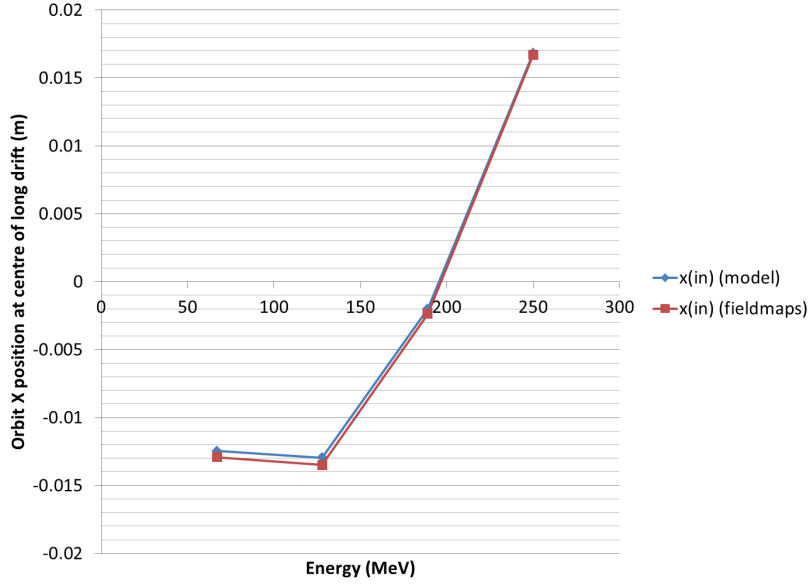


Figure 3.2.4: Transverse position (X, in metres) of the four closed orbits, as a function of energy, at the midpoint of the long drift in the Cbeta FFAG arc cell. Blue dots are from a Muon1 simulation using field models and red dots from a Muon1 simulation using OPERA-3D field maps.

This good agreement is partly due to a fortunate choice of fringe field length in Muon1’s soft-edged Maxwellian field model. Muon1 models the fall-off of multipole components near the entrance or exit of a magnet as proportional to $\frac{1}{2} + \frac{1}{2} \tanh(z/f)$ where z is the longitudinal position relative to the magnet end and f is a “fringe length” parameter (f). It was chosen to be 2.5cm here, roughly the same order of size as the magnet apertures. Detailed studies suggested the best agreement with these fieldmaps is obtained with $f = 2.7$ cm. For these short magnets in Cbeta, the fringe field makes up a large part of the field so it is important to include it consistently (some hard-edged models do not have good agreement with the optics).

The closed orbit matching process also determines the shape of the beam (optical alpha and beta functions) that will be preserved on traversing once through the cell. This also allows the single-cell tunes in the X and Y planes to be calculated. A similar comparison of tunes from the field map versus the original optimiser’s field model is shown in figure 3.2.5 and table 3.2.3 below.

The cell tunes are important because they determine the limits on the stability of the beam (0 and 0.5 being the unstable limits) and its response to errors, the tune determining the frequency of error oscillations. The largest discrepancy between field map and model field is found in the low-energy (67MeV) beam, where the model predicts 0.3833 and the field maps predict 0.3756, a difference of 0.0077 cycles per cell. This is not a large enough difference to put the beam into a resonance or drastically affect the optical behaviour of the machine.

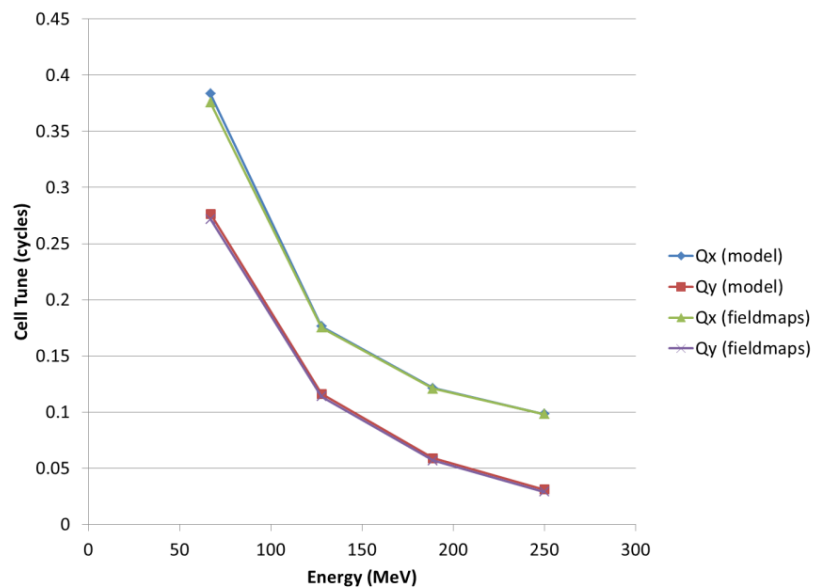


Figure 3.2.5: Comparison of the calculated X and Y tunes of the FFAG cell using Muon1's model field and OPERA-3D field maps as a function of energy.

Table 3.2.3: Comparison of the calculated X and Y tunes of the FFAG cell using Muon1's model field and OPERA-3D field maps.

Energy (MeV)	Q_x (model)	Q_y (model)	Q_x (fieldmaps)	Q_y (fieldmaps)
250	0.098132	0.031006	0.098272	0.029062
189	0.121474	0.058797	0.120911	0.056874
128	0.176315	0.11615	0.175274	0.113949
67	0.383309	0.276579	0.375643	0.271753

3.2.4 Window-Frame Correctors [Nick]

The property of the permanent magnets to be magnetically saturated allows superposition of the magnetic fields and therefore permanent magnets can accept electromagnets as corrector magnets with no distortion of the their magnetic field. Figure 3.2.6 is an isometric view of an OPERA model of a Halbach-type magnet surrounded by a window frame electromagnet acting as a corrector.

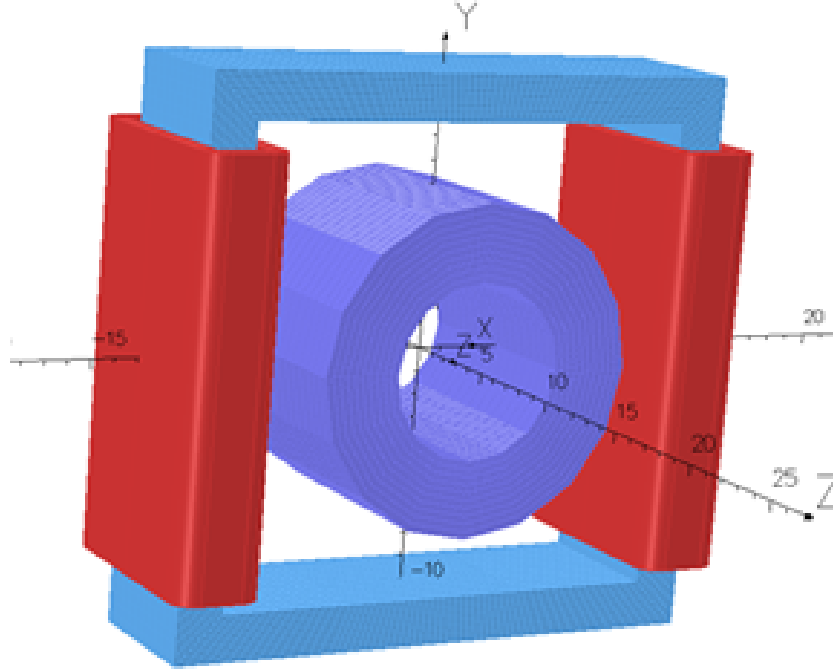


Figure 3.2.6: A window frame magnet with two coils generates a normal dipole field which is superimposed on the field of the permanent magnet.

In this section we will present results from the 3D OPERA calculations which prove the following statements:

1. The window frame magnets in spite their large aperture and short length, do not excite significant transverse magnetic multipoles except the ones are designed to produce.
2. An excited window frame magnet placed around a Halbach-type permanent magnet as in Figure 3.2.6 does not alter significantly the multipoles of the Halbach-type magnet (measurements are under way) and there is an almost perfect superposition of the fields of the two magnets.
3. The Halbach-type magnets lend themselves easily to window-frame corrector magnets and do not interfere with possible access to the beam instrumentation which is placed in the short drift spaces between the magnets.

4. Four Halbach-type magnets were placed next to each other along their symmetry axis with the magnets touching each other and the integrated multipoles of all four magnets was measured to be equal to the sum of the of the integrated multipoles of each magnet measured separately. This measurement provides an almost perfect proof of field superposition. (Measurements have been made thus no results from calculations will be presented).

The B field of a Window-Frame Electromagnet

Figure 3.2.7 is a picture of 3D OPERA model window frame magnet to be used as corrector around a Halbach-magnet.

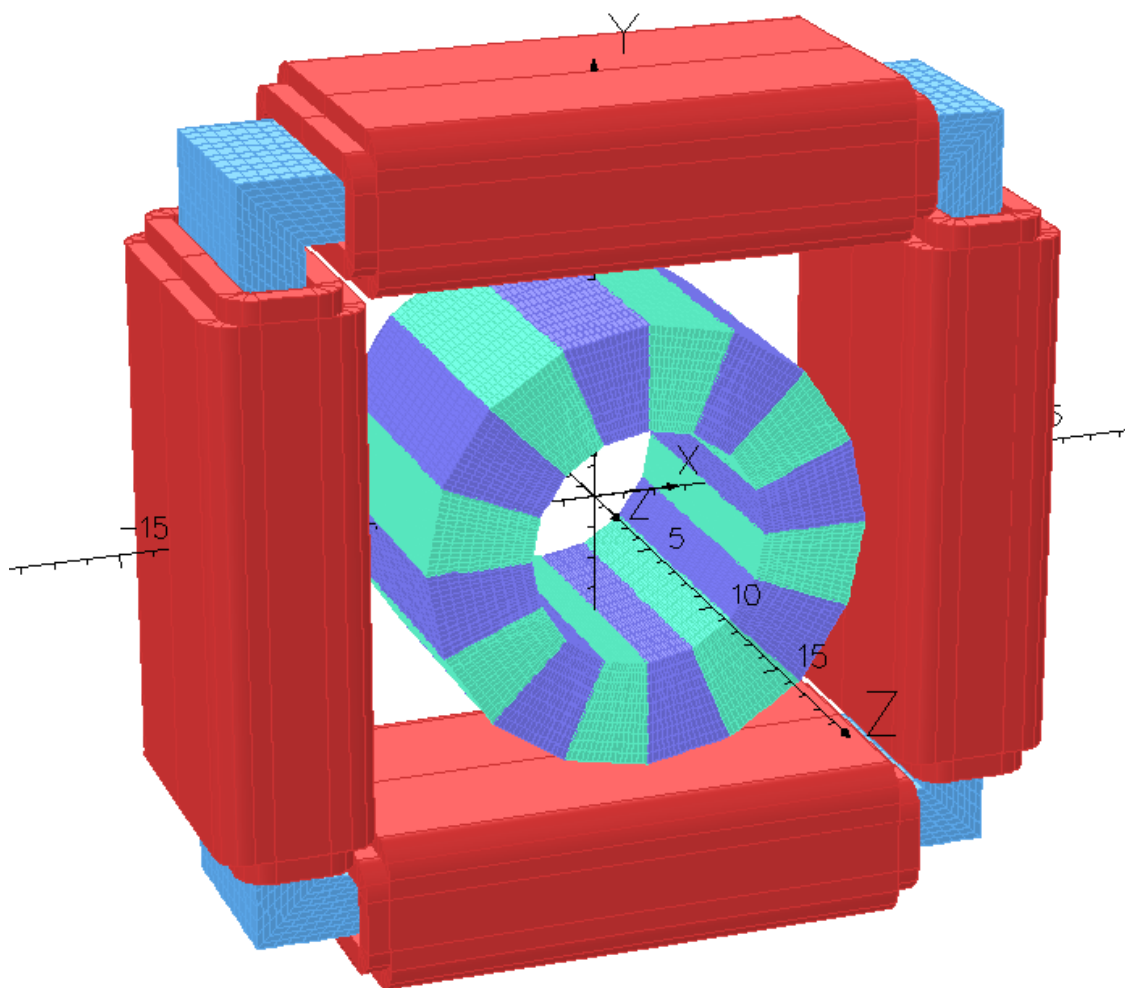


Figure 3.2.7: A window frame magnet with eight coils acting as normal and skew dipoles, and a normal quadrupole. By rotating the window frame by 45° we can generate a skew quadrupole instead of normal one.

Figure 3.2.8 below is a projection on the x,y plane of the window frame magnet which shows that the maximum transverse directions of the corrector magnet surrounding a Halbach magnet is less than 30 cm.

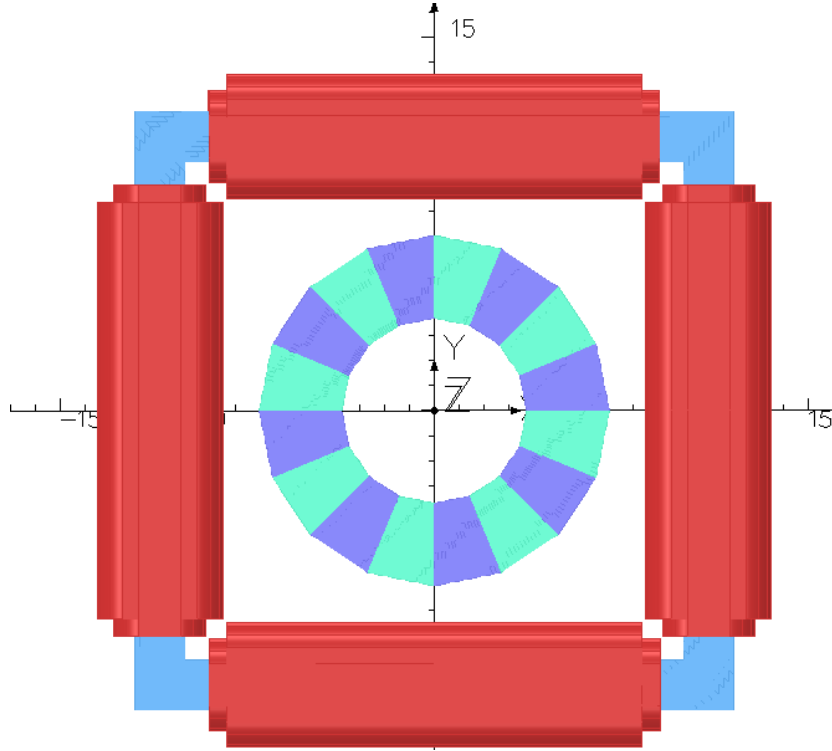


Figure 3.2.8: The projection of the window frame magnet on the x,y plane. The maximum transverse extend of the magnet is less than 30 cm.

Table 3.2.4 shows the integrated magnetic multipoles at $R=1$ cm of three different configurations of a quadrupole Halbach magnet and dipole window frame magnet. The 2nd row shows the integrated multipoles a dipole window frame magnet with no permanent magnet inside. Row 3 shows the integrated multipoles of a quadrupole Halbach-type magnet with no excitation of the dipole corrector and row 4 the multipoles of the dipoles window frame magnet excited, surrounding the quadrupole Halbach-type magnet. The permanent magnet material of the quadrupole magnet is NdFeB-N35 and the BH-curve for this material is shown in Figure 3.2.9. The results from Table 3.2.4 show that the field of the window frame magnet is simply superimposed on the field of the quadrupole magnet.

The results of Table 3.2.4 corroborate the ideal superposition of the fields generated by a Halbach-type permanent magnet with the fields of the window-frame magnet. Experimental measurements to prove these results are under way.

Figure 3.2.10 is an isometric view of a few permanent magnets of the Cbeta arc with correctors. This view shows that the window frame magnets do not extend into the drift space between the magnets. Figure 3.2.11 is the projection on the yz plane of the six magnets showing in Figure 3.2.10. The current through the coils of the window frame magnet can generate the required correction field for the permanent magnets.

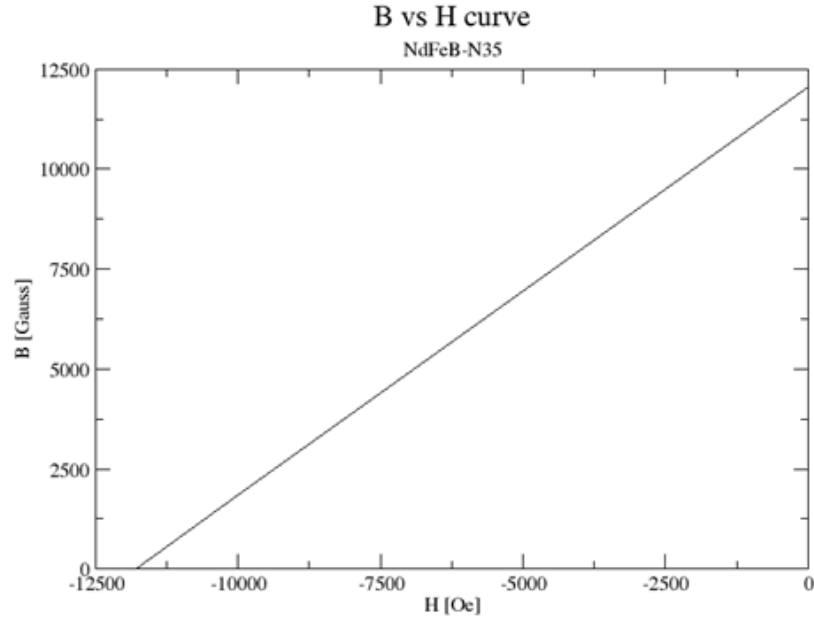


Figure 3.2.9: The BH curve of the NdFeB-N35 material.

Table 3.2.4: The integrated magnetic multipoles of the window frame magnet by itself (2nd row) of a quadrupole Halbach type magnet (3rd row), and of the window frame magnet surrounding the quadrupole Halbach-type magnet.

Setup	Dipole [Gauss.cm]	Quad [Gauss]	Sext. [Gauss.cm ⁻¹]	Oct. [Gauss.cm ⁻²]	Dec. [Gauss.cm ⁻³]	12pole [Gauss.cm ⁻⁴]
WF only	1931.14	-0.0013	1.02	0.00003	0.014	-0.000015
PM only	0.000003	27798.5	0.000003	0.00000002	0.000003	0.037
WF+PM	1933.7	27798.5	1.02	0.0123	0.017	0.016

Power dissipation on the coils of the window frame magnets

The dipole corrector field of a window frame magnet is generated by two coils wound around two opposite sides of the window frame as shown in Figure 3.2.6. The required dipole corrector field is ± 50 Gauss over the ~ 11 cm length of a permanent magnet. Calculations show that such a dipole field can be generated with two racetrack coils 8 mm thick as in Figure 3.2.6, when a current density of 50 A/cm^2 flows through each of the racetrack coil.

The quadrupole corrector field is generated by four racetrack coils (Panofsky Quadrupole) wound each around each side of the window-frame, as shown in Figure 3.2.7. The required quadrupole field is $\pm 0.45 \text{ T/m}$ over the ~ 11 cm length of a permanent magnet. Calculations show that such a quadrupole field can be generated with four racetrack coils 8 mm thick as in Figure 3.2.7, when a current density of 375 A/cm^2 flows through each of the racetrack coil.

The coils of either dipole or quadrupole correctors will be made of a hollow copper conductor of an approximate cross-section of $6\text{mm} \times 6\text{mm}$ with a hole to carry cooling water to abduct

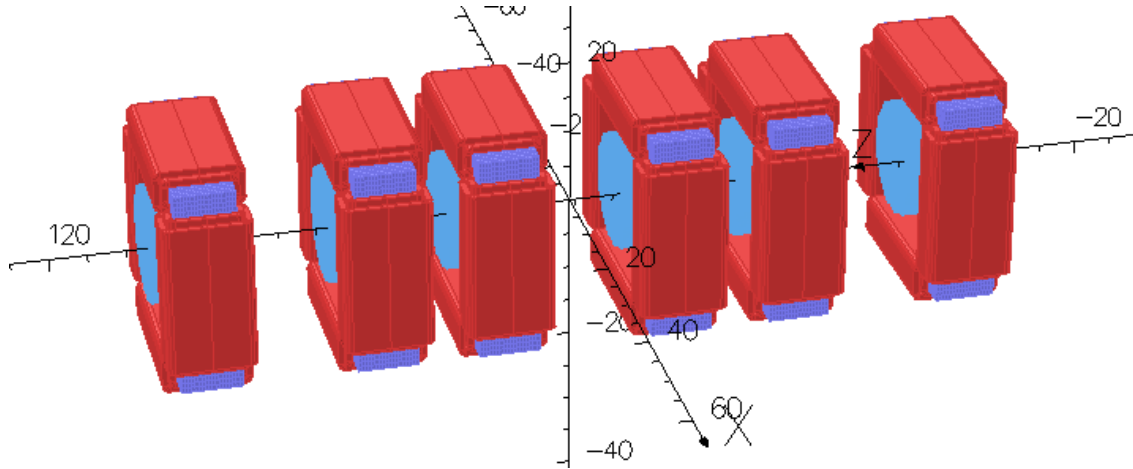


Figure 3.2.10: Isometric view of six of the permanent magnets of the Cbeta arc.

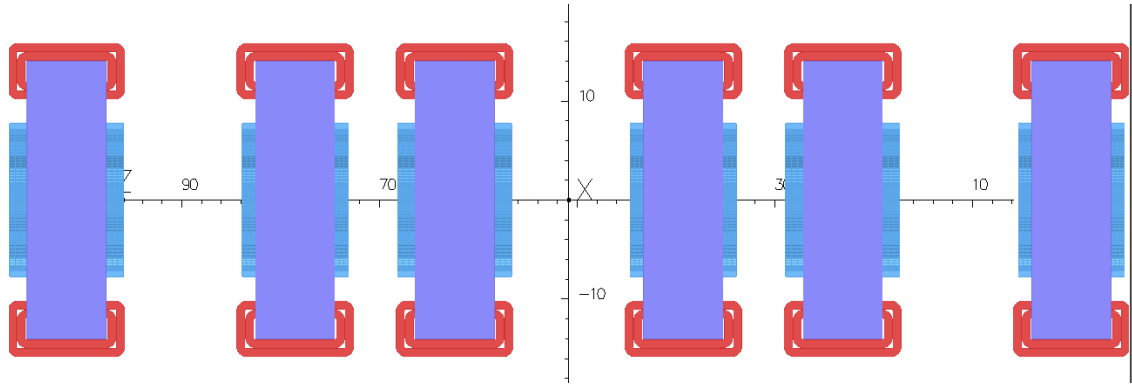


Figure 3.2.11: Projection on yz plane of the six permanent magnets of the Cbeta arc shown in Fig. 5a.

the heat generated by the relative large current density of 375 A/cm^2 required to excite the quadrupole multipole. It turns out that the power supply which will provide this large current density is expensive we may think of placing “additional copper” or increase the ampere turns of the quadrupole coils to reduce the current provided by the power supply.

The column 5 and 6 of Table 3.2.5 provides the power dissipation per unit length of each racetrack coil shown in figures 3.2.6, 3.2.7, 3.2.8, 3.2.10, to generate dipole or quadrupole field. To find the actual power dissipated per corrector, the values of column 6 in Table 3.2.5 must be multiplied by the length of the racetrack coil.

Temperature Stabilisation

As water cooling will be used for the window-frame corrector coils, it is inexpensive to add an additional layer of water in the magnet holder to stabilise the temperature of the permanent magnet blocks. This ideally will be the first place the cool water flows, before it gets heated up in the hollow copper conductors. A schematic of this scheme is shown in figure 3.2.12 below.

Table 3.2.5: Dissipated power in the racetrack coils to generate the required dipole or quadrupole field.

Type	Strength	# Racetrack coils	J [A/m ²]	Power/coil [W/m]	Power/corrector [W/m]
Dipole	± 50 Gauss	2	50	6	12
Quadrupole	± 0.45 T/m	4	375	150	600

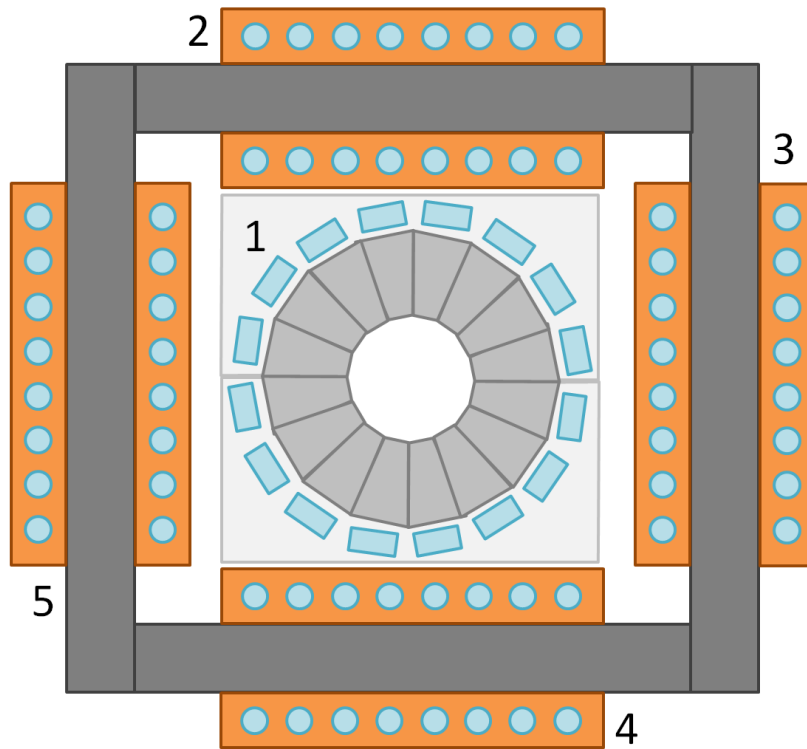


Figure 3.2.12: Schematic cross-section of the Halbach magnet and window-frame corrector assembly. Cooling water flows through channels in the magnet holder (1) before cooling the window frame corrector coils (2 through 5).

3.2.5 Halbach Magnet R&D and Shimming Results

BNL lab-directed R&D (LDRD) provided some money for constructing prototype permanent magnet quadrupoles for eRHIC, which is also an FFAG. Blocks were ordered from Shin-Etsu Corporation in August 2014 for three different designs, one of which was a Halbach quadrupole. The main differences between eRHIC and Cbeta magnets are that eRHIC requires an open midplane to allow synchrotron radiation to be dumped and eRHIC's magnets are $\sim 1\text{m}$ long, an order of magnitude longer than Cbeta's. However, to reduce cost, the eRHIC prototype magnets were built in 6cm sections, roughly the longest piece of permanent magnet the company could magnetise at once.

Table 3.2.6 below shows that the eRHIC prototype Halbach quadrupole is a good model for the Cbeta magnets too, at least until the parts for purpose-built Cbeta prototypes are delivered.

Table 3.2.6: Comparison of the Halbach shimming test magnet “5A” with requirements of Cbeta magnets.

Parameter	eRHIC prototype quad “5A”	Cbeta requirement QF	Cbeta requirement BD
Length	60.0mm	96.3mm	126.4mm
Gradient	27.5 T/m (measured)	-28.8 T/m	19.2 T/m
Central dipole	0 (by realignment)	0	-0.268 T
Material	SmCo R26HS (Shin-Etsu)	NdFeB N35SH (AllStar Magnetics)	NdFeB N35SH (AllStar Magnetics)
Min R of physical magnet pieces	22.5mm (design) 23.5mm (measured)	36.5mm	36.5mm
Max R of beam centroid	10mm (rotating coil) 15mm (extrapolated)	19.5mm	19.5mm
$R_{max,beam}/R_{min,magnet}$	43% (coil) 64% (extrapolated)	53%	53%

The eRHIC magnet was constructed out of SmCo instead of NdFeB for historical reasons: concerns about radiation resistance, with SmCo being more resistant. Since then, a radiation test has shown NdFeB of an appropriate grade survives >100 Gy of radiation on the RHIC beam dump during a run. SmCo also contains much more cobalt, which can lead to long-term Co-60 activation.

Repeatability of Unshimmed Halbach Magnets

Five 6cm-long permanent magnet quadrupoles were made for eRHIC prototyping, of the kind shown in figure 3.2.13 below. Note that the holder was made on a 3D printer and the design for eRHIC incorporates mid-plane gaps for synchrotron radiation to exit.

These were all measured on the BNL magnet division rotating coil to test the field quality of Halbach quadrupoles without shimming. Blocks from this factory, typically have 1-2% magnetisation strength error (the full width of magnetisation bins in the Shin-Etsu materials catalogue is $\sim 5\%$) and $\pm 1^\circ$ magnetisation direction error, according to the supplier's quote.

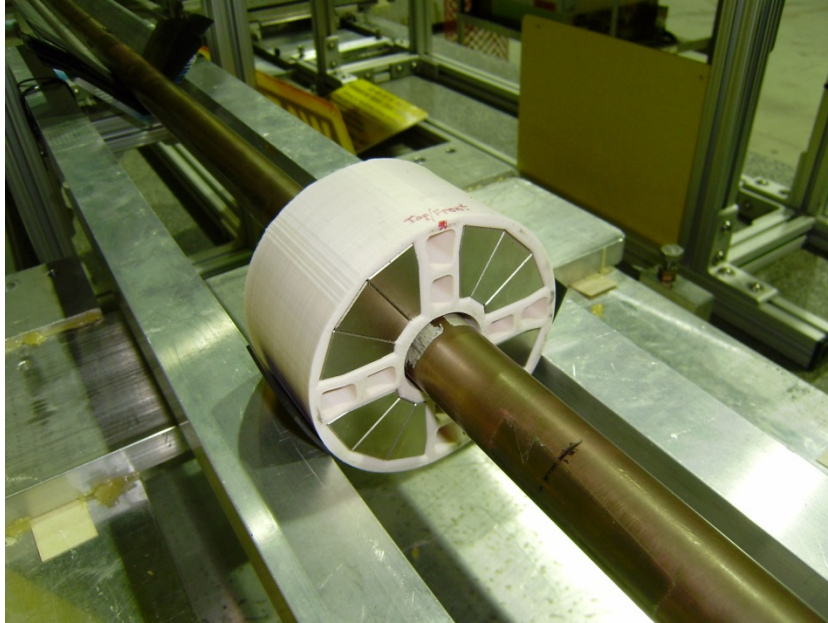


Figure 3.2.13: The 6cm-long eRHIC LDRD Halbach magnet being measured on the rotating coil at BNL's magnet division.

The five assemblies were measured on the rotating coil (not all the individual blocks), with results shown in table 3.2.14 below.

The Normal Dodecapole error of ~ 190 units present in all magnets should be ignored for this comparison, since it was a systematic error made by the manufacturer using the wrong information for magnetising some of the blocks. This was compensated for in later designs by moving the blocks.

The raw magnets have sextupole error magnitudes (normal and skew added in quadrature) of 13-57 units; octupole errors of 3-35 units; decapole errors of 6-13 units, with poles above dodecapole being less than 3 units. A unit is 10^{-4} relative to the main field, so these magnets are slightly better than 1% relative field error, which is roughly to be expected from the intrinsic magnetisation errors of the blocks they are made from. This on its own is not yet good enough for the 10^{-3} level accuracy required by the accelerator, so shimming is required as described in the next section.

The coil is calibrated to measure at 1cm radius, which is smaller than the Cbeta orbit excursion but as shown in the previous table 3.2.6, the eRHIC prototype magnet had a smaller aperture overall.

Unshimmed Magnet Theoretical Error Study

Although the above experiment has shown what the field errors are in reality, it is also possible to put random magnetisation errors into the simulation code in order to find out how specifications on the magnetisation error range translate into average errors in the Halbach magnets.

Summary of field measurements in eRHIC Permanent Magnet Quadrupoles (27-Apr-2015)Field harmonics are in "units" of 10^{-4} of the quadrupole field at a reference radius of 10 mm.

Quantity	PMQ_0001 Run 2	PMQ_0002 Run 3	PMQ_0003 Run 2	PMQ_0004 Run 3	PMQ_0005 Run 2	Quantity	PMQ_0001 Run 2	PMQ_0002 Run 3	PMQ_0003 Run 2	PMQ_0004 Run 3	PMQ_0005 Run 2
Integrated Gradient (T)	1.8647	1.9097	1.9053	1.8958	1.9024	Field Angle (mr)	--	--	--	--	--
Normal Dipole	--	--	--	--	--	Skew Dipole	--	--	--	--	--
Normal Quadrupole	10000.00	10000.00	10000.00	10000.00	10000.00	Skew Quadrupole	--	--	--	--	--
Normal Sextupole	27.83	-29.83	35.83	-4.53	-11.95	Skew Sextupole	-16.41	1.90	-43.69	28.96	-5.28
Normal Octupole	5.39	-3.12	32.81	16.50	3.61	Skew Octupole	-12.32	0.25	-12.55	4.03	-18.51
Normal Decapole	-4.92	-2.44	2.90	7.09	3.86	Skew Decapole	-11.98	-6.08	-5.68	-1.00	-8.52
Normal Dodecapole	-188.14	-194.57	-188.00	-192.96	-190.26	Skew Dodecapole	-2.27	-0.99	-3.12	0.87	-4.96
Normal 14-pole	-1.59	0.36	-0.67	0.43	1.03	Skew 14-pole	1.93	0.13	0.47	0.01	0.85
Normal 16-pole	-0.44	-0.22	-1.10	-0.58	-1.31	Skew 16-pole	-0.22	-0.09	-0.02	0.27	-0.13
Normal 18-pole	-0.24	0.19	-0.38	-0.25	0.07	Skew 18-pole	0.03	0.17	-0.06	0.05	0.10
Normal 20-pole	-2.37	-2.88	-3.13	-2.93	-2.91	Skew 20-pole	0.08	0.00	0.07	-0.20	0.01
Normal 22-pole	0.04	0.03	0.01	0.03	-0.01	Skew 22-pole	0.02	0.03	0.07	-0.05	0.00
Normal 24-pole	0.02	0.00	-0.02	0.01	0.04	Skew 24-pole	0.01	0.00	0.02	-0.02	0.01
Normal 26-pole	0.02	-0.01	0.02	-0.01	-0.02	Skew 26-pole	0.00	0.00	0.00	-0.01	0.01
Normal 28-pole	0.11	0.12	0.12	0.13	0.12	Skew 28-pole	0.00	-0.01	0.00	0.01	0.00
Normal 30-pole	0.00	0.00	0.00	0.00	0.00	Skew 30-pole	0.00	0.00	0.00	0.00	0.00

Figure 3.2.14: Table. Rotating coil measurements of 5 unshimmed Halbach permanent magnet quadrupoles.

Each block's magnetisation vector receives an independent random error. Since manufacturers give tolerances as total ranges (e.g. $\pm 2.5\%$ in strength), uniform distributions were used for these errors, with a parallel and perpendicular component being added for the magnetisation strength and angle errors respectively. In the study shown in tables 3.2.7 and 3.2.15 below, two cases were considered: a fairly good case where the strength error is 1% and magnetisation direction is also accurate to $1\% = 0.01$ radians = 0.57 degrees; and the worst case where the strength error is the full range of a material grade of 2.5% and the angle error is the worst quoted spec from a manufacturer of 5 degrees.

Table 3.2.7: Average over many runs of the total error in units (10^{-4} of the quadrupole amplitude), where the total error is the quadrature sum of all the normal and skew error poles, measured at the largest beam radius.

Magnet	Max magnetisation strength error	Max magnetisation direction error (radians)	Max magnetisation direction error (degrees)	Average total error (units = 10^{-4} of quad)
QF	1.00%	0.01	0.572958	31
QF	2.50%	0.0873	5	212
BD	1.00%	0.01	0.572958	29
BD	2.50%	0.0873	5	201

The two magnets QF and BD behave very similarly in terms of average field error size. The field errors also ought to scale linearly with the magnetisation error size. The real magnets ordered from Shin-Etsu Corporation in the previous section had total errors ranging from 26-67 units, with an average of 39, suggesting slightly ($\sim 33\%$) worse tolerances than the $1\%/0.57^\circ$

Amplitudes in units: (norm=24.8715)		Amplitudes in units: (norm=270.095)	
2-pole: -13.70	2-skew: 0.94	2-pole: -115.86	2-skew: -74.80
4-pole: 10000.00	4-skew: 5.05	4-pole: 10000.00	4-skew: 220.91
6-pole: 13.10	6-skew: 14.75	6-pole: 40.11	6-skew: -56.84
8-pole: -1.21	8-skew: -2.76	8-pole: -6.03	8-skew: -8.19
10-pole: -0.58	10-skew: -0.20	10-pole: -5.38	10-skew: -6.89
12-pole: -0.70	12-skew: 1.49	12-pole: 3.98	12-skew: 5.87
14-pole: 1.66	14-skew: -0.28	14-pole: -1.87	14-skew: 7.00
16-pole: 0.20	16-skew: 0.07	16-pole: -0.32	16-skew: 2.79
18-pole: -0.03	18-skew: 0.01	18-pole: -0.53	18-skew: 0.48
20-pole: -0.04	20-skew: 0.00	20-pole: 0.34	20-skew: -0.04
22-pole: -0.05	22-skew: -0.01	22-pole: -0.05	22-skew: -0.03
24-pole: -0.01	24-skew: 0.01	24-pole: -0.01	24-skew: -0.04
26-pole: 0.01	26-skew: -0.00	26-pole: -0.02	26-skew: -0.04
28-pole: 0.00	28-skew: 0.00	28-pole: 0.00	28-skew: 0.00
30-pole: 0.00	30-skew: -0.00	30-pole: -0.00	30-skew: 0.00
32-pole: 0.00	32-skew: -0.00	32-pole: 0.00	32-skew: -0.00
34-pole: -0.00	34-skew: 0.00	34-pole: -0.00	34-skew: -0.00

Figure 3.2.15: Multipole errors in two randomly-chosen instances of the QF magnet. (Left) a magnet with 1% magnetisation maximum amplitude error and 0.01rad maximum angle error. (Right) a magnet with 2.5% amplitude error and 5 degrees angle error.

case.

Field Quality Improvement after Iron Wire Shimming

The pieces from eRHIC magnet #5 were re-used to make a magnet that lacked the dodecapole error and served as a test-bed for shimming, as shown in figure 3.2.16 below.

The shimming method is that of “floating” iron shims, operating on the principle that a narrow iron cylinder placed in an ambient magnetic field will be magnetised in the same direction as the field. Provided the field is not so high that the iron saturates (assuming $\mu=\infty$ for the iron), the magnetisation will be proportional to the ambient field magnitude. The shim field contribution from the uniformly transversely magnetised iron cylinder is the same as that of a $\cos(\theta)$ superconducting dipole of the same dimensions: that is, an ideal external dipole field. The dipole moment is proportional to both the ambient field and the cross-sectional area of the shim.

An analytic field model of these iron wires was added to PM2D and 36 of the wires were placed at 10 degree intervals around the inner bore of the magnet. The code was asked to vary the radii (areas) of the wires in order to cancel the error multipoles observed in an initial measurement of the magnet with the rotating coil. The results of this process are shown in table 3.2.17 below.

An initial shimming designed to cancel only the sextupole was highly successful, reducing the sextupole amplitude from 20.5 units to 0.86 units, while the rest of the multipoles stayed roughly the same. It should be noted there is some logic to the shim arrangement: for the sextupole shim ($n = 3$) in a pure quadrupole background field ($m = 2$), the shim pattern has



Figure 3.2.16: The pieces of the eRHIC LDRD Halbach magnet placed in a new 3D-printed holder to form magnet “5A”. This is a corrected Halbach quadrupole whose holder incorporates holes for iron shims to be placed around the inside of the bore (iron wire grades shown in background).

pentagonal symmetry ($n + m = 5$) and areas proportional to $1 + \cos(5\theta + \phi)$ were used.

The optimiser was used to derive a shim distribution that would cancel all observed multipoles at once. The reduction was not as dramatic as with the sextupole alone, but reduced the quadrature sum of all error multipoles from 30.4 units to 4.34 units.

The rotating coil harmonics can be translated into polynomial fields with varying x across the $y=0$ midplane of the magnet, which is where the FFAG beam trajectories will be. These values are used in figure 3.2.18 below to calculate the relative error at any point across the aperture.

Reading off the worst values at the “53% of magnet aperture” value relevant to Cbeta, this magnet had a $4.6\text{e-}3$ relative field error on the midplane before shimming and a $1.2\text{e-}3$ relative field error after shimming. This is almost good enough for the accelerator and shimming R&D continues to try and improve on this. Better models of saturation effects in the iron wires may help.

eRHIC Permanent Magnet Quadrupoles PMQ_0005 & PMQ_005A (14-Oct-2015)

Field harmonics are in "units" of 10^{-4} of the quadrupole field at a reference radius of 10 mm.

Quantity	PMQ_0005 Run 2	PMQ_005A* Run 1_02(†)	PMQ_005A* Run 2(††)	PMQ_005A* Run 3(††)	Quantity	PMQ_0005 Run 2	PMQ_005A* Run 1_02(†)	PMQ_005A* Run 2(††)	PMQ_005A* Run 3(††)
Integrated Gradient (T)	1.9024	1.6501	1.6519	1.6537	Field Angle (mr)	--	--	--	--
Normal Dipole	--	--	--	--	Skew Dipole	--	--	--	--
Normal Quadrupole	10000.00	10000.00	10000.00	10000.00	Skew Quadrupole	--	--	--	--
Normal Sextupole	-11.95	-19.46	-0.58	0.87	Skew Sextupole	-5.28	-6.42	-0.63	-1.92
Normal Octupole	3.61	5.61	5.21	3.12	Skew Octupole	-18.51	-21.20	-21.18	-1.45
Normal Decapole	3.86	-0.99	-0.84	-0.32	Skew Decapole	-8.52	-4.02	-4.23	-0.70
Normal Dodecapole	-190.26	-1.03	-1.06	0.55	Skew Dodecapole	-4.96	0.22	0.32	-1.07
Normal 14-pole	1.03	1.25	1.04	-0.03	Skew 14-pole	0.85	0.07	-0.16	-0.51
Normal 16-pole	-1.31	-1.47	-1.52	-0.24	Skew 16-pole	-0.13	-0.31	-0.33	-0.30
Normal 18-pole	0.07	0.12	0.13	0.05	Skew 18-pole	0.10	-0.05	-0.06	-0.22
Normal 20-pole	-2.91	0.44	0.40	-0.01	Skew 20-pole	0.01	0.24	0.23	0.00
Normal 22-pole	-0.01	-0.03	-0.01	0.01	Skew 22-pole	0.00	0.00	0.01	0.06
Normal 24-pole	0.04	0.05	0.03	-0.09	Skew 24-pole	0.01	-0.01	-0.02	-0.03
Normal 26-pole	-0.02	-0.01	-0.01	-0.03	Skew 26-pole	0.01	0.00	0.01	0.00
Normal 28-pole	0.12	-0.12	-0.12	0.02	Skew 28-pole	0.00	0.00	0.00	0.02
Normal 30-pole	0.00	0.00	0.00	0.00	Skew 30-pole	0.00	0.00	0.00	0.00

* PMQ_005A is magnet built from magnets taken from PMQ_0005 and installed in a modified holder to reduce 12-pole

(†) Magnet was measured with the magnet rotated 90 deg. about its axis, and flipped end-for-end, as compared to PMQ_005 measurements. The data were transformed in post-processing to correspond to the old orientation.

(††) Runs 2 & 3 are measurement in PMQ_005A with two iterations of iron shims to reduce unallowed field harmonics.

(Note: Magnet name used for testing was ERHIC-PMQ_0105 to avoid non-numeric serial number).

Figure 3.2.17: Rotating coil measurements of the shimming test magnet before shimming (Run 1_02), with sextupole-only correction (Run 2) and with all-multipole correction (Run 3) using iron wire shims.

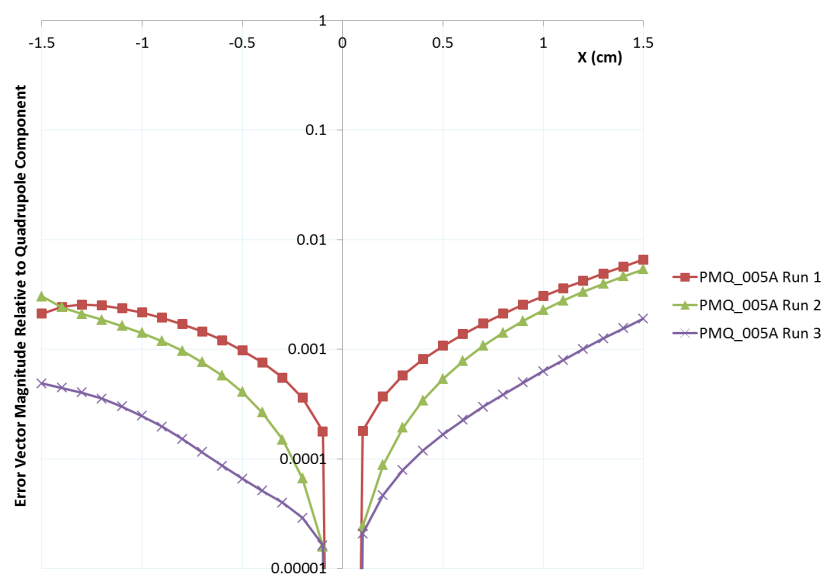


Figure 3.2.18: Relative field errors as a function of x on the y=0 midplane for the shimming test magnet: before shimming (Run 1, red); after sextupole cancellation (Run 2, green) and after all-multipole shimming (Run 3, purple).

3.2.6 Plan for BNL Cbeta Halbach Prototypes

Purpose-built prototype magnets for Cbeta have also been ordered, including the “lopsided Halbach” magnet BD. Due to the 2-3 month magnet lead times, these are from an old lattice design Cell_Brooks.2015-12-11 rather than the most recent Cell_Smoothpipe.2016-02-04 presented in this report, but they are similar. Delivery of permanent magnet pieces should occur at the end of March 2016. A comparison of the magnets in the two versions is given in table 3.2.8 below.

Table 3.2.8: Comparison of current lattice Halbach magnets to those of the Cbeta prototypes ordered.

Parameter	QF current	QF prototype	BD current	BD prototype
Length	96.3mm	114.9mm	126.4mm	123.7mm
Gradient	-28.80 T/m	-23.62 T/m	19.19 T/m	19.12 T/m
Dipole at centre	0	0	-0.2680 T	-0.3768 T
Max good field radius	19.5mm	20.2mm	19.5mm	13.7mm
Min inner radius	36.5mm	37.2mm	36.5mm	30.7mm
Max outer radius	70.2mm	62.4mm	69.3mm	59.4mm
Max field in good field region	0.56 T	0.48 T	0.64 T	0.64 T
Max field at “pole tip”	1.05 T	0.88 T	0.97 T	0.96 T

These have been ordered from AllStar Magnetics rather than Shin-Etsu (due to cost reasons), which means a larger magnetisation angle error in the blocks of ± 5 degrees as specified by their factory. Shimming methods will be tested to see if they can compensate for this larger error, possibly including shimming magnets instead of the iron wires.

3.2.7 Manufacturing Pipeline and Vendors

Discussions are starting with magnet manufacturing companies about what they can build for Cbeta. The pipeline of magnet manufacture and assembly onto the machine breaks down into the four stages below.

Permanent Magnet Wedges

These will be purchased, directly or indirectly, from a company. As mentioned previously, Shin-Etsu Corporation is a large manufacturer of the permanent magnet blocks with reasonably high quality. AllStar Magnetics has also provided BNL permanent magnets block in the past (for instance the radiation damage experiment), although they specify larger tolerances on their magnetisation angles. Electron Energy Corporation (EEC) has recently succeeded in an SBIR proposal for Cbeta and eRHIC magnet development worth \sim \$1M but this is spread over three years from April 2016 to April 2019. EEC manufactures both the blocks and magnet assemblies on-site in their machine shop. Finally, VacuumSchmelze GmbH has been contacted by Holger Witte for magnet blocks for the iron-poled quadrupole. Other companies not contacted yet include the undulator manufacturer KYMA.

Of these companies, AllStar generally provides the lowest cost but the least accurate magnetisation vector guarantee (± 5 degrees). Shin-Etsu provides ± 1 degree tolerance with some additional cost for tooling. EEC say even ± 0.5 degrees is possible but there is an associated cost since additional steps of demagnetising the block, re-grinding it to an accurate shape and re-magnetising it have to occur.

Magnet Assembly

Although in theory this could be done on the BNL or Cornell sites, it seems that several companies are willing to bid for this work and are capable of doing it. EEC could be used as an end-to-end vendor for these first two steps. RadiaBeam LLC will make assemblies and girders but have to get the PM blocks from another company. They previously gave a cost estimate for assembling the Cbeta magnets and girders and are the only ones to have significant accelerator field experience (in fact they also make Halbach magnets for electron microscopes). Their absolute tolerances on positioning magnets on the girders were 0.1mm.

Shimming and Rotating Coil Measurements

Discussions so far with magnet manufacturers are indicating that the rotating coil is a specialised piece of measurement equipment for accelerator applications. None of the companies contacted so far have functioning rotating coils, although Radiabeam and EEC have Hall probes for field mapping. The shimming method works best using a rotating coil, so this stage is likely to be done in the BNL magnet division, where they have done it before.

Alignment and Girder

Since the magnets will need to be removed to do separate rotating coil and shimming steps, a fully integrated manufacture (measurement while on girder) does not look possible. Instead,

survey fittings will be included in the non-magnetic body during the magnet assembly step and these will be used in the hall at Cornell to fit in with their on-site survey system. The survey references may also be used in the rotating coil stage to ensure alignment between the magnetic field and the magnet holder.

3.2.8 Early Cost Estimates for Wedge Blocks

For the whole FFAG part of the machine consisting of 148 FFAG cells (296 magnets), Shin-Etsu Corporation quoted a price of \$725k for all the permanent magnet wedges, which included \$24k of their own tooling to make the angles correct. Extrapolating AllStar Magnetics' price for 3 cells for the prototypes (\$7698) to the full machine gives \$380k, although bulk discounts may apply and this is with the looser tolerances on the magnetisation (5 degree angle rather than 1 degree).

The cost of the permanent magnet blocks does not dominate the cost of the FFAG, which includes magnet holders, correctors, girders etc. RadiaBeam LLC estimated a \$1.45M cost for assembling holders for the wedges and aligning them onto girders. This excludes the wedges themselves and also does not include the correctors or their power supplies, which will be significant.

3.3 Magnet Stands [Georg]- 1st draft due 04/28

3.4 Power supplies [John Barley]

The following sections describe possible magnet power supplies for the dipoles and quadrupoles in the spreaders and recombiners, and correction magnet power supplies for the spreaders, recombiners and arcs.

3.4.1 Dipole and Quad Power Supplies for the Spreaders

The present plan is to use off-the-shelf TDK/Lambda power supplies, which we have used successfully for many years. As soon as the current/voltage requirements are provided, we will add the appropriate model numbers and specifications.

3.4.2 Corrector Magnet Power Supplies

The machine will have correction coils for steering in the spreader and recombiner regions, as well as the FFAG arcs and straight section. The FFAG magnets will additionally have correction coils to adjust the quadrupole strengths. At the current time we do not have current/voltage requirements, nor a count of the number of magnets. The following three sections describe possible bipolar power supplies that may be appropriate. The quadrupole correction power supplies may or may not need to be bipolar.

Kepco BOP 20-10M

We were able to obtain a number of used Kepco power supplies from BNL, approximately 120 units. They provide ± 20 V and ± 10 A with a smooth transition through zero. The supplies are 3U size with 1U of cooling space between units, and ventilation on the top and rear. Each unit does not fill a rack width, thus wasting space on the sides. With an 8 foot rack, 13 supplies can be installed. See Fig. 3.4.1 and Fig. 3.4.1.

Kepco sells an upgrade card that allows for ethernet control on the supply. The upgrade includes a transformer replacement, rear panel modifications, and required about 2 man-days to complete the modifications and testing. We have contacted Kepco about having them install the cards, test each unit, and fix any problems. See Fig. 3.4.3 and Fig. 3.4.4 for details.

The ethernet boards cost \$1020 each. Brand new units cost just under \$4000 each. The static and dynamic specifications are shown in Fig. 3.4.5 and Fig. 3.4.6.

BiRa MCOR 12/30

BiRa produces blade power supplies in a 6U crate, with 2U for cooling fans and 1U for the bulk power supply (see Fig. 3.4.7). Each crate has 1 ethernet control card, 16 ± 12 A modules (or 8 ± 30 A modules). The 12 A modules can be configured to 2 A, 6 A, 9 A or 12 A maximum current.

We received a quote for a quantity of 200 (see Tab. 3.4.1, with a total cost of \$734,950 and a net cost of \$3675 per unit.



Figure 3.4.1: The front panels of the Kepco Supplies.

Table 3.4.1: Price breakdown for 200 Bira Modules and components

Description	quantity	Unit Cost	Total Cost
2510 MCor 12 Module	200	\$2,656.25	\$531,250
Ethernet Control Card	15	\$4,870	\$73,050
4922 MCor Blower (2U)	15	\$675	\$10,125
2507 DC Power Cable	15	\$350	\$5,250
2509 Magnet Cable			\$21,000
Bulk PS 2.4 kW 1U	15	\$3,000	\$45,000

CAEN 20-10 Easy Driver

Caen has 1U standalone units with ± 5 A and ± 10 A version, with an ethernet interface (see Fig. 3.4.8). They have low-noise output with digital regulation loops, internal protections and auxillary readbacks. An 8 foot rack can hold 54 channels.

The specifications are

- ± 20 V, ± 10 A
- $160 \mu\text{A}$ current setting resolution
- 20 bit output resolution for voltage and current
- output current ripple 50 ppm/FS
- output current stability 50 ppm/FS
- switching frequency 100 kHz

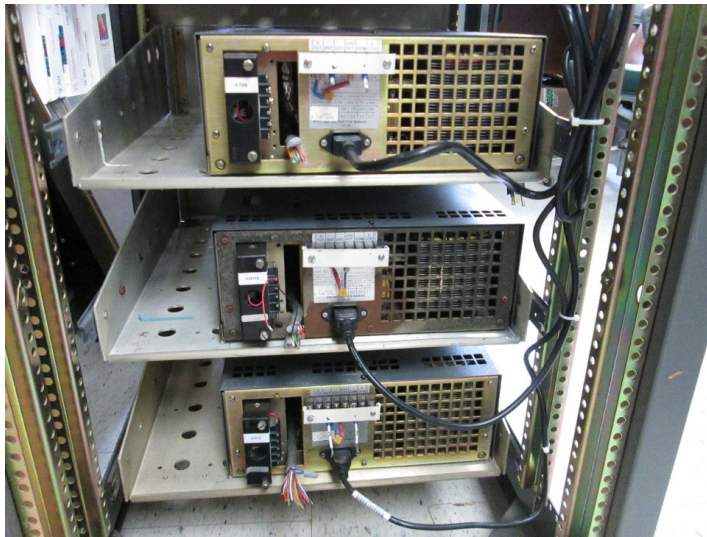


Figure 3.4.2: The back side of the Kepco supplies

- closed loop bandwidth 1 kHz

The Caen Easy-Driver 1020 digital bipolar power supply cost is \$3,250 per unit for a quantity of 250, with a 15% discount applied. The total price for 250 is \$690,625, or \$2,762.50 per unit including the discount.

They also quoted model FAST-PS 1020-20, a fast corrector current supply, for a total price of \$1,065,900, or \$4,263.60 including the discount.

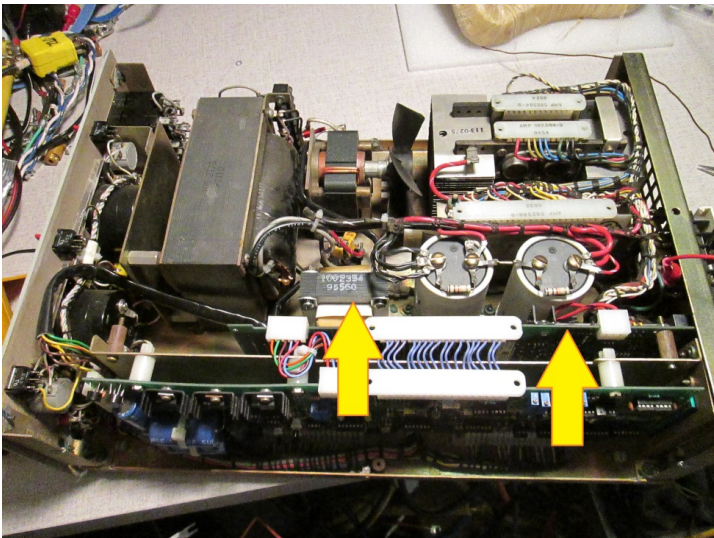


Figure 3.4.3: Modifications to install the ethernet card upgrade.



Figure 3.4.4: Back panel modifications to install the ethernet card upgrade

MODEL	BANDWIDTH (d-c to f _{3dB}) KHz (minimum) Mode		RISE & FALL TIME 10% to 90% µsec (minimum) Mode		LARGE SIGNAL FREQUENCY RESPONSE KHz (minimum) Mode		SLEWING RATE (mimumum) Mode		RECOVERY STEP LOAD µsec (minimum) Mode	
	V	I	V	I	V	I	V	I	V	I
	200 WATT									
BOP 20-10M	18	6	20	60	17	7	2V/µsec	0.4A/µsec	80	20

Figure 3.4.5: Dynamic specifications for the Kepco supply

INFLUENCE QUANTITY		OUTPUT EFFECTS ⁽¹⁾				PREAMPLIFIER OFFSETS ⁽⁴⁾		REFERENCE ±10V
		VOLTAGE MODE		CURRENT MODE		ΔE _{io}	ΔI _{io}	
		TYPICAL	MAXIMUM	TYPICAL	MAXIMUM			
Source (min.-max.)		<0.0005%	0.001%	<0.002%	0.005%	<5μV	<1nA	<0.0005%
Load (NL-FL)		<0.001%	0.002%	<0.5mA	1mA	—	—	<0.0005%
Time (8-hour drift)		<0.005%	0.01%	<0.01%	0.02%	<2.0μV	<1nA	<0.005%
Temperature, per °C		<0.005%	0.01%	<0.01%	0.02%	<2.0μV	<1nA	<0.005%
Ripple and Noise ⁽²⁾	rms	<1mV	3mV	<0.01%	0.02%	---	—	—
	p-p	<10mV	30mV	<0.01%	0.02%	---	—	—

Figure 3.4.6: Static specifications for the Kepco supply

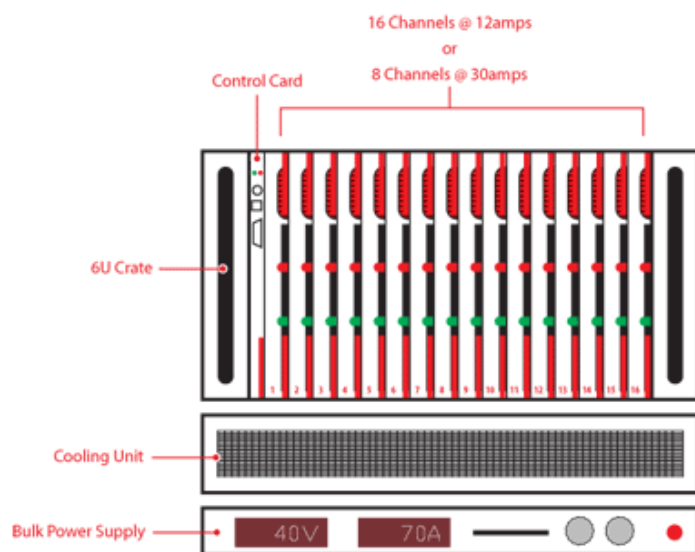


Figure 3.4.7: A schematic of the BiRa crate



Figure 3.4.8: The Caen magnet power supply unit.

	Easy - Driver	FAST-PS
Output Current	up to ± 10 A	up to ± 30 A
Output Voltage	up to ± 20 V	up to ± 80 V
Output Power	up to 200 W	up to 600 W
Local Display	✓	✓
Local Control	✗	✓
Control Loop Type	Digital	Digital
Control Loops	Current	Current Voltage
External Interlocks	1	2
Status Signals	1 solid state relay	1 solid state relay 1 magnetic relay
Remote Sensing	No	Yes
Remote Interface	10/100 Ethernet	10/100/1000 Ethernet SFP Fast Interface
Remote Update Rate	250 Hz	1 kHz - Ethernet 10 kHz - SFP Fast Interface
Other Features	Firmware Remote Update Configurable Thresholds/Limits Internal Protections	Firmware Remote Update Waveform loading and execution Configurable Thresholds/Limits Internal Protections Embedded Linux OS USB host External Trigger - <i>option</i> Analog Control Input - <i>option</i>

Figure 3.4.9: A comparison between the two Caen models.

4 Injector [Bruce]- 2nd draft 05/04

4.1 Introduction

The Cornell accelerator group now operates the worlds highest average current, high brightness photoinjector, a prerequisite for the emerging machines in nuclear physics, high energy physics, FEL facilities, and industrial application, see Fig. ?? . The beam is produced in a laser-driven photoemission gun (A1), accelerated to as much as 10 MeV in superconducting RF cavities (A2), after which beam parameters are measured (A4, C1, B1, C2), and finally absorbed in a beam dump (A5). Among the achievements are the world-record average current of 75 mA from a photocathode injector with many-day cathode lifetimes at currents above 60 mA [12,13], and beam emittances approaching the thermal (intrinsic) photocathode emittance at a bunch charge of 80 pC in the space-charge dominated regime [14]. This frontier R&D facility has in many ways cleared the path towards the ambitious future projects by demonstrating the worlds highest brightness and average current photoemission-based source of relativistic electrons.

Photoinjectors are used at the majority of the electron linac-based accelerators today, due to their efficiency, timing structure flexibility and ability to produce high power, high brightness beams. These properties make the Cornell injector an ideal electron source for the FFAG-based ERL described in this document. The details of the injector and all of the subsystems are described in the following sections.

4.2 The DC Photoemission Gun

High voltage DC photoemission electron guns offer a robust option for photoelectron sources, with applications such as Energy Recovery Linacs (ERLs), free electron lasers, ultrafast electron diffraction, and ultrafast electron microscopy. The technology for such guns was developed in the 1970's (ref 5) and the simple conceptual design has remained relatively unchanged since that time.

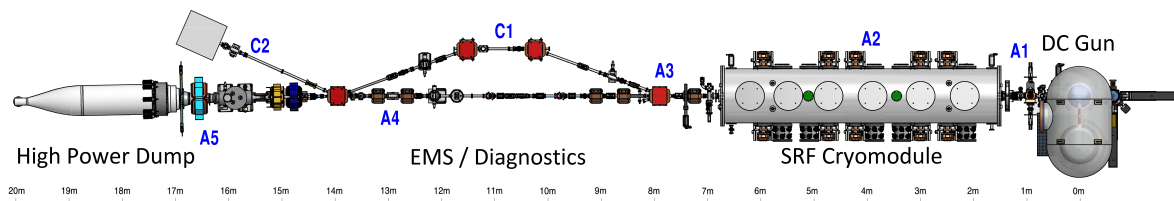


Figure 4.1.1: A schematic of the Cornell photoinjector, capable of providing beams up to 500 kW (5 MeV, 100 mA or equivalent).

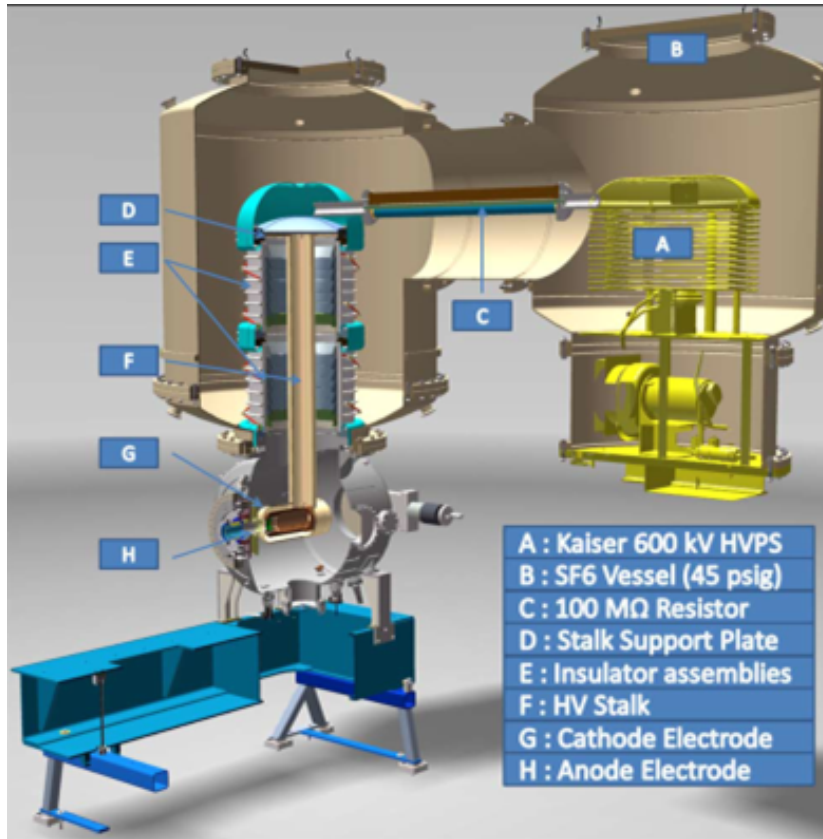


Figure 4.2.1: A cutaway view of the DC photoemission gun. Photocathodes are prepared in a load lock system mounted on the large flange at the left, and transported through the cathode cylinder to the operating position in the Pierce electrode shape on the right. The beam exits through the small flange to the right.

A DC gun for a high brightness, high intensity photoinjector requires a high voltage power supply (HVPS), usually some variant of the Cockcroft Walton multiplier, supplying hundreds of kV to the high voltage (HV) surfaces of the gun. The power supply and outer gun structures at HV are often enclosed by a chamber pressurized with sulfur hexafluoride (SF_6) as a dielectric buffer gas to suppress arcing in the HVPS. The HV surfaces of the gun chamber are held off from the grounded chamber surfaces via an insulator structure. Inside the chamber, the cathode electrode is suspended in the chamber center via a support stalk, which also connects the HV to the cathode electrode.

The anode electrode is constructed from titanium, and is isolated from ground using small alumina washers. This allows the anode to be biased in order to reject ions that backstream into the anode-cathode gap region from further down the beamline. The anode can hold off up to 5 kV. At the rear of the gun a vacuum load-lock system allows cathodes to be inserted and removed without disturbing the gun vacuum. The cathode is illuminated from the front side of the gun using mirrors that are mounted in a light box between the first solenoid and the buncher.

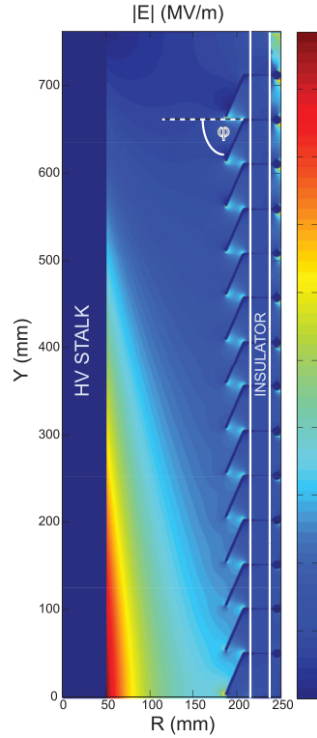


Figure 4.2.2: Simplified HV model made in the software Opera 2D. Shown is the HV stalk, insulator, and guard rings for the gun operating at 750 kV. Color corresponds to the magnitude of the electric field in MV/m. For simplicity, this HV model is monolithic, rather than made of two insulator assemblies (as built), and similarly does not show the triple point protection rings.

An overview of the gun and its major components is shown in Fig. 4.2.1. One of the most important design differences between this gun and the original Cornell DC gun (17) is the use of a segmented insulator structure (Fig. 4.2.1(E)). The entire insulating structure is composed of two smaller insulator assemblies. Both insulator assemblies were manufactured by Friatec AG. Each insulator assembly has 7 segments, or 14 in total installed on the gun. Each segment is a ring of Al_2O_3 with an inner diameter of 435 mm, 50 mm tall, and 20 mm thick. The dielectric strength of the Al_2O_3 is quoted by Friatec to be beyond 30 kV/mm, with a resistivity of $10^{15} \Omega \cdot \text{cm}$ at room temperature. The top segment and bottom segment of each assembly is brazed into a 22.125 inch 316LN wire seal flange.

A kovar ring is brazed between each of the insulator segments. In vacuum, the kovar ring allows the attachment of the insulator guard rings (described below). These rings also extend outside the insulator body into the SF_6 environment. In the SF_6 , a resistor chain from HV (at the top) to ground (at the bottom) connecting to each kovar ring directly defines the voltage on all segment interfaces and inner guard rings. Kovar was chosen as the interface ring material for its similar coefficient of thermal expansion to that of the Al_2O_3 , so that the braze joint would be minimally stressed during thermal cycling. The kovar rings at the top and bottom of the insulator are shaped to fit into 22.125 inch 316LN wire seal flanges and

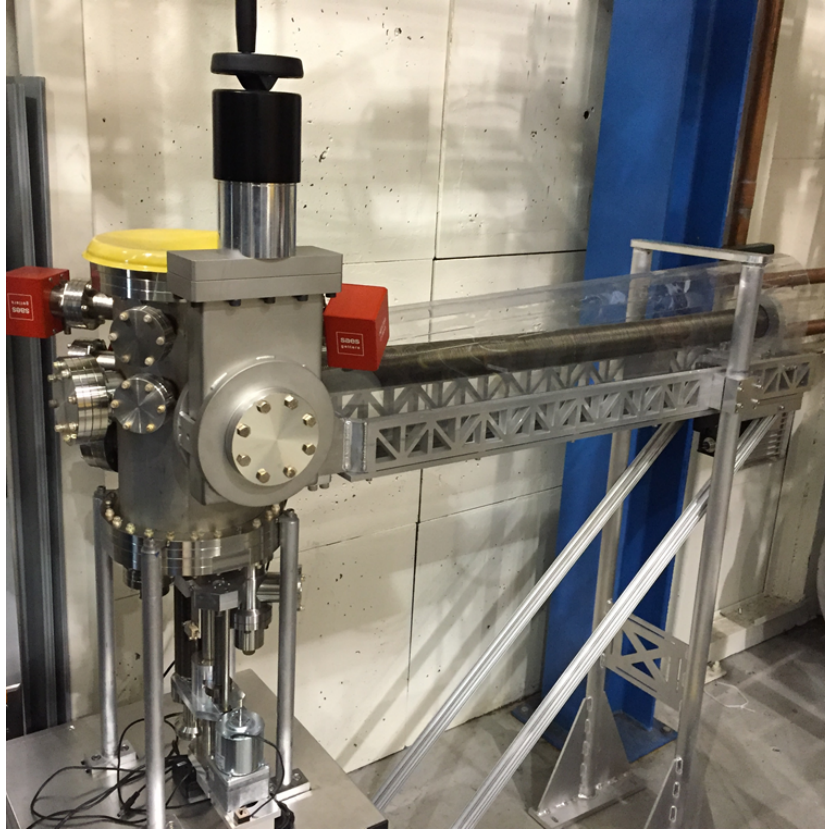


Figure 4.2.3: Cathodes are transported in a vacuum suitcase (not shown) and attached to the manual gate valve. Cathodes are moved from the suitcase into the central vacuum chamber, which can hold three cathode pucks. The bellows translation mechanism moves the pucks from chamber into the gun.

welded.

The insulator guard rings between each segment block field emitted electrons from landing on the insulator surface, reducing the possibility of insulator damage. The rings were made of copper due to its ease of machining and high thermal conductivity, thereby minimizing the heating of the ring and nearby braze joints from any stray field emission. A simplified high voltage model of the guard rings, insulator, and HV stalk are shown in Fig. 4.2.2. The angle of each ring with respect to the horizontal, 67.5° , was chosen such that no field emitted electrons could reach the surface of an insulator segment, based on particle tracking. The angle of the lowermost ring was increased to 72.0° as the electric field lines changed near the ground plane, and some electrons could have reached the insulator with the 67.5° angle.

One of the most vulnerable locations with respect to field emission on any vacuum insulator is the so-called triple point junction, which is the interface between the stainless steel, ceramic, and vacuum. These junctions are shielded by additional triple point protection (TPP) rings which attach directly to the interior of the flanges, and are also made of stainless steel. The HV stalk (Fig. 4.2.1(F)) is a 1.25 m long hollow cylinder with 125 mm outer diameter. The

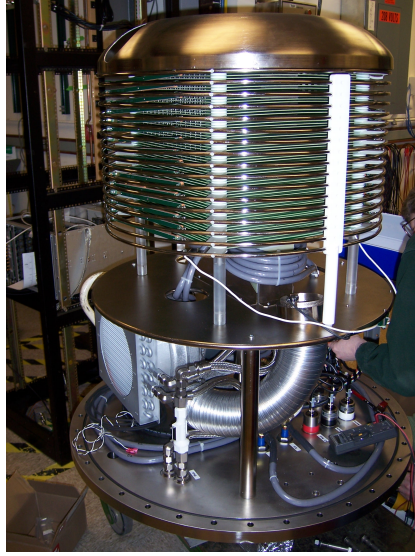


Figure 4.2.4: The HV section of the 750kV power supply. Individual circuit boards are visible inside the potential grading rings. The primary winding of the insulating core transformer is the large diameter gray-insulated wire below the circuit boards. The HV section is mounted in the pressurized SF_6 tank with its axis parallel to the axis of the gun ceramic.

stalk center axis is co-linear with the insulators center axis (in Fig. 4.2.2, the line at $R=0$), and is attached to a support plate (Fig. 4.2.1(D)) which rests on top of the uppermost TPP ring. As the stalk supports the cathode electrode, its height, angle with respect to the y-axis, and rotation angle about the y-axis are of direct importance for the symmetry of fields in the photoemission region. Thus, adjustment screws on the stalk plate permit the adjustment of height, both angular offsets from the y-axis, and the rotation of the stalk.

The insulators and stalk sit on the gun vacuum chamber, which is held at ground potential, along with the SF_6 chamber walls. The gun chamber is a 600 mm diameter cylinder shell, 5 mm thick, with its symmetry axis along the direction of the beam. Pumping is provided by a three non-evaporable getter modules (SAES Capacitorr D-2000) and two 40 l/s ion pumps. Each ion pump is placed behind a NEG module in a single assembly, so that any gas load produced by the ion pumps would first be pumped by the NEG modules before entering the gun chamber. Each of these combined pumping assemblies is attached to a 8 inch conflat flange on either side of gun chamber. A leak valve manifold with both a turbomolecular pump and a source of ultra-pure noble gas is attached to a UHV right-angle valve on the gun chamber for noble gas processing. The cathode electrode (Fig. 4.2.1(G)) design is identical to that of the original Cornell gun (17), as this design was shown to be an effective balance between providing optimal focusing and high photocathode field strength while having minimal electric fields outside of the photoemission region (18). Furthermore, this cathode design was shown to give excellent emittance for bunch charges up to 80 pC (16) for a gun operating at 350 kV. The cathode design is Pierce-type, with a focusing angle of 25° . The focusing introduced by this electrode angle serves to counteract the initial space charge expansion of an intense

photoemitted beam.

The cathode electrode is made of vacuum remelt 316LN stainless steel. It features a leaf spring assembly inside the cathode interior to hold and register a removable photocathode puck (Fig. 4.2.1(1)) in the center of the Pierce electrode. The back of the cathode electrode is terminated with a half-torus to keep electric fields low, with the torus hole permitting the transfer of photocathodes in and out of the interior holder.

In general, we follow the procedures developed for cleaning superconducting radio frequency (SRF) cavities whenever possible for surfaces supporting high electric fields. Although field emission is a poorly understood process, it is well known that the condition of the HV surface in terms of both roughness and contaminants strongly affect the fields at which field emission or pre-breakdown activity begins. Both particulate contaminants and scratches or roughness can cause field enhancements which precipitate field emission or vacuum breakdown (19, 20). Furthermore, both surface contaminants and dielectric inclusions in the metal can alter the work function of the material.

First, all metallic HV surfaces of the gun, including stalk, cathode electrode, copper rings, TPP rings, and anode, were mechanically hand-polished using silicon carbide. For the stainless steel electrodes, an additional polishing with diamond paste is performed. Then, a chemical polishing step was applied to all mechanically polished parts. For stainless steel parts (stalk, cathode electrode TPP rings), standard electropolishing was performed, removing 10 μm of material. For the copper rings, a weak citric acid etch was performed, as this was shown via interferometric microscopy to produce a surface with smaller root-mean-square (RMS) roughness than a more powerful copper etchant (such as nitric and sulfuric acid). After electropolishing, all stainless steel vacuum components (including chamber, stalk, and electrodes) are baked in air at 400 C for 100 hours to reduce hydrogen outgassing.

After surface treatment, all vacuum surfaces (including the chamber itself, but excluding the vacuum pumps) in the gun were high pressure rinsed with DI water in clean room conditions equivalent to ISO 5 or better, to remove particulate contamination. The insulator itself was rinsed with 300 psi water, whereas all metallic surfaces were rinsed with pressures 600 psi (minimum), for approximately 3 h per part. Both copper and TPP rings were rinsed on a separate rinse stand, apart from the insulator.

After a full air dry of all parts in the clean room, the insulators were populated with rings manually. The cathode electrode was assembled on a test stand, and then suspended in the chamber via a temporary support from the back of the gun. The insulators were installed on to the chamber and cathode assembly via a clean room crane. The stalk without top plate was similarly lowered through the insulators via the crane, and was attached to the cathode and temporary cathode support. Finally, the top plate was installed and attached to the stalk, allowing the cathode electrode support to be removed. Using surveying mounts installed in the photocathode holding structure, the height and angle of the electrodes were adjusted to be concentric with the axis defined by the anode and load-lock chamber angles. The gun was then sealed, evacuated and checked for leaks, then transported to its final location. A vacuum bake was performed at 150 C for approximately two days, followed by NEG activation at 500 C for 1 h. The final vacuum prior to processing was 2×10^{-11} torr.

The gun HV power supply, 750 kV at 100 mA, is based on proprietary insulating core transformer technology and was manufactured by Excelitas Technologies (formerly Kaiser Systems). It is comprised of a stack of circuit boards insulated from each other. Each board

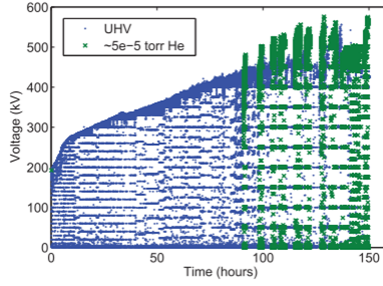


Figure 4.2.5: The voltage applied to the gun during conditioning, corrected for the voltage drop across the processing resistor. Data points are colored for UHV (blue dot) and gas (green x) conditioning.

contains two ferrite cores which couple a high frequency magnetic field from one board to the next. Each board can deliver up to 12.5 kV at 100 mA, and is only 5 mm thick, leading to a very compact supply. 62 boards are used in the full stack, which is shown in Fig. 4.2.4. The primary of the ferrite insulating core transformer is powered by an external high frequency driver.

HV conditioning to date has taken over 150 h. The gun was installed with a 600 kV DC power supply from Excelitas Technologies (we have a 750 kV and a 600 kV supply), in an SF_6 environment at 3 bar. The gun is connected to the power supply via three 300 M Ω film resistors (Nichrome Electronics, model 1000.300), each 1 m long, connected in parallel for redundancy. This processing resistor limits the current applied to the gun in case of a short circuit through an arc in the gun. Each segment of the insulator has two parallel sets of 1 G Ω resistors (Caddock resistor model MG815), giving the insulator a total resistance of 7 G Ω , as verified by an electrometer. Thus, a given voltage V applied by the power supply corresponds to a voltage across the gun of $(10.014) \times V$, as 1.4% of the supply voltage is dropped across the processing resistor.

A principle figure of merit during HV conditioning is the current drawn by field emitters or by fast emission events often called pre-breakdown events (20). This current is read by a floating ammeter attached to the HVPS at high voltage. The floating ammeter is powered by infrared diode laser and photocell, via a fiber optic feedthrough in the SF_6 tank. Data from the ammeter is transmitted via a fiber optic transmitter/receiver. In principle, the total current could be read from the power supply itself, however the power supply has an associated leakage current which makes this value difficult to interpret, and does not have adequate resolution. However, this value is used to trip off the gun during a pre-breakdown event. The value was chosen such that the vacuum and emitted currents were within acceptable levels.

The floating ammeter has a maximum readable current of 150 μA . Furthermore, the insulator resistor chain has an expected current draw for a given voltage of 10-100 μA . Thus, there is limited headroom for the measurement of any excess current, defined as the difference of the expected current to the actual current, which decreases with increasing voltage. As such, many pre-breakdown events saturated the floating current monitor. This saturation does not affect the reading of the resistor chain excess current monitor.

The conditioning was performed with an anode-cathode gap of 50 mm. The voltage across

the gun was slowly increased to a state of pre-breakdown, most often to the point of tripping off due to exceeding the current limit setting, with subsequent attempts permitting higher and higher voltages before tripping. The first voltage at which vacuum disturbance was detected was approximately 185 kV. Fig. 4.2.5 shows that the majority of our voltage progress was linear with time. Spikes of the resistor chain excess current correspond to emission from the HV stalk surface to the copper insulator guard rings, and was treated with extra caution, as such emission had previously caused punch-through in unprotected insulators. Large emission to the rings in the first 10 h of conditioning were found to abruptly cease, and the overall emission to the rings from them was usually less than 50 μ A. After approximately 30 h of conditioning, we found that the integrated gas load on the NEG pumps was nearing saturation. At this time we also observed a downturn in the slope of progress. We believed this to be due to the increased gas load in chamber, as residual gas that is not pumped can be ionized to initiate prebreakdown events. However, after NEG reactivation, the conditioning resumed without issue, and the slope of voltage progress increased back to its original value.

At voltages above 400 kV, field emitters began to be created that could not be pacified by normal UHV conditioning. We found that helium or krypton gas processing to be effective in suppressing these emitters (shown in green in Fig. 4.2.5). For gas processing, 5×10^{-5} torr of gas was introduced into the gun via leak valve, with all ion pumps off and an external turbo pump connected. Noble gases are not well pumped by the NEG's, so do not saturate them. The use of gas routinely allowed a voltage setting above 500 kV, at which fields the more stable field emitters would show a gradual decrease in current drawn, and ultimately each one is eliminated. Conditioning then continued with alternating rounds of UHV and gas conditions, allowed us to apply conditioning voltages above 500 kV in UHV. At this time, the gun is stable enough for operations at 450 kV, but further processing is needed to be stable at 500 kV.

4.3 Photocathodes

During the original work on the ERL injector, GaAs photocathodes were used, as they are known to have the lowest intrinsic emittance of any photocathode, and our group had extensive experience with GaAs from polarized electron sources. It quickly became clear that GaAs photocathodes should not be used, due to their extreme sensitivity to vacuum conditions and poor lifetime at high average currents.

We switched to alkali photocathodes, which are known to be more robust from previous RF gun use [ref dowell] and as detectors in photomultiplier tubes. Following on the work of others, we developed recipes to grow various alkali cathode (a,b,c) and measured their properties. Numerous papers by our team give details on thermal emittance measurements and high current operation. Overall, alkali-type cathodes have roughly the same thermal emittance as GaAs cathode (at 520 nm), but are much less sensitive to vacuum disturbances and thus have reasonable lifetime.

The properties of various alkali cathodes have been measured by our group (see references). For operations, we typically use NaKSb type photocathodes, which are known to survive even at elevated temperatures. We performed high average current lifetime measurements using a cathode of this type. Fig. 4.3.1 shows a plot of average current and quantum efficiency

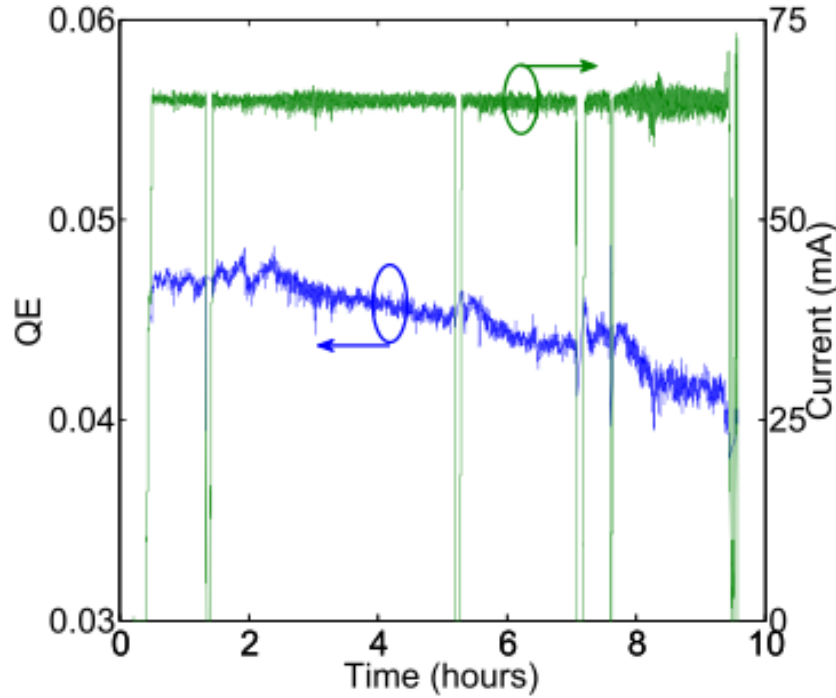


Figure 4.3.1: Photocurrent and QE of a NaKSb photocathode operated in a high average current run of the ERL injector. 65 mA of average current was been delivered for about 9 h. QE degradation with a $1/e$ time constant of 66 h was observed

as a function of time, demonstrating that, with adequate laser power, one can operate for approximately 1 week using a single cathode.

4.4 The Laser System

The key design parameters of the ERL photoinjector laser system are given in Tab. 4.4.1. A brief justification for these parameter choices follows. The wavelength chosen for the laser is 515–530 nm – corresponding to the frequency of doubled Ytterbium fiber laser. This wavelength is a reasonable match to the desirable properties of alkali cathodes, and it is relatively easy to generate significant average optical powers. Yb lasers allow the generation of a high frequency comb of pulses with a range of optical pulse widths. It is also relatively easy to shape these visible optical pulses transversely and longitudinally, and to control the light reaching the photocathode with fast electro-optic devices.

As noted earlier, it is realistic to deliver 100 mA average beam current for >50 hours from a small illuminated spot on an alkali photocathode provided that 20 W of optical power can be delivered to the photocathode. Between the exit of the laser and the photocathode, a large number of optical and electro-optical devices are necessary, to transversely and longitudinally shape the optical pulses, transport them from the laser exit to the photocathode, focus them on the photocathode, provide a suitable means to start up beam delivery for both tuning and

Table 4.4.1: Key design parameters for the ERL photoinjector laser system

Wavelength	515–530 nm
Average power at the cathode	20 Watts
Repetition rate	325 MHz
Synchronization to external an RF signal	Better than 1 ps rms
Pulse duration (rms)	10-30 ps
Pulse temporal shape	flat top, < 2 ps rise and fall
Transverse shape	Elliptical
Power stability	Better than 2%
Position stability	10 microns rms

full power operation, and finally to rapidly terminate beam delivery in the case of a fault. The large number of optical elements means that even with antireflection coatings on all surfaces, there will be a very significant optical power loss, from both reflection and absorption, between the laser and the photocathode. A factor of two loss is not exceptional, and indeed, requires care to achieve. Accordingly, we require that the laser system provide at least 50 W of average optical power at its exit, which has already been achieved. An even larger value may be required to provide additional headroom for optical losses, laser beam shaping, and feedback overhead.

The synchronization of the laser output pulses with the RF signal from the Master Oscillator affects the timing jitter of the beam bunches with the accelerator RF. This timing jitter is compressed during the bunching that takes place in the injector by a factor of 10–20. The present laser system has already achieved < 1 ps rms jitter.

The 10–30 ps optical pulse duration requirement is based on simulations showing that this pulse width range gives the smallest final beam emittance from the injector (the actual value is not very critical due to the presence of RF buncher). It is unlikely this pulse width range will be generated directly in the laser – rather it will be obtained by external optical pulse shaping. These simulations also show that the rise and fall times of the individual optical pulses must be no more than a few percent of the total pulse width, and that the smallest emittance is obtained with a transverse beam profile approaching elliptical shape (which can be well approximated with a truncated Gaussian beam).

A power stability of 1% is typically the best such a high power laser can produce without feedback. The sources of instability are thermal drift in mechanical components, vibrations in gain fibers or crystals, and noise in the pump lasers. For Yb-fiber lasers, the inversion time is on the order of milliseconds, producing noise at kHz rates, but the pulse-to-pulse stability at 325 MHz will be very good as the time between pulses is much shorter than this. Pump lasers can generate noise at many frequencies, from typical line frequencies to 100+ kHz for those using switching supplies. The electron beam current stability will need to be better than 1%, thus requiring a series of slow and fast feedback systems between the beam and the laser.

Poor pointing stability leads to a smearing out of the electron beam size (and shape), leading to emittance growth. Beam simulations show that a 10 μm rms position jitter is acceptable from the point of beam centroid jitter, which generally responds differently to the accelerator optics than the beam envelope in the space charge dominated regime of the photoinjector.

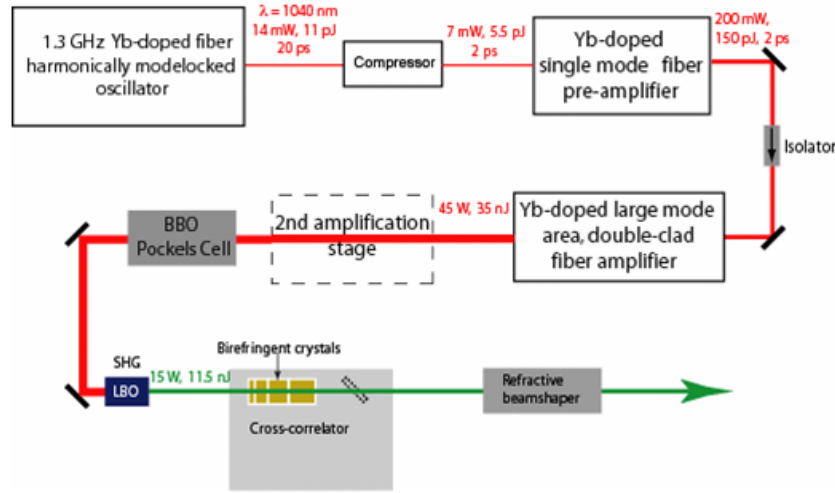


Figure 4.4.1: Drive laser system schematic.

Based on our experience, the laser can achieve $10\text{ }\mu\text{m}$ rms jitter directly after second harmonic generation (SHG) crystal, at the position of a beam waist. Using a series of 1:1 imaging telescopes to transport the beam to the photocathode, the low jitter after the laser can be maintained. For cases when the position jitter specification cannot be met, position feedback systems exist which promise positional stability at these levels (www.Thorlabs.com)

The laser system is shown schematically in Fig. 4.4.1. The oscillator is a commercially built- harmonically mode-locked fiber laser [1]. It provides a 1.3 GHz train of 20 ps-long pulses synchronized to an external clock. For this project, a new oscillator operating at 325 MHz will be needed. The pulses are fed to a single mode fiber pre-amplifier where the pulse energy is boosted to 150 pJ (200 mW average power). This pulse energy is small enough to avoid nonlinear effects in the fiber. The required pulse energy of 100 nJ is achieved through amplification in a double-clad large-mode-area fiber amplifier built to work in a nearly single mode regime. The pulses are compressed to 2 ps after the amplifier using a pair of gratings. The amplified IR pulses are frequency doubled in a LBO crystal to produce pulses centered at 520 nm. Currently, with one high power amplification stage we have achieved 110 W average IR power and 60W average green power with good stability. This is the highest average power achieved with a fiber laser at this frequency.

As is well known, generating low emittance beams from a photocathode gun depends strongly on the laser shape incident on the cathode. We have developed a technique to shape the pulses longitudinally by stacking 2^n short pulses in n birefringent crystals [2]. This technique produces a nearly flat-top laser pulse, has low optical losses, is easy to implement.

In the transverse plane, either a top-hat or an elliptical distribution is desirable for generating low emittance. We have tried a number of commercial devices with only moderate success. The old-fashioned method of expanding the laser before it passes through a pin-hole, then imaging the pinhole to the cathode is still the most reliable method. However, it wastes considerable beam power, leading to a rather high requirement for power at the laser exit. In our experience, the commercial devices are similarly inefficient in practical use.

Table 4.5.1: Buncher RF system specifications

Operating frequency	1.3 GHz
Cavity shunt impedance, $R_{sh} = V_{acc}^2/2P$	1.7 M Ω
Cavity quality factor	20,000
Nominal accelerating voltage	120 kV
Cavity detuning by beam current at nominal voltage	46.0 kHz
Cavity wall dissipation power at nominal voltage	4.24 kW
Maximum accelerating voltage	200 kV
Cavity detuning by beam current at maximum voltage	27.6 kHz
Cavity wall dissipation power at maximum voltage	11.8 kW
Maximum IOT output power	16 kW
Amplitude stability	8×10^{-3} rms
Phase stability	0.1° rms

4.5 Buncher System

To reduce emittance dilution due to space charge effects in the beam line between the gun and the first superconducting cavity, the electron bunches are created at the photocathode with the rms duration of 10-30 ps or 5-14° at 1.3 GHz. On the other hand, to minimize a nonlinear energy spread due to RF waveform in the main superconducting linac, a much shorter bunch duration of about 2 ps rms is desirable. Hence, the bunch length has to be compressed after the gun. The first stage of the bunch compression happens in the beam line between the gun and the injector superconducting linac. As the beam is still non-relativistic at this point, the simplest method of bunch compression is the velocity bunching, a well-known technique used, for example, in klystrons. Rather moderate requirements for the buncher cavity voltage (up to 200 kV) make it possible to use a normal conducting structure. Table 4.5.1 summarizes buncher cavity and RF system specifications.

In order to maximize the energy variation along the bunch at a given cavity accelerating voltage V_{acc} , the beam passes the buncher cavity -90° off crest, i.e. at its zero-crossing. The RF power required to maintain a constant field in the cavity is then given by

$$P_{forw} = \frac{V_{acc}^2}{R/Q \cdot Q_{ext}} \frac{(1 + \beta)^2}{4\beta^2} \left[1 + \frac{Q_0^2}{(1 + \beta)^2} \left(2 \frac{\Delta\omega}{\omega} - \frac{I_b R/Q}{V_{acc}} \right)^2 \right] \quad (4.5.1)$$

where $\beta = Q_0/Q_{ext}$ is the coupling factor of the input coupler, ω_c is the cavity resonant frequency, $\Delta\omega = \omega_c - \omega$, and ω is the RF frequency. It is desirable to minimize the required RF power with and without beam passing through the cavity. The minimum power of 5.8 kW is required at nominal accelerating voltage, if the cavity frequency is tuned to $1300.000 + 0.023$ MHz and if the coupling factor is $\beta = 1.7$. Amplitude fluctuations of the buncher cavity voltage will affect the resulting bunch length. If the bunch length fluctuation should not be more than 0.1 ps rms, the amplitude stability requirement is only 8×10^{-3} rms. The phase stability is derived from the required energy error and is 0.1° rms.

The buncher cavity [3] is a copper single-cell cavity that has an optimized spherical reentrant shape. A 3D view is shown in Fig. 4.5.1. The cavity input coupler is of a water-cooled coaxial

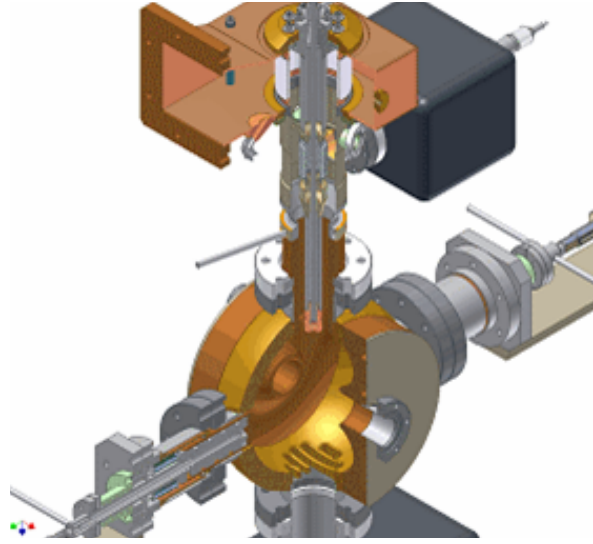


Figure 4.5.1: 3D view of the buncher cavity showing input coupler, plunger-type frequency tuner, pumping slots.

loop type. Its coaxial part is short and ends with a coax-to-waveguide transition, which incorporates a ceramic window. The coupling can be adjusted during installation by rotation of the coupling loop. The coupling loop, inner conductor and part of the outer conductor of coaxial line are water cooled. The cavity has two tuners with water-cooled 40 mm pistons. The pistons are moved by linear motion actuators with stepper motors. Two tuners provide a better field symmetry on the beam axis. Only one tuner is used for routine operation, the other one is used for preliminary frequency adjustment. During operation, the tuner has to compensate thermal effects (roughly 400 kHz from cold cavity to maximum voltage) and beam detuning. That corresponds to plunger travel of 2 mm. The full 15 mm stroke of one tuner gives a tuning range of 2.5 MHz.

The buncher RF power station in the injector [4] comprises low level RF (LLRF) electronics, a high power amplifier (HPA), and waveguide transmission line components connecting the HPA to the cavity. The block diagram of the buncher RF is shown in Fig. 4.5.2. The HPA incorporates a 16 kW IOT tube in a commercial broadcast unit a photo of which is shown in Fig. 4.5.3. The HPA efficiency is 60% with a gain of 21 dB at maximum power output. The amplitude and phase ripple noise without the LLRF feedback are 0.13% and 0.5° respectively.

4.6 Injector Linac

4.6.1 Introduction

The ERL injector linac contains 5 2-cell superconducting RF cavities, each providing an energy gain of up to 1.2 MeV at maximum 100 mA beam current. RF power is transferred to each cavity via two input couplers, ‘twin couplers’, up to 120 kW per cavity. Efficient absorption of the Higher Order Mode (HOM) power is achieved by placing broadband HOM absorbers in the beam tube sections between the cavities. The cryomodule design is based on the TTF-III

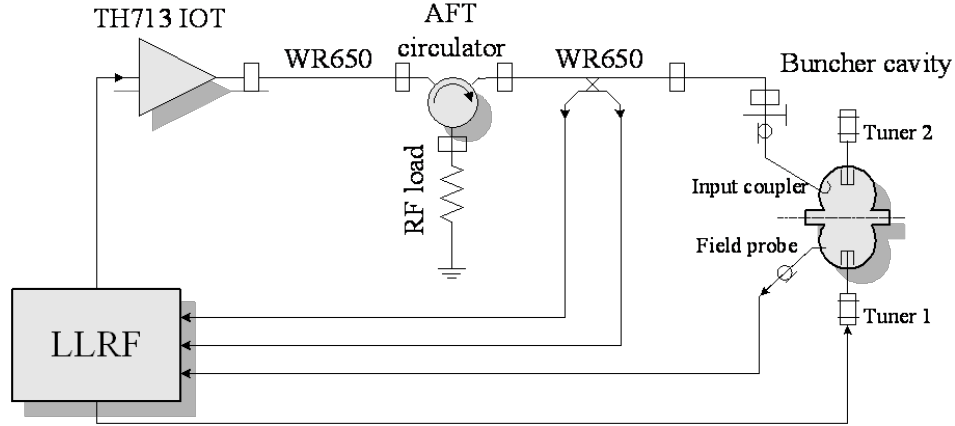


Figure 4.5.2: Block diagram of the buncher cavity RF system.

technology with modifications for CW operation.

A five-cavity injector cryomodule was designed and fabricated as part of the Cornell ERL Phase 1A effort with the goal of de In the following sections, the designs of the 2-cell SRF cavity, input coupler, HOM absorbers, LLRF system, and cryomodule are discussed in detail. The original injector was designed to support 100 mA beam currents, so this text reflects designs for 100 mA, even though we do not plan to operate at such a high level for the multi-pass ERL machine.

4.6.2 Injector cavities

Two-cell, 1.3 GHz superconducting cavities were developed for the ERL injector . The cavity design (Fig. 4.6.1) was optimized for handling high-current, low-emittance CW beams [5]. The cavity parameters are listed in Tab. 4.6.1. Efficient damping of the HOMs is essential to reduce resonant heating due to monopole HOMs and to avoid beam breakup instabilities due to dipole HOMs. Since the TTF-III technology was chosen as the baseline for the injector design, the inner iris diameter (70 mm) and the beam pipe diameter (78 mm) are identical to those of the TESLA cavity [6]. However, in this geometry the lowest dipole HOM (TE₁₁-like) is trapped. To facilitate propagation of this mode toward a beamline HOM absorber, the diameter of one of the cavity beam pipes was increased to 106 mm. A 78 mm diameter iris at this end of the cavity keeps the electromagnetic fields of fundamental mode from leaking out of the cell. The cell shapes were optimized for a maximum value of $G \cdot R/Q$ to minimize the cryogenic load while ensuring that the frequency of the lowest TE₁₁-like mode stays at least 10 MHz above the large beam pipe cut-off frequency.

To support a 100 mA CW beam, the input coupler has to be strongly coupled to the cavity and this induces a strong, non-symmetric local perturbation of the otherwise axially symmetric cavity fields. This produces a transverse kick to the beam even if it traverses the cavity on axis. To compensate for this kick, the injector cavity uses two identical symmetrically placed antenna type couplers (twin couplers) that are described below. An additional benefit of using twin couplers is a 50% reduction in the RF power per coupler. Optimization of the coupler antenna tip was part of the cavity design process. The result is a bent elliptic disc, which



Figure 4.5.3: IOT inside the transmitter.

conforms to the radius of the beam pipe [7] and is shown in Fig. 4.6.2. Bending of the disc increased the coupling by 20%. Since one of the goals for the ERL injector was to explore a range of beam energies from 5 to 15 MeV, the input coupler was designed to be adjustable.

The TE₁₁-like mode can have two polarizations resulting in two degenerate modes with identical resonant frequencies. The geometric perturbation introduced by the input couplers resolves the degeneracy and splits the modes into an ‘in-plane’ mode and a ‘perpendicular’ mode with respect to input couplers as shown in Fig. 4.6.3. The frequencies of the modes are different from the original one but stay high enough above the cut-off frequency. The in-plane mode is strongly coupled not only to the beam pipe but also to the input couplers resulting in an external Q of 250, compared to the Q_{ext} of 1000 for the perpendicular mode.

Six cavities, one and five production cavities, were fabricated for the ERL injector. The inner surface of each completed cavity was etched to remove $120\ \mu\text{m}$ with BCP 1:1:2 at a temperature below 15°C maintained by water-cooling the exterior of the cavity. Because of the vertical orientation during etching, the cavity needed to be flipped to eliminate asymmetric removal across the cells. Brazed joints and knife edges at the Conflat® flanges were protected with Teflon plugs to shield them from being attacked by the acid. After chemical etching, the cavity was rinsed with a closed-loop DI water system overnight followed by a four-hour session of high-pressure water rinsing in a clean room. All cavities reached the performance goal during vertical RF tests [8].

4.6.3 Injector input coupler

The input coupler is one of the key components of the injector linac due to strict requirements such as a high CW power transferred to the beam (up to 120 kW per cavity), strong coupling, wide range of coupling adjustment, and small distortion of transverse beam motion. Each injector cavity is equipped with two identical antenna type couplers symmetrically attached to a beam pipe of the cavity. This is a remedy to reduce RF power per single coupler, coupling

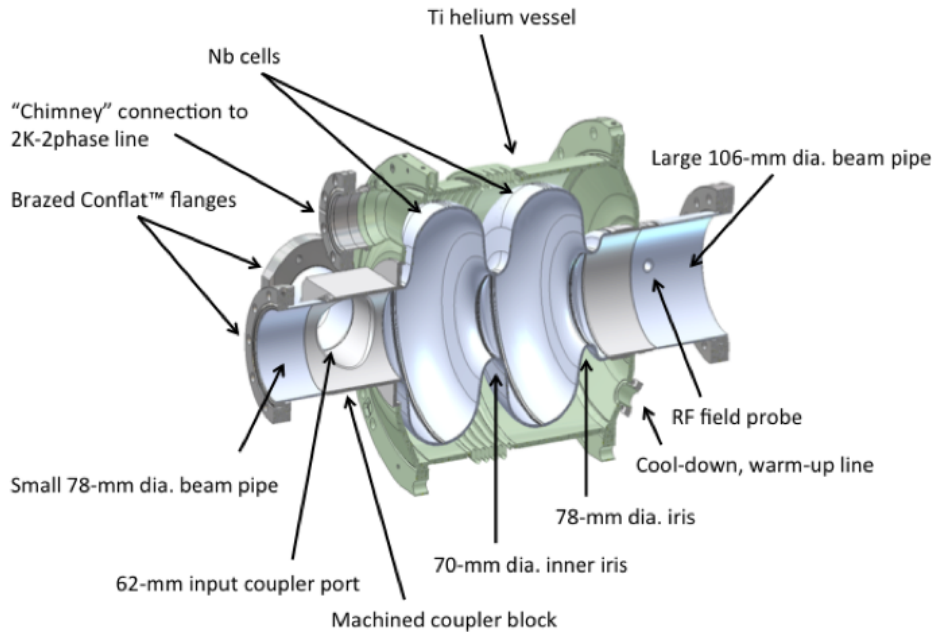


Figure 4.6.1: ERL injector cavity.

to the cavity, and the transverse kick to the beam.

The design of the ERL injector couplers is based on the design of TTF III input coupler [9], consisting of a cold section mounted on the cavity in the clean-room and sealed by a ‘cold’ ceramic window, and a warm section incorporating a transition from the evacuated coaxial line to the air-filled waveguide. The warm coaxial line is sealed by a ‘warm’ ceramic window. Both windows are made of alumina ceramics and have anti-multipacting titanium nitride coating. Bellows in the inner and outer conductors of the coaxial line of the coupler allow a few mm of motion between the cryomodule cold mass and the vacuum vessel when the cavities are cooled from room temperature to 2 K. A low thermal conductivity is achieved by using stainless steel pipes and bellows with a 10–30 μm copper plating at the radio frequency conducting surfaces. Also, the bellows allow 16 mm of center conductor movement for coupling adjustment.

The ERL injector coupler design has, however, significant modifications necessary to handle much higher average RF power [10]:

- The cold part was completely redesigned using a 62 mm, 60 Ω coaxial line (instead of a 40 mm, 70 Ω) for stronger coupling, better power handling, and alleviating multipacting.
- The antenna tip was enlarged and shaped for stronger coupling.
- The ‘cold’ window was enlarged to the size of the ‘warm’ window.
- The outer conductor bellows design (both in warm and cold coaxial lines) was improved for better cooling (heat intercepts were added).
- Forced air cooling of the warm inner conductor bellows and warm ceramic window was added.

Table 4.6.1: Parameters of the injector cavity

Resonant frequency (π mode)	1.3 GHz
Accelerating voltage	1.2 MV
Accelerating gradient, E_{acc}	5.5 MV/m
Cells per cavity	2
R/Q	222 Ω
Geometry factor, G	261 Ω
Cavity quality factor, Q_0	$> 1 \times 10^{10}$
Nominal external quality factor, Q_{ext}	5.4×10^4
Cell-to-cell coupling	0.7%
$E_{\text{pk}}/E_{\text{acc}}$	1.94
$H_{\text{pk}}/E_{\text{acc}}$	42.8 Oe/(MV/m)
Small beam pipe diameter	78 mm
Large beam pipe diameter	106 mm
Inner iris diameter	70 mm
Active cavity length	0.218 m
Cavity length flange to flange	0.536 m

The parameters of couplers for the injector cavities are summarized in Tab. 4.6.2. The general design of the coupler is shown in Fig. 4.6.5.

Installed in a cryomodule, high power input couplers require conditioning at high RF power, especially if they were not pre-conditioned before installation. However, *in situ* conditioning is not as flexible as that in a dedicated set up: it is limited to only standing wave (full reflection) mode of operation. All input couplers were processed in pulsed mode up to 25 kW per coupler (50 kW klystron power) at full reflection. All couplers conditioned well, reaching these power levels within 25 to 75 hours (RF on time) of processing multipacting. If the conventional RF processing of multipacting is a limiting factor, two additional built-in measures of alleviate this phenomenon can be employed. First, the warm couplers can be baked *in situ* using special heating elements install on them. Second, a special capacitor assembly

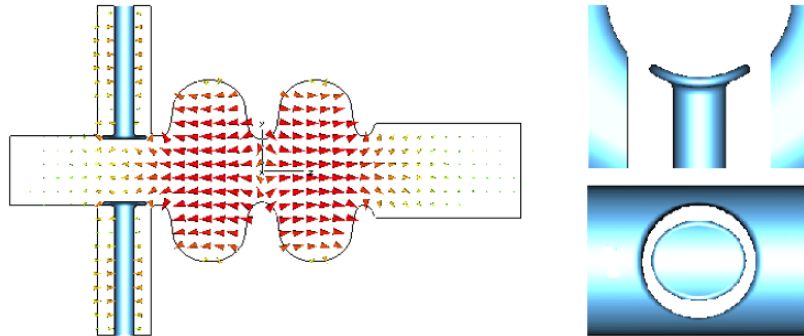


Figure 4.6.2: Geometry of the cavity and details of the coupler antenna with the electric field lines of the fundamental mode indicated

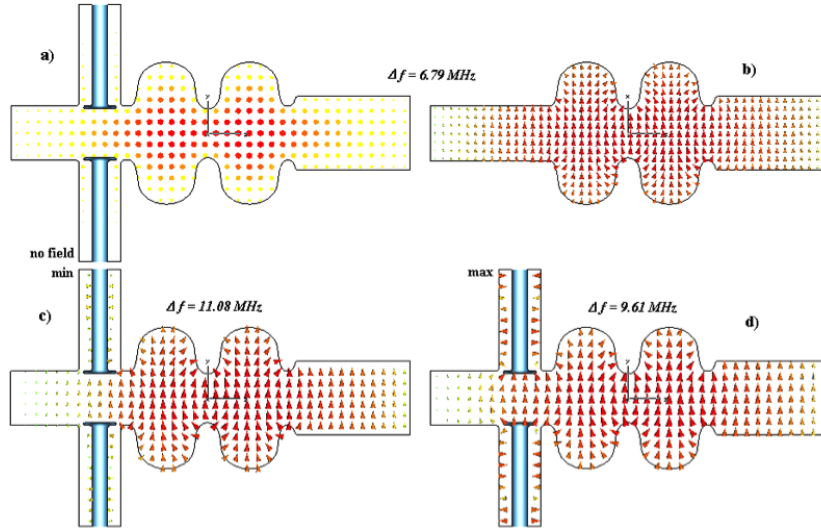


Figure 4.6.3: Electric field of the two dipole modes: a) and b) the ‘perpendicular’ mode; c) and d) the ‘in-plane’ mode with electric and magnetic walls at the ends of coaxial lines, respectively

can be installed, isolating the center conductor from ground and allowing use of DC bias for multipactor suppression.

4.6.4 Wakefield and HOM calculations

When the 100 mA beam current passes through the beam line in the injector cryomodule, the electron bunches will leave behind significant electromagnetic fields. The power transferred to these wakefields needs to be intercepted in the Higher-Order-Mode (HOM) absorbers located in the beam pipe sections between the individual cavities. In addition, these HOM absorbers need to damp monopole and dipole modes sufficiently to avoid excessive HOM power in case of resonant excitation of a monopole mode and to guarantee beam stability.

The longitudinal loss factor $k_{||}$ of a beam line section can be used to estimate the average power transferred from the beam to electromagnetic fields excited by the beam:

$$P_{\text{average}} = k_{||} \cdot q \cdot I, \quad (4.6.1)$$

where q is the bunch charge and I is the average beam current. The total longitudinal loss factor of the beam line section with five 2-cell injector cavities as shown in Fig. 4.6.6 was calculated [11]. The result is a longitudinal loss factor of 6.4 V/pC per one-cavity section (32 V/pC for 5 cavities) at the design bunch length of $\sigma = 0.6$ mm, see Fig. 4.6.7. Accordingly, the average monopole mode HOM power excited by the 100 mA, 77 pC beam is found to be ≈ 50 W per cavity section, i.e. per HOM absorber.

To verify the effectiveness of the HOM damping scheme with HOM beam pipe absorbers located between the cavities as shown in Fig. 4.6.6, the resulting HOM damping was studied both numerically and experimentally. Figure 4.6.8 shows simulation results for the quality factors of monopole modes between 1.5 GHz and 5.5 GHz, as well as the product of $(R/Q)Q$,

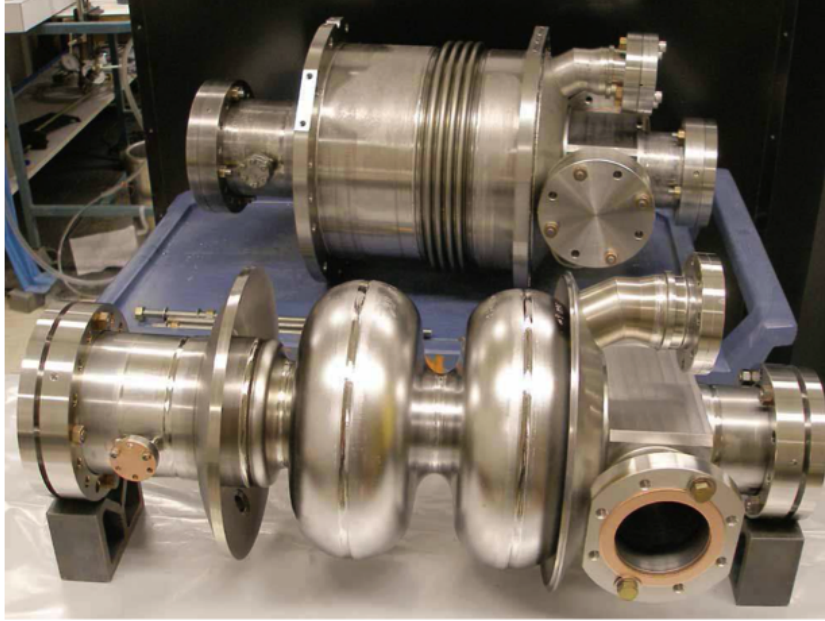


Figure 4.6.4: 2-cell cavity before and after welding the helium vessel

which is the figure of merit in case of resonant excitation of an HOM by the beam. The quality factors of the modes are reduced strongly to very low values of typically 100 to a few 1000. Only the modes of the accelerating TM₀₁₀ passband at 1.3 GHz remain unaffected by the HOM dampers because their frequencies are below the cut-off frequency of the beam pipes at the cavity ends. Even in the unlikely event of resonant mode excitation, the power transferred to any of these strongly damped modes would be modest and well below the maximum power handling specifications of the HOM dampers. HOM measurements at the Cornell ERL injector cryomodule have confirmed these simulation results [12].

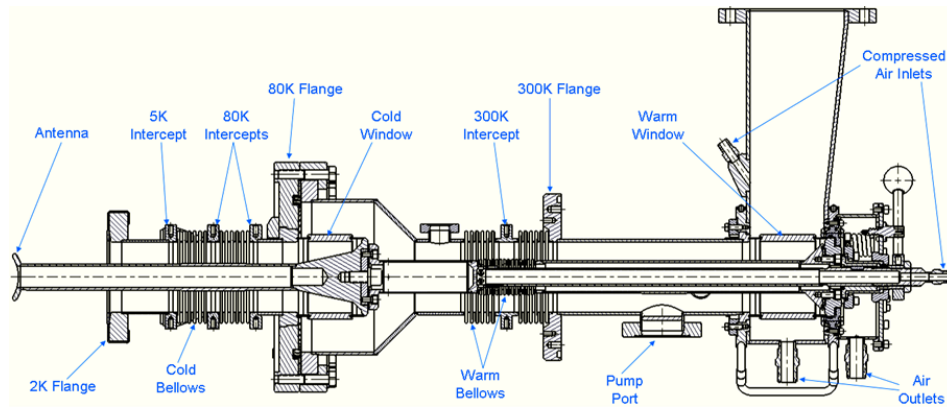


Figure 4.6.5: 2D section view of the injector input coupler.

Table 4.6.2: Parameters if the injector input power couplers

Central frequency	1.3 GHz
Bandwidth	± 10 MHz
Maximum RF power transferred to matched load	60 kW
Number of ceramic windows	2
Qext range	9.2×10^4 to 8.2×10^5
Cold coaxial line impedance	60Ω
Warm coaxial line impedance	46Ω
Coaxial line OD	62 mm
Antenna stroke	16 mm
Heat leak to 2 K	< 0.2 W
Heat leak to 5 K	< 3 W
Heat leak to 80 K	< 75 W

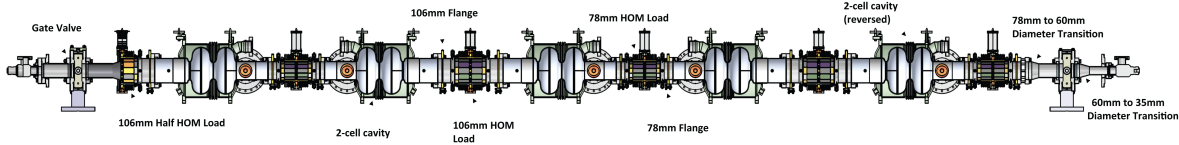


Figure 4.6.6: CAD model view of the Cornell ERL injector cryomodule beam line with five 2-cell cavities. Note that the full ERL injector will have 12 2-cell cavities. Beam line components from left (beam entrance) to right (beam exit): gate valve; 106 mm half HOM load; first SRF cavity; 78 mm HOM load; second SRF cavity; 106 mm HOM load; third SRF cavity; 78 mm HOM load; fourth SRF cavity; 106 mm HOM load; fifth SRF cavity; 78 mm HOM load; 78 mm to 60 mm diameter transition; gate valve; 60 mm to 35 mm diameter transition.

4.6.5 Injector HOM dampers

The requirements on the beam pipe HOM absorbers in the ERL injector are similar to the HOM damping requirements in the ERL main Linac. The only differences are (1) a factor of ≈ 4 smaller average power to be intercepted per load and (2) slightly different beam pipe radii (39 mm and 53 mm instead of 55 mm in the main Linac). Therefore, the HOM dampers in the ERL injectors will be a modified version of the beam pipe HOM dampers developed for the ERL main Linac. Refer to §5.24 for a detailed discussion of the main Linac HOM dampers.

Cryogenic HOM beam pipe absorbers have been tested successfully in the Cornell ERL injector. Figure 4.6.9 shows one of the HOM loads prior to installation in the ERL injector beam line. The damping of HOMs in the injector cavities by these beamline absorbers was investigated using a vector network analyzer to excite modes via pick-up antennas located at the cavity beam tubes and at the HOM loads (see Fig. 4.6.10). Preliminary results confirm very strong suppression of monopole and dipole modes with typical quality factors of only a few 1000 as predicted by simulations. Heater elements on the HOM absorber load bodies were used to verify the effective heat exchange to the high pressure cooling gas up to the maximum

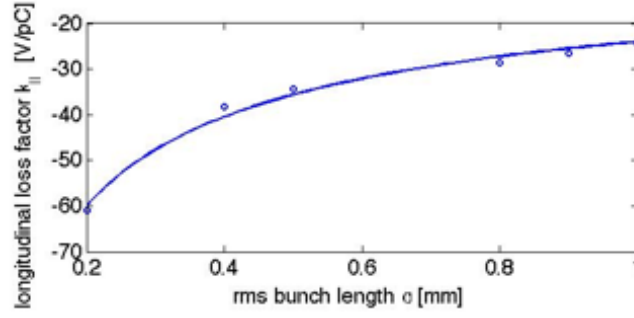


Figure 4.6.7: Total loss factor in the injector cryomodule beam line with 5 2-cell cavities as a function of bunch length.

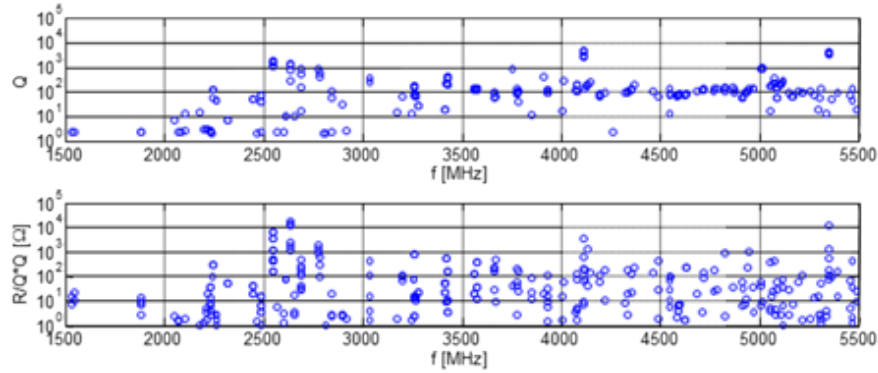


Figure 4.6.8: Simulated monopole mode damping in the full ERL injector (CLANS results). Top: Quality factor of all monopole modes between 1.5 GHz and 5.5 GHz. Bottom: $R/Q \cdot Q$ of these modes. Realistic complex dielectric properties were used in these simulations for the RF absorbing materials in the HOM dampers.

design heat load of 200 W; see Fig. 4.6.10. The measured temperature increase of the HOM load body was found to be in good agreement with simulation results.

The injector HOM designs suffered from several problems. The RF tile soldering was not robust, and several tiles detached and fell, generating dust and particles. In addition, two of the three tile types became insulating enough at 80 K that any charge accumulated on their surfaces would not bleed off. This charge could be from electrons scattered during beam tuneup, or from x-rays and UV light generated during cavity processing. The electrostatic fields generated from the charge buildup severely distorted the beam passing through the cryomodule, making the beam unusable. The tiles facing the beam were removed, and the solder joints improved on the others to eliminate these problems.

4.6.6 Injector RF stability requirements and LLRF

The intra-bunch energy spread after the injector is about $\sigma_{\text{inj}} = 15 \text{ keV}$. It is desirable for the bunch-to-bunch energy fluctuation (bunch centroid energy) at the end of the injector to be below the intra-beam energy spread so that the total energy spread of the beam is

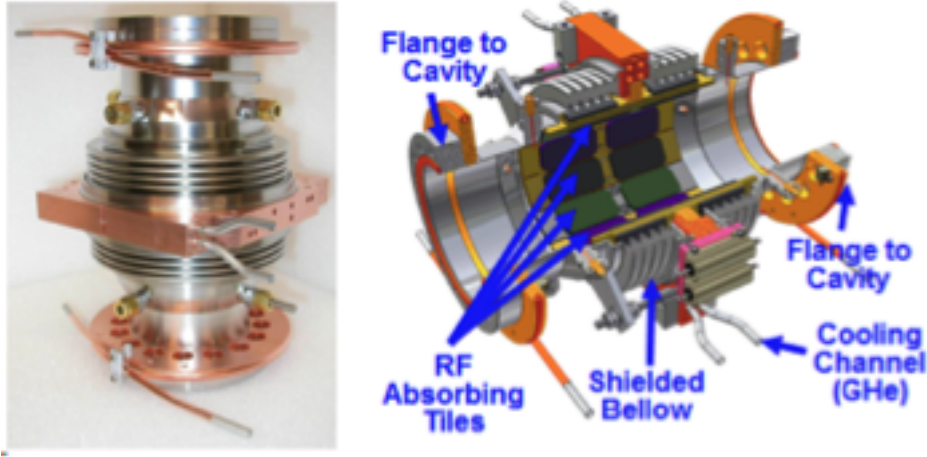


Figure 4.6.9: Cornell ERL injector HOM load. Left: Finished load. Right: Cut-open CAD model of the load showing the RF absorber tiles.

dominated by the intra-bunch energy spread. The gun laser timing jitter, the buncher cavity as well as the five superconducting injector cavities each contribute to a bunch-to-bunch energy variation in the injector. We have to distinguish between uncorrelated and correlated (from cavity to cavity) errors. For the ERL injector cavities, small fluctuations in the 100 mA beam loading will be the dominating source of field perturbation, which will cause correlated field errors. Accordingly, we shall assume here correlated field errors in the injector cavities. We will require that the bunch-to-bunch energy fluctuation caused by the injector SRF cavities increases the total energy spread at the end of injector by no more than 20%, i.e. to a total of 18 keV rms. Accordingly, the maximum allowable bunch-to-bunch centroid energy gain fluctuation is 10 keV, assuming no correlation between the intra-bunch energy spread and the bunch-to-bunch gain fluctuation. We will allow for 5 keV energy spread contribution from each phase errors and amplitude errors in the 12 injector cavities. This simple estimate results in a requirement for the relative amplitude stability of $\sigma_A/A = 5 \text{ keV}/15 \text{ MeV} = 3.3 \times 10^{-4}$. Assuming acceleration with a phase within 5 deg of on-crest then gives a requirement for the phase stability of $\sigma_p = 0.2^\circ$.

A digital LLRF control system will be used to stabilize the RF fields in the injector cavities in amplitude and phase to these stability levels. A combination of feedforward and feedback control will be used to stabilize the cavity fields in the presence of strong beam loading and other perturbations of the RF fields. Sensors will be used to monitor all relevant signals, including the cavity fields, the incident and reflected RF power, and the beam current. Any disturbances due to klystron noise and ripple can be handled using feedforward. Extremely reliable hardware, a high degree of automation, and sophisticated built-in diagnostics will ensure a high degree of operability, availability and maintainability of the LLRF system.

The LLRF control system has been tested extensively, showing excellent performance (see Fig. ??). This LLRF system is an improved generation of the LLRF system previously developed for CESR [13], with lower loop latency ($< 1\mu\text{s}$), reduced noise, and increased sample rates and ADC resolution (16 bits). The integral and proportional gains of the fast feedback loop used to stabilize the RF fields in the cavities were optimized. At optimal gains,

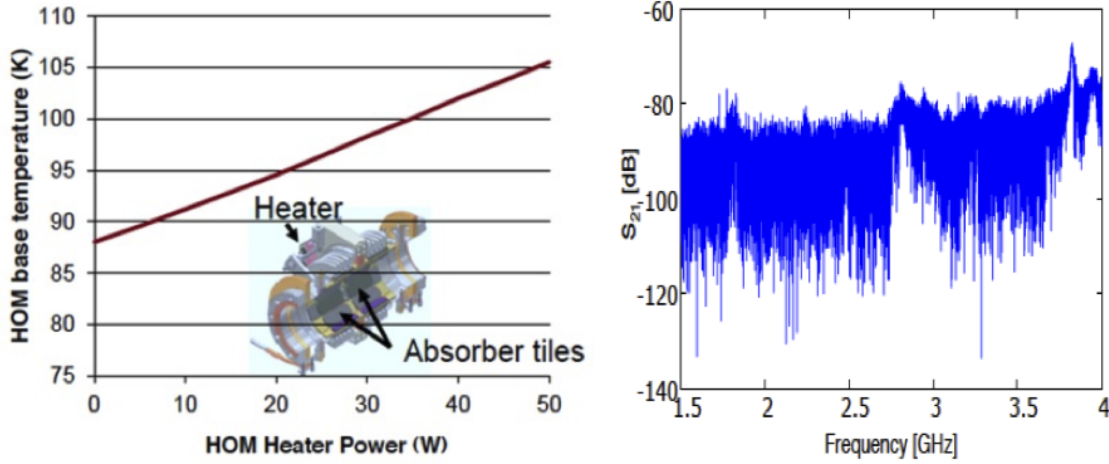


Figure 4.6.10: Left: Temperature of the HOM load temperature as function of power intercepted. The test was done at a relatively low cooling gas flow speed. Right: Vector network analyzer scan for HOMs between 1.5 GHz to 4 GHz. Shown is the transmission amplitude vs. scan frequency. Pick-up antennas on the cavities and HOM loads were used to couple to the HOMs.

exceptional field stabilities of $\sigma_A/A < 2 \times 10^{-5}$ in relative amplitude and $\sigma_p < 0.01^\circ$ in phase (in-loop measurements) have been achieved, far exceeding the ERL injector and ERL main linac requirements. In addition to the fast feedback loop, the system employs feedforward control to compensate beam loading and fluctuations in the high voltage of the klystrons, a state machine for automatic start-up and trip recovery, trip detection, and cavity frequency control.

4.6.7 RF Power System for the Injector Linac

The injector cryomodules house five 2-cell SC cavities, each delivering up to 120 kW to the beam. Because the cavities operate independently, the system consists of five identical channels. Each channel includes a set of LLRF electronics and RF interlocks, a klystron based HPA, and a waveguide distribution network. RF power is delivered to the cavities via twin input couplers [10] each carrying 60 kW. The main parameters of the system are given in Tab. 4.6.3 and a block diagram is presented in Fig. 4.6.11. A motorized, adjustable short-slot hybrid power splitter and a two stub phase shifter in one of the waveguide arms are used to tune relative amplitude and phase between the two couplers [14]. A 170 kW ferrite circulator is used for klystron protection.

The klystrons were designed and manufactured by e2V cavity klystrons and have 165 kW saturated power output. Similar tubes are anticipated for the 12 cavity injector complement. To provide stable regulation of the cavity field the klystron must have finite gain and thus cannot run in saturation. The maximum power output for the tube was defined as 0.5 dB/dB of drive and specified to be no less than 120 kW. At this level the efficiency of the tubes is at least 50% and the bandwidth not less than ± 2.5 MHz at -1 dB level and not less than ± 3 MHz

Table 4.6.3: Main parameters of the injector cryomodule RF system and power source

Number of RF channels	5
RF power per cavity	120 kW
Maximum useful klystron output power with incremental gain of 0.5 dB/dB	≥ 120 kW
Klystron efficiency at maximum useful power	$> 50\%$
Tube bandwidth at -1 dB	± 2 MHz
Tube bandwidth at -3 dB	± 3 MHz
Klystron gain at nominal operating conditions	> 45 dB
Klystron beam high voltage	45 kV
Typical klystron current	5.87 A
Maximum klystron CW output power	135 kW
Klystron saturated output power (pulsed)	165 kW
Tube efficiency at saturated power	$> 60\%$
Cavity field amplitude stability	9.5×10^{-4} rms
Cavity field phase stability	0.1° rms

at -3 dB level.

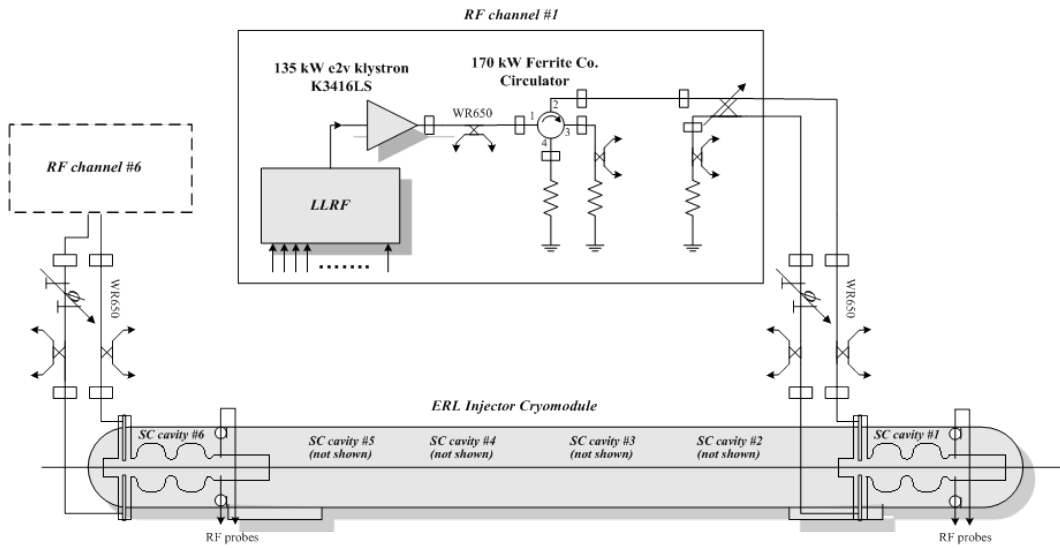


Figure 4.6.11: Block diagram of the ERL injector RF system (one cryomodule is shown).

4.6.8 Injector cryomodule

The ERL injector cryomodule design is based on TTF III technology with modifications for CW operation. This builds upon the considerable development work performed for this linac technology over the past 15 years. TTF III technology is at the forefront of SRF linac performance in regard to cavity gradient, Q , power coupled to the beam, cavity tuning, minimal cryogenic heat load, industrial fabrication, and operational reliability.

The modifications to TTF III technology for CW operation of an injector cryomodule are structurally subtle, but have significant operational differences. Among the modifications to the TTF III cryomodule are the following:

- Use 2 coax RF input couplers per cavity, where one 120 kW CW klystron feeds a cavity coupler pair, each coupler rated at 60 kW CW.
- The coax RF input couplers have outer conductors with 62 mm diameter and increased cooling for high average power.
- The SRF cavities have only 2 cells per cavity with a 0.2 m active length, operated at a nominal gradient of 6 MV/m (1.2 MeV) to deliver the 120 kW klystron power to the beam.
- 5 SRF cavities in the injector cryomodule.
- One side of the SRF cavity has a larger beam tube diameter, 106 mm, to allow better propagation and damping of Higher Order Modes (HOMs).
- Implement beamline HOM Loads for strong broadband damping of HOMs generated by the high current and short bunches.
- Cooling of thermal intercepts is provided by small ‘jumper’ tubes with flowing He gas, such as to the HOM loads and the RF couplers, as opposed to copper straps.
- Use the INFN blade tuner with the addition of piezos for fast tuning.
- Locate access ports in the vacuum vessel to allow the tuner stepper motor to be accessible for replacement while the string is in cryomodule.
- Use precision fixed surfaces between the beamline components and the Gas Return Pipe (GRP) for easy ‘self’ alignment of the beamline.
- Use rails mounted on the inside of the vacuum vessel and rollers on the composite support posts to insert the cold mass into the vacuum vessel, as opposed to Big Bertha.
- Increase the magnetic shielding so that the cavity Q is limited only by the BCS resistance.
- Do not include a 5 K shield.
- Increase the diameter of the cavity helium vessel port to 10 cm for the high CW heat load.
- Increase the diameter of the 2-phase 2 K He pipe to 10 cm for the high CW gas load.

- Use a module end-cap and cryogenic feed-cap with reduced length.

The ERL injector cryomodule is based on the TTF III module structure. All of the cavity helium vessels are pumped to 1.8 K (12 Torr) through a common 25 cm inside diameter Gas Return Pipe (GRP) which also serves as the mechanical support from which the beamline components are suspended. To minimize the heat load to the refrigeration plant, all of the 1.8 K cryomodule components are surrounded by 5 K intercepts to minimize the heat leak to 1.8 K, and the 5 K intercepts are likewise surrounded by 100 K intercepts, which absorb the heat load from the 293 K vacuum vessel. The GRP is suspended from composite support posts that are constructed from low-thermal conductivity G-10 fiberglass. The composite posts have integral metal stiffening disks and rings that also serve as thermal intercepts at 5 K and 100 K between the 1.8 K face that attaches to the GRP and the 293 K face that attaches to the vacuum vessel bosses that support the cold mass. There are stainless steel manifolds of smaller diameter than the GRP running the length of the module that transport the supply of liquid helium and the supply and return of 5 K and 100 K helium gas for the thermal intercepts. Jumper tubes with 5 mm inner diameter are connected between the 5 K and 100 K supply and return manifolds to the various thermal intercepts within a module. A shell of 6 mm thick, grade 1100 aluminum sheet surrounds the beamline and the GRP and is linked to the 100 K manifold to serve as a thermal radiation shield between the 293 K vacuum vessel and the cold mass. The aluminum 100 K shield has apertures through which the RF couplers pass and also has panels with instrumentation feedthroughs. The 100 K shield is mechanically suspended from one of the integral metal stiffeners in the composite support posts. Multi-layer insulation is wrapped around the exterior of the 100 K shield as well as all of the 1.8 K and 5 K cold mass components.

The magnetic shielding in the cryomodule must keep the field in the region of the SRF cavity to < 2 mG to have negligible residual SRF wall loss and provide a good safety margin for the goal of cavity $Q_0 = 2 \times 10^{10}$. Such a low field is accomplished by de-gaussing the carbon-steel vacuum vessel, lining it with co-netic mu-metal shielding that will be at 293 K, and then wrapping each cavity's 1.8 K helium vessel with a magnetic shield that is formulated to have maximal shielding at the low temperatures around 4 K [15].

The injector cryomodule delivers high average power to the injected beam. Even with a modest cavity gradient of 6 MV/m and only 2 cells per cavity, the input RF power of 120 kW CW per cavity to the 100 mA beam is pushing the limits of input couplers, as described in §4.6.3. Having two RF couplers per cavity requires the vacuum vessel RF ports to be symmetrically located on each side of the cryomodule, as opposed to one coupler per cavity with ports along only one side of the module. Having only two cells per cavity makes the cavity much shorter than 7-cell or 9-cell cavities, and the cryomodule structure in the vicinity of the cavities more congested. The blade tuner is then slightly longer than the cavity helium vessel and the helium pumping port must be located on the end cone rather than on the OD of the helium vessel.

The beamline consisting of the cavities, HOM loads, cold couplers, tapers, and gate valves (Tab. ??) is assembled in a class 100 or better clean room. All components are flushed with filtered water or alcohol and individually receive a mild vacuum bake at 120° C for 24 hours. The components are mounted on an assembly fixture one by one in the clean room. Each added component is aligned to the other components with the only critical alignment being

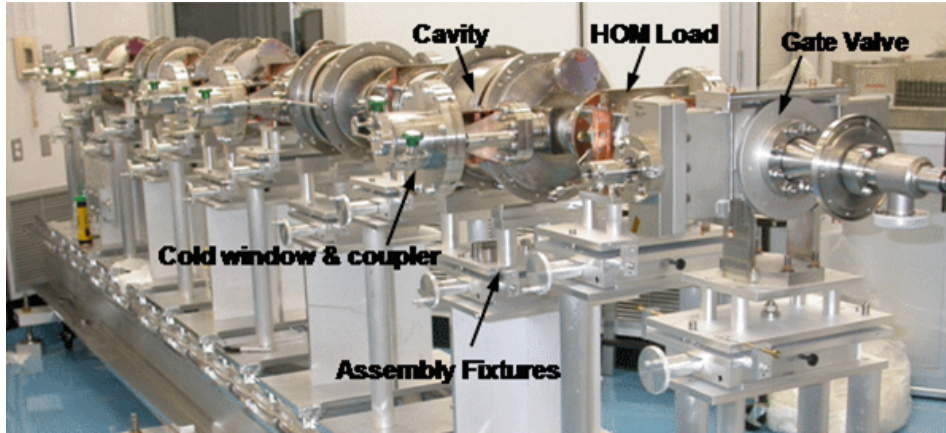


Figure 4.6.12: Assembled ERL injector beamline string in the clean room.

the azimuthal position about the beam axis. The azimuthal alignment is needed so that the flat precision mounting surface at their tops will mate to the planar precision surfaces on the GRP. This alignment can be accomplished with a simple accurate spirit level. Any longitudinal spacing or planar shift errors of the mounting surfaces are accommodated by the flex in the HOM load bellows. The component mating vacuum flanges are then bolted together. A photograph of the assembled ERL injector beamline string in the clean room is shown in Fig. 4.6.12. After all components are assembled, the beamline string is vacuum leak tested while still in the clean room so that only filtered particulate-free air will pass through any potential leak. The pumping and purging during the leak test is performed at a slow rate of 1–2 Torr/minute through the viscous flow range of 760 Torr–1 Torr to minimize propagation of any particulate contamination throughout the beamline.

As a parallel operation to the beamline string assembly in a clean room, the cold mass assembly fixture can be set up in a high-bay area with overhead crane access. The composite support posts are attached to the GRP and the GRP is hung from the assembly fixture by the composite posts. The 2-phase pipe is then mounted to one side of the GRP and its exhaust is welded into the GRP.

After the beamline string passes the vacuum leak test, it is removed from the clean room and positioned underneath the cold mass assembly fixture. The string is raised and the precision mounting surfaces on the string and the GRP are brought together with integral alignment pins being engaged. The mating surfaces are then bolted together. A photograph of the injector beamline hung from the GRP is shown in Fig. 4.6.13. String attachment to the GRP in this manner proved to be quick and easy for the ERL injector, the entire procedure taking about 1 hour.

After the beamline is hung from the GRP, magnetic shielding layer I is attached to the helium tanks of the cavities. This shielding will reside at 1.8 K. Traditional co-netic ‘mu-metal’ shielding derates at cryogenic temperatures to about 15% of its 300 K shielding capacity, so the magnetic shield I material is formulated to have maximal shielding at low temperatures [15].

The cavity blade tuners are attached after the magnetic shielding. The stepping motors of

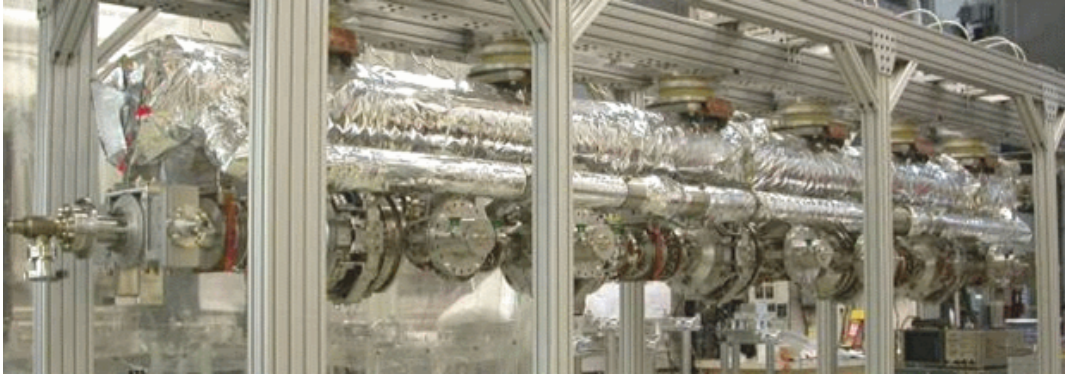


Figure 4.6.13: Beamline string hung from the GRP for the ERL injector .

the tuners have to be wrapped in a copper sleeve that is tied to 5 K to prevent the motor heat from propagating to the helium vessel. The stepping motors are also wrapped with low temperature magnetic shielding since they can have stray fields of a few hundred mG, which would otherwise be present in close proximity to apertures in magnetic shield I.

Several cryogen manifolds run the length of the cryomodule. These manifolds include a 1.8 K liquid helium supply to the ‘fill’ ports located at the bottom of each of the cavity helium vessels, the supply and return of 5 K helium gas, and the supply and return of 100 K helium gas.

The liquid helium and 5 K gas manifolds are mounted close to the GRP using G-10 standoffs, thus keeping similar temperatures in close proximity to each other with low thermal conductivity connections between them. These manifolds are the next components mounted on the cold mass. Jumper tubes with 6 mm ID are then routed from the liquid helium manifold to the helium vessel fill ports. Jumper tubes from the 5 K gas manifolds are then connected to thermal intercepts on the HOM loads and RF couplers. This final joining of the stainless steel jumper tubes from the manifold to the thermal intercepts is performed by orbital welding. In standard TTF technology, the connections between the manifolds and the thermal intercepts are accomplished by copper straps. For the ERL injector with CW operation, both the 5 K and 100 K heat loads are large enough to require gas flow from the manifolds to the intercepts through jumper tubes.

The 100 K manifolds are mounted outboard of the 5 K manifolds and are attached to the 100 K thermal radiation shield. One of the 100 K supply lines cools the shield, and the return lines are hung from low thermal conductivity hangars. The material of the 100 K shield is grade 1100 aluminum, chosen for its high thermal conductivity and light weight. The shield is fabricated from standard flat panels that are cut and formed to shape. The top portion of the shield is attached to the 100 K ring of the composite support post and is 6 mm thick to support the weight of the cryogen manifolds and the lower portion of the shield.

After the cryogen manifolds and intercept jumpers are attached to the cold mass, low thermal conductivity coax cable is routed from the cavity RF field probes with thermal anchoring to the 5 K manifold, along with cabling from temperature sensors, helium level sticks, and other instrumentation. The lower half of the 100 K shield is attached and the instrumentation cabling is thermally anchored at this point to a 100 K instrumentation feed-through panel



Figure 4.6.14: Photograph of the completed ERL injector 100 K shield being wrapped with MLI.

on the shield. The 100 K shield is then wrapped with 30 layers of Multi Layer Insulation (MLI) and the cold mass is ready for insertion into the vacuum vessel. A photograph of the completed 100 K shield being wrapped with MLI is shown in Fig. 4.6.14.

The cold mass that is wrapped with MLI is pushed into the vacuum vessel and then leveled and aligned inside of the vacuum vessel using jack screws connected to the composite support posts at the top ports. The warm portions of the RF couplers are attached to the cold portions through side ports on the vacuum vessel while under small portable clean rooms. The vessel end plates are attached to the vacuum vessel and it is pumped out and vacuum leak tested.

References

- [1] PriTel, Inc., Naperville, IL 60567.
- [2] Bazarov, I. V., *et al.* *Efficient temporal shaping of electron distribution for high-brightness photoemission electron guns.* Phys. Rev. ST AB, **11** (4) (2008).
- [3] Veshcherevich, V. and S. Belomestnykh. *Bunchner Academy for ERL.* In *Proceedings of the 2003 Particle Accelerator Conference*, pages 1198–1200. Portland, USA (2003).
- [4] Belomestnykh, S., *et al.* *CW RF systems of the Cornell ERL Injector.* In *Proceedings of the XXIV Linear Accelerator Conference*, pages 857–859. Victoria, BC, Canada (2008).
- [5] Shemelin, V., *et al.* *Dipole-mode-free and kick-free 2-cell cavity for the SC ERL injector.* In *Proceedings of the 2003 Particle Accelerator Conference*, pages 2059–2061. Portland, USA (2003).
- [6] Aune, B., *et al.* *Superconducting TESLA cavities.* Phys. Rev. ST Accel. Beams, **3** (9), page 092001 (Sep 2000). doi:10.1103/PhysRevSTAB.3.092001.
- [7] Liepe, M., *et al.* *Design of the CW Cornell ERL injector cryomodule.* In *21st Particle Accelerator Conference (PAC 05)*, page 4290 (2005).
- [8] Geng, R. L., *et al.* *Fabrication and performance of superconducting RF cavities for the Cornell ERL injector.* In *Proceedings of the 2007 Particle Accelerator Conference*, pages 2340–2342. Albuquerque, NM (2007).
- [9] Dwersteg, B., *et al.* *TESLA RF Power Couplers Development at DESY.* In *Proceedings of the 10th Workshop on RF Superconductivity*, pages 443–447. Tsukuba, Japan (2001).
- [10] Veshcherevich, V., *et al.* *Design of High Power Input Coupler for Cornell ERL Injector Cavities.* In *Proceedings of the 12th International Workshop on RF Superconductivity*, pages 590–592. Ithaca, NY (2005).
- [11] Liepe, M. and R. Wolf. *Wake Fields in the Cornell ERL Injector.* In *the 2009 International Workshop of RF Superconductivity*. Berlin, Germany (2009).
- [12] Liepe, M., *et al.* *High-current ERL Injector.* In *Proceedings of the 2009 International Workshop of RF Superconductivity*. Berlin, Germany (2009).
- [13] Liepe, M. *et al.* *A new Digital Control System for CESR-c and the Cornell ERL.* In *SRF03* (2003).
- [14] Belomestnykh, S., *et al.* *Development of High Power RF Power Delivery System for 1300 MHz Superconducting Cavities of Cornell ERL Injector.* In *Proceedings of XXII International Linear Accelerator Conference*, pages 694–696. Luebeck, Germany (2004).
- [15] Amuneal Manufacturing Corp. Technical report, Philadelphia, PA, USA, Amumetal 4k (A4K) (2010). <http://www.amuneal.com/magnetic-shielding/idea-share/whats-new-cryogenic-shielding>.

5 Linac and RF systems[Matthias]- 1st draft due 04/28

5.1 Introduction

For CBeta, the main accelerator module will be the MLC, which was built as a prototype for the Cornell Energy Recovery Linac (ERL) project. This cryomodule houses six superconducting cavities as well as higher order mode absorbers next to each cavity. The module, shown in Fig. 5.1.1 was finished by the Cornell group in November 2014 and successfully cooled-down and operated starting in September 2015. Most of the design parameters for this cryomodule can be found in the ???. In the following sections we will describe the main features and describe the performance that has been measured so far.

5.2 Module Layout

The conceptual layout of the linac cryomodule is shown in Fig. 5.3.1. The 10 m long module houses six superconducting cavities, operated in cw mode at 1.8 K. These 7-cell, 1.3 GHz cavities with a Q of 2×10^{10} will provide an energy gain of 16 MV/m. Each cavity is fed by a 5 kW power coupler. Due to the high beam current combined with the short bunch operation, a careful control and efficient damping of the Higher Order Modes (HOMs) is essential, leading to the installation of dampers next to each cavity. In the linac module, there exists a room to accommodate a quadrupole/ steerer section at the end of the module. However, the magnet section was omitted in the prototype describe further on as it in contrast to the other components- technically does not represent a challenge. Never the less, this space exists and it might be used for diagnostic purposes if needed.

The mechanical concept foresees that all components within the cryomodule will be suspended from the Helium Gas Return Pipe (HGRP). It should be mentioned that this differs from the layout of ILC or TESLA based cryomodules [5-7]. This large diameter (280 mm) titanium pipe will return the gaseous helium boiled off the cavity vessels to the liquefier and act as a central support girder, being described in more detail below. As a consequence the whole cold mass will shrink during cooldown, requiring a rather large transversal displacement flexibility of up to 10 mm (to be allowed for by the outmost coupler [8]).

5.3 Cryomodule layout, design choices and components

The general layout of the Main Linac Cryomodule (MLC) has been described in detail by Eichhorn (2013). It houses six superconducting 7-cell cavities and has an overall length of 10 m. The cavities were optimized in shape to have a high beam-break-up (BBU) limit for



Figure 5.1.1: The Cornell Main Linac Cryomodule (MLC) on the day of its completion

the beam current. As we expect an average of 200 W of higher order mode (HOM) power per cavity, HOM beam line absorbers are placed between the cavities, damping the RF by absorption. The cryo-module design has been guided by the ILC Cryomodule while necessary modifications have been made to allow CW operation. In addition, we decided to align all components inside the module by reference surfaces on the helium gas return pipe (HGRP). Fig. 5.3.1 gives an impression of the module layout.

5.4 Cryogenic Cooling Scheme

The cryogenic cooling scheme of the module consists in principle of 3 different loops. The cavities will be cooled by liquid helium obtained by a JT-Valve located at the module entrance. Sub-cooled to 1.8 K by pumping the He-atmosphere down to 20 mbar ensures an optimum operation regime for the superconducting cavities. To minimize the pressure drop over the whole linac string, a big aperture for the gas return pipe (HGRP) was chosen. In order suppress pressure fluctuations a single chimney connects all cavities within one module to that return. The second loop consisting of supercritical 5 K helium is used to cool the intercept all transitions to warmer temperatures in order to assure a minimal heat transfer to the 1.8 K system. Finally, a 80 K loop provides cooling for the coupler intercepts, cools the thermal radiation shield of the module and removes the heat generated in the Higher Order Mode

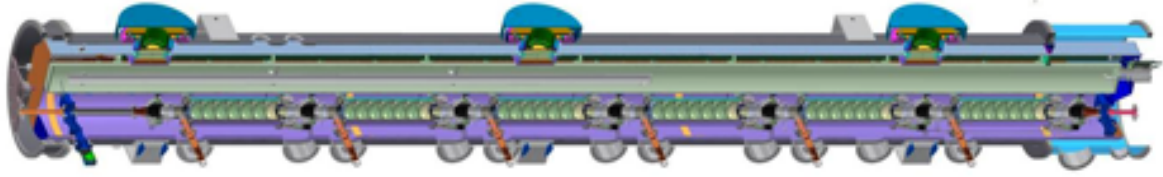


Figure 5.3.1: 3-D CAD model of the Main Linac Cryo-module (MLC) prototype, the fabrication of which has started recently. It houses 6 superconducting 7-cell cavities with Higher Order Modes (HOM) loads located between them. The vacant space on the left will house a magnet/ BPM section in the series module. The overall length will be 9.8 m.

(HOM) absorbers- the operation temperature of the later was chosen for efficiency reasons. As shown in Figure 2, the loads are partially in parallel, partially in series. As the expected heat load especially at the HOM absorbers (due to its principle character) are expected to vary individually on a scale of 0 to 400 W, concerns were raised on the thermal stability of this arrangement. Based on findings on an earlier cryomodule built for the injector [9] a careful investigation on the stability of parallel flows was performed, being reported in another paper [10]. The cryogenic scheme is visualized in Figure 2, Figure 3 gives the crosssection of the module showing the spatial arrangement.

5.5 Piping Manifold

As indicated in Fig. 5.4.1 and Fig. 5.4.2, a number of cryogenic piping run along the module. Table 1 summarizes their properties and design pressures as well as temperatures. Six lines of 50mm diameter run through the entire half-linac (items 3, 4, 5, 8, 9, and 10 in table 1). Due to the fact that this half linac will be 350 m long, the pressure drop even with these large diameter lines would be significant. To keep the diameter reasonable local manifolds (items 2, 6, 7, and 11 in table 1) help delivering the cryogens. Four valves (1.8K, pre-cool, 4.5K, and 40K) located at the entrance of each cryomodule will manage the flow division amongst the modules.

5.6 Mechanical Design

All components within the cryomodule will be suspended from the Helium Gas Return Pipe (HGRP). This large diameter titanium pipe has a combined function: it will return the gaseous helium boiled off the cavity vessels to the liquefier and act as a central support girder. The HGRP is Grade 2 Titanium, 280 mm in diameter with a wall thickness of 9.5 mm which will be supported by 3 support post, the middle one being fixed while the outer two slide by 7 and 9 mm, respectively. With a 1 ton weight force of the beamline string, the maximum vertical displacement of the HGRP would be 0.1 mm and the natural frequency would be 88 Hz. This simulation (see figure 4 for details) shows that a 3-posts support system is well suited to ensure an acceptable vertical displacement and vibration characteristics.

The 2-Phase 2 K pipe (item 2, Table 1) feeds helium to the helium vessel of cavities and the superconducting magnets through 7 chimneys. It is supported with sufficient clamps to the HGRP. Its natural frequency is calculated to be 144 Hz. It should be mentioned that the diameter of this pipe is strongly increased (compared to the ILC cryomodule design) to accommodate CW operation.

SW-110 Thermal Shield

In the extruded pipe, a convective heat transfer coefficient of $0.11 \text{ W/cm}^2\text{-K}$ was estimated. The variation with gas temperature, hence a function of time with a known cooling rate,

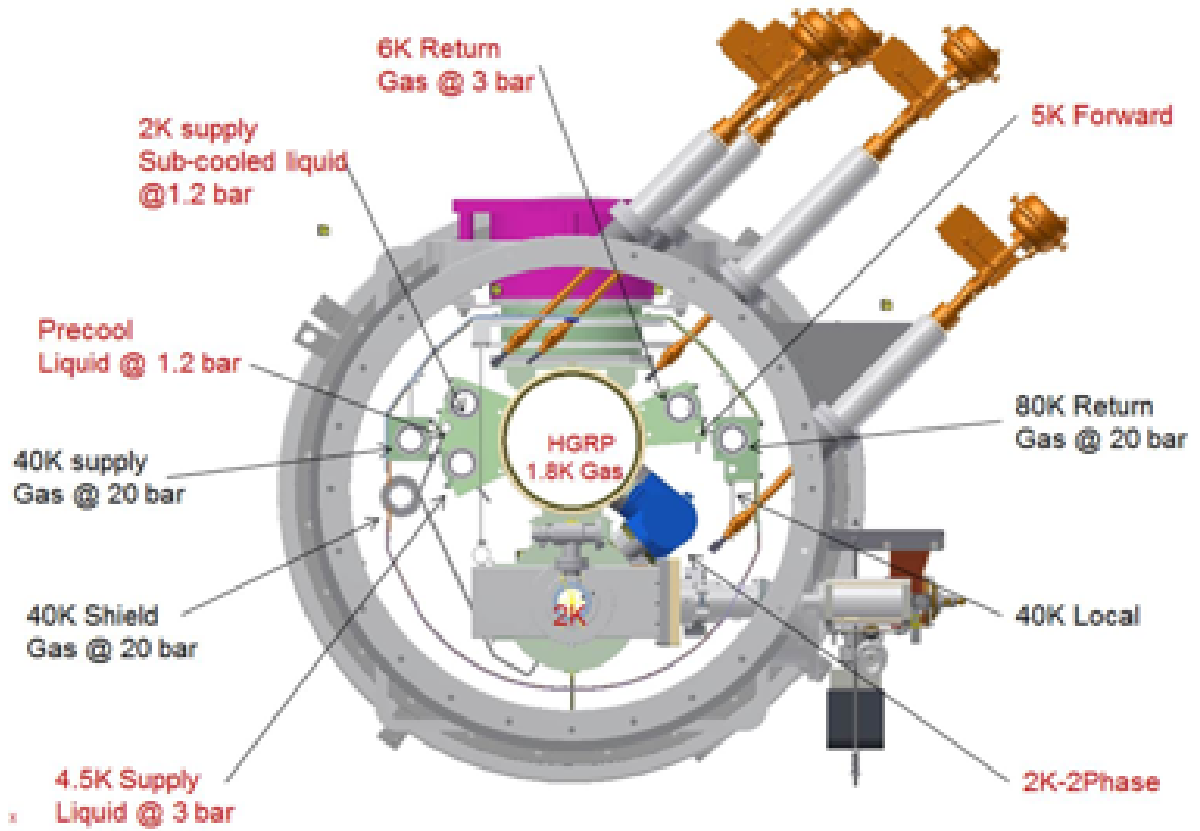


Figure 5.4.2: Cross-section of the MLC, giving more details on the piping (summarized in table 1) and positioning of the components.

was taken into account. Static heat loads includes conduction through the support post and radiation from room temperature vacuum vessel. The radiation heat load is reduced by wrapping the 40 K shield with 30 layer multilayer insulation (MLI) blankets. The radiation heat fluxes are assumed to be 1.2 W/m^2 from 300 K to 40 K. The simulated results indicated that with a cooling rate of 4 K/hour, the temperature gradient reaches a maximum of 13 K on the entire shield, occurring 15 hours after the start of the cool down. This situation is shown in Figure 5. Once fully cooled down, the steady state maximum temperature gradient is only 2.2 K (as shown in Figure 6). It should be mentioned that the thermal shield will be bent during cooldown estimated to be 6 mm maximum.

5.8 SRF Cavities

Five years ago, when the R&D on cavities started, the goal for achieving low cryogenic losses of an SRF cavity, denoted by its quality factor was thought to be very ambitious. At that time, Q 's of 2×10^{10} at a gradient of 16 MV/m were hard to imagine even at 1.8 K operating temperature. As a matter of fact, a prototype program was launched. The first 1.3 GHz, 7-cell main-linac cavity was fabricated based on a design that maximized the beam-break up

current. After stamping half-cells and welding them into dumbbells, their resonant frequencies were measured and trimmed accordingly [11] before welded together to form an entire cavity. The cavity received a bulk buffer-chemical polish (BCP) of 150 μm , was outgassed at 650 C for 12 hours, and was tuned to 1297.425 MHz, and then received a final 10 μm BCP and two eight-hour high pressure rinse cycles. The cavity was then cleanly assembled and attached to a stand for vertical testing. On the test stand the cavity was baked at 120 C for 48 hours.

After meeting quality factor and gradient specifications in the vertical test, the cavity was removed from the vertical test stand, and while still maintaining a clean RF surface, temperature sensors were attached to the outer surface and a helium jacket was welded to the cavity. The prototype cavity was then tested in a short horizontal cryomodule (Horizontal Test Cryostat - HTC) in a three tier approach: With HTC-1, the cavity was only equipped with a low power probe coupler; the HTC-2 rebuilt added the RF power coupler to the cavity; and the final HTC-3 step added the Higher Order Mode (HOM) absorbers to the cavity package.

After each step, the Q vs E points were measured through standard RF methods utilizing two RF probe ports and cryogenically by determining the power dissipated from the cavity. Cryogenic quality factor measurements used two methods: by measuring helium gas mass flow passing through pumps, and by watching the helium level drop. For both techniques, the 1.8 K helium input valve was shut, and calibrations were performed by using a heater to boil off helium while keeping constant bath temperature. The mass flow at the pumps and rate of helium drop directly relate to the power dissipated in the helium bath. When there is RF in the cavity, the power absorbed by the helium bath is simply the sum of RF power dissipated in the cavity walls, heat from a heater and the static heat load. Knowing the ϕ eld in the cavity, the quality factor is easily determined by subtracting heater power and static heat load from the total power extracted by the cryogenic system. As a summary, only the latest result on the cavity, gained with HTC-3, is shown in Figure 7.

For the superconducting cavities, operated in CW mode, an operation temperature of 1.8 K has been chosen based on an optimization process. For these 7-cell cavities, oscillating at 1.3 GHz a quality factor of 2×10^{10} at an accelerating gradient of 16 MV/m has been envisaged, which, at the time of the decision, seemed to be very ambitious. So part of the R&D program was to ensure that these parameters can be achieved reliably. In addition, to guaranty a high BBU-limit, tight mechanical tolerances on the cavity shape had to be met.

All cavities for the MLC have been produced in-house. The process began with half cells formed by a deep drawing process in which sheet metal of 3 mm RRR niobium is radially drawn into a forming die by a first press at 3 tons, then a second forming press (100 tons). The dies for the centre cells were carefully designed to deal with the spring back effect. The equators of each cup have an additional straight length on them (1.5 mm). The purpose of this extra length is to allow for trimming later on to meet the target frequency and length. Those dumbbells are built in an intermediate step by welding two cups together on their irises. Ultimately six dumbbells were be welded together by electron beam welding to form the centre-cells of the seven cell cavity and end-cells with end-groups are added After welding, the assemblies were cleaned by both chemical etching and a high purity water rinse to rid them of any surface impurities that may have accumulated during the production process.

For the preparation of the cavity, a simple recipe based on BCP has been chosen. Starting after fabrication, the damage layer is removed by bulk buffered chemical polishing (BCP, 140 μm). While we started to measure the removal rate with a witness sample first we learned that

an on-line ultrasonic head measurement is more appropriate. The hydrogen degassing is done at 650 C for 4 days while we monitor the hydrogen residual gas inside the furnace. Studies showed that a higher temperature (800 C) seems to remove more hydrogen but would slightly soften the cavity which would still be acceptable. One cavity has been treated such, showing a slightly higher Q. During the cavity production, we improved the mechanical tolerances in the cavity forming and welding, leading to a mean length deviation of the last three cavities by only 0.2 mm. Bullock (2013) reported the measures taken. The SRF properties of the 7-cell main Linac cavity were characterized at several stages before completing the assembly. Figure 2 shows the Q data of all six cavities. As can be seen, all cavities surpass the design specifications. In addition, we saw a very reliable and reproducible performance which is quite remarkable.

For the cavities, a 7-cell, 1.3 GHz design was made while an envisaged Q of 2×10^{10} was targeted at a gradient of 16 MV/m. All six cavities for the MLC module have been produced in-house starting from flat metal niobium sheets. To investigate microphonics, we decided to build 3 unstiffened cavities as well as 3 cavities with stiffening rings. All cavities were tested vertically, the summary of these tests are given in figure 4 and 5. All six cavities exceeded the design quality factor, averaging to 2.9×10^{10} at 1.8K. At 2 K, the average Q was 1.8×10^{10} , at 1.6 K we found 4.3×10^{10} [9]. It should be noted that the Q we measured on the prototype cavity at 1.8 K was 2.5×10^{10} in the vertical test, but 6×10^{10} in the horizontal test where magnetic shielding is more efficient [10].

The reproducibility of the Q versus E curves for all cavities is remarkable, also the fact that none of the cavities needed additional processing - giving a 100% yield.

5.9 HOM absorbers

The center assembly of the higher order mode (HOM) absorber consists of the absorbing cylinder which is shrink fit into a titanium cooling jacket and flange (see Fig. 3). The cooling jacket and flange locate, support, and provide cooling at 80 K to the absorbing cylinder using a cooling channel inside the titanium. For these production pieces, the absorbing material is Silicon Carbide, SC-35 from Coorstek. The shrink fit is designed so that all materials have a safety factor of at least 2 to yielding at 5 K and the fit will stay tight during a bakeout at 200 C. Details on that fit have been reported by He (2013).

The end pieces of the assemblies contain a 3 convolution bellows, a 5 K cooling plate, and taper seal flange to mate with the cavities. The bellows allows for small length variations in the string, small angular misalignments of cavity flanges, as well as adds a long thermal path from 80 K to 5 K. Any rotational misalignment is accounted for in slots in the bolt holes of the central 3 flanges which allow for a few degrees misalignment of the cavity flanges on either end. There are positive stops that prevent the bellows from compressing and closing the gap between the 5 K cooling jacket and the absorbing cylinder to less than 1 mm. This prevents any rubbing of metal to ceramic that could create particles. The beam tubes have a copper plating about 10 micron thick to prevent beam induced heating.

The overhead support is designed to have a similar spring rate to the transverse spring rate of the bellows so that the vertical load is evenly shared between the three springs. The plates are titanium to try to match the thermal expansion coefficient of the vertical supports on the other

string components. The G10 pieces are included to reduce the thermal conduction from the 80 K cooling jacket to the helium gas return pipe it is bolted to. A prototype of the absorber has been tested on a cavity running an electron beam of up to 40 mA. As Eichhorn (2014) reported, no significant heating was observed with all higher order modes were sufficiently damped.

5.10 Vacuum Vessel

The cylinder of the vacuum vessel is 965.2 mm in diameter, rolled longitudinally welded carbon steel (A516 GR70) pipe and stainless steel flanges that use O-ring seals. Due to the vendor's limited capability of final machining of the entire length of the vessel in a single setup, the vacuum vessel is made from three spool pieces. The spools are bolted with pins for alignment, and then welded together from the inside of the joining flanges to make up the full length. All precision required surfaces are machined in a single spool piece setup. Dowel pins and reference surfaces on the end flanges are used for the alignment to meet the GD&T requirements of the final vessel. Both the interior and exterior steel surfaces are painted, the interior being painted with PSX 700 Engineered Siloxane while a marine paint was chosen as the exterior paint. Figure 4 on the left shows a photograph.

5.11 Alignment

The Helium Gas Return Pipe (HGRP) is fabricated from a rolled and welded Grade 2 Titanium cylinder. During test fit of the baffle sub-assembly (which is needed in the prototype to guide the cold helium gas stream through the full length of the HGRP which lags the downstream flow from an adjacent module) in the Ti pipe, it was noticed that the baffle tube was flexible and the spoke support rods did not all make contact to the Ti pipe. This was solved by extending the support rods to ensure a tight fit with an extra pressure.

Being the reference for the alignment of the beam-line string, the surfaces of the HGRP top and bottom supports are precision machined with a single machine tool setup at the final stage after all welding is done. The beam-line string is suspended under the Helium Gas Return Pipe (HGRP) which acts as the beam-line backbone and is supported by three support posts to the vacuum vessel (see Fig. 5). To accommodate the HGRP thermal contraction at cold relative to the vacuum vessel, the two side posts are slide-able over the top flanges while the central post is locked in position. The central position of the side posts are pre-shifted at room temperature and will be concentric to the vacuum vessel flange at cold.

The posts have a same design as those used in the TTF cryomodule, which is an assembly of a low thermal conduction composite material pipe (G10 fiberglass pipe) and four stages of shrink-fit metal discs and rings. The two stainless steel disc/ring sets are connected respectively to the room temperature and to the 2 K cold mass environments. The two aluminum disc/ring sets provide thermal intercepts at 40 K and 5 K, with the 40 K set also providing structural support to the 40 K thermal shield. The heat load through conduction of each post (see Fig. 5) is estimated to be 8.58 W to 40 K, 0.54 W to 5 K and 0.05 W to 1.8 K, respectively.

The HGRP defines the reference for the precision alignment of the beam-line string. Relative vertical alignment is ensured by precision machining on the interfacing surfaces of the supports,

with a single machine tool setup at the final stage after all welding is done and a vibration stress relief is performed. The transverse and longitudinal alignment is obtained by the alignment pins on the support plates. The alignment key or a flexible cavity support allows the beam-line components to slide longitudinally relative to the HGRP during thermal cycling. The assembly sequence is that the beam-line string will be assembled in the clean room, and then attached to the HGRP. Once the cold mass is assembled, it will be rolled into the vacuum vessel on its rail system which seems to be more elegant than the ILC cryomodule assembly.

For the cold mass assembly, the HGRP was mounted to the 80-20 support structure (Fig. 4, right) via the 3 composite post support columns. An initial reference check of the 24 mounting feet along the bottom was conducted by pulling a string secured from the first and last mounting feet tight over the 10 m length of the HGRP. The mounting surfaces near the center section of the HGRP appeared to be high by 5 mm. This indicated a slight banana shape was present in the HGRP which was confirmed by laser tracking surveys.

During these surveys, it was observed that the Gr-2 Ti HGRP was more flexible than was initially understood through calculation and simulation. These surveys also indicated that a significant twisting along the HGRP axis was not present. Upon mounting the HGRP back on the support structure, an upward bow of now 3 mm was observed. After much discussion and experiment, it was observed that the mounting surfaces on the bottom of HGRP could be brought to within 1 mm of flatness across the entire span by applying an 400 kg load near the center of the HGRP. It was understood that this load would be present naturally when the 3 ton cold mass was mounted and fully dressed. After mounting the raw cavity string, a final laser tracker survey was completed that indicated these surfaces to be within an acceptable tolerance and work resumed to complete assembly (see Fig. 4, right).

5.12 Fundamental Power Couplers

Besides the cavities described above, the module currently under fabrication houses additional components which cannot be described in full detail within this paper (see [12] for details on the higher order mode absorbers). It is worthwhile to mention the power coupler shown in Figure 8. Even though these ERL main linac input couplers only have to deliver up to 5 kW CW RF power to the cavities, the design is rather sophisticated: The design approach chosen for the whole module requires compensating the lateral movement between the straight mounting situation and the dog-leg geometry gained after cool-down (with an off-set of up to 1 cm). In addition, the mounting procedure is such that the cold part is fully mounted inside the cleanroom, hermitically closing the cavity. This approach has been found to be very successful as we have seen no cavity Q degradation after the coupler mounting procedure. The warm portion of the coupler is mounted outside the cleanroom with no special precaution on extreme cleanliness.

The external Q of the coupler is 6×10^7 (with the option to adjust it using a three-stub tuner) in order to minimize the RF power requirements taking into account the microphonics inside the module. A first prototype of the coupler was successfully tested to 5 kW CW RF power under full reflection. This was done without any conditioning required to reach this power level using a commercial 5 kW solid state RF amplifier. Meanwhile, the series has been ordered and delivery is expected for August 2013.

Figure 5.13.1: A photograph of a TTF-III cryomodule in the FLASH tunnel at DESY.

All couplers have been procured at CPI and were tested upon receiving on a test stand, applying 5 kW CW RF power under full reflection without seeing any vacuum action. Essentially, no conditioning was required to reach this power level. Figure 7 shows the layout of the coupler, testing data is given in figure 8.

5.13 Magnetic Shielding

The fabrication of the 40 K thermal shield and magnetic shield, being attached to each other, are handled by the same vendor, to ensure they fit well at pre-mounting. Due to a limited furnace size for the hydrogen annealing after forming of the Mu-metal sheet, the magnetic shield sections are consists of many small patches in 1 m x 1.2 m, with overlaps at joints. Enough clearance is ensured between sections and the joints, to account for differential thermal contractions between the magnetic shield (Mu-metal) and the thermal shield (Al1100-14). Details are shown in Fig. 1. It should be noted that every cavity is enclosed by a second magnetic shield, made from cryoperm.

5.14 Parallel Flows

As indicated in figure 2 the module relies on active cooling provided by parallel cryogenic flows. We have investigated the challenges associated with that in the past [7,8]. For the MLC a more careful analysis was required for the 80 K circuit, where the coolant first cools the intercept of the power coupler and then HOM absorber. Six streams exist in parallel, with a seventh stream only feeding one HOM absorber. While the heat load on the coupler, predicted by a simulation, is 10-15 W, the heat load of on the HOM absorber is- by the nature of the higher order mode power- a statistical quantity, and the expectation range is from 0 to 400 W. As a consequence, a flow with no HOM power parallel to a flow with 400 W heat load would be highly imbalanced.

The analytical model (based on a configuration as depicted in figure 3 on the left) we set up investigated the stability of the parallel under the variation of the heat load on one branch while the heat-load on the other branch remained constant at 200 W. As can be seen by the middle plot of figure 3, adding an inlet impedance on every branch can significantly reduce the change in the mass flow ratio between the channels under variation of the heat load. This non linear behaviour is also described by figure 3, right plot, where a parameter study was made investigating the influence of the pipe diameter on the stability of the system.

5.15 Assembly Process

While production of components started earlier, the virtual assembly began in March 2014, when the first cavities where connected to a string inside the cleanroom. For space reasons, two half strings, consisting of three cavities with attached cold section of the coupler and 4

HOM absorbers as well as a gate valve were assembled. Each substring was leak checked and connected to the other later on. In May, cold mass assembly continued outside the cleanroom. Mating the pre-aligned cavity string with the precision surfaces on the HGRP strong-back turned out to be not an issue at all. All bellows located at the HOM absorber package were able to compensate for deviations and only the longitudinal position of one HOM absorber had to be adjusted.

Installation of the cavity magnetic shield, the tuner, the thermal and magnetic shield, all cryogenic piping and jumpers, instrumentation and cabling as well as a wire position monitor to track alignment during cool-down took 3 months. After a minor modification of the wheel, supporting the cold-mass on our rail system we were able to slide it into the vacuum vessel in September. As final assembly steps we installed the warm portion of the couplers, feed-throughs and cryogenic valves. All circuits were leak checked and pressure tested. In November, the team could celebrate the completion of the module, which was achieved within time and budget.

5.16 Preparation for Testing

In preparation for the testing of the MLC, the module was transported across the Cornell campus. No special damping frame was used. However, all movements were done with extreme care and transportation speed was set to 5 km/h max. In addition, we measured mechanical shocks using accelerometers. The data, given in figure 11, revealed a maximum g force of 2.3 (lasting less than 10 ms), which occurred while pulling the module (sitting on its own wheels) in place after lifting it from the truck. During the road trip, max g-factors were below 1.5. As of May 2015, preparations continue for the first cool-down being scheduled for July.

5.17 First Cool-down

In order to facilitate a smooth and controlled cool-down, a new heat exchanger can was built—the piping diagram is given in Fig. 2. It allows to add a warm stream of gas forwarded to the cold-mass, resulting in a very controlled cool-down, as shown in Fig. 3. This was mandatory as the thermal shield is cooled by conduction only with an extruded pipe running just along one side. As a result, the cool-down of the shield is asymmetric and we calculated stress limits on the aluminum transitions which required us to keep the temperature spread across the shield below 20 K. In the initial cool-down we maintained 10 K, becoming 15 K below 200 K with an average cool-down rate of 1.25 K/h. More details on the heat exchanger can which we found extremely convenient are published in [5]. During cool-down, we also monitored the movement of the two outer, sliding support posts. In contrast to the ILC, our cryomodule is aligned via the helium gas return pipe, made out of titanium, being suspended from the vacuum vessel by three support posts. As a result of the cold-mass shrinking as a whole, the central post is fixed while the two outer posts are sliding. Figure 4 gives the movement of these posts as the temperatures on the cool-mass go down. The movement was as expected and deviations from the predicted position was considered an abort criterion.

5.18 Cool-down Cycles

Recent findings have indicated that the performance of an SRF system also depends on details of the cool-down process. Findings at Cornell indicate that for conventionally treated cavities a slow cool-down leads to a higher quality factor of the cavity [6]. We were able to explain this finding by describing the role of thermo-currents that are excited at the material transitions between the niobium (cavity) and the titanium (enclosing helium vessel), driven by temperature gradients [7,8]. So-called nitrogen-doped cavities, however, seem to require a fast cool-down and it was found that this helps expelling residual magnetic field more efficiently than a slow cool-down [9]. It should be noted that N-doped cavities are stronger effected by trapped magnetic flux compared to conventional treated cavities. As a matter of fact, there is an interest in understanding slow and fast limitations on the cool-down speeds for a cryo-module as a whole as well as on reproducibility of these cycles. We therefore went through a total of 5 thermal cycles, trying very slow and extremely fast cool-downs. Results are given in Fig. 5. We found that for a slow cool-down some cavities went through transition several times with some unwanted warm-up in between. We also learned that on the fast procedure the final cool-down speed depended on the cavity position, especially how close the cavity was in relation to the Joule-Thompson valve

5.19 RF Test Results

Test results from all 6 cavities are summarized in Fig. 6 and Tab. 1. After some initial processing 5 of the 6 cavities perform close to their design specifications. One cavity is currently limited by a premature quench which we hope to overcome by a thermal cycle and pulse processing. Even so the quality factors are slightly lower than the design, the cavities (except #4) easily reach the design gradient. From Fig. 6 one could also conclude that in our case the cool-down speed did not significantly affect the cavity performance. However, the data shows slightly higher Q 's for the slow cool-down. This might indicate that we have a slightly higher residual magnetic field inside the MLC (as compared to our short test module HTC).

We also performed a higher order mode scan on one cavity, results are given in Fig. 7, diagram to the right. This figure also shows the design of our absorber on the left, which is described in more detail in [10]. It is a beam line absorber being positioned next to each cavity on either end. The design goal for the absorber was to have no dipole mode resonating with an external Q higher than 104 in order to guarantee a high BBU threshold current. The measured Q 's in Fig. 7 being 10^7 are rather unexpected, however, they belong to quadrupole and sextupole modes which do not contribute to the BBU limit. Currently, HOM scans on the remaining cavities continue in order to confirm the results.

5.20 Tuning and Microphonics

To better understand the trade-offs in the mechanical behavior of the cavities, the MLC was built with two types of cavities: three had stiffening rings added in order to minimize the pressure responds (df/dp) and to minimize microphonics while the remaining three cavities were built without stiffening. One concern was that the stiffened cavities might overload the

tuner and may not be tuned to frequency. In addition, our initial testing indicated that an unstiffened cavity would meet our requirements and in addition would be easier to fabricate.

Figure 8 shows the pressure response curve for a stiffened and an unstiffened cavity. As expected, the pressure sensitivity of the stiffened cavity is smaller by more than a factor of two. However, with the pressure stability in our system being 0.1 mbar both figures are well acceptable. Table 2 gives figures for all cavities, while also reporting on the tuning that was necessary after cool-down. As two cavities are close to their tuning range we will slightly lower our operating frequency to 1299.9 MHz.

A typical curve that we measured on the coarse tuner is given in Fig. 9, displaying a 150 Hz hysteresis which will be counteracted by the piezos being used for fine tuning. The tuner is based on the TTF design. First measurements on the microphonics indicated a rather high level of mechanical motions leading to cavity bandwidths well above our designed 10 Hz. Especially the unstiffened cavities seem to have a very strong mechanical resonance at 60 Hz. We are currently in the process of taking accelerometer data as well as fast He-pressure sensor data to understand the source of the microphonics and the path under which the creep into the module.

5.21 Principles Governing the Baseline Design

The ERL Linac design is based on TTF-III technology with modifications for continuous wave (CW) operation. This builds upon the considerable development work performed for this Linac technology over the past 15 years. TTF-III technology is at the forefront of SRF Linac performance in regard to cavity gradient, quality factor Q , power coupled to the beam, cavity tuning, minimal cryogenic heat load, industrial fabrication, and operational reliability. This technology is characterized by module-vacuum vessels joined end-to-end with large lengths of the Linac sharing a common insulation vacuum. For the baseline design, the ERL Linac will have a north and a south section; the north will have 35 modules and is 344 m long, and the south will have 29 modules and is 285 m long. Placement of an insulation-vacuum break in each of the long Linac sections is under study.

The modifications to the TTF-III technology for CW operation and energy recovery have significant operational differences. From a facility point of view, because the resistive power dissipated in the SRF cavities is absorbed by the refrigeration system at 1.8 K, having CW cavity operation makes the refrigeration system a major utility component. This favors relatively low-cavity gradient as cryogenic power per unit length scales as the square of the gradient. Another consideration that favors lower gradient is that field emission and consequent radiation produced within a given cavity scale exponentially with cavity gradient. This not only adds to the cryogenic load but will also produce a significant radiation level in CW operation. A lower cavity gradient will lessen field emission, and thus shielding requirements.

Achieving as high a cavity Q as possible at a given temperature has a direct benefit of reducing the size of cryoplant. There are three components needing control for highest Q : the BCS component with exponential temperature dependence; the temperature-independent residual resistance, which depends on the surface processing; and the trapped magnetic flux component, which depends on the effectiveness of the magnetic shielding. The latter requires the magnetic shielding in the cryomodule to reduce the background magnetic fields at the

cavities to < 2 mG to ensure that residual RF losses due to flux pinning are negligible. This will be accomplished by using a demagnetized carbon-steel-vacuum vessel, a mu-metal lining of the vacuum vessel at 293 K, and a shield around each cavity using material formulated for optimal magnetic performance at 1.8 K. With cavity Q dominated by BCS resistance, selection of the cavity temperature then becomes an optimization of refrigeration power and scaling of the BCS resistance with temperature, which favors a cavity temperature of 1.8 K [1].

Reliability and uninterrupted run time of the ERL light source is a performance goal for the machine. With the Linac total of 384 SRF cavities, the trip rate per cavity needs to be below once per several years to accomplish a machine trip rate of less than once per day. A modest cavity gradient will play a major role in making this feasible, since it has been demonstrated at all of the facilities listed in Table ?? that operation of SRF cavities is extremely reliable if the cavity gradient and input RF power are not pushed to the limits. The input RF power to each cavity is low due to the energy recovery, typically 2 kW average and 5 kW peak power, so trips due to RF couplers should occur at a very low rate.

The RF-source architecture is likewise designed for reliable machine operation; there will be a dedicated source for each cavity. With this configuration, the loss of one RF source translates to the loss of only one cavity. Having a dedicated source per cavity also allows the flexibility to tune for the best performance of each cavity, which in conjunction with gradient and RF power overhead, will be utilized to compensate for a tripped cavity to provide uninterrupted machine operation. The challenge to the RF system will be in the form of the high loaded quality factor Q_{ext} of the input couplers. This will place tight constraints on maintaining the RF field phase and amplitude in both absolute terms along the length of the Linac and in local terms due to microphonic perturbations of individual cavities. The RF feedback system will be capable of compensating for microphonic perturbations at the expense of increased average forward power, as demonstrated in the ERL-injector prototype at Cornell. An important developmental task will be to show that the fast-piezo component of the cavity tuner can be used to mechanically compensate for microphonics, and thus lower the Linac RF-power budget.

The short bunch length of 0.6 mm ($\approx 2 \text{ ps} \cdot c$) and high average beam current of 100 mA CW in both the accelerating and decelerating beams in the ERL demands heavy damping of the higher order modes (HOMs) in the cavities. The loaded Q 's of such modes and their shunt impedance place direct limits on the beam-breakup (BBU) limited-beam current. The average HOM power is expected to be 200 W per cavity, assuming no resonant excitation of any particular mode. Most of the power will be in the frequency range of 1-10 GHz, but the short bunch length will contain HOM spectral content up to the 100 GHz range. The HOM damping scheme must have strong coupling over this broad bandwidth and be able to dissipate the average power. Beamline-HOM loads have been chosen in the baseline design to accomplish these requirements. The beamline loads will operate at 100K to minimize the cryoplant load, and thus necessitate thermal gradients along the beamline between cavities by way of cooled intercepts. Operation of the ERL-injector prototype at Cornell has given important insight as to the requirements of the RF-absorbing material in the beamline loads, and new robust materials have been developed as a result. The alternate use of waveguide and loop-HOM couplers are the subjects of ongoing investigations [2–4], and while they have the benefit of transporting the HOM power to external-room temperature loads, it is still to be determined if they will have the requisite bandwidth and power capability, and how the

Table 5.21.1: Beamline components and lengths of the Linac cryomodule.

	Component	Length (m)
	Gate Valve	0.0750
	Taper	0.0500
Repeat 6 times	HOM Absorber	0.0600
	110mm Cu beam tube	0.0476
	110mm Nb beam tube	0.2150
	Cavity active length	0.8061
	110mm Nb beam tube	0.2150
	110mm Cu beam tube	0.0476
	HOM Absorber	0.0600
	Taper	0.0500
	BPM	0.0750
	Quadrupole	0.4500
	X-Y Steering Coils	0.1500
	Gate Valve	0.0750
	Intermodule flex	0.4885
	Module Length	9.8213
	Fill Factor	0.49

structural complexity will compare to beamline loads. Another consequence of the short bunch length and high HOM frequencies is that the design of the mechanical contour of the beamline must have careful consideration of any features with dimensions of ~ 0.6 mm or larger, such as flange gaskets and RF pickups, to avoid excitation of high frequency modes and consequent heating.

5.22 Cavity

The superconducting cavities in the main Linac of the ERL significantly influence the performance, cost and reliability of the accelerator in several ways. The design of the cavity must be optimized according to the ERL specific requirements.

The optimization of the main Linac cavity design is driven by the three primary objectives:

- The cavities must be able to support beam currents up to the design value of 2×100 mA, and strong suppression of Higher-Order-Modes (HOM) in the main Linac is therefore essential. In addition, fluctuations in the HOM frequencies from cavity to cavity are desirable to reduce coherent effects and thereby increase the BBU threshold current.
- A large value of R/Q for the fundamental mode (at 1.3 GHz) is highly desirable to minimize the dynamic cryogenic load by the accelerating RF field in the cavities.
- The performance of the cavity design must be robust under small shape imperfections, which are always present due to finite fabrication tolerances.

Figure 5.22.1: CAD model of the 7-cell ERL main Linac cavity.

Linked to the cavity design are the operating parameters of the cavity. Most of these can be chosen and optimized freely (within certain boundaries). The intrinsic quality factor Q_0 of the cavity is not a free parameter, and it is crucial to assume a realistic value for it, since it determines the size of the cryogenic refrigerator required. The following sections discuss the ERL main Linac cavities and their baseline operating parameters in detail. Subsequent sections present the RF and mechanical design of the main Linac cavities in detail, including the choice of cavity flanges, the LHe vessel design, and the inner magnetic shielding of the cavity. The final sections briefly cover the fabrication of the cavities and their surface preparation.

5.22.1 Cavity operating parameters: Q_0 , E_{acc} , and Q_{ext}

The three main cavity operating parameters are the intrinsic quality Q_0 factor of the SRF cavity (which also depends on the operating temperature T), the operating accelerating field gradient E_{acc} , and the external quality factor Q_{ext} . All three parameters strongly impact the ERL main Linac design and cost. While the intrinsic quality factor is determined by the cavity preparation, the operating temperature and the magnetic shielding in the cryomodule, the other two parameters can be chosen freely (within limits).

5.22.2 The baseline ERL cavity

This section discusses the RF and mechanical design of the baseline main Linac superconducting RF cavity. The baseline cavity is a standing-wave 7-cell structure of solid niobium with a fundamental mode frequency of 1.3 GHz (see Fig. 5.22.1). Power is coupled into the cavity via one coaxial RF input power coupler located at an end-beam tube. Large diameter beam tubes ensure propagation of all monopole and dipole HOMs to beam tube RF absorbers located between the individual cavities to ensure strong suppression of HOMs and thereby support operation of beam currents up to 100 mA. The cells of the cavity are surrounded by a LHe tank to immerse the cavity into 1.8 K LHe. Each cavity is further equipped with a frequency tuning system (slow tuner driven by a stepping motor and fast tuner driven by piezoelectric crystals), and a field pick-up probe to monitor the cavity-RF fields. Table 5.22.1 summarizes the main parameters of the main Linac cavity. The following subsections give more details on the cavity design.

5.22.3 RF design

This section discusses details of the RF design of the shape of main Linac cavity.

Design philosophy

The shape of a multi-cell SRF cavity is defined by a large number of parameters, which can be adjusted according to the design goals of the specific accelerator. In the case of the ERL, the cavity design needs to fulfill the following requirements:

Table 5.22.1: ERL main Linac cavity design parameters. Note that R/Q is always in the circuit definition.

Parameter	Value
Type of accelerating structure	Standing wave
Accelerating mode	$\text{TM}_{0,1,0} \pi$
Fundamental frequency	1.3 GHz
Design gradient	16.2 MV/m
Intrinsic quality factor	$> 2 \times 10^{10}$
Loaded quality factor	6.5×10^7
Cavity half bandwidth at $Q_L = 6.5 \times 10^7$	10 Hz
Operating temperature	1.8 K
Number of cells	7
Active length	0.81 m
Cell-to-cell coupling (fundamental mode)	2.2%
Iris diameter center cell / end cells	36 mm / 36 mm
Beam tube diameter	110 mm
Geometry factor (fundamental mode)	270.7Ω
R/Q (fundamental mode)	387Ω
$E_{\text{peak}}/E_{\text{acc}}$ (fundamental mode)	2.06
$H_{\text{peak}}/E_{\text{acc}}$ (fundamental mode)	41.96 Oe/(MV/m)
$\Delta f/\Delta L$	350 Hz/ μm
Lorentz-force detuning constant	1 Hz / $(\text{MeV/m})^2$
Cavity total longitudinal loss factor for $\sigma = 0.6 \text{ mm}$	14.7 V/pc
Cavity longitudinal loss factor for $\sigma = 0.6 \text{ mm}$, non-fundamental	13.1 V/pC
Cavity transverse loss factor for $\sigma = 0.6 \text{ mm}$	13.7 V/pC/m

- The RF design should reduce dynamic losses by the fundamental mode as far as possible while still satisfying the other design goals.
- The RF design needs to support operation of the ERL at a 100 mA accelerating beam current.
- The performance of the RF design needs to be stable under small shape imperfections, which are unavoidable in the fabrication process of deep drawing and welding.
- The ratio of peak electric surface field to accelerating field $E_{\text{pk}}/E_{\text{acc}}$ shall not exceed 2.1 to reduce the risk of field emission (the ratio of electric fields in the ILC cavity is 2.0).
- The cell shape shall be non-reentrant. This simplifies cavity cleaning and surface treatment.
- Transverse kick fields in the coupler region shall be minimized to avoid emittance growth.

The RF design of the cavity is complicated by the fact that there are a large number of free parameters in the cavity shape and that there are different objectives for the design, which are partly contradictory because optimization for minimal losses and for maximal HOM damping lead to different shapes of the cells. In designing the ERL main Linac cavity, the following approach has been taken to reduce the number of free parameters in each step by breaking the design work down into several steps, each focusing on a specific design objective:

- The center cells of the multi-cell main Linac cavity are identical and have been optimized initially to minimize dynamic wall losses by the RF field while keeping $E_{\text{pk}}/E_{\text{acc}} < 2.1$.
- The end cells were optimized to reduce the strength of the strongest dipole HOMs to increase the beam break-up (BBU) current above the design goal of 100 mA.
- The design was then evaluated for robustness under small shape imperfections and the shape of the center and end cells was iterated slightly to achieve sufficient robustness.
- The maximum number of cells was found by adding additional center cells to the multi-cell cavity design, and the BBU performance of the resulting cavity was simulated.
- The loss factor of the final cavity shape was computed and the input coupler region at one of the two end beam tubes was designed.

Center cell design

The center cells of the ERL main Linac cavity are identical and have been optimized initially to minimize dynamic losses while keeping $E_{\text{pk}}/E_{\text{acc}} < 2.1$. The shape of the cell was optimized for different iris radii between 30 and 43 mm (see Fig. ?? using a computerized optimization routine and the electromagnetic eigenmode code CLANS [5]. In each case, the shape dependent factor GR/Q was maximized to minimize the dynamic wall losses of the accelerating mode at a given field gradient. The usual basic cell shape consisting of two elliptical sections connected by a tangential line was used to ensure avoidance of multipacting in the cells.

Reducing the iris radius reduces the dynamic heat load by the RF field in the cavity, but increases the magnitude of the loss factor of the cavity. An increase in loss factors means an increase in average HOM power excited by the electron beam. Further, reduction of the radius reduces the cell to cell coupling and thus coupling of the HOM power to the beamline loads and the robustness of the design against small manufacturing errors. As discussed in [6], the parameter set resulting from the indicated compromises are presented in Tables 5.22.2 and 5.22.3.

End cell design and HOM performance

The ERL is specified to run accelerating currents of 100 mA through the main Linac. This current is limited by higher-order-modes in the cavity that are excited by the beam and can cause beam instability. In a 1-turn ERL, the threshold current I_{th} , through an isolated cavity with a single HOM, has been modeled as

$$I_{\text{th}} = -\frac{\omega_{\lambda}}{e \left(\frac{R}{Q}\right)_{\lambda}} \frac{1}{Q_{\lambda} T_{12} \sin(\omega_{\lambda} t_r)}, \quad (5.22.1)$$

Table 5.22.2: Comparison of figures of merit and geometries for center cells before and after re-optimization to increase the width of HOM passbands. Cryogenic losses are slightly increased. The geometry factor and $E_{\text{pk}}/E_{\text{acc}}$ are for the fundamental mode. Key: Equ.=Equator, Horiz.= Horizontal, Vert.=Vertical. The last four dimensions are half-axes of ellipses, measured in cm.

	$(R/Q)G$	$E_{\text{pk}}/E_{\text{acc}}$	Wall angle	Iris radius	Equ. horiz.	Equ. vert.	Iris horiz.	Iris. vert.
Before	15576Ω	2.00	85	3.5	4.399	3.506	1.253	2.095
After	14837Ω	2.06	77	3.598	4.135	3.557	1.235	2.114

Table 5.22.3: Frequency width of the first 6 dipole passbands. Note that bands 3 and 6 were widened significantly while the other bands had their widths decreased only slightly.

Dipole band	$\sim 1.8\text{ GHz}$	$\sim 1.9\text{ GHz}$	$\sim 2.5\text{ GHz}$	$\sim 2.7\text{ GHz}$	$\sim 3.1\text{ GHz}$	$\sim 3.4\text{ GHz}$
Before	192 MHz	95 MHz	31 MHz	277 MHz	55 MHz	10 MHz
After	188 MHz	73 MHz	107 MHz	227 MHz	47 MHz	20 MHz

where ω_λ is the HOM frequency, Q_λ is the quality factor of the mode, R/Q is in units of Ω/cm^2 (in circuit definition), t_r is the bunch return time, and the transport matrix element T_{12} describes how a transverse momentum is transported to a transverse displacement after one turn [7]. Equation 5.22.1 suggests that the parameter $(R/Q)Q/\omega$ should be used as a figure of merit in the cavity design when optimizing it for maximal BBU threshold current. However, the ERL main Linac will have a large number of cavities, and coherent effects will influence I_{th} through the Linac. This coherent effect will depend on the variation of the HOM frequencies from cavity to cavity and on the quality factor of a given type of mode. Lower quality factors will result in wider HOM-resonance curves and therefore in more overlapping of the modes in different cavities, more coherence, and a lower threshold current. Thus, a new BBU figure of merit parameter was determined for an ERL Linac with a large number of cavities by running BBU simulations and varying the parameters of a given HOM in the cavities. The conclusion of the BBU runs is that

$$I_{\text{th}} \propto \frac{\omega_\lambda}{\left(\frac{R}{Q}\right)_\lambda \sqrt{Q_\lambda}} \quad (5.22.2)$$

for an ERL Linac with a large number of cavities and for $10^2 < Q < 10^6$.

Accordingly, the end-cells of the ERL main Linac have been optimized with the goal to minimize the maximum value $(R/Q)_\lambda \sqrt{Q_\lambda}/f$ of any dipole HOM of the cavity. The end cells were optimized by varying 5 free parameters per end cell. The dipole mode fields and their

Figure 5.22.2: Shape of the main Linac cavity with HOM absorber sections at the beam tube ends.

Figure 5.22.3: Average beam breakup current versus relative frequency spread for simulated ERLs. The blue circles mark the threshold current through an ERL with every cavity having the same nominal HOM frequency, Q , and R/Q values of the worst higher-order modes as a function of relative cavity-to-cavity frequency spread. The red triangles denote the average threshold current for ERLs generated from realistically shaped cavities, having different frequencies, Q s and R/Q s from shape imperfections, and no artificial cavity-to-cavity frequency spread. The lower (upper) error bars mark the threshold current that 90% (10%) of the simulated ERLs achieve. For small values, as machining tolerances loosen, the frequencies of cavity HOMs are spread over a larger range, contributing to larger threshold currents. When the machining errors are more than 0.5 mm, the underlying properties of the optimized cavity geometry are lost, and the threshold current plummets. In all cases except the 1 mm variation size, simulated ERLs well exceed the design specification of 100 mA current, denoted by the dashed horizontal line.

damping were calculated with the 2D finite element codes CLANS2 [8] for HOM frequencies up to 10 GHz. The 2D-cavity model used is shown in Fig. 5.22.2, and includes the cavity itself, and half of an HOM absorber at either end (the center of an HOM absorber is the symmetry plane for a string of main Linac cavities). This model therefore simulates the Q in a string of cavities. The model includes the dielectric losses by the selected RF absorbing material in the HOM absorbers ($\epsilon' = 30$; $\epsilon'' = 20$; $\mu' = 1$; $\mu'' = 0$). Particle tracking was then used to compute the final threshold current through an ERL composed of these cavities. The blue curve in Fig. 5.22.3 shows that as the relative cavity-to-cavity HOM frequency spread increases, so does the threshold beam current. In practice, the frequency spread will be the result of slight variation in cavity shapes in the cavity fabrication process. This is shown as the red curve in Fig. 5.22.3.

Typical fabrication tolerances of ± 0.25 mm to ± 0.5 mm result in a cavity-to-cavity frequency spread σ_f/f of about 1×10^{-3} to 3×10^{-3} . At this frequency spread, particle tracking for the optimized 7-cell cavity predicts a BBU threshold current of about 300 mA to 500 mA, several times the 100 mA requirement for the accelerating beam of the ERL. If needed, the BBU threshold can be increased considerably by intentional means. An ensemble of cavity designs giving an approximately uniform frequency spread to the important HOM dipole bands will be created for the manufacture of the ERL cavities.

Figure 5.22.4: Monopole modes strength $(R/Q)Q$ for all monopole modes in the optimized 7-cell cavity up to 10 GHz. Green lines indicate the beam harmonics. The red line shows the $(R/Q)Q = 1000 \Omega$ limit for modes within $\Delta f = 10^{-3} \cdot f$ of these harmonics. Modes with $(R/Q)Q > 1000 \Omega$ that are not close to the green lines are benign.

All monopole modes up to 10 GHz have been calculated for the Linac cavity shape to ensure that modes that might be driven resonantly are sufficiently damped. The HOM power transferred to a mode by the beam in case of resonant excitation is given by

$$P = 2 \left(\frac{R}{Q} \right) Q I^2, \quad (5.22.3)$$

where Q is the quality factor of the mode and I is the average beam current (0.2 A for the combined accelerated and decelerated beam in the main Linac). Requiring that the maximum HOM power in case of resonant excitation is below 400 W per cavity then gives $(R/Q)Q < 10^4$ for any mode that could be excited resonantly, i.e. which has a frequency within $\Delta f = 10^{-3} \times f$ of a beam harmonic at $f = N \times 2.6$ GHz. Calculation shows that all monopole modes near the first 3 beam harmonics are sufficiently damped in the 7-cell ERL main Linac cavity. These results are shown in Fig. 5.22.4.

Short range wakefields

The longitudinal loss factor $k_{||}$ of a cavity determines the average power transferred from the beam to electromagnetic fields (wakefields) excited by the beam,

$$P_{\text{average}} = k_{||} q I, \quad (5.22.4)$$

where q is the bunch charge and I is the average beam current. The longitudinal loss factor and the wake potential of the 7-cell ERL main Linac cavity have been calculated for a bunch length of $\sigma = 0.6$ mm yielding $k_{||} = 14.7$ V/pC, where the fundamental mode contributes 1.6 V/pC and the HOMs contribute 13.1 V/pC. Note that the main Linac cavities are one of the main contributors to the total impedance of the ERL and thereby make a significant contribution to the final intra-bunch energy spread. The average HOM power excited by the beam in a main Linac cavity is then about 200 W. Individual cavities will have smaller or larger power values, depending on their actual HOM frequencies (which will vary from cavity to cavity as a result of small cavity-shape imperfections), which will change the number of modes excited resonantly by the bunch train.

Input coupler port and transverse coupler kicks

The position of the 40 mm input coupler port on one of the cavity end-beam tubes was found such that the tip of the inner conductor of the coax input coupler protrudes 2.7 mm inside of the beam tube wall at an external Q of 6.5×10^7 (see Fig. 5.22.5). Non-zero transverse fields can be present in the input coupler region even on the beam axis since the coupler port breaks

Figure 5.22.5: Input coupler port of the ERL main Linac cavity with $Q_{\text{ext}} = 6.5 \times 10^7$ and symmetrizing stub at the opposite site of the beam tube.

Figure 5.22.6: Mechanical vibration modes of the main Linac 7-cell cavity for different radial positions of the stiffening between the individual cells. r_{eq} is the cell equator radius.

the axial symmetry. Such transverse coupler fields are highly undesirable, since they will cause emittance growth of the beam passing the ERL main Linac. One way of reducing the emittance growth is adding a small symmetrizing stub across from the coupler as illustrated in Fig. 5.22.5. The stub is used to minimize the asymmetry in the beam pipe, causing the transverse fields in the coupler region. The method reduces amplitudes of the off-axis fields and thus reduces the magnitude of the coupler kick with weak dependence on the depth of the stub once it is over 10 mm deep [9]. Our preliminary design therefore uses 20 mm depth.

5.22.4 Mechanical design

This section gives an overview of the mechanical design of the Cornell ERL main Linac cavity, including its LHe vessel and inner magnetic shield.

Mechanical modes

The cavity cells will be fabricated out of 3-mm thick Niobium sheets for mechanical strength, with stiffening rings between the individual cells. The optimal position of these stiffening rings will be found by mechanical simulations with ANSYS. The objectives of these optimizations are (1) to increase the resonance frequencies of mechanical vibration modes of the cavity to reduce cavity vibration excitation by external sources, and (2) to decrease the frequency shift of the accelerating mode by fluctuations in the LHe bath pressure surrounding the cavity. The power density of the ground vibration spectrum decreases with frequency so high mechanical resonance frequencies of the cavities are desirable to reduce driven vibrations. Figure 5.22.6 shows the lowest frequency mechanical vibration modes of the main Linac cavity structure for different radial positions of the stiffening rings between the cells. As expected, the frequencies of the modes increase with the radial position of the stiffening rings. An upper limit for the radial position is given by the requirement that the cavity needs to remain tunable in length by the frequency tuner, and by the second objective that the sensitivity to LHe pressure changes should be minimized.

As the example in Fig. 5.22.6 shows, the radial position of the stiffening rings also changes the sensitivity of the cavity frequency to fluctuations in the pressure of the liquid helium surrounding the cavity cells. Optimizing the position of the rings allows minimizing this contribution to the cavity microphonics.

The beam tubes of the main Linac cavity will be fabricated out of 1.5 mm thick, low-RRR niobium to reduce static heat loads from the HOM absorbers located between the cavities at 100 K to the 1.8 K cavities.

Figure 5.22.7: Zero-gap KEK flange design [12].

Figure 5.22.8: Vacuum flange hybrid of the KEK zero-gap, a DESY diamond seal and a taper seal flange.

Cavity flanges

Different types of flanges have been used on superconducting cavities in the past, including niobium flanges with indium wires, ConFlat-flanges, and aluminum diamond shaped gaskets with NbTi flanges. The main objective of these flanges is to provide a clean, highly reliable connection to the next element in the beamline. However, in high current accelerators like the ERL, it is also crucial that the impedance of the flange design be as small as possible to eliminate potential heating issues, since they are inside the cryomodule vacuum and therefore cooled only via conduction through the beam-pipe.

KEK has developed a zero-gap (zero-impedance) flange design, which uses a copper gasket compressed between two small, flat surface rings with 90° edges [10] (see Fig. 5.22.7). NbTi versions of such a zero-gap flange design will be considered for use in the ERL main Linac for the cavity flanges. An R&D program has been started to verify the high reliability of this flange design found in previous studies [11]. In parallel, a new flange design will be studied which is a hybrid of the KEK zero-gap [10], a DESY diamond seal [11] and a taper seal flange [12]. This configuration shown in Fig. 5.22.8 may allow for the reliability of the DESY diamond seal with low compression force and elastic spring as well as the minimal wall perturbation of the KEK zero-gap.

LHe vessel

The cavity cells are welded into a cylindrical titanium vessel, which holds the superfluid helium needed for cooling the cavities to 1.8 K. The tank further serves as part of the cavity-frequency tuning system, including a short bellow section to allow the length of the cavity to be adjusted, and is used to support the cavity in the cryomodule. Titanium has a thermal contraction which is almost identical to that of niobium, thereby minimizing any buildup of mechanical stresses during cool-down of the cavity from room temperature to 1.8 K. A stainless steel vessel would have a 2 times larger thermal contraction than the niobium cavity and would result in intolerable stresses in the cavity, resulting in plastic deformation unless the tuning mechanism is operated during cool-down. Titanium has the additional advantage that it can be welded directly to the Nb/Nb-Ti conical vessel end plates on the cavities using either TIG welding or electron-beam welding.

The heat flux (power per cross-sectional area) through superfluid helium in the LHe vessel needs to be less than the limiting heat flux of $\sim 1.5 \text{ W/cm}^2$, at which the temperature of the bath at the heat source would reach the lambda point, and the helium would cease to be superfluid. The smallest cross-sectional areas of the helium in the tank surrounding the cavity are at the cell equators (see Fig. 5.22.9). The diameter of the LHe vessel has been chosen such that the heat flux in these areas stays well below 1.5 W/cm^2 at the chosen operating parameters.

Figure 5.22.9: Heat flow in the LHe vessel and the chimney connecting the tank to the two phase line. The heat flow in the superfluid helium is below 0.5 W/cm^2 everywhere.

Figure 5.22.10: Overall accuracy of the cavity cup shape, measured with a coordinate-measuring machine. The deviation from the ideal shape is well below $200 \mu\text{m}$, being better than required by the BBU limit estimated above.

During initial cool-down, the LHe vessels of the cavities can be filled via a warm-up - cool-down pipe connected to the bottom of the LHe tanks. A chimney of sufficiently large diameter ($> 20 \text{ cm}^2$) connects each LHe tank to the two-phase He pipe in the cryomodules as shown in Fig. 5.22.9.

The cavity-helium tank structure is a mechanical structure with many eigenmodes driven by external vibration sources and pressure fluctuations the LHe bath. The mechanical design of this structure is optimized to avoid low-frequency mechanical resonances and resonances at multiples of the 60 Hz line frequency to minimize cavity microphonics. Measurements at the Cornell ERL injector cryomodule have shown that the dominating source of microphonics is due to fast fluctuations in the LHe pressure [13]. The stiffness of the cavity-helium tank structure is therefore designed to minimize the frequency shift of the cavity with changes in LHe pressure.

Inner magnetic shield

It has been shown that a DC residual magnetic flux present at the cavity will be trapped when the cavity is cooled through the transition temperature. This results in a residual resistance of about $0.35 \text{ n}\Omega$ per mG of trapped flux at 1.3 GHz [14]. The earth's field must be adequately shielded to achieve high Q_0 factors. The residual DC-magnetic field at the cavity locations needs to be much less than 30 mG to achieve residual resistances below $10 \text{ n}\Omega$ and intrinsic quality factors above 2×10^{10} at 1.8 K. In the ERL, this will be achieved by three layers of shielding of the Earth's magnetic field: an outer vacuum vessel made out of carbon-steel, an outer magnetic shield at room temperature lining the inside of the vacuum vessel, and an inner magnetic shield around the LHe vessels of the cavities. The inner shield will be made out of A4K, [15], which has a high permeability at cryogenic temperatures, and will be heat treated for operation at 2 K. The shielding design goal is $< 2 \text{ mG}$.

5.22.5 Cavity fabrication

The ERL main Linac cavities will be fabricated from high-purity ($\text{RRR} > 300$) bulk niobium. RRR 300 Niobium has become the standard in SRF cavity fabrication, with higher RRR values often produced by post-purifying the cavity at around 1400°C . This improves the thermal conductivity of the material, which in turn safeguards against quenches due to normal-conducting defects. An eddy-current scan or newer techniques based on SQUID scans of the delivered sheets will be used to detect such defects in the niobium before it is used for cavity

Table 5.22.4: Summarized target frequencies for all cavity production steps.

Production Step	Frequency (MHz)
Cavity designed shape in vacuum	1299.655
Cavity designed shape in air	1299.234
Cavity nominal desired freq as built	1298.985
Air, 20C, 150 μm BCP	1297.425
Vacuum, 20 C	1297.884
Vacuum, 2 K	1299.700
Vacuum, 2 K, tuned 300 kHz (stretched)	1300.000

Figure 5.22.11: RF measurement set-up to determine the dumbbell trimming. This individual trimming process ensures a proper compensation of the small shape variations, leading to an almost perfect cavity after all fabrication steps

production. The half cells for the cavities are deep-drawn and then electron-beam welded to fabricate the full 7-cell cavity. As shape variations play an important role in determining the BBU limit, a careful analysis of all pressed cups is essential. Our data on 7 prototyped cavity showed the maximum deviation being less than 200 μm . Figure 5.22.10 shows a typical measurement, taken with a coordinate-measuring machine (CMM).

After pressing the cups, two of them are welded at the iris to form dumbbells. These dumbbells have excessive length at the equator and trimmed individually to account weld shrinkage, chemical etching, and cooling to 1.8 K. Table 5.22.4 summarizes the different frequencies targeted during the production steps, ensuring that the cavity will have the correct frequency at its operating temperature. The trimming length for the dumbbells is determined by an RF measurement, shown in Fig. 5.22.11.

After trimming the dumbbells, the full cavity is welded together. The beam-tube sections are of extruded, low RRR-niobium tubes, with NbTi flanges (ratio 45/55 by weight) electron-beam welded to them.

The field flatness of a cavity fabricated in that manner is shown in Fig. 5.22.12. Even though the field flatness (as a result of the dumbbell trimming) is pretty good, the whole cavity is tuned to field flatness after the chemistry process again. The apparatus to do this is also shown in Fig. 5.22.12. The procedure described above is suitable for a large series production have been developed and transferred to industry before [16].

Figure 5.22.12: Left: This setup is used to tune each cavity to a flat field. It slightly pushes or pulls on the irises, while the field flatness is measured with a bead-pull. Right: Measured field flatness of a cavity as welded and after field flatness tuning, measured with a bead-pull set-up.

5.22.6 Cavity treatment

Numerous techniques for cavity surface preparation exist [17]. These include an initial degrease, chemical etching with BCP (HF, HNO₃ and H₃PO₄, usually in a ratio of 1:1:1 or 1:1:2) or electropolishing, followed by high-pressure water rinsing, and heat treatments at 600 to 1400° C for hydrogen degassing or post purification, respectively. These steps may have to be repeated several times. A final treatment often includes in-situ baking at around 120° C for 48 hours, which has been shown to improve the BCS losses and often removes the so-called “high-field Q -slope” that frequently limits the cavity performance [18].

It is desirable to simplify the treatment of the ERL main Linac cavities as much as possible while still meeting the performance specifications. Chemical etching with BCP has been shown to reliably yield accelerating gradients of 20 to 25 MV/m in multi-cell cavities [19]. Following fabrication of the cavity, a “damage layer” of 100 to 200 μm will be removed from the inner cavity surface in several steps by BCP to achieve good RF performance. This removal is taken into account in the cavity design. The acid is cooled below 15° C during the process to minimize hydrogen migration into the niobium. After high pressure rinsing with ultra-pure water and drying in a class 10 clean room, the cavities will be annealed at 800° C in an ultra-high-vacuum furnace to out-gas hydrogen and relieve mechanical stress built up during the cavity-fabrication process. This heating step is followed by tuning the individual cavity cells for field homogeneity of the accelerating mode and a second, light BCP ($\sim 10 \mu\text{m}$). In the final step the cavities will be high pressure rinsed again, evacuated and heated at 120° C for 48 hours to minimize the BCS surface resistance. The performance of the cavities will be verified in an RF vertical acceptance test in a superfluid helium bath cryostat.

Current research indicates that electropolishing might result in higher intrinsic quality factors at medium field gradients [20] and thereby compensate for the added cost and complexity of electropolishing. If future research confirms this, one or both of the BCP steps in the ERL cavity preparation might be replaced by electropolishing.

5.23 Tuner

The function of the tuner is to stretch or compress the SRF cavity along its beam axis to adjust the frequency of the accelerating π -mode at 1.3 GHz. This adjustment is needed to synchronize the resonant frequencies of all 384 cavities in the Linac to the master oscillator.

As part of the tuner-cavity mechanical system, the cavity’s cylindrical helium tank will incorporate a short bellows section to minimize the tank’s longitudinal mechanical stiffness, leaving only the stiffness of the niobium cavity cells for the tuner to act upon. The tuner is attached to the helium tank with attachment points that span the tank’s bellows. Thus nearly all of the tuner components must operate at the helium tank temperature of 1.8 K.

Two different operating regimes are required of the tuner. First, a slow time-scale response of the order 1 Hz with a coarse-cavity tuning range of $\sim 600 \text{ kHz}$ is needed to adjust the cavity frequency due to influences such as:

- contractions upon cooldown to 1.8 K
- variations in helium bath pressure

- manufacturing irregularities
- de-tuning a problematic cavity to minimize beam interaction.

Slow tuning is typically accomplished by a stepping motor with gearing and levers to provide the requisite force along the cavity axis. The slow portion of the tuner is utilized after cavity cooldown to adjust the frequency operating point, and exercised rarely thereafter until warmup. The cavity must be parked in a specific state of compression by the slow tuner prior to cooldown from 293 K to 1.8 K so that the differential thermal contraction between the tuner and the cavity does not plastically deform the cavity. The same requirement for the parked condition applies during warm-up.

The second tuning regime is a fast time-scale response of the order of 1 kHz with a fine cavity tuning range of ~ 1 kHz. The fast tuning is needed to adjust the cavity frequency due to influences such as:

- Lorentz force detuning during cavity field ramp up
- correction of microphonic perturbations of the cavity
- feedback control within the low-level RF system to adjust beam-transit phase,

Fast tuning is accomplished by sandwiching piezo-electric ceramic stacks between the slow tuning mechanical linkages and their cavity attachment locations. The actuated piezo force/displacement then adds in series to the slow-tuning mechanism to result in a superposition of the forces upon the cavity. The piezos must be rated for an adequate blocking force and elongation given a reasonable actuation voltage in the cryomodule vacuum insulation environment. The piezo actuation voltage should be less than 1000 V at maximum displacement for reliable wiring within the vacuum vessel. Listed in Tab. 5.23.1 are the performance parameters required for both the fast and slow components of the ERL Linac SRF cavity tuner.

5.23.1 Design of the main Linac cavity tuner

Several proven options are available for the cavity-tuner design. The choice for the baseline tuner was between adaptations of the Saclay I tuner [21–23] and the INFN-blade tuner [24], related to earlier work at DESY. Both designs have performed well in SRF cavity tests at various facilities and have experienced several generations of optimization, but both designs require modest modifications for the ERL Linac application. The Saclay I tuner was chosen for the ERL Linac due to the following features that are advantageous to CW, high Q_{ext} cavity operation:

- lower group delay in its tuning response, resulting in lower phase lag for microphonic compensation [25, 26]
- more compact, making integration of the magnetic shield simpler
- mechanically simpler, reducing manufacturing and assembly cost
- greater reliability statistics given its use in the FLASH facility

Table 5.23.1: ERL Linac cavity tuner performance specifications.

Parameter	Value
Cavity elongation tuning	350 Hz/ μ m
Cavity spring constant	4.63×10^6 N/m
Cavity force tuning	289 Hz/N
Cavity lowest mechanical resonance	91 Hz
Slow tuner response bandwidth	1 Hz
Slow tuner cavity frequency range	600 kHz
Slow tuner dimensional range	368 μ m
Fast tuner response bandwidth	1 kHz
Fast tuner cavity frequency range	1.5 kHz
Fast tuner dimensional range	0.9 μ m
Minimum piezo blocking force	2073 N
Maximum piezo voltage	1000 V
Minimum tuner spring constant	6×10^9 N/m
Minimum tuner mechanical resonance	1000 Hz
Tuner operating temperature	1.8 K

Figure 5.23.1: Illustration and photograph of the a Saclay I tuner.

Also, since the Saclay tuner will be used in the XFEL facility presently under construction, a foundation of production testing and industrial experience will be established.

An illustration and photograph of the Saclay I tuner is shown in Fig. 5.23.1. The modifications to the tuner in Figure Fig. 5.23.1 will be to increase the bore diameter to fit over a larger diameter beam tube of the 7-cell cavity and to select a piezo stack matched to the tuning forces of the cavity.

5.24 HOM load

The Higher Order Mode (HOM) loads in the cryomodule are intimately linked to the SRF cavity design and mitigation of the beam breakup instability (BBU) as described in §5.22.3. The average HOM power is expected to be 200 W per cavity. Most of the power will be in the frequency range 1-10 GHz, but the short ERL bunch length will allow HOM spectral content up to the 100 GHz range. The HOM damping scheme must then have strong coupling over this broad bandwidth and be able to dissipate the high average power. Among the options for an HOM damping configuration are:

- beamline loads where the RF absorber is a lining of the beampipe
- loop-coupled antenna located in side apertures on the beampipe that absorb HOM power at 2–5 K or transport RF in coax to remote loads

- waveguide loads coupled transversely to the beampipe that transport the RF to remote loads
- button-type pickups located in small apertures on the beampipe that transport RF in coax to remote loads.

The beamline loads are conceptually straightforward, where HOMs propagate as TE or TM modes in the circular beampipe and are heavily damped at the absorber. This provides broadband damping with only modest dependence on the RF absorber properties and no need for careful geometrical tuning of coupling structures. To avoid an undue load on the refrigeration plant from the expected 200 W of HOM power, the RF absorber is maintained at 100 K and thus necessitates thermal gradients along the beamline between cavities. The thermal gradient is defined by a 5 K intercept between the 1.8 K cavity and the 100 K HOM absorber, where selection of the 100 K temperature was a result of an optimization process to minimize the total cryogenic load of the full module as described in §5.28.12 below.

The challenge with beamline loads is that since the RF absorber resides on the beamline, only tens of centimeters from the SRF cavity, in addition to RF absorption it must also be: high vacuum compatible, have finite DC conductivity to drain static charge, be able to withstand significant radiation, have no particulate generation, and have the requisite thermo-mechanical properties to operate at cryogenic temperatures as configured in an HOM- load assembly. Such beamline loads have performed well at room temperature as part of the CESR-B [27] and KEK-B [28] cryomodules for over a decade. A cryogenic version of a beamline load was installed in the ERL injector prototype cryomodule [29] and valuable insight was gained from the cold tests and beam operation. In the HOM prototypes, it was discovered that all three types of RF absorbing materials have their DC conductivity drop at cryogenic temperatures, and can thus accumulate considerable static charge and deflect low energy beams [30]. Also, thermal expansion differences between the RF absorbers and their heat sinks can result in long-term fatigue than can eventually cause solder bonds to delaminate. This insight has guided development of a next-generation beamline load that resolves these issues as described in §5.24.1 below. A cryogenic version of a beamline load has also been developed for the XFEL cryomodule [31] and has been shown to perform well in that application, although its power limit of about 100 W may not be sufficient for the ERL Linac.

Loop-coupled HOM loads are prevalent on several SRF cavity designs, such as XFEL, ILC, and SNS [32, 33]. In these pulsed-beam applications, the average absorbed HOM power is only a few watts. Much larger powers were absorbed in the HERA electron ring with 50 mA beam current. There have nevertheless been challenges revealed with loop couplers in operating machines, such as with antenna overheating, multipactor, and mis-tuning due to fabrication variations [34] [35]. The button-type HOM couplers are still at the conceptual and modeling stage of their development, and it is expected that they will face bandwidth, power, and tuning challenges analogous to those of the loop couplers. A challenge with the modeling and analysis of loop and button-HOM damping is that they have non-axisymmetric geometries and require 3D-simulation tools. The meshing and computational demands then become time consuming and can restrict the number of modes and accuracy of the analysis, raising the concern that a BBU susceptible HOM could be missed, especially with component fabrication variations [36].

Waveguide-HOM couplers have been successfully used at JLAB for many years at lower powers, typically around 10 W [37].

Figure 5.24.1: CAD model cross section of the ERL main Linac beamline HOM load.

Figure 5.24.2: Measured RF and DC electrical properties of a carbon-loaded RF absorbing ceramic.

The use of waveguide-HOM coupling is the subject of ongoing investigations [3], and while they could have the benefit of transporting the HOM power to external room-temperature loads, it is still to be determined if they will have the requisite damping bandwidth, and how the full structural complexity will compare to that of beamline loads.

Beamline-HOM loads have been chosen for the baseline Cornell ERL main Linac design to best accomplish the damping requirements that are critical to mitigating BBU. Details of their design are presented in the following sections.

5.24.1 ERL main linac HOM load

A CAD model of the ERL main Linac beamline HOM load is shown in Fig. 5.24.1. The load has an RF absorber as a unitary cylinder brazed into a tungsten-heat sink, stainless-steel bellows for flexibility of flange alignment and cavity length variations. There will be 5 K intercepts at the transition between the bellow and the end-group section, the later will be copper plated to avoid excessive RF heating. The HOM load will be mounted to the Helium Gas Return Pipe (HGRP) as well.

RF-absorbing materials that have the requisite properties are in advanced development and full scale samples are in hand. They are based on SiC or AlN with embed carbon nanotubes or graphite. A key is to have a sufficient fractional loading of carbon so as to exceed the percolation threshold in the material and establish a DC conductivity that is nearly independent of temperature. This will also provide a satisfactory broadband dielectric loss tangent of $\delta = 0.2 - 0.6$. Plots of measured RF and DC electrical properties of a carbon-loaded RF absorbing ceramic are shown in Fig. 5.24.2. This material appears to satisfy all of the electrical and particulate requirements of a beamline HOM load absorber [38]. First in situ tests show adequate RF absorption, while the DC conductivity may slightly differ from batch to batch.

For the HTC program, two prototype HOM absorbers have been fabricated (see Fig. 5.24.3 showing the HOM absorber installed under the HGRP and connected to the cavity). Based on this prototype experience some optimization is currently underway. This is mainly dedicated to get reliable batch to batch material properties and to accommodate for the rather low CTE of the material. As a cost saving measure, the material can be shrink-fitted to Titanium which we successfully proved on a sample cylinder.

Figure 5.24.3: HOM absorber installed under the HGRP within the HTC cold mass

5.25 Input coupler

The fundamental RF-input coupler has two main functions: i) efficient transfer of power from an RF power source to the accelerating mode of a beam-loaded RF cavity, i.e., a passive impedance matching network, and ii) providing an RF-transparent barrier between a gas-filled transmission line, coaxial or waveguide, and the ultra-high vacuum of the beamline RF cavity, which necessitates the use of at least one ceramic RF window.

Several CW and pulsed RF-power couplers have been developed at different laboratories around the world for superconducting cavities, both rectangular waveguide and coaxial configurations [39]. Since the ERL superconducting Linac cryomodule is based on TTF technology, early on in the project we decided [40] to use coaxial couplers derived from the TTF-III design [41, 42]. This input coupler has the following important features:

- Low static heat leak
- Two ceramic windows - one warm and one cold - allowing sealing of the SRF cavity input coupler port during an early assembly stage in a clean room, thus reducing the risk of cavity contamination
- Coupling to the cavity adjustable over one order of magnitude by varying the axial position of the inner-conductor antenna
- Bellows accommodating lateral movement of the cavity in a cryomodule by up to 15 mm during cool-down from room temperature to 2 K

The TTF-III coupler was designed for a pulsed superconducting Linac application. Hence not all of the features of the TTF-III design are relevant for the ERL main Linac, which operates CW with 2/5 kW CW average/peak power. Further, there are features specific to CW operation that must be added to the TTF-III design. A wealth of experience in designing, fabricating, testing, and successfully commissioning CW RF couplers has been gained for the prototype-ERL injector, described in §4.6. Here we describe a conceptual design for the ERL main Linac RF coupler.

5.25.1 ERL main Linac coupler design

The input couplers for Cornell Energy Recovery Linac must deliver up to 5 kW CW RF power to the main Linac cavities, though under nominal conditions they will operate with 2 kW average and 5 kW peak power. The 5 kW peak power is required for transient modulation to compensate for cavity detuning due to microphonic perturbations. Due to the principles of energy recovery in a superconducting cavity, the couplers will operate under conditions with full reflection for the great majority of the time and thus require active cooling of the inner conductor as in the ERL injector input couplers. To make the design more economical, the couplers will provide fixed coupling to the cavities with $Q_{\text{ext}} = 2 \times 10^7$. Coupling adjustability can be achieved using three-stub tuners in the feed-transmission line to have a range of $2 \times 10^7 - 1 \times 10^8$, with the nominal operational $Q_{\text{ext}} = 6.5 \times 10^7$.

The design of the ERL main Linac coupler takes into account experience gained from the ERL injector couplers [43]. The proposed main Linac coupler is shown in Fig. 5.25.1 and

Figure 5.25.1: CAD model of the fully assembled ERL Linac input coupler.

Figure 5.25.2: Section view of the ERL Linac input coupler.

Fig. 5.25.2 [44]. This design utilizes a rectangular-waveguide-feed transmission line, though it is possible that a coaxial-feed line could be implemented to reduce space if it is compatible with the design of the full RF-power delivery system. As with the TTF-III and ERL-injector couplers, the ERL main Linac coupler consists of three sub-assemblies: the cold and warm coaxial sub-assemblies, and the waveguide. The two coaxial portions of the coupler and their ceramic windows are the same size as those in the TTF-III coupler. The cold portion of the coupler with the protruding antenna attaches to the SRF-cavity coupler-port flange, which will be at a temperature slightly above 2 K. A copper thermal intercept held at 5 K is located on the coupler outer conductor a few cm from the cavity flange to minimize the heat load to the 1.8 K-cavity helium vessel. An 8" ConFlat flange then joins the cold coupler to the warm coupler. The warm coupler has two bellows sections on both the inner and outer conductors for flexible compliance, as will be described in the next paragraph. The warm coupler has a copper thermal intercept held at 100 K located on the outer conductor a few cm from the vacuum vessel flange to minimize the heat load to the 5 K system. The vacuum vessel flange resides at 293 K, beyond which is a vacuum pumping port on the outer conductor for the warm portion of the coupler, an instrumentation port, and then the coax-rectangular waveguide transition. All coaxial components, with the exception of the inner-conductor antenna portion and the thermal intercepts, are made of stainless steel with copper plating on surfaces carrying RF currents.

Similar to the TTF-III couplers, the ERL Linac couplers must accommodate lateral movement of the cavities during cool-down of up to 10 mm, since one end of the coupler is attached to the moving cavity and the other end is attached to the fixed vacuum vessel port. For the TTF-III couplers, bellows on the inner and outer conductors of the warm assembly and on the outer conductor of the cold assembly provide some flexibility. This arrangement, however, causes the antenna to skew. If the lateral movement is large enough, the antenna can touch the outer conductor of the cavity coupler port. Besides shorting the coax coupler, the scratching of the surfaces will generate copious particulate and significantly degrade the SRF-cavity performance. For the ERL Linac coupler, this problem is overcome by placing two sets of bellows only on the warm portion of the coupler, on both the inner conductor and on the outer conductor, as shown in Fig. 5.25.3. In this way, high flexibility is achieved while keeping the cold antenna fixed relative to the cavity coupler port.

The static and dynamic heat loads of the ERL main Linac input coupler are listed in Tab. 5.25.1. The elimination of a thin-walled bellows on the cold sub-assembly to maintain a fixed antenna alignment slightly increases the static heat load to the 5K thermal intercept.

Figure 5.25.3: The ERL Linac input coupler is mechanically flexible, yet maintains alignment of the cavity antenna.

Table 5.25.1: Heat loads of the ERL main Linac input coupler.

	Static Heat Load	Dynamic Load at 2 kW CW
2 K	0.03 W	0.15 W
5 K	1.55 W	1.94 W
80 K	2.26 W	9.33 W

Figure 5.26.1: Isometric view of the quadrupole lens cold mass (at the left) and the set of four coils without the iron (at the right).

However, this contribution to the total refrigeration load of a Linac cryomodule is a small percentage, as summarized in §5.28.12.

The ERL main Linac input coupler has been modeled for multipactor susceptibility using the code Mutipac2.1 [45]. The results showed no evidence of mutipacting in the ERL RF coupler.

5.26 Superconducting quadrupole and dipoles

Each Linac cryomodule contains one quadrupole with adjacent horizontal and vertical steering coils.

5.26.1 Quadrupole design

A iron yoke magnet design has been selected for the quadrupole since the relatively low gradient can be realized with a conventional iron-based design using superconducting coils, allowing the quadrupole to utilize the 1.8 K liquid helium available in the cryomodule. A CAD model of the yoke and coils is shown in Fig. 5.26.1, with the coils also shown separately for clarity. The pole pieces have a hyperbolic shape with a 70 mm bore and the coils lie flat except at the ends. The coils for this type of lens are single layered and can be manufactured with minimal effort [46]. Numerical simulations of the quadrupole were performed with MERMAID and take into account the real properties of the yoke material (Steel 1010). A detailed parameter list of the quadrupole is given in Tab. 5.26.1. A CAD model of the full quadrupole and dipole package is shown in Fig. 5.26.2. The length of the assembly is ~ 350 mm.

The stray magnetic field from the magnet package must be carefully minimized inside of the cryomodule to maintain a high SRF cavity Q_0 . The typical background magnetic field inside of the module vacuum vessel will be about 25 mG, and additional shielding intimate to the SRF cavity will reduce this to < 2 mG at the cavity walls. The amplitude of the unshielded quadrupole magnetic field along the beamline at a 1 cm radius is shown in Fig. 5.26.3. The

Figure 5.26.2: The superconducting quadrupole and dipole lenses in their helium vessel with the HTS leads.

Table 5.26.1: Parameters of the ERL main Linac superconducting quadrupole magnet.

Winding type	Flat coils
Iron yoke inner diameter	70 mm
Iron yoke outer diameter	107 mm
Maximal current	110 A
Maximal gradient	19.4 T/m
Linac module current range	0.75 – 49 A
Linac module gradient range	0.13 – 8.6 T/m
Magnetic length	125.6 mm
Number of turns	86/pole
Wire diameter (bare/insulated)	0.33/0.41 mm
Copper to superconductor ratio	2:1.66
RRR	> 100
Filament diameter	20 μ m
Twist pitch	25.4 mm
Iron yoke length	100 mm
Coil length	137 mm
Stored magnetic energy at max current 100 A	45 J
Self inductance	0.009 H
Integrated gradient at current 100 A	2.21 T
Integrated b ₆ /b ₂ at current 100 A, at 30 mm	1.8×10^{-3}
Integrated b ₁₀ /b ₂ at current 100 A, at 30 mm	2.7×10^{-3}
Coil peak field	0.76 T
Gradient at 2.5 A	0.00437 T/m
Saturation at nominal current 100 A (integrated)	0.17%

Figure 5.26.3: Unshielded quadrupole field dependence along the beamline at a 1 cm radius. The iron yoke ends at 5 cm.

field drops off rapidly, where at a distance of 15 cm from the edge of the yoke it is $< 3.7 \times 10^{-5}$ of its value at the center of the quadrupole, corresponding to a maximum unshielded stray field of ~ 65 mG. Cryogenic magnetic shielding will also be wrapped around the magnet package to ensure that the stray field is negligible.

5.26.2 Dipole design

For the dipole corrector, a single-layer coil is chosen similar to that for the quadrupole. However, the dipole coil is placed inside of the iron yoke as this gives minimal stray fields outside of the corrector, as seen in Fig. 5.26.4 and Fig. 5.26.5. Again, numerical simulations of the dipole were performed with MERMAID and take into account the real properties of the yoke material (Steel 1010). A detailed parameter list of the dipole is given in Tab. 5.26.2. The stray magnetic field from the dipole does not decay as rapidly as for the quadrupole field, as seen

Figure 5.26.4: The dipole corrector superconducting coils and iron yoke.

Figure 5.26.5: Unshielded dipole field dependence along the beam axis. The iron yoke ends at 10 cm.

in Fig. 5.26.5. The stray dipole field is still quite low, however, and the dipole will be located downstream of the quadrupole, away from the SRF cavity closest to the magnet package, so that it is adjacent to the gate valves, as shown in Fig. ??.

5.26.3 Installation in the cryomodule

The magnet package body will reside at the 1.8 K temperature of the helium vessel. The four HTS current leads coming out of the assembly will have a 5 K heat sink and then a 100 K heat sink at the module thermal shield. The four leads will be wired as:

1. Quadrupole supply
2. X-dipole supply
3. Y-dipole supply
4. Common return

The typical heat leak for a 200 A, 150 mm long HTS lead between 77 K to 4.2 K is 20 mW. So the total heat leak to 1.8 K could reach 0.08 – 0.1 W/package. The HTS leads will also be wrapped by magnetic shielding to reduce their stray-magnetic fields. From this analysis, the heat load of the entire magnet system is negligible compared to the dynamic load of the cavities.

5.27 Cryomodule beam position monitor

A beam position monitor (BPM) will be included in every main Linac cryomodule and will be located adjacent to the magnet package. The BPM will be held at a temperature of about 5 K. Under consideration are both a button-style BPM similar to that developed for the XFEL at DESY [47] and a compact design as used in CESR-TA. Both types are shown in Fig. ??.

5.28 Cryomodule

The ERL Linac cryomodule design is based on TTF-III technology with modifications for CW operation. In this technology scheme, the cryomodule units that are about 10 m long are connected by bellows with no intervening warm breaks, and all connected units share a common insulation vacuum. The cryogen transfer lines are internal to the module vacuum vessel and are connected between units in situ by welding together flexible joints. The beamline is also connected in situ between units under a portable clean room.

Table 5.26.2: Parameters of the ERL main Linac superconducting dipole magnets.

Winding type	Flat coil
Yoke aperture square side	70 mm
Yoke outer diameter	107 mm
Maximal current	22 A
Maximal field	0.071 T
Typical current	11 A
Typical field	0.03 T
Magnetic length	138 mm
Number of turns	88
Wire diameter (bare/insulated)	0.33/0.41 mm
Copper to superconductor ratio	2:1.66
RRR	> 100
Filament diameter	20 μ m
Twist pitch	25.4 mm
Iron yoke length	100 mm
Coil length	170 mm
Stored magnetic energy at nominal current 20 A	1.4 J
Self inductance	0.007 H
Integrated b1 at nominal current 20 A	0.935 Tcm
Integrated b3/b1 at nominal current 20 A, at 30 mm	3.2×10^{-3}
Integrated b5/b1 at nominal current 20 A, at 30 mm	1.7×10^{-3}
Coil peak field	0.6 T
Saturation at nominal current 20 A (integrated)	0.1 %

The ERL Linac cryomodule (shown in Fig. ??) is based on the TTF-III module structure. All of the cavity-helium vessels are pumped to 1.8 K (16 mbar) through a common 30 cm inside diameter Gas Return Pipe (HGRP), which also serves as the mechanical support from which the beamline components are suspended. To minimize the heat load to the refrigeration plant, all of the 1.8 K cryomodule components are surrounded by 5 K intercepts to minimize the heat leak to 1.8 K, and the 5 K intercepts are likewise surrounded by 100 K intercepts, which absorb the heat load from the 293 K vacuum vessel. The HGRP is suspended from composite support posts that are constructed from low-thermal conductivity G-10 fiberglass. The composite posts have integral metal stiffening disks and rings that also serve as thermal intercepts at 5 K and 100 K between the 1.8 K face that attaches to the HGRP and the 293 K face that attaches to the vacuum vessel bosses that support the cold mass. There are stainless steel manifolds of smaller diameter than the HGRP running the length of the modules that transport the supply of liquid helium and the supply and return of 5 K and 100 K helium gas for the thermal intercepts. Jumper tubes with 5 mm inner diameter are connected between the 5 K and 100 K supply and return manifolds to the various thermal intercepts within a module. A shell of 6 mm thick, grade 1100 aluminum sheet surrounds the beamline and the HGRP and is linked to the 100 K manifold to serve as a thermal radiation shield between the 293 K vacuum vessel and the cold mass. The aluminum 100 K shield has apertures through which

the RF couplers pass and also has panels with instrumentation feedthroughs. The 100 K shield is mechanically suspended from one of the integral metal stiffeners in the composite support posts. Multi-layer insulation is wrapped around the exterior of the 100 K shield as well as all of the 1.8 K and 5 K cold mass components.

As the full ERL main Linac is assembled in the tunnel, cryomodule units are brought into place, the beamlines are aligned, and a flexible joint connected under a portable clean room then mates the beamline module-to-module. The cryogenic manifolds are welded together with short bellows sections as well as the HGRP. A short section of 100 K shield is inserted between modules to maintain its continuity and a flexible sleeve adapter then joins the adjacent vacuum vessels.

The magnetic shielding in the cryomodule must keep the field in the region of the cavities to < 2 mG to have negligible residual wall loss and provide a good safety margin for the goal of cavity $Q_0 = 2 \times 10^{10}$. Such a low field is accomplished by de-gaussing the carbon steel vacuum vessel, lining it with co-netic mu-metal shielding that will be at 293 K, and then wrapping each cavity's 1.8 K helium vessel with a magnetic shield that is formulated to have maximal shielding at low temperatures around 4 K [48].

5.28.1 ERL Linac modifications to TTF-III technology

The CW, high current operation of the ERL Linac necessitates several changes to standard TTF technology which has evolved for low-duty factor operation. Additional changes unrelated to CW operation have been implemented here as a result of experience gained from fabrication and operation of TTF modules. Most of these changes were also implemented in the ERL injector prototype cryomodule, as described in §4.6, and have proven to be successful [49]. Briefly, the main differences between the ERL Linac cryomodule and the TTF-III module are:

- Implement beamline HOM loads for strong broadband damping of HOMs generated by the high current and short bunches.
- Use a high average power coax RF input coupler per cavity, with lateral flexibility for cool down and fixed coupling. Detailed modeling and appropriate cooling for the prototype ERL injector have shown that overheating can be avoided.
- Do not include a 5 K shield
- Increase the diameter of the cavity helium vessel port to 10 cm for the high CW heat load
- Include a JT valve in each cryomodule for the high CW heat load.
- Increase the diameter of the 2-phase 2K He pipe to 10 cm for the high CW gas load.
- Use precision fixed surfaces between the beamline components and the HGRP for easy “self” alignment of the beamline
- Use rails mounted on the inside of the vacuum vessel and rollers on the composite support posts to insert the cold mass into the vacuum vessel, as opposed to the “Big Bertha” handler

- Cooling of thermal intercepts is provided by small “jumper” tubes with flowing He gas, such as to the HOM loads and the RF couplers, as opposed to copper straps
- Locate access ports in the vacuum vessel to allow the tuner stepper motor to be accessible for replacement while the string is in cryomodule

5.28.2 Cryomodule beamline components and lengths

The ERL Linac cryomodule length is chosen as a balance between beam optics considerations and keeping the unit physically manageable. The maximum module length for transport on a standard flat-bed truck is about 16 m or 52 ft. To maximize the Linac’s active acceleration fill factor, it is desirable to place quadrupoles as sparsely as possible. Beam optics simulations show that the maximum quadrupole spacing is about one doublet every twelve 7-cell cavities. This would give a cryomodule length of about 19 m, which is too long. The fill factor can be maintained while shortening the module length by having six cavities with one quadrupole and one set of horizontal and vertical corrector coils per module. Thus the quadrupole doublet is accomplished in every two modules with a manageable module length of 9.82 m or 32.2 ft. Listed in Tab. 5.28.1 are the ERL main Linac cryomodule beamline components, their individual lengths, and the total length of the module.

5.28.3 Cryomodule components and assembly

Cryomodule assembly starts with the beamline and proceeds as a layered growth out to the vacuum vessel and warm coupler attachment. The specific choices for the configuration of many of the components also impacts the configuration of other components. For example, the choice between using a blade tuner vs. a Saclay tuner dictates the type of bellows and support flanges on the cavity helium vessel, as well as the permalloy magnetic shield around the helium vessel. Similarly, the choice of the required power rating of the coupler significantly alters not only the complexity of the coupler, but also the details of the vacuum vessel coupler ports, such as their dimensional and alignment error tolerance, which is a cost driver. Described in the following is the assembly sequence of the baseline choices for the principle cryomodule components, along with descriptions of the components not discussed in previous sections.

5.28.4 Beamline string assembly

The beamline consisting of the cavities, HOM loads, cold couplers, quadrupole, steering coils, beam position monitor, tapers, and gate valves (Tab. 5.28.1) is assembled in a class 100 or better clean room. All components are flushed with filtered water or alcohol and individually receive a mild vacuum bake at 120° C for 24 hours. The components are mounted on an assembly fixture one by one in the clean room. Each added component is aligned to the other components with the only critical alignment being the azimuthal position about the beam axis. This azimuthal alignment is needed so that the flat precision mounting surface at their tops will mate to the planar-precision surfaces on the HGRP. This alignment can be accomplished with a simple accurate spirit level. Any longitudinal spacing or planar shift errors of the mounting surfaces is accommodated by the flex in the HOM load bellows. The component mating vacuum flanges are then bolted together. A photograph of the assembled ERL injector

Figure 5.28.1: Cryogenic and RF rated pneumatic gate valves for the beamline.

Figure 5.28.2: Cryogenic-rated pneumatic gate valve installed in the ERL Injector vacuum vessel.

prototype beamline string in the clean room is shown in Fig. 4.6.12. After all components are attached, the string is vacuum leak tested while still in the clean room so that only filtered particulate-free air will pass through any potential leak. The pumping and purging during the leak test is performed at a slow rate of 1-2 Torr/minute through the viscous flow range of 760 Torr to 1 Torr to minimize propagation of any particulate contamination throughout the beamline.

A beamline component not described in previous sections is the gate valve. To maintain the cleanliness of the beamline, the gate valves at each end of the string must be closed after the vacuum-leak test in the cleanroom and rarely opened again until the cryomodule is installed in its final tunnel location. A cryogenic-rated gate valve is available from VAT, which also has an “RF aperture” to provide RF shielding in the open position for accelerator beamline service. A photograph of this valve is shown in Fig. 5.28.1. This valve was also designed to have a demountable pneumatic actuator that includes a vacuum vessel flange. With this feature, the cold mass can be inserted into the vacuum vessel without the actuator, then have the actuator attached through a vacuum vessel port with the controls and pneumatic connections available exterior to the vacuum vessel. The Linac interlock control system can then seal off any cryomodule in the event of a vacuum trip. A photograph of the valve installed in the ERL-injector prototype vacuum vessel is shown in Fig. 5.28.2. The addition of a pneumatic actuator differs from the gate valves used in TTF modules where the valve is only manually operated, is inaccessible from the vacuum vessel exterior, and is opened just prior to sealing the vacuum vessel joint between modules with no possible automated interlock closure.

5.28.5 Cold mass assembly fixture and HGRP attachment

As a parallel operation to the beamline string assembly in a clean room, the cold mass assembly fixture can be set up in a high-bay area with overhead crane access. The composite support posts are attached to the HGRP and the HGRP is hung from the assembly fixture by the composite posts. The 2-phase pipe is then mounted aside the HGRP using G-10 standoffs and its exhaust is welded into the HGRP. A photograph of the ERL Injector HGRP hung from the cold mass assembly fixture by the composite posts is shown in Fig. 5.28.3.

The choice of the number of composite posts supporting the HGRP and the HGRP wall thickness were determined by analyses of the static deformation of the titanium HGRP due to the estimated 4082 kg (9000 lb) weight of the cold mass and by the desire to lessen the relative motion of beamline components due to thermal contraction. The result was a decision

Figure 5.28.3: HGRP and 2-phase pipe hung from the cold mass assembly fixture by the composite posts for the ERL Injector.

Figure 5.28.4: Beamline string hung from the HGRP for the ERL Injector.

Figure 5.28.5: The tuner pre-bias operation for the ERL Injector.

to employ four posts per cryomodule with two sections to the HGRP. A schedule 80 pipe section was selected for the HGRP. With these choices the resulting static deflection is computed to be 0.07 mm with peak stress of 17 MPa providing a large safety factor compared to the 275 MPa yield published for Grade 2 Ti.

5.28.6 Beamline string attachment to HGRP

After the beamline string passes the vacuum leak test, it is removed from the clean room and positioned underneath the cold mass assembly fixture. The string is raised and the precision mounting surfaces on the string and the HGRP are brought together with integral alignment pins and keys being engaged. The mating surfaces are then bolted together. String attachment to the HGRP in this manner proved to be quick and easy for the ERL injector, the entire procedure taking about 1 hour. Shown in Fig. 5.28.4 is the injector beamline hung from the HGRP.

5.28.7 Cavity magnetic shielding and tuner

After the beamline is hung from the HGRP, the helium tanks of the cavities are wrapped with magnetic shielding. This shielding will reside at 1.8 K. Consequently, this magnetic shielding layer is fabricated from A4K [48], which retains its shielding properties at cryogenic temperatures.

The cavity tuners are attached after the magnetic shielding. The stepping motors of the tuners have to be wrapped in a copper sleeve that is tied to 5 K line to prevent the motor heat from propagating to the helium vessel. The stepping motors are also wrapped with A4K shielding since they can have stray fields of a few hundred milliGauss in close proximity to access apertures in the cavity shield. Part of the tuner attachment process is pre-bias of the tuner force on the cavity. This bias is required to compensate for stresses developed during cooldown due to CTE differences between the cavity materials and the tuner materials. Without the pre-bias force, it is possible that the cavity could plastically deform, the piezos could crack, or the piezos could become loose, depending on the specific configuration of the tuner. A good measure of the bias force is the frequency of the cavity at room temperature. The tuner is initially attached with the cavity in its relaxed position. Then Belleville washers in the piezo support mechanism are compressed with adjustment nuts until the cavity is at its target biased warm frequency. Note that the beamline cold couplers have protective caps placed on them in the clean room, and the caps include a spring-loaded RF contact from the coupler center conductor to an SMA header on the cap. This allows the cavity frequency to be monitored during the tuner bias operation. A photograph of the tuner bias operation for the ERL injector is shown in Fig. 5.28.5.

5.28.8 Liquid He, 5 K gas manifolds and thermal intercepts

Several cryogen manifolds run the length of the cryomodule and are welded to those of the next module during module installation in the Linac tunnel. These manifolds include a liquid helium supply to the JT valve required per module, a liquid helium supply to the “warm-up/cool-down” ports located at the bottoms of the helium vessels needed for convective flow, the supply and return of 5 K helium gas, and the supply and return of 100 K helium gas. A JT valve is required per module due to the high cavity heat load and helium mass flow for CW operation.

The liquid helium and 5 K gas manifolds are mounted close to the HGRP using G-10 standoffs, thus keeping similar temperatures in close proximity to each other with low thermal conductivity connections between them. These manifolds are the next components mounted on the cold mass. Jumper tubes from the liquid helium manifolds are then routed to the JT valve and the helium vessel fill ports. The 5 K gas supply and return manifolds must then be routed to thermal intercepts on the HOM loads and RF couplers by way of jumper tubes having 3-5 mm ID. In standard TTF technology, the connections between the manifolds and thermal intercepts are accomplished by copper straps. For the ERL Linac, both the 5 K and 100 K heat loads are large enough to require gas flow from the manifolds to the intercepts through jumper tubes. If high RRR copper or aluminum straps were used as heat sinks, the cross-sectional area would be tens of cm^2 and consume too much space, as well as not being sufficiently flexible. Flexible straps made of “tough pitch” copper attached between the 5 K manifold and the composite support post 5 K rings provide sufficient thermal conductance for this intercept.

5.28.9 100 K manifolds and thermal shield

The 100 K manifolds are mounted farther outboard of the 5 K manifolds, one of which is integral to the 100 K shield. The material of the 100 K thermal radiation shield is grade 1100 aluminum, chosen for its high thermal conductivity and light weight. The shield is fabricated from standard flat panels that are cut and formed to shape. The top portion of the shield is attached to the 100 K ring of the composite support post and is $\frac{1}{4}$ ” thick to support the weight of the cryogen manifolds and the lower portion of the shield, as shown in Fig. 5.28.6, at this stage of cold-mass assembly. A thermal model of the 100 K shield with an integral 100K manifold with heat loads from radiation, the composite post, and feedthroughs shows that the shield resides at less than 2 K above the manifold gas temperature [50].

Table 5.28.1: ERL main Linac cryomodule beamline components, their individual lengths, and the total length of the module.

	Component	Length (m)	Length (in)
	Gate valve	0.0750	2.953
	Taper	0.0500	1.9
Repeat 3 times	Large Cu beam tube	0.0794	3.125
	Large beam tube HOM absorber	0.0600	2.362
	Large Cu beam tube	0.0794	3.125
	Large Nb beam tube	0.1864	7.338
	Large beam tube transition	0.0307	1.211
	Cavity active #1	0.8059	31.729
	Small Nb beam tube	0.1495	5.885
	Small Cu beam tube	0.0794	3.125
	Small beam tube HOM absorber	0.0600	2.362
	Small Cu beam tube	0.0794	3.125
	Small Nb beam tube	0.1495	5.885
	Cavity active #2	0.8059	31.729
	Large beam tube transition	0.0307	1.211
	Large Nb beam tube	0.1864	7.338
	Large Cu beam tube	0.0794	3.125
	Large beam tube HOM absorber	0.0600	2.362
	Large Cu beam tube	0.0794	3.125
	Taper	0.0500	1.969
	BPM	0.0750	17.717
	Steering Coils	0.1500	5.906
	Quadrupole	0.4500	2.953
	Gate valve	0.0750	2.953
	Intermodule flex	0.3297	12.981
	Module Length	9.8213	386.667 (= 32.22 ft)

Figure 5.28.6: CAD model of the top portion of the 100K shield attached to the cold mass.

Figure 5.28.7: Photograph of the completed ERL Injector 100 K shield being wrapped with MLI.

After the cryogen manifolds and intercept jumpers are connected to the cold mass, low-thermal conductivity coax cable is routed from the cavity RF field probes, as well as the cabling from temperature sensors, helium level sticks, and other instrumentation. The lower half of the 100K shield is attached and the instrumentation cabling is thermally anchored to an instrumentation feed-through panel in the shield. The 100K shield is then wrapped with 30 layers of Multi Layer Insulation (MLI) and the cold mass is ready for insertion into the vacuum vessel. A photograph of the completed ERL injector 100K shield being wrapped with MLI is shown in Fig. 5.28.7.

5.28.10 Vacuum vessel and magnetic shield

The vacuum vessel must support the weight of the cold mass, withstand the atmospheric pressure differential, have ports for RF couplers and instrumentation, ports for gate valve actuators, mounts for support in the Linac tunnel, lifting points for transport, and end flanges to accommodate the bellows sleeve that link the cryomodules. The locations of the ports on the vacuum vessel are dictated by the cold-mass components. The vacuum vessel supports have some freedom of location, though vessel deformation under loading must not exceed acceptable limits. The maximum deformation of the top ports that bear the load of the cold mass by way of the composite posts was modeled and found to be 0.13 mm.

The majority of the material of the vacuum vessel will be carbon steel, with the vacuum flanges that will have o-ring seals made of stainless steel to ensure that there will be no oxidation of the seal surfaces. The interior of the vacuum vessel will be burnished and painted with low vapor pressure vacuum compatible polyurethane paint. The exterior will likewise be burnished and painted with a marine paint.

Since carbon steel is a magnetic material, the vessel will be de-gaussed and care taken to not re-magnetize the vessel. Bench tests of carbon steel tubes show that local magnetization of the tube by permanent magnets can result in remnant magnetic fields in the interior of a few Gauss. The steel can be easily de-magnetized by intimate coils carrying 5300 Amp-turns, such that the remnant magnetic fields in the interior are reduced to about 250 mG. Further lining the interior of the vessel with Co-Netic mu-metal shielding then reduces the remnant magnetic fields in the interior to about 5 mG. However, the interior field could rise to the 25 mG level if the steel vessel is re-magnetized with permanent magnets. At the SRF cavity, these background magnetic fields are further attenuated by the cryogenic A4K magnetic shield [48] that will surround each SRF cavity. The cavity shield will reduce the magnetic field at the cavity to levels of < 2 mG, which then contributes negligible residual resistance to the SRF cavity surface.

The bellows section that mates adjacent cryomodule vacuum vessels will differ from the TTF-III bellows section since the ERL Linac will utilize at least one pneumatic gate valve per

module. The pneumatic gate valves will allow any module to be isolated upon an interlock trip, and the pneumatic actuator will be connected through a port on the bellows section.

5.28.11 Cryomodule and cavity alignment

The prototype ERL injector cryomodule serves as the basis for the design of the cryomodule and cavity alignment system for the main Linac elements. Perhaps the most challenging element of the assembly procedure is the alignment of the quadrupole magnets to the needed tolerance ($< 500 \mu\text{m}$) lateral displacement with respect to the beam axis). Reference of the magnetic center of the quadrupoles to a reference point on the outside of the cryomodule when the magnet is cold will be essential for the successful operation of the ERL. The reproducibility of this translation will be one of the components of the study of the prototype Linac cryomodule. It will determine whether or not externally adjustable mounts for the quadrupoles will be required to be able to use beam based alignment techniques to align the quadrupoles to the required tolerance. The tolerances for the location of the accelerating cavities in the cryomodules are given in Tab. ??.

The assembly of the cryomodules will be carried out in clean rooms using fixtures and techniques very similar to the ones used for the assembly of the ERL injector cryomodule and the FLASH cryomodules and planned for the XFEL cryomodules. The finished ERL cryomodules will be transported in the tunnel in a manner similar to the transport of the LHC cryomodules with a tape or wire guided vehicle to their location and then translated onto their supports. A guided vehicle sized for the tunnel and beam line height can have a vertical lift capability of up to 25 cm with lateral push and pull sufficient to place and remove the cryomodules.

The interconnection and leak testing of the connected cryomodules will be carried out in a manner very similar to that used for the FLASH cryomodules and planned for the XFEL. Connection of the cryomodules to the cryogen supply lines and the warm transitions needed to connect to other accelerator components will also be modeled after the ones planned for the XFEL.

5.28.12 Linac cryomodule heat loads

Having determined that the optimum cavity-operating temperature is 1.8 K, the optimal intermediate temperatures and corresponding heat loads are next to be determined. An important consideration arising from the configuration of the cavities is that the cavity beamtubes protruding from the cavity helium vessel must be superconducting. Considering the convenience of using helium gas just above boiling temperature, we choose 5 K as the next higher intermediate temperature. The thermal radiation shields and the HOM absorbers will need to be at some intermediate temperature between 5 K and 293 K. Detailed modeling shows a broad optimum at 100 K, as shown in Fig. 5.28.8. The models include analysis of the cold components and their material properties vs temperature as well as the Coefficients of Performance of refrigeration vs temperature derived from reports of manufacturers.

The distribution of wall-plug refrigeration power among cryomodule components for the 100 K intermediate temperature case is shown as a pie chart in Fig. 5.28.9. The SRF cavity dynamic load is about 52% of the total refrigeration load, with the dynamic HOM load being

Figure 5.28.8: Wall-plug refrigeration power for a 64-module ERL main Linac with the SRF cavities having $Q_0 = 2 \times 10^{10}$ as a function of the intermediate intercept temperature.

Figure 5.28.9: Distribution of wall-plug refrigeration power for the 64-module main Linac with a 100 K intermediate temperature.

the next largest. The thermal gradient along the beamline due to the HOM loads being held at 100 K contributes the most to the static heat load. Table 5.28.2 lists the heat loads and wall-plug power per cryomodule and for the full Linac at the 100 K optimum.

As noted in the section on the cryogenic system and utilities, two helium refrigeration companies were asked to make studies of refrigerators that could handle the estimated thermal loads then estimated. In their studies, they utilized available suites of compressors and expanders with some practical compromises for control systems. The reports are available as references [51] [52]. The calculated operating electric powers using the available compressors and expanders are reported in the utilities section with a safety factor of 1.5 included.

To validate the predicted ERL heat loads listed in Tab. 5.28.2, Tab. 5.28.3 shows the predicted and typical measured static heat loads for the late-model FLASH TTF-III cryomodules [53]. The measured static load to 2 K is about 25% higher than predicted, but the other measured static loads are very close to the predicted values. These measured heat loads would be accommodated by a cryoplant that had a 50% capacity safety factor.

5.28.13 Cryomodule vacuum system

During operation the cryopumping of the accelerating cavities dominates all other pumping in the cryomodules. The challenge is to develop a pump down strategy that minimizes the risk of contamination of the accelerating cavities. A single piece of dust (even in μm size) will lead to field emission lowering Q_0 and a possible quench of the cavity. A slow pump down sequence minimizes this risk. After the clean assembly of the cavity string in the cryomodule, the beam line will be pumped down and closed off by the beam line gate valves at either end of the cryomodule. The beam line will remain under vacuum during transport to the final location of the cryomodule. Cold cathode ion gauges will be used to monitor the beam line vacuum at all times. Leak testing will be carried out at each stage of the cryostat assembly following the procedures that were developed during the ICM assembly. These procedures were very similar to the one followed for the assembly of the FLASH cryomodules and the ones proposed for the XFEL cryomodules.

After placement of the cryo-modules in the Linac tunnel, interconnection vacuum beampipes will be installed to complete the Linac beamline vacuum. Each interconnection includes stainless steel beampipes, a flexible bellows (with proper RF-shielding or absorbers), a vacuum pumping port and gauge port. As the interconnections are enclosed in the Linac insulation vacuum walls, extensions are added to the pump/gauge port(s) to allow access to the port(s). Proper RF screens must be incorporated in the vacuum pump/gauge ports to minimize HOM heating at the screens. All components used on the interconnection (including ion pumps

Table 5.28.2: Heat loads and wall-plug power per cryomodule and for the full Linac with the SRF cavities having $Q_0 = 2 \times 10^{10}$.

Per Module	ERL Linac	
	Heat Load	Wall plug
1.8 Static (W)	7.28	5,240
1.8 Dynamic (W)	68.99	49,692
1.8 Total (W)	76.26	54,932
5 K Static (W)	45.16	8,882
5 K Dynamic (W)	25.65	5,045
5 K Total (W)	70.82	13,928
100 K Static (W)	50.09	598
100 K Dynamic (W)	1455.50	17,369
100 K Total (W)	1509.41	17,966
Module wall plug (W)		86,826
# modules	64	
Linac wall plug (W)		5.56×10^6
Safety factor	1.5	
Linac wall plug \times safety factor (W)		8.34×10^6

Table 5.28.3: Predicted and typical measured static heat loads for late-model FLASH TTF-III cryomodules.

Per Module	FLASH Predicted	FLASH Measured
2K Static (W)	2.80	3.5
4.5K Static (W)	13.90	13
70K Static (W)	76.80	78

and vacuum gauges) must be cleaned in a Class 100 clean room to remove particulates, and properly bagged for transportation to the site. A portable clean room capable achieving Class 100 will be set up to enclose the entire interconnection during the installation process.

The insulation vacuum will be maintained after initial pump down by the cryopumping of the outer surface of cavity helium vessels. There will be a pump port closed off by a suitable valve to allow this pump down. There will also be suitable ports to allow monitoring of the insulation vacuum along with appropriate gauges to continuously record the condition of the insulation vacuum. In case of sudden accidental release of cryogens inside the cryostat module, it will be equipped with safety blowoff ports that will require 10 psi overpressure to release.

5.28.14 Cryomodule instrumentation

Instrumentation for the cryomodule needs to be sufficient to correctly monitor the operation of the cryomodule. Since it will be replicated 64 times for the full Linac, care needs to be taken to avoid unnecessary monitoring. The required monitors would include helium level sensor

for the JT/2-phase-pipe, temperature sensors in a number of locations with different types of sensors depending on the requirements, helium pressure sensors, and low level rf probes for accelerating gradient control. In addition there will be the tuner stepper and piezo drives, heaters and cavity alignment sensor if experience with the prototype cryomodule currently under construction indicates that this will be needed. As with other aspects of the main Linac cryomodules, the final design of the instrumentation package will be guided by the experience from the ICM, FLASH, and the planning for the XFEL.

5.29 Manufacturing plan

The Cornell ERL program is presently in the development phase to prove out the performance of key components of the facility. A great deal of insight has already been gained from the ERL injector and other prototypes at Cornell. A prototype main Linac cryomodule will be designed and fabricated in the next two years. Following this, a final cryomodule design will be completed that is compatible with all of the contiguous infrastructure of the ERL facility. The highlights of the development phase of the main Linac are described in the next section, followed by a description of the production phase.

5.29.1 Main Linac prototype cryomodule

As part of the Cornell ERL development program, prototypes will be fabricated and tested for the main Linac SRF cavity, RF coupler, HOM loads, and cavity tuner. After establishing satisfactory performance of the prototypes, production versions will be fabricated to complete one full Linac cryomodule. In parallel, the rest of the Linac cryomodule will be designed and a full prototype fabricated. There are several logistical options available that will allow the 10 m long prototype cryomodule to be assembled at Cornell with minimal modification to the existing facilities.

Testing of the prototype Linac cryomodule will include the following high-level tasks of increasing complexity:

- Cryogenic test of cooldown, cavity alignment, and heat leaks
- RF test of the cavity field, Q , and microphonics.

The first test of cooldown can easily be accomplished with existing Cornell facilities. The RF test would require a modest RF source and radiation shielding around the test area due to field emission from the cavities. A beam test of dressed, prototype cavities (i.e. cavities with HOM absorbers), coupler and field probes attached, will be beam tested at high beam current using the prototype injector to measure the cryogenic consequences of high current running on HOM absorber heating and search for trapped modes that could engender BBU in the full linac.

5.29.2 Main Linac 64-module production

The pace for production of the 64 cryomodules for the ERL main Linac is targeted to be 2 cryomodules per month, requiring about 2.7 years to complete the full Linac, with 1-2 more

Figure 5.29.1: Block diagram of the space required for typical cryomodule production tasks to assemble two cryomodules per month.

months added to produce spare cryomodules. The production pace is determined by the size of the test and assembly facility (for comparison refer to [54]). Since this facility is comprised of costly components, such as a clean room and refrigeration plant, and would likely have a one-time use, it is unlikely that an industrial partner would invest in such a facility without a longer term use. It is possible that such facilities that will be required by other laboratories for cryomodule production programs could be utilized if they have no commitments in the ERL production time frame.

An example layout of a cryomodule production facility is shown in Fig. 5.29.1, which is sized to produce 2 cryomodules per month. The facility includes:

- Clean room with HPR-cavity rinse, vacuum and gas feeds, equipment lock air showers, and 2 beamline string assembly areas
- High bay assembly area to accommodate 3 modules, overhead crane access, an adjacent overhead door to allow flatbed truck entry for loading and unloading
- Cryomodule test area with radiation shielding
- Cavity chemistry etch area
- Cavity 120° C vacuum bake area
- Cavity vacuum furnace for H₂ de-gassing (800° C) or purification (1400° C)
- Cavity tuning equipment
- Cavity vertical test pits with radiation shielding
- Cavity helium vessel Ti welding area
- De-ionized water production and storage
- Liquid helium refrigeration plant including an LN₂ tank for cavity vertical test and module tests

The utilities for the production facility would include considerable AC power for the refrigeration plant and vacuum furnaces, a chilled water supply, and N₂ gas distribution from the LN₂ tank boil-off. It is possible that this facility could be erected in the existing Wilson Lab using existing portable shielding and the existing refrigeration plant.

5.30 Tunnel Filling

5.30.1 General Considerations

The tunnel is driven in two sections as shown in the overall layout Fig. ???. As discussed earlier, this affords the opportunity to compensate for wake-driven energy spread and other

Figure 5.30.1: Tunnel cross-section showing safety provision for persons passing, equipment placement, shielding and utility pipes and ducts.

transit time manipulations. For both economy and proximity of the low-level RF electronics to the cavities being controlled, the electronics and high power amplifiers are placed as close to the cryomodules as shown in Fig. 5.30.1.

There is expected to be significant radiation in the Linac tunnels because of field emission in the cavities, and the magnitude of this can be estimated from experience at FLASH [55]. Accordingly the electronics racks will be shielded by 6-inch thick panels of heavy concrete as shown in Fig. 5.30.1. The intention is to have the panels on sliders so that they can be moved easily for access to the electronics behind.

5.30.2 Utility considerations

Tunnel equipment requires water and forced air for cooling as well as electric power, clean nitrogen for venting, and compressed air for the activation of valves. The quantities are found in the utility tables in §???. A tentative disposition of the supply pipes and cables together with equipment placement is shown in Fig. 5.30.1.

5.30.3 Safety considerations

A primary determinant of the tunnel size is the requirement that a person can pass safely between the cryomodules in place and a cryomodule being transported in the tunnel for installation or removal as shown in Fig. 5.30.1. Ventilation by air at a velocity of 400 fpm is provided when the tunnel is occupied to sweep away helium spills, and fire barriers are provided to separate the tunnel from the x-ray halls. Proposals to achieve these safety objectives can be found in the architectural and conventional engineering report of the Arup company [56]. Helium safety matters are presented in §??.

References

- [1] Petersen, B. *Some aspects of the layout and optimization for the cryogenic supply of superconducting linacs*. Nucl. Instr. and Meth. A, **557** (1), pages 280 – 286 (2006). ISSN 0168-9002. doi:DOI:10.1016/j.nima.2005.10.084. Energy Recovering Linacs 2005 - Proceedings of the 32nd Advanced ICFA Beam Dynamics Workshop on Energy Recovering Linacs.
- [2] Rimmer, R. *Higher-order mode calculations, predictions and overview of damping schemes for energy recovering linacs*. Nucl. Instr. and Meth. A, **557** (1), pages 259 – 267 (2006). ISSN 0168-9002. doi:DOI:10.1016/j.nima.2005.10.080. Energy Recovering Linacs 2005 - Proceedings of the 32nd Advanced ICFA Beam Dynamics Workshop on Energy Recovering Linacs.

- [3] Marhauser, F., *et al.* *HOM Survey of the First CEBAF Upgrade Style Cavity Pair*. In *The 23rd Particle Accelerator Conference*, pages 2123–2125. Vancouver, British Columbia, Canada (2009).
- [4] Hammons, L. and H. Hahn. *HOM Absorber Development for BNL ERL Cryomodules*. In *The International Workshop on Energy Recovery Linacs, ERL09*. Ithaca, NY, USA (2009). <http://accelconf.web.cern.ch/accelconf/ERL2009/html/author.htm>.
- [5] Myakishev, D. G. and V. P. Yakovlev. *The new possibilities of SuperLANS code for evaluation of axisymmetric cavities*. In *1995 Particle Accelerator Conference (PAC95)*, pages 2348–2350. Dallas, Texas, USA (1995). <http://accelconf.web.cern.ch/AccelConf/p95/ARTICLES/MPC/MPC17.PDF>.
- [6] Valles, N. and M. Liepe. *Seven-Cell Cavity Optimization for Cornell’s Energy Recovery Linac*. In *2009 International Workshop of RF Superconductivity (SRF2009)*, pages 538–542. Berlin, Germany (2009). <http://accelconf.web.cern.ch/AccelConf/SRF2009/papers/thppo008.pdf>.
- [7] Hoffstaetter, G. and I. Bazarov. *Beam-Breakup Instability Theory for Energy Recovery Linacs*. *Phys. Rev. ST-AB*, **7**, page 054401 (2004). ISSN 0168-9002. doi:DOI:10.1103/PhysRevSTAB.7.054401.
- [8] Myakishev, D. *CLANS2-A Code for Calculation of Multipole Modes in Axisymmetric Cavities with Absorber Ferites*. In *1999 Particle Accelerator Conference (PAC1999)*, pages 2775–2777. New York, NV, USA (1999). <http://accelconf.web.cern.ch/AccelConf/p99/PAPERS/THA76.PDF>.
- [9] Buckley, B. and G. H. Hoffstaetter. *Transverse emittance dilution due to coupler kicks in linear accelerators*. *Phys. Rev. ST Accel. Beams*, **10** (11), page 111002 (Nov 2007). doi:10.1103/PhysRevSTAB.10.111002.
- [10] Matsumoto, H., *et al.* *Experience with a Zero Impedance Vacuum Flange at He Super-Leak Temperature for the ILC*. In *The tenth European Particle Accelerator Conference, EPAC’06*, pages 753–755. Edinburgh, Scotland (2006).
- [11] Zapfe-Duren, K., *et al.* *A New Flange Design for the Superconducting Cavities for TESLA*. In *The Eighth Workshop on RF Superconductivity*, pages 457–462. Abano Terme (Padova), Italy (1997).
- [12] Kurokouchi, S., S. Morita, and M. Okabe. *Characteristics of a taper-seal type gasket for the Conflat ®; sealing system*. *Journal of Vacuum Science Technology A: Vacuum, Surfaces, and Films*, **19** (6), pages 2963–2967 (November 2001). ISSN 0734-2101. doi: 10.1116/1.1415359.
- [13] Conway, Z. and M. Liepe. *Electromagnetic and Mechanical Properties of the Cornell ERL Injector Cryomodule*. In *2009 Particle Accelerator Conference (PAC09)*, pages 915–917. Vancouver, Canada (2009). <http://accelconf.web.cern.ch/AccelConf/PAC2009/papers/tu5pfp042.pdf>.

-
- [14] Padamsee, H. *RF Superconductivity for Accelerators*. John Wiley and Sons, Inc (1998).
- [15] Amuneal Manufacturing Corp., Philadelphia, PA <http://www.amuneal.com/>.
- [16] Singer, W. *et al.* *Preparation Phase for the 1.3 GHz Cavity Production of the European XFEL*. In *2010 International Particle Accelerator Conference (IPAC10)*, pages 3633–3635. Kyoto, Japan (2010). <http://accelconf.web.cern.ch/AccelConf/IPAC10/papers/thoara02.pdf>.
- [17] Kneisel, P. *SRF cavity technology*. In *International Accelerator School for Linear Colliders 19-27 May 2006*. Sokendai, Hayama, Japan (2006). http://linearcollider.org/files/ilc_school/Lecture_11_Peter_Kneisel.ppt.
- [18] Ciovati, G. *Effect of low-temperature baking on the radio-frequency properties of niobium superconducting cavities for particle accelerators*. *Journal of Applied Physics*, **96** (3), pages 1591 – 1600 (2004). ISSN 0021-8979. doi:DOI:10.1063/1.1767295.
- [19] Weise, H. *Superconducting EF Structures - Test Facilities and Results*. In *2003 Particle Accelerator Conference (PAC03)*, pages 673–677. Portland, Oregon (2003). <http://accelconf.web.cern.ch/Accelconf/p03/PAPERS/ROPC007.PDF>.
- [20] Valles, N. *et al.* *Exploring the Maximum Superheating Fields on Niobium*. In *14th International Conference on RF Superconductivity (SRF 2009)*, pages 406–410. Berlin, Germany (2009). <http://accelconf.web.cern.ch/AccelConf/SRF2009/papers/tuppo072.pdf>.
- [21] Bosland, P. and B. Wu. *Mechanical study of the Saclay piezo tuner PTS (Piezo Tuning System)*. Technical Report CARE-Note-2005-004-SRF, DAPNIA - CEA Saclay (2005). http://jra-srf.desy.de/sites/site_jra-srf/content/e86/e123/e125/e429/infoboxContent432/note-2005-004-SRF.pdf.
- [22] Liepe, M., W.D.-Moeller, and S. Simrock. *Dynamic Lorentz Force Compensation with a Fast Piezoelectric Tuner*. In *The 2001 Particle Accelerator Conference (PAC 2001)*, pages 1704–1706. Chicago, Illinois, USA (2001).
- [23] Bosotti, A., *et al.* *A fully automated device for checking XFEL piezo-tuner installation*. In *14th International Conference on RF Superconductivity (SRF 2009)*, pages 693–697. Berlin, Germany (2009). <http://accelconf.web.cern.ch/AccelConf/srf2009/papers/thppo049.pdf>.
- [24] Pagani, C., *et al.* *ILC Coaxial Blade Tuner*. In *The tenth European Particle Accelerator Conference, EPAC'06*, pages 466–468. Edinburgh, Scotland (2006). <http://accelconf.web.cern.ch/AccelConf/e06/PAPERS/MOPCH171.PDF>.
- [25] Neumann, A., *et al.* *Microphonics in CW TESLA Cavities and their Compensation with Fast Tuners*. In *12th International Conference on RF Superconductivity (SRF 2007)*, pages 377–383. Beijing, China (2007).
- [26] Kugeler, O. *Cavity Tuners*. In *The International Workshop on Energy Recovery Linacs, ERL09*. Ithaca, NY, USA (2009). <http://accelconf.web.cern.ch/accelconf/ERL2009/html/author.htm>.

- [27] Chojnacki, E. and W. J. Alton. *Beamline RF Load Development at Cornell*. In *1999 Particle Accelerator Conference*, pages 845–847. New York, USA (1999). <http://accelconf.web.cern.ch/AccelConf/p99/PAPERS/MOP77.PDF>.
- [28] Tajima, T., et al. *HOM Absorbers of Superconducting Cavities for KEKB*. In *European Particle Accelerator Conference, EPAC'96*, pages 2127–2129. Barcelona, Spain (1996). <http://accelconf.web.cern.ch/AccelConf/e96/PAPERS/WEPL/WEPO61L.PDF>.
- [29] Shemelin, V., M. Liepe, and H. Padamsee. *Characterization of ferrites at low temperature and high frequency*. Nucl. Instr. and Meth. A, **557** (1), pages 268 – 271 (2006). ISSN 0168-9002. doi:DOI:10.1016/j.nima.2005.10.081. Energy Recovering Linacs 2005 - Proceedings of the 32nd Advanced ICFA Beam Dynamics Workshop on Energy Recovering Linacs.
- [30] Chojnacki, E., et al. *DC Conductivity of RF Absorbing Materials*. In *14th International Conference on RF Superconductivity (SRF 2009)*, pages 643 –647. Berlin, Germany (2009). <http://accelconf.web.cern.ch/AccelConf/srf2009/papers/thppo035.pdf>.
- [31] *The European X-Ray Free-Electron Laser Technical Design Report (XFEL), DESY 2006-097*. Technical report. ISBN 978-3-935702-17-1 http://www.xfel.eu/documents/technical_documents/.
- [32] Sekutowicz, J. *Higher Order Mode Coupler for TESLA*. In *The Sixth Workshop on RF Superconductivity*, pages 426–439. Virginia, USA (1993). <http://accelconf.web.cern.ch/AccelConf/SRF93/papers/srf93g04.pdf>.
- [33] Watanabe, K., et al. *New HOM coupler design for ILC superconducting cavity*. Nucl. Instr. and Meth. A, **595** (2), pages 299 – 311 (2008). ISSN 0168-9002. doi:DOI:10.1016/j.nima.2008.06.048.
- [34] Kneisel, P. et al. *Testing of HOM Coupler Designs on a Single Cell Niobium Cavity*. In *2005 Particle Accelerator Conference*, pages 4012–4014. Knoxville, Tennessee (2005). <http://epaper.kek.jp/p05/PAPERS/TPPT077.PDF>.
- [35] Kim, S. et al. *Study on Fault Scenarios of Coaxial Type HOM Couplers in SRF Cavities*. In *2006 Linear Accelerator Conference (LINAC06)*, pages 770–772. Knoxville, Tennessee (2006). <http://accelconf.web.cern.ch/accelconf/106/PAPERS/THP081.PDF>.
- [36] Kazimi, R., et al. *Observation and Mitigation of Multipass BBU in CEBAF*. In *The eleventh European Particle Accelerator Conference, EPAC'08*, pages 2722–2724. Genoa, Italy (2008). <http://accelconf.web.cern.ch/AccelConf/e08/papers/wepp087.pdf>.
- [37] Campisi, I. et al. *CEBAF Cryomodules: Test Results and Status*. IEEE Transactions on Magnetics, **27** (2), pages 2300–2303 (1991). ISSN 0018-9464. doi:DOI:10.1109/20.133677.
- [38] Huang, Q., et al. *Carbon Nanotube RF Absorbing Materials*. In *14th International Conference on RF Superconductivity (SRF 2009)*, pages 648–651. Berlin, Germany (2009). <http://accelconf.web.cern.ch/AccelConf/srf2009/papers/thppo036.pdf>.
- [39] Belomestnykh, S. *Overview of input power coupler developments, pulsed and CW*. In *The 13th Workshop on RF Superconductivity*, pages 419–423. Beijing, China (2007).

-
- [40] Belomestnykh, S., *et al.* *High average power fundamental input couplers for the Cornell University ERL: requirements, design challenges and first ideas*. Technical Report Cornell LEPP Report ERL 02-8 (2002).
- [41] Moeller, W.-D. *High power coupler for the TESLA Test Facility*. In *9th Workshop on RF Superconductivity*, pages 577–581. Santa Fe, NM, USA (1999). For the TESLA Collaboration.
- [42] Dwersteg, B., *et al.* *TESLA RF Power Couplers Development at DESY*. In *Proceedings of the 10th Workshop on RF Superconductivity*, pages 443–447. Tsukuba, Japan (2001).
- [43] Veshcherevich, V., *et al.* *High power tests of input couplers for Cornell ERL injector*. In *The 13th Workshop on RF Superconductivity*, pages 517–519. Beijing, China (2007).
- [44] Veshcherevich, V. and S. Belomestnykh. *Input coupler for main linac of Cornell ERL*. In *The 14th International Conference on RF Superconductivity*, pages 534–545. Berlin, Germany (2009).
- [45] Yla-Oijala, P. *Electron multipacting in TESLA Cavities and Input Couplers*. Particle Accelerators, **63**, pages 105–137 (1999). <http://cdsweb.cern.ch/record/1120324/files/p105.pdf>.
- [46] A. Mikhailichenko and T. Moore. *Simple Procedure for Superconducting Coil Winding*. In *The 2001 Particle Accelerator Conference (PAC 2001)*, pages 3645–3647. Chicago, IL (2001).
- [47] Lorenz, R. *et al.* *Measurement of the Beam Position in the TESLA Test Facility*. In *1996 Linear Accelerator Conference (LINAC96)*, pages 527–529. Geneva, Switzerland (1996). <http://accelconf.web.cern.ch/accelconf/l96/PAPERS/TUP76.PDF>.
- [48] Amuneal Manufacturing Corp. Technical report, Philadelphia, PA, USA, Amumetal 4k (A4K) (2010). <http://www.amuneal.com/magnetic-shielding/idea-share/whats-new-cryogenic-shielding>.
- [49] Chojnacki, E., *et al.* *Design and Fabrication of the Cornell ERL Injector Cryomodule*. In *The eleventh European Particle Accelerator Conference, EPAC'08*, pages 844–846. Genoa, Italy (2008). <http://accelconf.web.cern.ch/AccelConf/e08/papers/mopp123.pdf>.
- [50] Chojnacki, E., *et al.* *Cryogenic Heat Load of the Cornell ERL Main Linac Cryomodule*. In *The 14th International Conference on RF Superconductivity*, pages 638–642. Berlin, Germany (2009). <http://accelconf.web.cern.ch/AccelConf/SRF2009/papers/thppo034.pdf>.
- [51] *Cryogenic Plant Study and Budgetary Estimate for ERL Facility, Proposal, November 2006*. Proposal submitted to CLASSE by Linde Kryotechnik, AG. Report is on file at Cornell.
- [52] *Helium Refrigeration system for the ERL Cornell Project – Technical Proposal, December, .* Technical report, Air Liquid (2006). Proposal submitted to CLASSE, Modified May, 2010.

- [53] Peterson, T. *An Overview of the International Linear Collider (ILC) Cryogenic System*. Cryogenic Operations Workshop at SLAC (May 09, 2006). <http://www.slac.stanford.edu/econf/C0605091/present/PETERSON.PDF>.
- [54] Napoly, O. *XFel Module Assembly at CEA-Saclay*. Fermilab Accelerator Seminar (February 17, 2009). <http://beamdocs.fnal.gov/AD-public/DocDB/ShowDocument?docid=3311>.
- [55] R.J. Hernandez Pinto, M. V., M. Otto. *Radiation Measurements in the FLASH Tunnel in Summer 2006*. Technical report, DESY, Hamburg (2006). DESY Technical Note 2006-04.
- [56] ARUP. *Energy Recovery Project Definition Design, Volume I Report*. Technical report (2010).

6 Cryogenics[Eric Smith]- 2nd draft 05/04

6.1 Overview

6.1.1 Thermal loads expected

Covering cooling stream temperatures provided, loads at each temperature static and dynamic, both for initial 1 mA milestone operation and for eventual 40 mA operation.

6.1.2 Use of existing Wilson Lab cryoplant

6.1.3 Subsystem Components

Changes to building infrastructure, such as transfer lines, pumping lines, pumping skids. Separate but similar systems for ICM and MLC, including use of heat exchanger cans (HXC) for modification of the primary LN₂, pressurized gaseous He and liquied helium (LHe) to more useful coolant streams.

6.2 Heat Exchanger Cans

6.2.1 Construction and Interfacing

6.2.2 Prior performance

6.3 Cryogenics for the Injector Cryomodule

6.3.1 Construction and Interfacing

(schematic diagram of coolant distribution, mention of some of the unusual demands related to high-average-current superconducting cavity use).

6.3.2 Prior performance

6.4 Cryogenics for the Main Linac Cryomodule

6.4.1 Construction and Interfacing

6.4.2 Prior performance

6.5 Sensors and Controls for the cryogenics system

6.6 Safety Issues (that have already been considered for our prior test operations)

6.7 Aspects still under development

Primarily microphonics isolation for the MLC, which is the subject of ongoing measurement and analysis, and which will likely be OK for the 1 mA operations stage, but needs to be improved for some cavities to meet the 40 mA plan-while this is mostly a difficulty for the SRF performance, it is not clear to what extent the cryogenic system including the pumping skids, contributes to the noise. Also a need to verify the ICM operation after its warmup and modifications in Newman, and transportation back to Wilson Lab.

References

7 Vacuum System [Yulin]- 1st draft due 04/28

7.1 Layout

Vacuum system layout will conform to the accelerator lattice layout. Accordingly, the vacuum system will consist of the following sections, as shown in Fig. 7.1.1.

- Injector and merger
- Main LINAC cryo-module
- Demerger and beam dump
- Spreaders and recombiners
- FFAG arcs and straight

The injector includes the electron gun and the injector cryo-module (ICM). This section is already exist from the Cornell Prototype ERL Injector project, and is to be relocated and re-used for the Cbeta project. The detail of this section is described in the Injection section of this report. The short merger beam line that connects the injector to the main LINAC is also described in the injector section.

The main LINAC cryo-module (MLC) is a self-containing accelerator section from vacuum system point of view, and is described in a separated section in this report. The interface between the MLC and the rest of the Cbeta vacuum system will be described in sub-section 4 below. The electron beams of 4 different energies (exiting and entering the MLC) will be split into four separated beampipes and then recombined into a single beampipe for optics and timing reasons. The most important feature of this section is to provide beam path length adjustments for each of four energy electron beams.

The FFAG arcs and long straight sections consist of more or less repetitive structures of magnets. Thus units of repetitive simple beampipes will be designed for the FFAG sections. The energy recovered electron beam (with lowest energy) is demerger into a high power beam dump. The beam dump transport beamline is also exist from the Cornell Prototype ERL Injector project, and is to be relocated and re-used for the Cbeta project.

7.2 Requirements and Design

Vacuum beampipes are part of beam transport system. A list of vacuum requirements and design considerations is given below.

- Produce adequate level of vacuum, through proper beampipe material selection and preparation, and vacuum pumping. The required level of vacuum will be determined by acceptable beam losses due to residual gas scattering, among other factors.

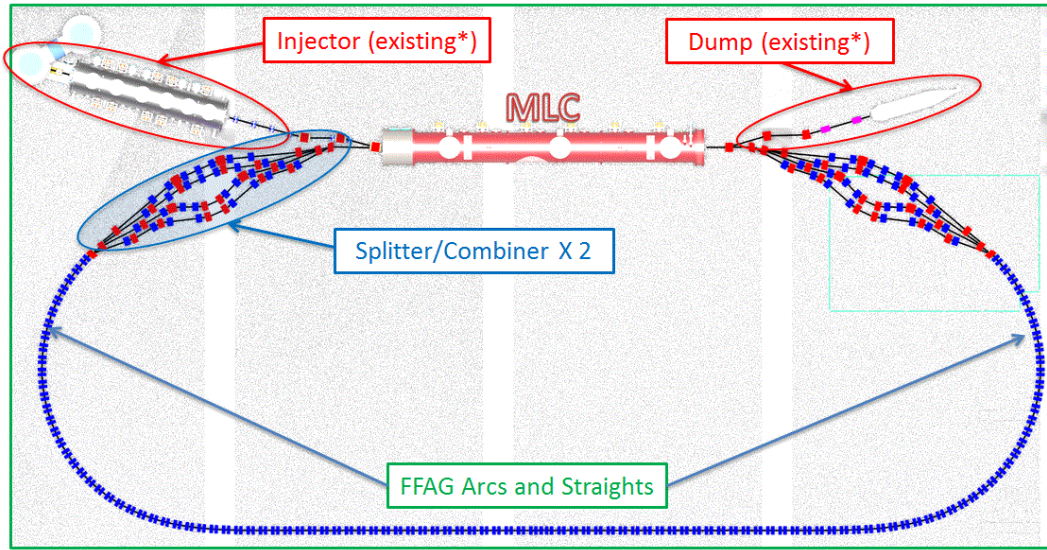


Figure 7.1.1

- Aluminum (6061-T6 or T4) is preferred material for the beampipes for its good electric conductivity (resistive-wall), no residual radioactivity (from beam losses) and low magnetization (from cold work and welding etc.)
- Provide sufficient large beam apertures, while allowing magnets position adjustment.
- With high beam current and closely spaced electron bunches, design efforts will be made to keep low beam impedance, including smooth beampipe inner profiles, RF shielded bellows and gate valves, gentle transitions between different beampipe cross sections, etc.
- Beampipes will host various beam instrumentation and diagnostics, such as BPMs and instrumentation ports (for beam viewers, etc.)

7.3 Construction, Installation and Operation

7.3.1 FFAG Arcs and Straight Sections

In the FFAG arcs and straight, permanent magnets are arranged in more or less periodic double-magnet cells. The relatively short drifts between magnets are reserved as much as possible for vacuum pumping, beam instrumentation. Therefore, it is efficient use of these drifts by constructing beampipe assembly through multiple FFAG magnet cells, reducing number of beampipe flanges. A typical 4-cell beampipe assembly is depicted in Fig. 7.3.1. The FFAG beampipes may be made of extruded 6061-T6 (or T4) aluminum with cross section designed to meet both required beam apertures and magnet clearances.

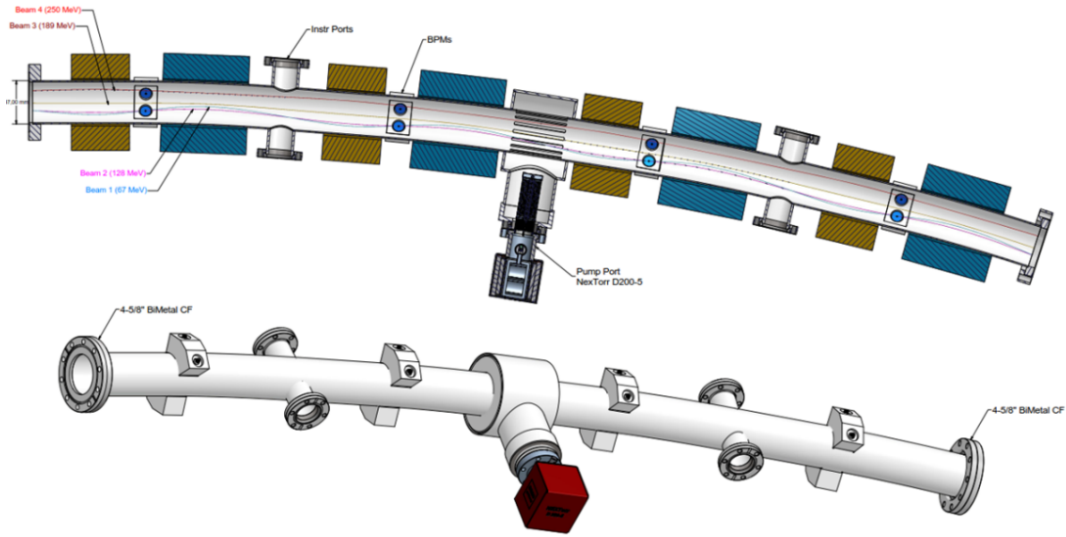


Figure 7.3.1: A suggest FFAG arc 4-cell beampipe design. The 1.6 m long beampipe assembly houses 4 sets of BPMs, two beam instrumentation ports and one pump port.

7.3.2 Spreaders and Recombiners

To keep low beam impedance, the beam splitting and combining vacuum chambers may be made of aluminum (6061-T6) with smooth beam path transitions, as illustrated by an example vacuum chamber used for the Cornell Prototype Injector project, in Fig. 7.3.2. The separated beampipes will be designed to allow independent beam path length adjustment by using sets of 4 RF-shielded bellows. Beam collimators (or/and scrappers) may also installed in these single beam chambers, together with BPMs and other beam instruments.

7.3.3 Ion Clearing

Ion trapping may not be avoidable without active clearing method, due to the nature of in the final CBETA CW beam operations. Low impedance clearing electrodes may be deployed at various locations to reduce ill-effect from the ion trapping. Thin electrodes directly deposited onto the interior walls of beampipes have been successfully deployed in CEsrTA and Super KEKB. A clearing electrode beampipe of this style was made and tested in the Cornell prototype ERL injector (see Fig. 7.3.3).

7.3.4 Construction and Installation

All vacuum beampipes will be fabricated following stringent UHV procedure and practice. All beampipe assemblies will be certified to be leak-free, and will be baked in vacuum up to 150 C. Most of the beampipes will be delivered to BNL to be assembled to the girder units. The baked beampipes will be back-filled with chemically filtered nitrogen (with moisture and THC at ppb level) for transportation and girder assembling. The same nitrogen system must be used to purge the beampipes whenever any flange is to be opened for connection, etc.

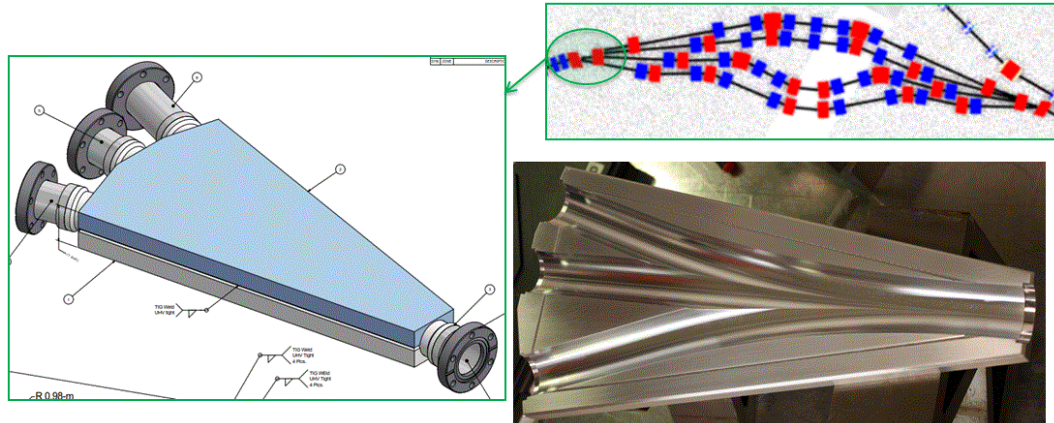


Figure 7.3.2: Example design for beam splitting and combing chamber, by welding two machined aluminum halves with smooth beam path transitions.

Operational experiences of Cornell prototype ERL injector, as well as CESR vacuum systems have demonstrated that in situ bakeout is not necessary with above beampipe preparation and installation procedures.

The injector, the ICM and the beam dump are to be installed and surveyed into locations. These sections are equipped with RF-shielded gate valves. The splitter/combiner and the FFAG sections will be installed in corresponding girder units. The detail installation sequence will be developed during the engineering design process to minimize air exposure of the vacuum beampipes. Further system and cost optimization will be carried out to decide if any additional RF-shielded gate valves are needed in these sections.

7.3.5 Pumping

With very limited spaces between magnets, compact and high capacity non-evaporable getter (NEG) pumps will be used, such as CapaciTorr (sintered NEG modular pump) and NexTorr (combination NEG and ion pump), see Fig. 7.3.4 for example pumps. The locations of pumps will be optimized during CBETA engineering designs, with aid of vacuum simulations (see Section 4).

7.3.6 Instrumentation

Ionization vacuum gauges and ion pumps will be used as primary vacuum signals. Residual gas analyzers (RGAs) will also be installed in strategic location for vacuum system diagnostics and in-situ trouble-shooting. Vacuum system inter-lock based on combinations of ion gauges, ion pumps and low vacuum gauges (such as Pirani gauges) will be implemented to protect critical accelerator components, such as the DC photo-cathode electron gun, ICM and MLC, etc.

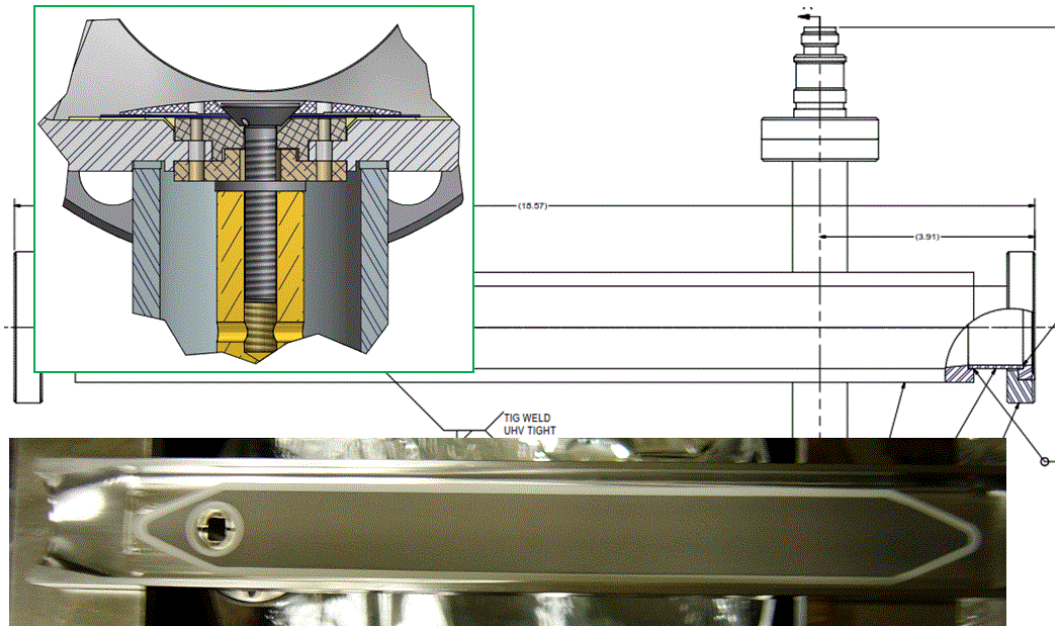


Figure 7.3.3: Low impedance ion clearing electrode chamber tested in the Cornell prototype ERL injector. The electrodes are made of a tungsten thin film (0.1 mm in thickness) on top of a thin (0.2 mm) alumina substrate. Both alumina and tungsten thin films are deposited via thermal-spray technique. A low profile electric connection is shown in the insert.

7.4 Vacuum Pumping Simulations

With highest beam energy of 200 MeV, synchrotron radiation induced gas desorption from the beampipe wall is negligible. Therefore thermal outgassing is the only source of gas in the beampipes. With pre-installation bakeout of all beampipes, and venting/purging with chemically filtered nitrogen, low thermal outgassing rate ($< 1^{-9}$ torr-l/s-cm²) can be achieved within 24 hour of pumpdown, and continuing decrease with time as $q = q_i t^{-\alpha}$, with $\alpha \sim 1$.

Vacuum system performance design will be aided by 3D vacuum simulations, using a 3D tracking program, MolFlow+ (<http://test-molflow.web.cern.ch/>). As examples, Fig. ?? compares simulated pressure profiles with two different pumping configurations in a 4-cell FFAG beampipe, and the results showed one pump per 4-cell beampipe is sufficient. Fig. 7.4.2 demonstrates the continuing improvement over time for a 4-cell FFAG beampipe with one pump per cell. Vacuum simulations will be carried out for all the CBETA sections as more engineering details of the beampipes becoming available.

References

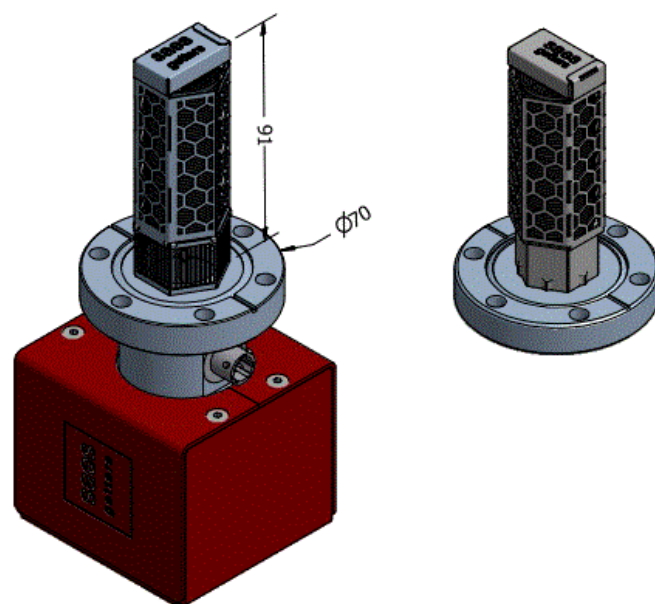


Figure 7.3.4: Typical vacuum pumps for CBETA vacuum system, with a 200-l/s NexTorr (left) and a 200-l/s CapaciTorr (right)

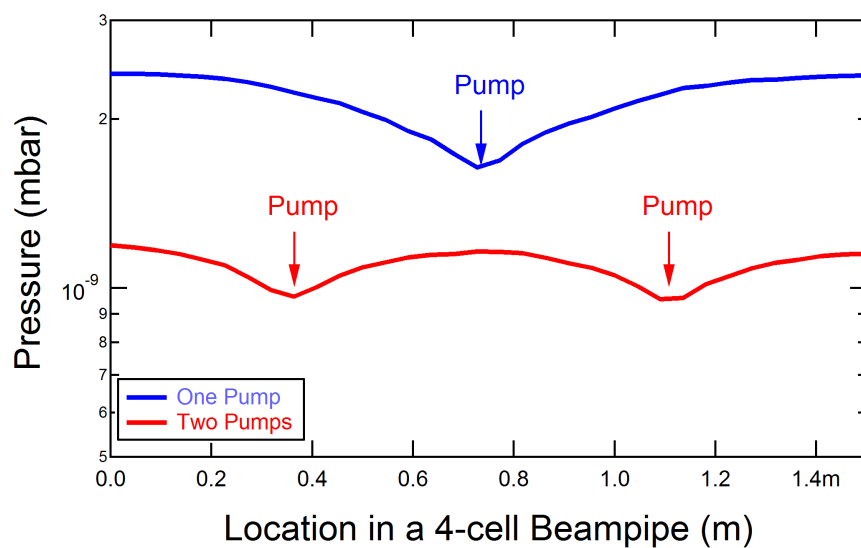


Figure 7.4.1

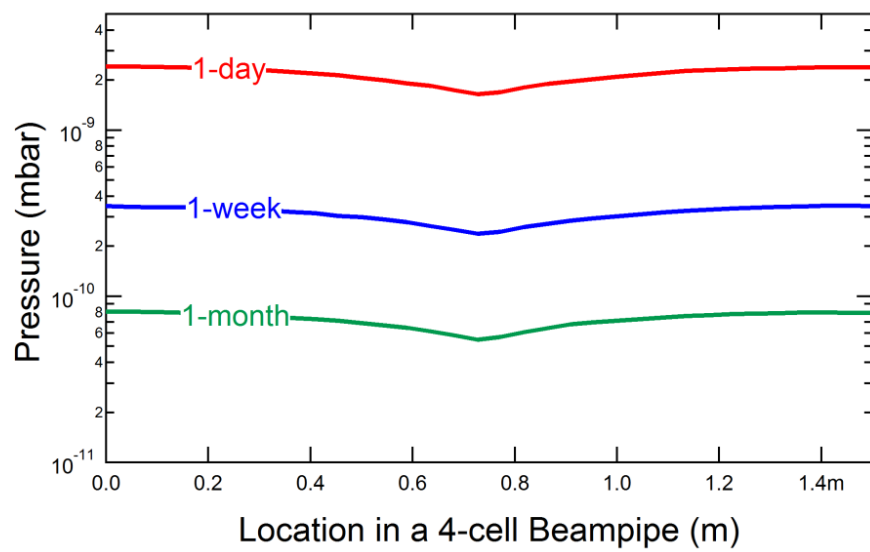


Figure 7.4.2

8 Diagnostics and Control[Dobbins]- 1st draft due 04/15

8.1 Introduction

The salient feature of $C\beta$ for diagnostics is the presence of multiple beams that need to be individually diagnosed and controlled. The following sections describe the components of the beam diagnostics and control system with particular attention given to how these components will handle multiple beams.

8.1.1 Beam position measurement system

The transverse beam size in the $C\beta$ FFAG arcs is measured in tens of microns. Lattice errors in the arcs that are a fraction of the beam size can lead to orbit oscillations which will degrade the beam quality. Somewhat larger lattice errors can lead to beam loss. Commissioning and operation of $C\beta$ will require the ability to measure and correct orbits at the micron level. While these tolerances are tight, they are within the state of the art in presently operating accelerators. $C\beta$ presents the additional requirement of measuring the orbit of multiple beams simultaneously.

$C\beta$ will support multiple operating modes, single pass and multi-pass/multi-energy, pulsed and CW, with and without energy recovery. Many of these modes are only intended for commissioning and machine studies. High current running of $C\beta$ is only possible with energy recovery. How the beam position monitor(BPM) system operates will be a function of the operating mode.

The RF cavities in the $C\beta$ linac operate at 1300 MHz. The injector must supply bunches at a sub-harmonic of this frequency. The multiple passes of these bunches through $C\beta$ produce inter-bunch timing patterns which depend on the injection frequency and the revolution period. Additionally the decelerating bunches must have a timing which is an integer + one-half RF cycles offset from the accelerating bunches.

Figure 1 illustrates the bunch timing pattern at the start of the the linac for bunches injected at 325 MHz. (1300/4 MHz.)

For the case of injection at 325 MHz the BPMs would see a different energy bunch with a different orbit every half RF cycle (385 pS). To resolve the orbit of each species the BPMs would need to be able to resolve signals from bunches separated by this amount. Moreover the FFAG optics correction requires being able to make orbit measurements at many locations, perhaps up to every other arc magnet cell. This would require a large number of high bandwidth electronics channels which would be prohibitively expensive. Additionally, the aggressive schedule for $C\beta$ precludes the development of new electronics solutions. A survey of existing BPM electronics indicates the ability to resolve bunches separated by several nS.

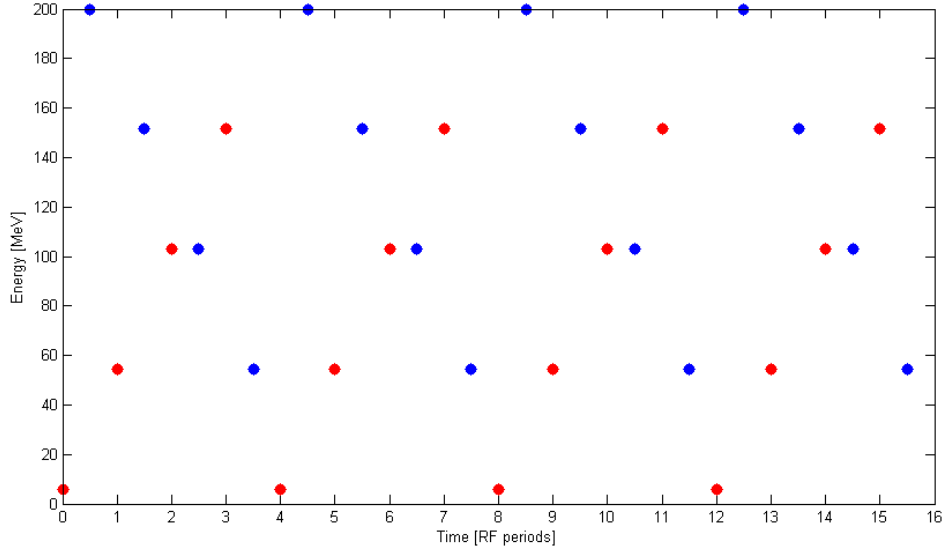


Figure 8.1.1: Bunches passing a reference point at the start of the linac, with one accelerating bunch and one decelerating bunch in every RF period. Red and blue dots represent accelerating and decelerating bunches, respectively.

Injection at lower frequencies produces more widely spaced bunches, however the time spacing of the bunches is generally irregular with some inter-bunch gaps being large and some small. The revolution period of C β is 333 RF cycles. For this revolution period a unique case exists for injection at 1300/63 MHz (20.635 MHz). This case results in regularly spaced bunches separated by nine RF buckets modified by the fact that accelerating bunches are offset by 1/2 RF cycle relative to decelerating bunches. The result is that the BPM will see signals from different energy beams separated by 8 1/2 or 9 RF cycles, i.e between 6 and 7 nS, within the time resolution capability of existing BPM system implementations. In this case a time-domain BPM system would acquire position information on each bunch which would then be averaged by species over multiple turns.

This mode of operation would provide orbit information for each species at each BPM which will be essential for machine commissioning. During commissioning injection can be further modulated (limited to trains of bunches at 1300/63 Mhz) to allow operation at very low currents but with bunch charge representative of high current operation. Injection at 1300/63 MHz will allow for for a per energy beam current of 2 mA at 100 pC bunch charge and therefore enables achievement of all the Key Performance Parameters.

Note the following provisos to this solution:

- This solution is tied to a specific revolution period, 333 RF cycles. If the revolution period is changed this solution can be broken.
- In full energy recovery operation, i.e. 4 accelerating and 4 decelerating passes in the linac, the bunch injected into the linac and the bunch being decelerated for delivery to the dump are only 1/2 RF cycle apart. There are no BPMs in the linac so this is not

an issue in the linac. however there are two sections of beam-line, the first between the ring injection point and the linac and the second between the linac and the exit to the dump, where resolving these two bunches will not be possible.

- Shaping of the BPM pick-up signal to a relatively flat top pulse without a long tail is required. This was accomplished in EMMA using a strip-line coupler and a mixer. [?]]
...

To operate at higher currents the injection scheme must change. One possible scheme is injection at 325 MHz (1300/4 MHz) with periodic gaps in the bunch stream containing a single pilot bunch. This is illustrated in Figure 2.

For the BPMs to see the pilot bunch separated from other bunches of different energy beams it is additionally necessary for the gap containing the pilot bunch to be preceded and followed by additional gaps separated from the pilot bunch gap by a revolution period. Figure 3 shows the gap containing pilot bunch plus additional preceding and following gaps.

The same time domain BPM electronics that is used in the low frequency injection scheme serves here also. Each BPM measures the pilot bunch as it passes with successively increasing then decreasing energy.

8.1.2 Bunch Arrival Monitors

Operation of $C\beta$ requires measurement and control of phase of the beam arrival at the linac relative to the RF.

In previous work frequency domain beam monitors have been developed for the injector which provide beam phase information. These monitors achieved a phase accuracy of 0.1° under typical operation conditions. The monitors compare the 1.3 GHz frequency component of the beam signal to the RF master oscillator signal. Similar monitors can function in the presence of two beams by measuring both the 1.3 GHz and 2.6 GHz frequency components of the beam signal. Placing these monitors near the end of end of the spreaders (where there are only two beams) just before the linac will provide the required bunch arrival time information.

The bunch arrival time is controlled through adjustment of the path length through the spreaders.

8.1.3 Beam Size

View screens with resolution of about 30 μm will be used to obtain the beam profile for low beam currents. While the beam size in the FFAG arcs is comparable to this the screens may still be useful for detecting conditions which cause the beam size to grow. In the spreaders the horizontal beam size will be larger due to dispersions and view screens will then provide useful quantitative measurements.

Two different screen materials will be used to cover several orders of magnitude in beam current: BeO that is sensitive to sub-nano-Ampere average currents, and less sensitive CVD diamond screens that can take up to 1 A of beam current. RF shielded assemblies will be employed throughout when the screens are retracted to minimize perturbations due to wakefields on the beam and heating effects.

View screens are a destructive monitor, observation of the beam results in elimination of all subsequent passes. For this reason one may not observe decelerating beams in $C\beta$ on view screens, i.e. a screen inserted to intercept a decelerating beam will first intercept the accelerating beam. In the FFAG arcs one can insert a view screen from the outer radius so as to intercept only the highest energy beam, or by inserting further intercept the next lower energy beam. The two lowest energy beams have insufficient horizontal separation to allow viewing the second energy beam while still allowing the lowest energy beam to pass.

8.1.4 Beam Loss Monitors

Beam losses in accelerator with continuous injection can contain high power. A high energy 20 μ m size electron beam of 40 mA is capable of drilling through a 3 mm thick aluminum beam pipe in as little as 10 μ s[?]. The radiation associated with partial beam losses can make operation of the accelerator problematic. Thus beam loss monitoring is required for both machine protection and facilitation of operation.

BPM based current measurements or wall current measurements comparing the current out of the injector to the current delivered to the dump can provide a measure of the total beam loss around the ring. At current levels high enough to present a prompt machine hazard this total loss measurement will be one input to the machine protection system.

Beam loss will additionally be monitored by gamma and neutron radiation detectors to provide localized measurements of losses around the ring.

References

9 Personnel Safety[Heltsley]- 1st draft due 04/28

9.1 General considerations

All CBeta-related activities will be organized and operated within CLASSE and its safety protocols. CLASSE holds no higher priorities than ensuring the health and safety of all. These values have been woven into the fabric of laboratory administration and operation. Synergistic relationships with CLASSE and Cornell University provide important policy guidance, institutional support, and oversight. The CLASSE approach to workplace safety is built around three overlapping commitments: to continuously provide a *safe laboratory environment*, to engender an abiding *culture of safety* in all personnel, and to address and anticipate safety challenges with *proactive management*.

The first line of defense against potential hazards is a *safe laboratory environment*. Exterior doors are locked outside of business hours; entry at off-hours is by keycard access or explicit permission of a staff member. Fire alarms are tied into the University centralized systems. State fire officials conduct inspections of the entire laboratory on an annual basis. Designated staff members are trained for specific roles in emergency situations. Only trained and/or licensed personnel operate industrial equipment, such as cranes, forklifts, and large vehicles. Machine tools are periodically inspected for correct operation and presence of appropriate guards. A spill control plan is in place for oil-filled transformers. An arc-flash hazard study of laboratory high-voltage AC distribution panels is nearly complete and recommended changes will be implemented soon. A lock-out/tag-out program is in place to cover work near equipment with remote power control, as is a policy governing hot work and welding. Personal protective equipment and safety training specific to their tasks is made available to workers who need it. Fume hoods for handling chemical samples are used, and detailed written safety procedures exist for hazardous tasks. MSDS are stored in notebooks near where the hazardous substances are used. Cryogenic installations and transfer lines are protected with sufficient insulation, redundant overpressure protections, oxygen-deficiency measurements where useful, and a multitude of instrumentation monitoring details of operation.

Radiation safety at CLASSE is regulated by Cornell's Environmental Health and Safety policies and authorized via a permit system, which are, in turn, governed by the New York State Department of Health (NY is an NRC-agreement state, and the regulations are embodied in 10 NYCRR Part 16¹). Cornell University is licensed by New York State to internally regulate radioactive material (RAM) and RPE, and has its own Radiation Safety Manual², Radiation Safety Officer (RSO), and Radiation Safety Committee (RSC).

¹https://www.health.ny.gov/environmental/radiological/radon/radioactive_material_licensing/docs/part16.pdf

²<https://sp.ehs.cornell.edu/lab-research-safety/radiation/radiation-safety-manual/Pages/default.aspx>

Mitigation of radiation hazards from radiation-producing equipment (RPE) is dealt with via redundant engineering controls and administrative controls as well. Permanent shielding, generally consisting of concrete, lead, and/or iron, surrounds all RPE so as to restrict potential exposure to personnel outside its shielding to below 2 mrem in one hour or 100 mrem in one year. Locations just outside the shielding where radiation dose rates are expected to be below those listed above but which are considered potentially vulnerable to higher levels, are designated as *controlled areas*, in accordance with Cornell University policy. Access to controlled areas is restricted to authorized personnel wearing radiation badges or those accompanying a CLASSE host with a real-time-readout dosimeter. Entrances to controlled areas are clearly signed. Exclusion areas, inside which personnel should not be present during RPE operation, are protected by more sophisticated access controls: all entryways are equipped with interlocked gates and/or light beams that, if tripped during RPE operation, cut power to the RPE and cause audible and visible alarms. Radiation detectors monitor the radiation in controlled areas, and trip off the RPE if conservative thresholds are exceeded. Exclusion area interlocks cannot be set until a full in-person search has been conducted; the integrity of interlock operation is verified by periodic operational tests of interlock components.

CLASSE seeks to establish and maintain a *culture of safety*, which entails much more than simply compliance with a set of rules. A culture of safety is embodied by: each of us taking responsibility for our own safety and that of people we work with, supervise, or host; safety being valued on par with scientific achievement and/or task completion; safety concerns always being taken seriously and promptly addressed; safety challenges being approached with intellectual rigor; new activities being planned from the start with safety in mind; new participants receiving relevant safety training immediately. Such practices are self-reinforcing, but can be undermined by even occasional lapses, so considerable vigilance on the part of supervisory personnel is required.

Proactive management ensures that: specific safety responsibilities of each staff member, student, user, or visitor are clearly delineated and communicated; appropriate training and resources are provided to those who need it; mechanisms are in place to maintain accountability and establish and publicize appropriate safety-related policies; compliance with relevant University and governmental safety and environmental regulations and ordinances is attained; and intra-university resources are leveraged when helpful.

CLASSE has an extensive online Safety Handbook³. A central safety document database has been implemented (using the CERN EDMS system) and is home to procedures, radiation permit applications, meeting minutes, internal incident reports, and more. An in-house training database has tracked safety training history for each worker for nearly ten years. Conversion to a University-wide Learning Management System (LMS) will occur in June 2016. The new LMS uses a Saba cloud-hosted and browser-based solution, and manages courses, classes, learner transcripts, and web-based content and assessments, allowing learners and administrators alike access to what they need to achieve safety objectives.

Clear lines of accountability for performance related to safety have been shown to be crucial to superior safety achievement, especially in academic research settings. The CLASSE Safety Committee and CLASSE Safety Director, which set, communicate, and implement laboratory safety policy, speak and act with the imprimatur of the CLASSE Laboratory Director, who

³<https://wiki.lepp.cornell.edu/lepp/bin/view/Safety/Handbook/WebHome>

appoints both. Each staff member is accountable to a supervisor, and each student to an advisor.

9.2 More on Radiation Safety

The ERL linac, including its gun, accelerating components (ICM), and beam dump(s), as well as the CBeta SRF main linac cryomodule (MLC) have already been operating safely and compliantly in the L0E high-bay area at Wilson Laboratory for several months; aside from the MLC, those components operated similarly in the adjacent L0 high-bay area for a decade prior. A Cornell University RPE permit is in force, and will be amended as upgrades toward CBeta progress. The current layout of shielding blocks, actively interlocked radiation monitors, area dosimeters, and entry interlocks will all be modified, in stages, as the project progresses.

9.3 Accident Rate and Training Compliance

Cornell University tracks all accidents, injuries and exposures for the campus as a whole, and CLASSE tracks its approximately 300 workers separately. One metric that allows for comparison with other institutions is that of OSHA's *Total Recordable Cases* (TRC), defined as the number of accidents, injuries, or exposures that results in treatment beyond first aid or lost work time, per 100 workers per year. Campus-wide the TRC rate has hovered just above 2 for many years, in line with other colleges and Universities. CLASSE has maintained a TRC rate below 2.0 for 15 years (as long as it has been tracked), and below 1.0 since 2013, comparable to the DOE-lab average trend over 15 years, as seen in Fig. 9.3.1.

CLASSE administers more than two-dozen internal safety trainings, each specific to a particular hazard at the Laboratory. Cornell University Environmental Health and Safety also provides a large assortment of general safety trainings, of which about two dozen are taken by Laboratory personnel. Most such trainings are recurring (meaning the training must be retaken periodically), with recurrence times ranging from one to five years (comporting with state and/or federal regulations when applicable). Many trainings are in-person instructor-led trainings (ILT) and many are web-based trainings (WBT). The new LMS will ease access to these trainings while minimizing the administrative burden. The learning plan of each worker is populated with courses appropriate to her duties: the average CLASSE worker has about eight such courses on their learning plan, with large variations from one person to the next, depending on duties. In recent years we have tracked compliance on a person-trainings basis (treating each course assigned to any worker as the countable item), and on a people basis (treating each worker as 100% compliant with all required trainings or not as the countable item). Since tracking these metrics began, compliance has improved up to 98% and 88%, respectively, as shown in Fig. 9.3.2. (Due to recurring courses, individuals can cycle out of compliance when a course expires but regain it by refreshing the training, so the individuals out of compliance are a constantly churning group of different people temporarily in that state.) New workers are not permitted to engage in hazardous activities until relevant training is completed.

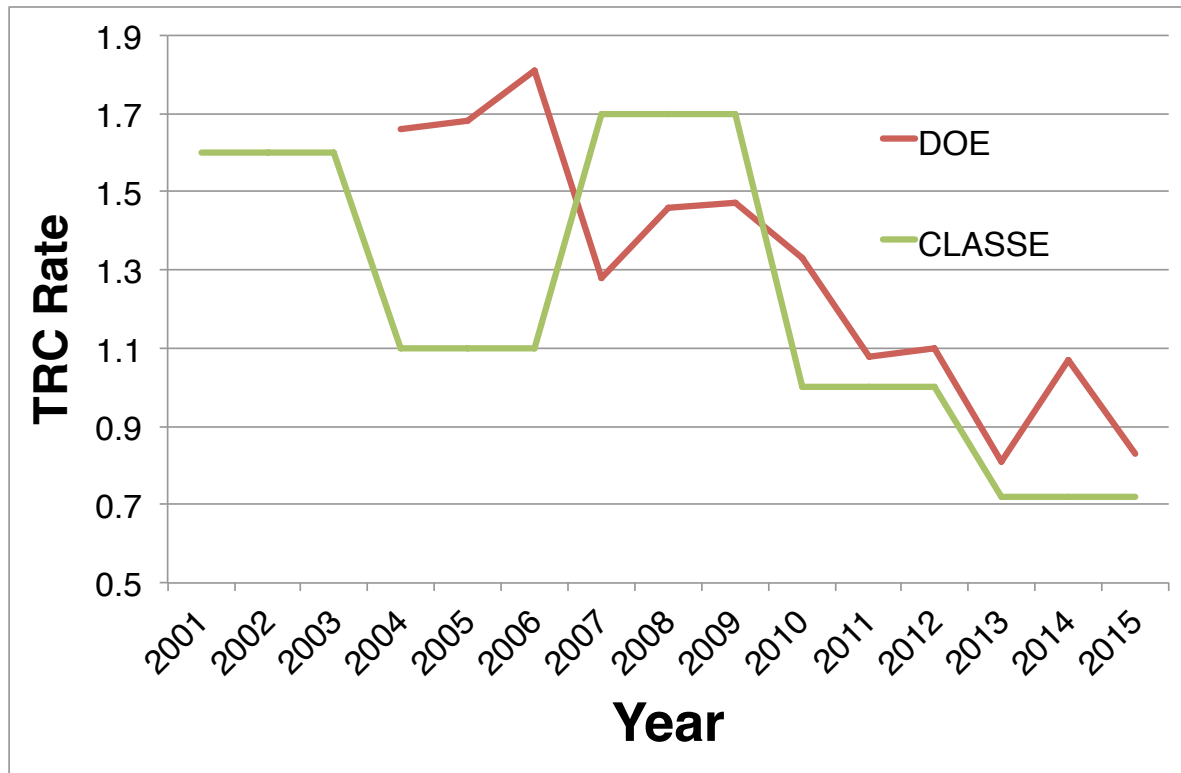


Figure 9.3.1: Accident rate at CLASSE and DOE-Lab-average vs. time. The TRC rate counts accidents that result in either lost time or treatment beyond first aid, or both, per 100 workers per year.

9.4 Cbeta-specific safety challenges

9.4.1 New collaborators

CLASSE already has a large variety of personnel using its facilities: technical staff, faculty, postdocs, undergraduate and graduate students, Cornell and (mostly) non-Cornell CHES users, and visiting scientists. New onsite CBeta collaborators will be subject to the same requirements as everyone else with regard to training and compliance.

9.4.2 Radiation safety

Personnel safety systems will be designed using similar criteria and equipment as other systems at CLASSE, meeting University and NY State standards. CLASSE has experience shielding electron beams at CESR, which have higher energy (5.3 GeV) and lower currents (~ 100 mA). Shielding will be designed with the largest credible beam loss scenario, and likely require iron-loaded concrete walls to a tunnel enclosing the ring on sides and top. The simulation tool MCNP will be employed for this task.



Figure 9.3.2: Compliance percentage for all CLASSE staff vs. time, where person-trainings counts each individual required training for each person as the countable unit, and people counts those with 100% compliance on all their required trainings relative to all CLASSE personnel.

9.4.3 Cryogenic safety

The CBeta cryogenic plant will be part of the larger CLASSE central facilities, which already satisfy CESR and existing ERL/MLC operations. Liquid helium and liquid nitrogen lines and volumes are designed to avoid trapped volumes and equipped with overpressure relief and backup burst disks, as elsewhere in the Laboratory. Particular attention will have to be paid to worst-credible-case accidents inside the shielding tunnel.

9.4.4 Electrical safety

All electrical lines are designed and built with best-practice criteria, including separation of high-voltage and low-voltage cable/conduit runs. Remotely powered equipment will be serviced with OSHA-compliant lock/tag/verify capabilities and procedures.

References

10 Commissioning

10.1 Overview

(This is still an early draft, with placeholder outline text, or reminders to myself.)

The overall plan is to first commission the injector and merger, with the goal of matching the target emittance and twiss parameters for a variety of bunch charges, booster settings, and linac settings. We also want to test our ability to correct settings using our online simulation. Next, the FFAG will be commissioned one pass at a time, first at zero average current then slowly raising the current to see what problems arise and when they arise.

10.2 Injector and Merger

These tests will be performed before the FFAG is completed, as preliminary tests of the injector components.

10.2.1 Injector through Merger

Procedure is already established and tested, we are just repeating here, with the exception that we are now also targeting specific twiss parameters at the end of the merger.

Notes:

Verify design injection energy (6 MeV) Calibrated dipole? BPM Phase? What precision is needed?

Measure H/V emittance below 1 mm-mrad at 100 pC

Match approximate alpha/beta functions before MLC

Determine how to change alpha/beta without affecting emittance

Similar settings for a variety of bunch charges / bunch lengths

10.2.2 Injector though Linac

Phase the MLC. Assume requires all cavities on to get beam through. Rough phasing: scan phase and watch RF forward power. Then use energy gain (dipoles) after cavities for fine tuning. Verify energy gain is correct. Calibrated dipole? What precision is needed?

10.3 FFAG First Pass

10.3.1 First Splitter

Alignment through 1st splitter. What needs to be checked here? How sensitive is the FFAG injection orbit?

10.3.2 FFAG

FFAG alignment. Align using transmission? How do we verify its on the design orbit? Are the BPMs positioned accurately enough for this?

Potentially requires physically moving magnets depending on how well they are made?

Look for correlations in the magnet corrections? E.g. if all corrections are low, then does that indicate something, such as the need to move magnets or restart injection orbit?

What will long term temperature stability do to all of this?

10.3.3 Second Splitter

Alignment / Path length in 2nd splitter Need to know bunches arrival phase with respect to 325 MHz (in the right bucket). How do we adjust phase coarse / fine?

10.3.4 First Pass Energy Recovery

Verify final energy = injection energy

Orbit into dump

10.4 First Pass High Current

Option 1: Raise current by increasing number of bunches? Is rejected beam badly matched to lattice? Estimate needed extinction ratio (currently it is 100 in this mode of usage)

Option 2: Raise current by increasing bunch charge. Need a path of optics settings to lead from 0 to full charge, roughly preserving FFAG twiss parameters. Or maybe we don't? Need to check simulation.

Require ≥ 1 mA operation, targeting significantly higher current.

Halo Management: Do we even have any free knobs to turn?

10.5 Multiple Passes

Orbit correction without ruining first pass.

Depending on bunch structure, may not be able to see all passes in high current mode. How do we monitor / maintain our orbit / optics?

What else is significantly different during subsequent passes? BBU becomes important. Machine protection becomes increasingly more important. What else?

10.6 Summary

This seems hard!

References

11 Cost Estimate[Bruce]- 1st draft 05/04

The project is divided into thirteen separate subsystems, described in the following list with the WBS number.

- 1.1 Project Management
- 1.2 Design and Accelerator Physics
- 1.3 Injector and Beam Dump
- 1.4 Linac and LLRF
- 1.5 Permanent Magnets and Girders
- 1.6 Conventional Magnets and Girders
- 1.7 Power Supplies
- 1.8 Instrumentation and Controls
- 1.9 Vacuum System
- 1.10 Cryogenics
- 1.11 Infrastructure and Installation
- 1.12 Commissioning
- 1.13 Safety

For each subsystem, the cost account manager prepared a cost estimate, including labor, equipment and M&S.

References